Università
Ca'Foscari
Venezia

UNIVERSITÀ
ITALO
FRANCESE

UNIVERSITÉ
FRANCO
ITALIENNE

Corso di Dottorato di ricerca

in Scienza e Gestione dei
Cambiamenti Climatici

ciclo 33

Tesi di Ricerca
in cotutela con Université Paris-Saclay

Dating and investigating climate variability at high resolution in the deep portion of the TALDICE ice core

SSD: GEO 08

Coordinatrice del Dottorato
Prof.ssa Enrica De Cian

Supervisori
Prof.ssa Barbara Stenni
Prof. Carlo Barbante

Supervisore cotutela
Prof.ssa Amaelle Landais

Dottoranda
Ilaria Crotti
956336

Abstract in Italian

Le carote di ghiaccio sono lunghi cilindri estratti dalle calotte polari e contengono informazioni riguardanti le passate condizioni climatiche ed ambientali. La carota di ghiaccio TALDICE, profonda 1620 m, é stata estratta a Talos Dome, in Antartide orientale. Studi precedenti si sono focalizzati sulla datazione di questo archivio e sulla costruzione della sua cronologia, che è stata definita fino alla profondità di 1438 m, corrispondente ad un'età di 150,000 anni fa. Questa tesi si concentra sull'esplorazione della porzione di TALDICE al di sotto di 1438 m di profondità.

Nella prima parte delle tesi, le nuove misure isotopiche effettuate sia nella matrice ghiaccio che in quella gas vengono utilizzate per costruire la scala d'età TALDICE deep1, con l'applicazione del modello IceChrono1. La cronologia della parte più profonda della carota è definita fino alla profondità di 1548 m ed estende il record climatico fino all'età di 343,000 anni. La seconda sezione della tesi è dedicata all'interpretazione del segnale isotopico di TALDICE durante i passati tre periodi interglaciali. L'ipotesi qui proposta è che le anomalie osservate nel segnale isotopico siano state prodotte dalla diminuzione dell'altitudine del sito di Talos Dome, dovuta alla perdita di volume di ghiaccio conseguente all'arretramento della linea di ancoraggio della calotta del bacino subglaciale Wilkes. La terza sezione della tesi è invece dedicata allo sviluppo della metodologia di datazione con l'argon, riducendo la quantità di ghiaccio necessaria. Questo nuovo metodo è applicato per datare 9 campioni di ghiaccio di TALDICE, e qui vengono presentati i risultati preliminari.

<u>Abstract in English</u>

Ice cores are long cylinders extracted from ice sheets containing information about past environmental and climatic conditions. The TALDICE ice core is a 1620 m depth core drilled at Talos Dome, in East Antarctica. Several previous studies focused on dating this core and an age scale has been defined only until 1438 m depth at an age of about 150,000 years ago, limiting the past climate reconstructions to the last climatic cycle. This thesis focuses on the poorly explored deep portion of the core below 1438 m depth.

In the first part of the thesis, new TALDICE isotopic measurements in both ice and gas matrixes below 1438 m are used to build the final TALDICE deep1 ice/gas age-depth relationship with the IceChrono1 model. The chronology for the deeper part of the core is here defined until 1548 m depth and extends the climatic record back to 343,000 years ago. The second part of this thesis is centred on the interpretation of the unique TALDICE isotopic signal during past interglacials. The proposed interpretation indicates that the interglacial anomalies in the isotopic record have been produced by lowering of the site elevation at Talos Dome due to ice loss and inland retreat of the Wilkes Subglacial Basin grounding line. The third and last part of this work focuses on the development of the argon dating technique, with the aim of reducing the amount of employed ice. This novel methodology has been tested on 9 TALDICE samples, and preliminary results are here shown.

Abstract in French

Les carottes de glace sont de longs cylindres extraits des couches de glace contenant des informations sur les conditions environnementales et climatiques passées. La carotte de glace TALDICE est une carotte de 1620 m de profondeur forée à Talos Dome, en Antarctique de l'Est. Plusieurs études antérieures se sont concentrées sur la datation de cette carotte et une échelle d'âge n'a été définie que jusqu'à 1438 m de profondeur à un âge d'environ 150 000 ans, limitant les reconstructions du climat passé au dernier cycle climatique.

Dans la première partie de la thèse, les nouvelles mesures isotopiques de TALDICE dans les matrices de glace et de gaz sous 1438 m sont utilisées pour construire la relation âge-profondeur finale de TALDICE deep1 glace/gas avec le modèle IceChrono1. La chronologie pour la partie profonde de la carotte est ici définie jusqu'à 1548 m de profondeur et étend l'enregistrement climatique jusqu'au 343,0000 ans. La deuxième partie de cette thèse est centrée sur l'interprétation du signal isotopique unique de TALDICE pendant les interglaciaires passés. L'interprétation proposée indique que les anomalies interglaciaires dans l'enregistrement isotopique ont été produites par l'abaissement de l'élévation du site du dôme de Talos en raison de la perte de glace et du retrait vers l'intérieur de la ligne d'ancrage du bassin sous-glaciaire de Wilkes. La troisième et dernière partie de ce travail se concentre sur le développement de la technique de datation à partir des isotopes de l'argon, dans le but de réduire la quantité de glace utilisée. La nouvelle méthodologie a été testée sur 9 échantillons TALDICE, et des résultats préliminaires sont présentés.

<u>Acknowledgements</u>

This thesis is the results of four amazing and challenging years of scientific research and personal growth.

First of all, I would like to thank my supervisors Barbara Stenni and Amaelle Landais who wonderfully supported me and provided scientific guidance during all my doctoral path. My gratitude also goes to Anais Orsi, who patiently introduced me to the Ar dating methods, and to Carlo Barbante, who provided constant support. I want also to thank Massimo Frezzotti for his willingness to share his great knowledge about TALDICE and Antarctica. My thanks go also to Aurélien Quiquet who provided great help on the modelling experiments and to all the other scientist who contributed to this scientific work.

My gratitude extends to the University of Venice and to the LSCE-CEA for the funding opportunity to undertake my studies and to the Università Italo-Francese/Université Franco-Italienne for the financial support.

I would like to extend my sincere thanks to Roxanne Jacob for her precious technical and human contribution and to Giuliano Dreossi and Frédéric Prié for their assistance in the lab. I am also thankful to my mentor Estelle Roth for her enlightening career and personal life advices.

In the end I want to thank all the amazing people that I met in Bologna, Venice and Paris who gifted me with their friendship. They turned those years into an extraordinary journey.

Last but not least, I am thankful to my family and especially to my mother for her endless support and love.

Table of Contents

Introduction and outline

The participants of the COP 26 that took place in Glasgow in November 2021 recognized the urgency to tackle human-induced climate change, limiting global warming to 1.5°C above pre-industrial level and drastically reducing the use of fossil fuels by 2050. The current global warming produces a large variety of effects on our planet, from the loss of biodiversity to the increase of sea level caused by oceans thermal expansion and melting of land ice.

The Antarctic Ice Sheet, which is the largest land ice reservoir on Earth, has been largely subjected to ice loss due to the increase of oceanic temperatures in the last decades (The IMBIE Team, 2018). However, the response of Antarctica to future warming is still under debate (Fox-Kemper et al., 2021). To improve the quality of future predictions is necessary to understand how the Antarctic Ice Sheet responded to past oceanic and atmospheric warming events. The analysis of tracers trapped in the ice and in the air bubbles from Antarctic ice cores can help answering this question.

The TALDICE ice core is a 1620 m deep archive drilled at Talos Dome, an ice dome located at the periphery of the East Antarctic plateau. The Talos Dome site has been considered sensitive to sea level fluctuations, compared to other sites of the East Antarctic ice sheet, since the ice at the site flows towards the reverse-slope Wilkes Subglacial Basin, which is mostly below sea level and sensitive to warm water intrusions (Warner & Budd, 1998). The core has been extensively studied in the last decade, however its chronology and the past climate reconstruction have been extended only until 150 thousands years ago (ka), at a depth of 1438 m (Bazin et al., 2013). The isotopic signal (δD and δ^{18}O) revealed a unique feature in comparison to the other Antarctic cores during both the Holocene and the Last Interglacial (LIG or Marine Isotopic Stage -MIS- 5.5), consisting in presence of a second peak before the glacial inception, not observed in the other Antarctic ice cores signal (Masson Delmotte et al., 2011). Such peculiar record has been interpreted as an expression of the sensitivity of the TALDICE isotopic record to localized sea ice extent in the Ross Sea (Mezgec et al., 2017) and/or local elevation changes (Bradley et al., 2013; Goursaud et al., 2020; Sutter et al., 2020).

This thesis focuses on the investigation of the deeper and unexplored part (below 1438 m depth to the bottom) of the TALDICE ice core. In particular, the main objectives consist in extending the chronology for the portion of the core below 1438 m depth and interpreting the new high-resolution (5cm) isotopic records (δD and δ^{18}O). In addition, new developments of the Ar dating technique (copper method) have been tested on TALDICE ice samples.

This thesis is subdivided in 5 chapters. The first chapter consists in a broad introduction to ice core science and a deeper focus on the TALDICE project, providing a literature overview on previous studies and highlighting the main research questions that are tackled in this thesis. Chapter 2 focuses on the analytical methods applied in this thesis. In particular, water stable isotopes in the ice matrix (δD and δ^{18}O) and oxygen and nitrogen isotopes in the gas matrix ($\delta^{18}O_{atm}$, δ^{15}N and $\delta O_2/N_2$) are presented

and their signal interpretation (not only climatic) is explained. The analytical techniques of Cavity Ring Down Spectroscopy and Mass Spectrometry are introduced. In this chapter the principles on which is based the ^{81}Kr dating technique applied on 3 TALDICE samples, and the Atom Trap Trace Analysis methodology, are presented. The third chapter presents the published paper by Crotti et al. (2021) centred on the construction of the TALDICE deep1 chronology for the core below 1438 m depth. The age-depth relationship is based on new measurements of δD, $\delta^{18}O_{atm}$, $\delta^{15}N$ and $\delta O_2/N_2$ and the application of the IceChrono1 probabilistic model (Parrenin et al., 2015). In addition, three layers have been dated with the ^{81}Kr technique, to provide absolute age values. Chapter 4 consists in a manuscript (submitted) focused on the interpretation of the new TALDICE $\delta^{18}O$ record during the past three interglacials MIS 5.5, 7.5 and 9.3. The investigation is performed through the comparison of $\delta^{18}O$, ssNa$^+$ fluxes and *d*-excess TALDICE records with the U1361A marine sediment core record and GRISLI ice sheet modelling experiments. The last and fifth chapter of this work presents the results of new developments of the Ar dating copper method technique (Kobashi et al., 2008; Severinghaus et al., 2003), aiming at reducing the sample size, applied on TALDICE samples and its comparison to the getter technique (Bender et al., 2008). The results obtained with both techniques are compared to the TALDICE chronologies in order to evaluate the two different Ar dating methodologies.

1 <u>State of the art</u>

1.1   Ice cores as climate archives

Ice cores are cylinders of ice drilled from ice sheets and glaciers. They can be defined as frozen time capsules holding information of the past climate. Data contained in ice and in air bubbles represent helpful tools to understand dynamics and processes of past climate variations, and to improve predictions of future climate change and impacts on our society.

1.1.2   Historical background

The study of ice cores as archives of past climate is a relatively new field, which greatly developed in the last 70 years. In the early 1930's scientists started to focus their attention on the interior of ice sheets through adventurous expeditions in Greenland and Spitzbergen (Svalbard Islands), where they collected snow pit samples. During the Alfred Wegener Expedition to central Greenland (1930–1931) the glaciologist Ernst Sorge examined the structural features and physical properties of snow pit profiles and determined the characteristics of the individual limits of annual snow accumulation (Langway, 2008). This finding validated the hypothesis that annual snow accumulation cycles could be preserved in ice sheets and unlocked the door to the future studies on ice cores.

The intuition that ice sheets may conserve traces of past climatic conditions came first to Willi Dansgaard during the 1950's, when he was a young researcher at the Biophysical Laboratory in Copenhagen. At that time, he started to wonder if rainwater isotopic composition might change depending on the temperature of the precipitation and if old water, contained in glaciers ice, may still carry information about past temperatures. His fortunate encounter with Per Scholander in 1956, who introduced Dansgaard to the idea that air bubbles trapped in the ice may conserve the past atmospheric composition, led the two of them to Greenland with the aim of studying icebergs to prove their theories. This encounter boosted Dansgaard's future research efforts and set the basis of ice cores science as we know it.

Figure 1.1 :Pictures of collection icebergs samples during the "Bubble Expedition" in 1958 (Dansgaard, Frozen Annals).

Several great campaigns and ice coring scientific programs followed Dansgaard's famous "Bubble Expedition" (Figure 1.1), with the aim of drilling and analysing long ice cores from the largest ice sheets on Earth which could provide hints on the past climate of our planet.

1.1.3 Ice sheets are time capsules

Greenland and Antarctica, which started growing respectively 34 Ma and 3 Ma ago (Bo et al., 2009; Lunt et al., 2008), represent the most suitable areas to conduct research on the ice core field since they provide deep and isolated ice sheets, ideal to drill long ice cores. Permanent cold climatic conditions allow the preservation of snow -and then ice- up to several hundreds of thousands years (ka). Antarctica contains the largest ice sheet, which complete melting may potentially contribute up to 58 m to sea level increase (Fretwell et al., 2013), while Greenland 7.2 m (Aschwanden et al., 2019).
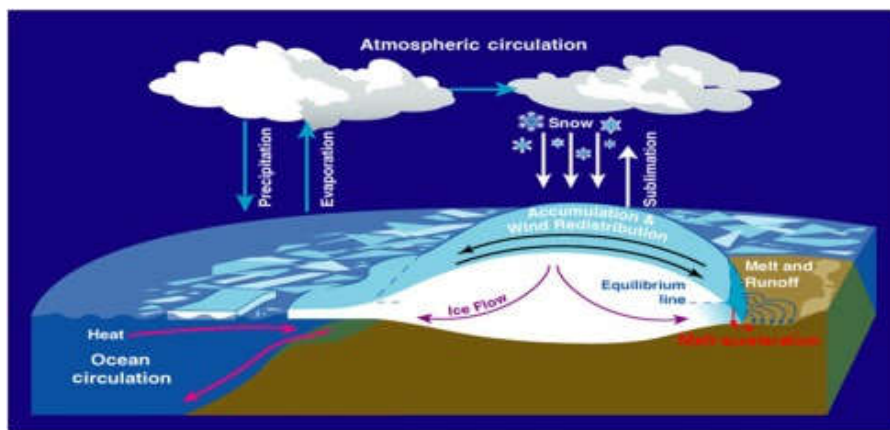
Figure 1.2: Schematic of main processes acting on Antarctic ice sheet (Hanna et al., 2020).

Ice sheets have been formed through millennia of continuous snow layers' deposition (Figure 1.2), reaching thickness of the order of kilometres. Snow layers may take centuries or even millennia, depending on the snow accumulation rate and temperature at the site, before turning into ice. Such slow process allows the formation, with depth, of an intermediate porous medium called firn, in which exchanges of air with the atmosphere are still possible. Once the firn reaches the critical density of 800 kgm^{-3} it turns into ice, and all the air gets trapped inside bubbles with no further exchange with the atmosphere.

Air masses that turn into snow carry with them several chemical compounds, pollens, dust and various isotopic species coming from source regions of humidity, from the atmosphere, continents or collected during their path to Antarctica or Greenland. When snow turns into firn and then ice, it creates a unique environment where tracers may be conserved in the ice matrix or trapped in the sealed air bubbles in the innermost layers of the ice sheets. The analysis of those compounds in the ice or in the gas matrix, provide scientists the unique chance to reconstruct past environmental and climatic changes, as well as past atmospheric composition. A great variety of chemical elements, compounds and even

micro-fossils could be found and analysed in the ice. Here a short list of the most studied and well-known proxies in ice cores:

a) *Stable water isotopes ($\delta^{18}O$ and δD):* the isotopic composition of water molecules in the ice has been firstly identified by Dansgaard (1964) as tracer to reconstruct past temperatures. Depending on the time resolution of the ice archive, seasonal to millennial temperature variations can be studied. In addition, the second order parameter *d-excess*= δD - $8 \cdot \delta^{18}O$ carries information about conditions prevailing in the moisture source regions (Stenni et al., 2001). A full detailed explanation of those tracers is available in Chapter 2.

b) *Aerosols* are suspended particles in atmosphere, whose dimension ranges from a few nanometres to tens of micrometres. These particles result from direct emission (sea salt, mineral dust) into the atmosphere or as products from chemical reactions (sulphate, nitrate, ammonium) occurring in the atmosphere. Aerosols trapped in ice cores can be used to reconstruct a great variety of past climatic/environmental conditions in their source regions, from sea ice extension (Abram et al., 2013), to continental dustiness (Abram et al., 2013), as well as large-scale atmospheric transport patterns (Fischer et al., 2007). In addition, peaks in sulphate aerosols represent signatures of past volcanic eruptions (Severi et al., 2012).
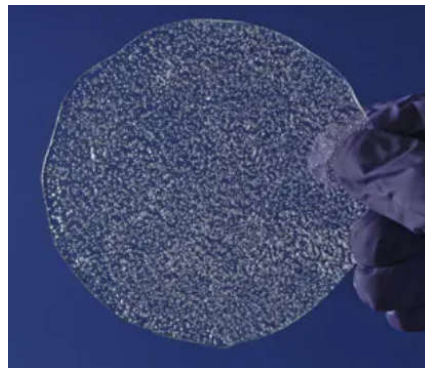
Figure 1.3: A slice of ice core where is possible to clearly observe trapped air (British Antarctic Survey).

c) *Greenhouse gases (GHGs)* concentrations in atmosphere have been continuously measured only in the past 60 years. The analysis of air bubbles trapped in ice sheet deep layers (Figure 1.3) allowed identification of the sharp increase of GHGs (as CO_2 and CH_4) concentration in the last century due to the anthropogenic emissions, and the reconstruction of the natural atmospheric composition of the last 800 ka provided by the EPICA Dome C deep ice core (Loulergue et al., 2008; Lüthi et al., 2008). However, the gas trapping process in the ice matrix requires a long time (from centuries to millennia), depending on the accumulation rate and temperatures at the site. For this reason, the air enclosed in the bubbles is always younger in comparison to the surrounding ice, and this difference is called Δage.

d) *Stable isotopes in gases* represent another set of records that could be analysed in air bubbles. Several isotopes of main elements as oxygen, nitrogen and their ratios ($\delta^{18}O_{atm}$, $\delta^{15}N$ and $\delta O_2/N_2$)

and other trace elements (as [81]Kr) have been used as dating tools as well as to reconstruct low latitude water cycle and processes acting in the firn (Landais et al., 2006, 2010a) (full details are provided in Chapter 2).

1.1.4 Drilling projects
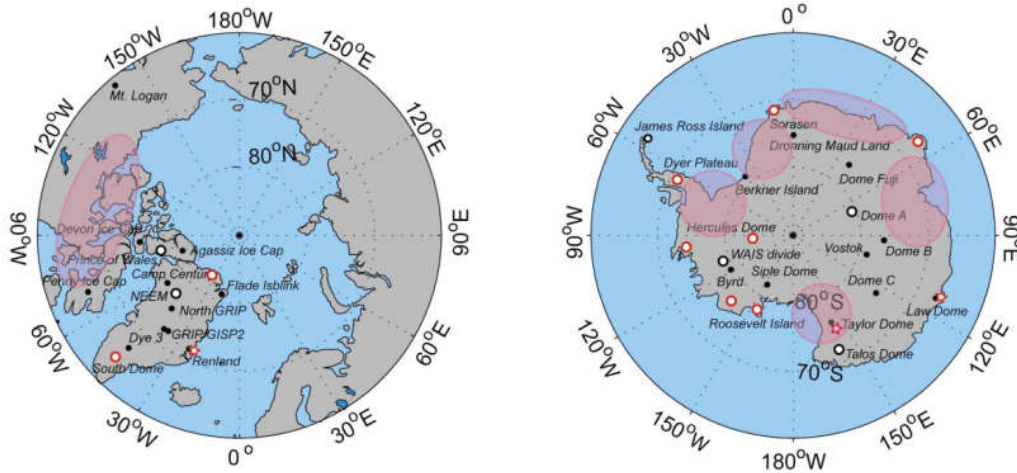
Figure 1.4: Maps of Antarctica and Greenland showing the main ice core drilling sites (Jouzel, 2013).

The temporal resolution of paleoclimatic records and the time spanned from ice core records strictly depend on the drilling site geographical position and on the annual snow accumulation rate. Greenland and peripheral Antarctic ice cores (Figure 1.4) contain highly expanded records, where the annual snow layers can be directly or indirectly identified, while central Antarctic ice cores provide condensed and longer records, with lower time resolution (from decadal to centennial resolution for the ice phase and centennial up to millennial for the gas phase) (Orombelli et al., 2010). The oldest ice core has been drilled in Antarctica, covering the past 8 climatic cycles up to the Lower Pleistocene (EPICA community members, 2004), while Greenlandic ice cores span the Holocene and Upper Pleistocene (North Greenland Ice Core Project Members, 2004). Here below some of the main drilling projects in Antarctica and Greenland are reported:

i. *Antarctica*

    a) *Vostok (VK)* is the first deep ice core that was drilled in the Antarctic Plateau by the Russian team. At that time glaciologists wanted to make their contribution to establish the validity of the Milankovitch theory of ice ages, but no ice core extending beyond the last glacial period was available. The first drilling started in 1980, but due to several technical issues, mainly consisting in the blockage of the drilling system, three different cores have been retrieved, with the support of the French and US teams. The third and final core drilling started in 1990 and a depth of 3350 m was reached in January 1996, with an estimated age of 420 ka at 3310 m (Petit et al. 1999). The deep drilling continued until 2012, when the drilling finally reached above the interface with the subglacial

Lake Vostok, at 3,750 m depth (Cressey, 2012). However, the ice in the deeper portion of the core (below 3310 m depth until 120 m above the interface with the subglacial Lake Vostok) is mixed, making the climatic interpretation of the records difficult (Jouzel, 2013) (Figure 1.5). One of the main scientific impacts of the Vostok project was the observation of the great increase of CO_2 and CH_4 concentrations during the past two hundred years caused by anthropogenic emissions and the connection to the recent global warming (IPCC, 1992).
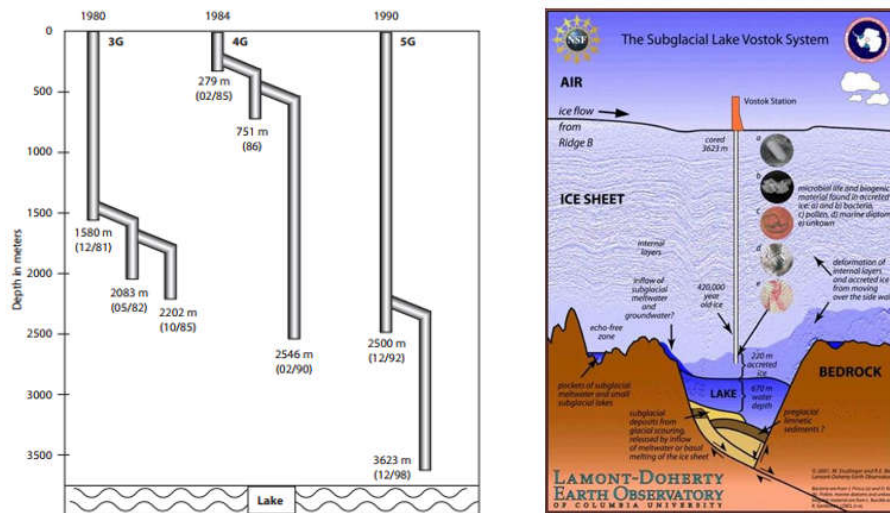
Figure 1.5: Left. Schematic of the historical path of the Vostok drilling project (Jouzel, 2013) Right. Vostok drilling and bedrock/subglacial lake system (Lamont-Doherty Earth Observatory).

b) *EPICA Dome C (EDC)* probably represents the most famous drilling project as, by now, provided the oldest ice core spanning 8 glacial/interglacial cycles, up to 800 ka (EPICA community members, 2004). The Dome C drilling started in the year 1996 and ended in 2005, extracting a 3270 m long core. The EPICA Dome C project allowed to reconstruct the greenhouse gases (CO_2 and CH_4) record back to 800 ka (Figure 1.6), confirming the climatic role of the anthropogenic GHGs emissions (Jouzel, 2013).

c) *Dome Fuji (DF) and West Antarctic Ice Sheet (WAIS)* represent two other well studied ice core records. The DF record is a composite record made by 2 cores drilled in the Atlantic Sector of the East Antarctic Plateau, DF1 has been drilled during the season 1996 and DF2 during the season 2007. The composite record of the 2 cores reaches the depth of 3035 m and covers the past 720 ka and, with EDC and Vostok, represents one of the oldest ice core ever drilled (Uemura et al., 2012, 2018). The WAIS ice core drilling operations ended in 2011, in the centre of West Antarctica. The project allowed to obtain one of the longest Antarctic ice cores, 3404 m depth, spanning the past 68 ka at extremely high resolution. In addition, the peculiar position of the core

helped in reconstructing past dynamics of the vulnerable Western Antarctic Ice Sheet (Buizert et al., 2015; Payne et al., 2004).
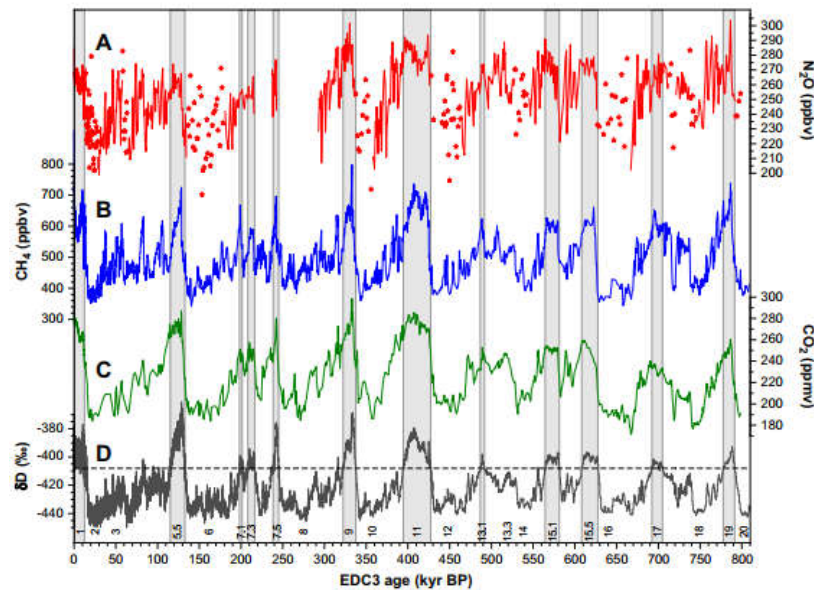
Figure1.6: Reconstruction of greenhouse gas concentrations from Antarctic ice cores. (A) Red: EDC N_2O. (B) Blue: EDC CH_4 (C) Green: Vostok CO_2 between 20 and 390 ka, EDC CO_2 elsewhere. (D) Dark grey: EDC δD. Grey shaded areas mark interglacials. N_2O, CH_4, CO_2 and δD are plotted on the EDC3 time scale (Schilt et al., 2010).

d) *Talos Dome Ice Core (TALDICE)* is a 1620 m long core drilled by the Italian-French team in 2004-2008 at the periphery of the East Antarctic Plateau, in the Ross Sea Sector. Several dating efforts have been performed to date the first 1438 m back to ~150 ka (Bazin et al., 2013). More details on the TALDICE ice core are available in Section 1.3.

ii. **Greenland**

a) *Summit (GRIP and GISP2)* are two deep ice cores drilled at the beginning of the 1990's in central Greenland, respectively 3027 m and 3053 m long, have played a key role in documenting rapid climate changes during the Last Glacial period. However, due to the disturbances in the deep portion close to the bedrock, it quickly became clear that it was not possible to extend the climatic record back into the Eemian (the Last Interglacial period) (Chappellaz et al., 1997).

b) *North Greenland Ice Core Project (NGRIP)* drilling was motivated by the necessity to extend the climatic record of the Northern Hemisphere back to LIG period. The NGRIP core, with its 3085 m long core, was drilled between 1996 and 2003 and provided an extended climatic record back to 120 ka (North Greenland Ice Core Project members, 2004) (Figure 1.7).

c) *NEEM* ice core has been drilled during the seasons 2008-2012 with the aim of obtaining a full record for the Eemian interglacial (115-130 ka) from a Greenland ice core. The core is 2540 m long, but the reconstruction of the past climate was possible only until

2206 m depth at 108 ka since below this depth the ice is disturbed and folded (NEEM community members, 2013).
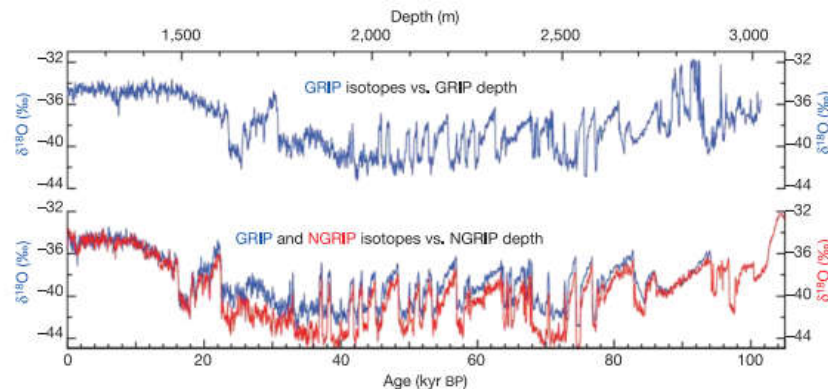
Figure 1.7: Top. The GRIP oxygen isotopic profile - δ^{18}O - (blue) with respect to depth at GRIP. Bottom. The NGRIP oxygen isotopic profile - δ^{18}O - (red) with respect to depth at NGRIP and the GRIP record (blue) plotted on the NGRIP depth scale (North Greenland Ice Core Project members, 2004).

1.2   Dating ice cores

Accurate timescales are fundamental for reliable interpretation of paleoclimate archives (Winstrup et al., 2019) and in this Section (1.2.1) the most common ice core dating methods are summarized, and in Section 1.2.2 the new dating techniques employed in this thesis work are briefly introduced.

1.2.1   Classic approaches

Different dating methodologies have been developed in the last 60 years to provide accurate age scales of ice cores archives. Here the five most frequently used techniques are briefly described.

a) *Annual layer counting* has been the first technique applied to guess the age of ice samples in the early days of ice cores science. It consists in manually counting seasonal/annual cycles registered by water isotope as well as impurities records (Dansgaard, 1964; Hammer et al., 1978). Annual-layer-counted ice core timescales can be produced for ice cores drilled in areas characterized by sufficiently high annual snow deposition and reasonably regular throughout the year, like Greenland and coastal Antarctica, while it is not applicable for low accumulation rate sites, e.g. the Antarctic Plateau. Several annual-layer-counted ice core timescales have been produced like the one of GISP2 (Meese et al., 1997) and the common Greenland Ice Core Chronology (GICC05), which incorporates proxy data from North GRIP, DYE-3 and GRIP (Svensson et al., 2008). Nowadays, manual annual layer counting has been substituted by machine learning algorithms for pattern recognition to reduce errors and saving researchers' time (Winstrup et al., 2012).

b) *Marker horizons synchronization* is based on the assumption that the signature of some naturals or anthropic events, as volcanic eruptions or nuclear bomb tests, could be used to synchronize

ice cores age scale from the same hemisphere, but also from the two hemispheres. The most used markers are: (i) tephra layers and/or sulphuric acid spikes from volcanic eruptions (Abbott et al., 2012; Hammer, 1980), (ii) high fluxes of ^{10}Be cosmogenic radionuclides caused by changes in solar activity, reduction of the Earth's magnetic field, or cosmic events (Horiuchi et al., 2008; Raisbeck et al., 2017), (iii) layers of enhanced radioactivity (^{239}Pu) or ^{36}Cl peaks resulting from nuclear bomb tests (Arienzo et al., 2016; Delmas et al., 2004). The identification of those markers is extremely important as they represent useful tools to constrain the age scale and to reduce the uncertainties associated with the chronologies.

c) *Gas synchronization* consists in the stratigraphic matching (tie points) of past atmospheric composition measured in the air bubbles trapped in ice, as its variations are estimated to be globally synchronous for species with long residence time (Blunier & Brook, 2001). In particular the δ^{18}O of atmospheric O$_2$ (δ^{18}O$_{atm}$) (Sowers & Bender, 1995) and CH$_4$ (Blunier et al. , 1998) concentration records are suitable for defining relative age scales of different ice cores from both Greenland and Antarctica. Due to its atmospheric turn over time of 1-2 ka, δ^{18}O$_{atm}$ can be used to perform synchronization on millennial and multi-millennial scales (Capron et al., 2010), while CH$_4$ is applied for decadal and centennial scales synchronization due to its shorter residence time in the atmosphere (5 to 10 years) (Schüpbach et al., 2011).

d) *Orbital tuning* is based on the assumption that the climate record is affected by changes in insolation due to variations in the tilt of Earth's spin axis, precession of the equinoxes, and eccentricity of Earth's orbit about the sun (Bender, 2002). In particular, the δ^{18}O$_{atm}$ record from air trapped in ice appears to be highly correlated with the insolation curve and mid-June 65°N or precession (Bender et al. 1994; Dreyfus et al., 2007; Jouzel et al., 1996; Petit et al., 1999). However, Landais et al. (2010) and Extier et al. (2018), have recently highlighted that the δ^{18}O$_{atm}$ is a complex signal, not only influenced by insolation changes, but also by low latitude water cycle changes, global productivity, and ice sheet size. Bender et al. (2002), on the other hand, proposed δO$_2$/N$_2$ in air bubbles as a new dating tool. The δO$_2$/N$_2$ signal in ice cores is assumed to be influenced by Antarctic summer insolation, as it affects snow metamorphism and grain properties in firn. During the firnification, the signal is preserved down to the pore close-off depth, where it modulates the relative loss of O$_2$ with respect to N$_2$. In addition, a third and last orbital dating tool is the air content of ice core bubbles. Air content exhibits a comparable strong dependence from the insolation since its variations can be explained by a similar mechanism invoked for the δO$_2$/N$_2$ (Raynaud et al., 2007). The uncertainty associated with this dating tool is estimated to be equal to 4 ka (Parrenin et al., 2007; Bazin et al., 2013).

e) *Glaciological modelling* represents a very powerful dating methodology, since it provides a chronology with realistic event durations (gas/ice age as a function of depth), derived from physical equations (Parrenin et al., 2004). Models use four different elements: (i) a mechanical model, (ii) a way to estimate past accumulation rates, (iii) some age markers along the core, and

(iv) an inverse method applied to constrain the poorly known parameters of the modelling from the age markers (Parrenin, Dreyfus, et al., 2007). Ice and gas age markers obtained from ice core analysis are necessary input data for the model, as they allow to better constrain ice flow parameters like velocity profiles, past accumulation variations and melting and sliding at the base of the core. In this thesis work, the TALDICE chronology has been built through the use of the inverse method IceChrono1 (Parrenin et al., 2015), based on the same approach of the Datice tool (Lemieux-Dudon et al., 2010). IceChrono1 aims at finding the best compromise between (i) an *a priori* chronology and ice and (ii) gas markers obtained from the ice core analysis. The *a priori* chronology is a preliminary chronology, defined to run the model and based only on the measured glaciological quantities of accumulation, thinning function and *Lock-in Depth* (LID). The LID is a parameter that indicates the depth at which the atmospheric air stops diffusing in the snow column (Buizert et al., 2013). A description of the model and its application are reported in Chapter 3.

1.2.2 New dating techniques

Radiometric dating, based on the well-known radioactive decay of certain isotopes, is the most famous dating method since it provides the absolute age of a sample. However, common radiometric dating methods, as ^{14}C, fail when it comes to polar ice due to its limited dating range (50 ka) and the in situ production of ^{14}C in ice (Aeschbach-Hertig, 2014). Such necessity drove ice cores scientists to develop absolute dating techniques that could be applied to deep and old ice layers, also affected by stratigraphy disruption. New ^{81}Kr and ^{40}Ar radio-dating techniques and their recent developments appear to be the most promising methodologies.

a) *^{81}Kr* is naturally produced in the upper atmosphere by cosmic-rays spallation and neutron activation of stable krypton and characterized by a long residence time in the atmosphere (Jiang et al., 2012). The radioisotope dissolves in water or is trapped in ice, so it represents a potential tool for dating ancient air conserved in polar ice, allowing radiometric dating in the 0.3-1.3 Ma age range of ice layers that might be affected by disturbed stratigraphy or discontinuous record (Lu et al., 2013). Until now this methodology has been employed only on big samples (40-80 kg) of outcropping ancient ice from the Tibetan Plateau and blue ice areas in Antarctica (Buizert et al., 2014) (Figure 1.8). However, new improvements of the Atom Trap Trace Analysis (ATTA) machine allow to reduce the sample size down to 10 kg of ice (Tian et al., 2019) and to employ this methodology in this research work. Further details on ^{81}Kr dating technique are described in Chapter 2.

b) *^{40}Ar:* Argon is a noble gas with three stable isotopes, ^{36}Ar, ^{38}Ar and ^{40}Ar. ^{40}Ar has been slowly increasing in the atmosphere during time due to the radioactive decay of ^{40}K in the crust, upper mantle, and lower mantle while ^{36}Ar and ^{38}Ar have been essentially constant throughout recent geologic time. The ^{40}Ar outgassing rate has been estimated equal to 0.066

±0.077 ‰/a while the increase rate of $^{40}Ar/^{36}Ar$ (or $^{40}Ar/^{38}Ar$) ratio in the atmosphere is constant through time and equal to 0.040 ‰/Ma (Bender et al., 2008) (Figure 1.9). Yau et al. (2016) showed that Ar isotopes could be used to date the paleoatmospheric air trapped in ice cores and that this method is well suited for deep cores with disturbed stratigraphy at their base, as GRIP and Dye-3 cores from Greenland. Ar dating methodology uses up to 500 g of ice (Bender et al., 2008). In Chapter 5 new developments that reduce the samples weight to ~65 g are presented.
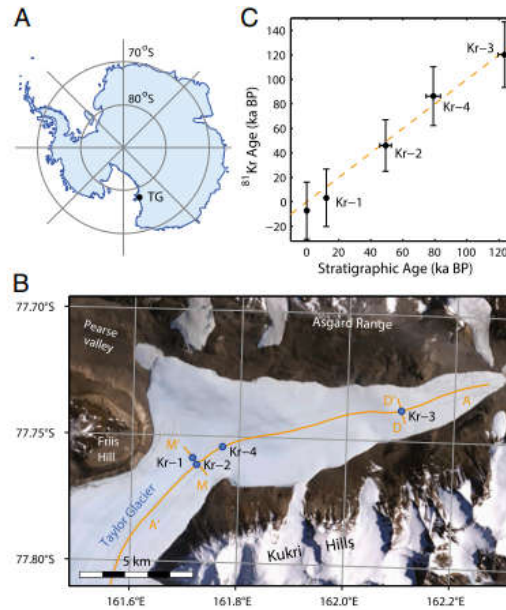
Figure 1.8: Radiometric ^{81}Kr dating at the Taylor Glacier, Antarctica. (A) Position of Taylor Glacier on map of Antarctica with the Greenwich meridian upwards. (B) Satellite image of Taylor Glacier. Stratigraphically dated profiles indicated with A-A' (along-flow), M-M' (main transect) and D-D' (downstream transect). Blue dots are ^{81}Kr sampling points. (C) Comparison of stratigraphic age with ^{81}Kr radiometric ages in thousands of years before 1950 C.E. (ka) (Buizert et al., 2014).
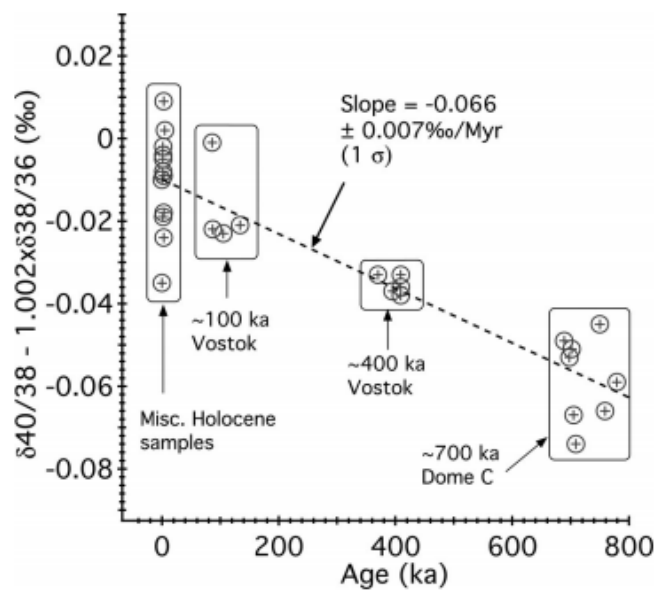
Figure 1.9: $^{40/38}Ar$ ratio in air bubbles plotted versus age for Vostok, Dome C ice and Holocene samples (Bender et al., 2008).

1.3   TALDICE project

Figure 1.10: TALDICE project official logo

The TALos Dome Ice CorE (TALDICE) is a European ice core international project aiming at drilling a deep ice core from a peripheral dome of East Antarctica to reconstruct and study the climate of Holocene and of late Pleistocene glacial/interglacial cycles. Five nations have been involved in the project (Italy, France, Germany, Switzerland, United Kingdom), which started in 1996 with the first survey to find the appropriate drilling site. The camp was built in 2004 and the drilling started the same year, but the main efforts took place during the summer field season of years 2006 and 2007, with the recovery of a 1620 m deep ice core.

1.3.1   Scientific aim

The scientific necessity of drilling a new ice core located in the coastal sector of East Antarctica came from the controversial findings from Taylor Dome and Siple Dome (Ross Sea Sector) ice cores, two near-coastal sites in Antarctica. Their isotopic records spanned respectively the past 150 ka and 28 ka (Grootes et al., 2001; Steig et al., 2000; Taylor et al., 2004) and showed different features in comparison to the other plateau ice cores (Vostok, Dome C, Byrd, Dome Fuji). In particular, the isotopic signature of Taylor Dome appeared similar to the one registered in the Greenlandic cores of GRIP and GISP2, indicating the presence of synchronous climate changes with the North Atlantic (Grootes et al., 2001). The investigation of climate change synchronicities between Antarctica and Greenland (Morgan et al., 2002), and within Antarctica (Watanabe et al., 2003) during the Last Glacial Transition, appeared suddenly essential to assess causes and mechanism of rapid climate change and understand modern and future climate changes (Frezzotti et al., 2004). Since at that time only few ice cores records were available at coastal sites, the scientific community pointed out the necessity to drill a new deep ice core close to the Ross Sea spanning at least the past two glacial/interglacial cycles (250 ka), to provide records of past environmental conditions and processes acting in the Southern Ocean sector.

The main scientific objectives of the TALDICE project were:

a)   Identify spatial and temporal patterns in environmental parameters describing the ocean surface conditions (e.g., sea ice, marine biological productivity, storm activity) in the Southern Ocean/Ross Sea region.

b)   Reconstruct at high resolution the sequence of climatic events, including forcings and responses, during the past two glacial-interglacial cycles across Antarctica.

c) Synchronise the TALDICE records of CH_4, CO_2, $\delta^{18}O_{atm}$ in air bubbles and volcanic markers with other ice core records from both Antarctica and Greenland.

d) Define climate modes and teleconnection schemes acting under various boundary conditions as atmospheric composition, orbital forcing and extension of ice sheets.

e) Collect evidences of rapid climate/environmental transitions during the Holocene.

f) Reconstruct changes in ice volume, local ice sheet altitude and variations in snow accumulation rate at inland and coastal sites, from the Last Glacial Maximum (LGM) to the present.

Figure 1.11: Map of Antarctica with the main drilling sites in 2009. TALDICE is located in coastal sector of the East Antarctic Ice Sheet (www.taldice.org).

1.3.2 Talos Dome and ID1 drilling site

Investigations to identify the drilling site started in 1996, within the framework of the France-Italy ITASE programme. Two traverse surveys were performed in the Talos Dome area in November 1996 and January 2002, and intermittent field activities have been carried on since 1999. Airborne radar surveys were conducted in 1997, 1999, and 2001.

Talos Dome is an ice dome located on the periphery of the East Antarctic plateau; about 290 km from the Southern Ocean, 250 km from the Ross Sea, 275 km from the Italian station (Mario Zucchelli Station at Terra Nova Bay), 550 km north of Taylor Dome, 1500 km northwest of Siple Dome and 1100 km east of Dome C. The Talos Dome summit (72°47'14'' S, 159°04'21'' E; 2318.5 m.s.l.) is situated above a sloped bedrock about 400 m in elevation, covered by about 1900 m of ice (Frezzotti et al., 2004). Internal layering below the summit is characterized by irregular and discontinuous horizons, which does not make the dome summit an ideal drilling site.

The bedrock topography below the dome consists of a deep basin, connected to a low bedrock zone, where the ice thickness ranges from 800 to 2900 m. The bedrock becomes relatively flat, 5-6 km far from the summit, characterized by an elevation of about 750 m (WGS84) covered by 1550 m of horizontally layered ice (Urbini et al., 2006) (Figure 1.12).
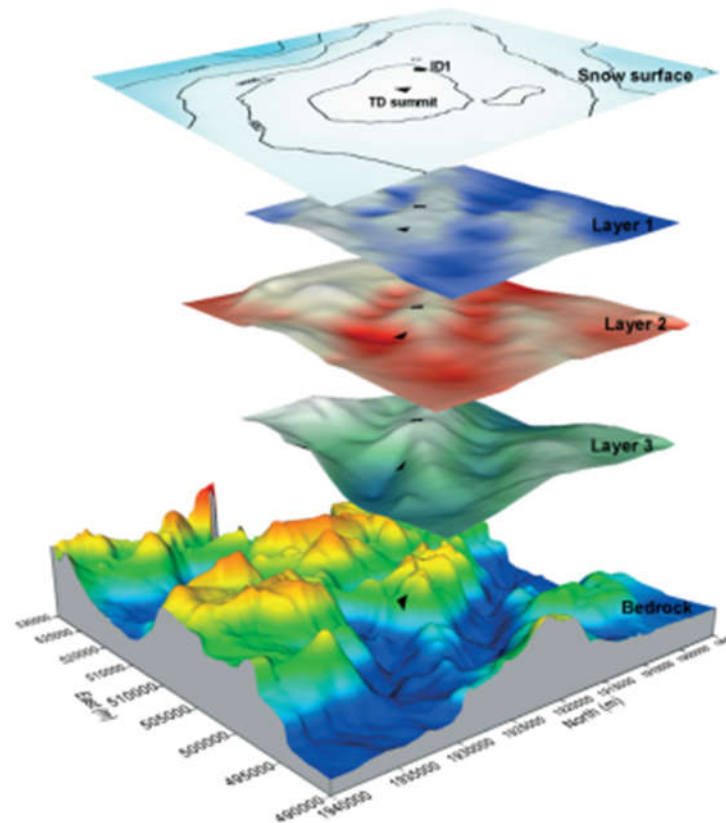
Figure 1.12: Ice surface, bedrock topography and three internal layers over Talos Dome area. The internal stratigraphy is modified in accordance to the morphology of the bedrock. The positions of ID1 (drilling site) and of Talos Dome summit are reported (black triangles) (Urbini et al., 2006).

The ice flow at Talos Dome is complex and split in two different directions (Figure 1.13): northwest into Rennick and Matusevich Glaciers, which drains into the Southern Ocean, and southeast from this ridge into Priestley and Reeves outlet glaciers, which drain into the Ross Sea (Frezzotti et al., 2004). In addition, the north-western drainage area is based on the Wilkes Subglacial Basin, which is mostly below sea level, and is considered to be more sensitive to sea level fluctuations and climatic changes, compared to other sectors of the East Antarctic ice sheet (Warner & Budd, 1998). Ice domes are known to migrate because of the interplay between surface elevation, ice load, bedrock and snow accumulation at summit (Frezzotti et al., 2004). Repeated GPS measurements and GPR surveys (300 km) performed at Talos Dome, identified a decrease in velocity in the NE portion and an increase in the order of mm yr^{-2} in the SW portion. This information, coupled with the observed decrease in accumulation rate in the SW side for the period 1835–1920 anno domini (AD), in comparison to the periods 1635–1835 AD and 1920–2001 AD, is indicative of a probable migration towards SE of Talos Dome during the last few centuries (~500 years) (Urbini et al., 2008). Knowing past changes in the position of the ice divide represents an essential information to accurately interpret ice core records, as

models of depth–age relations for deep ice cores are sensitive to migration of the dome position (Urbini et al., 2008).
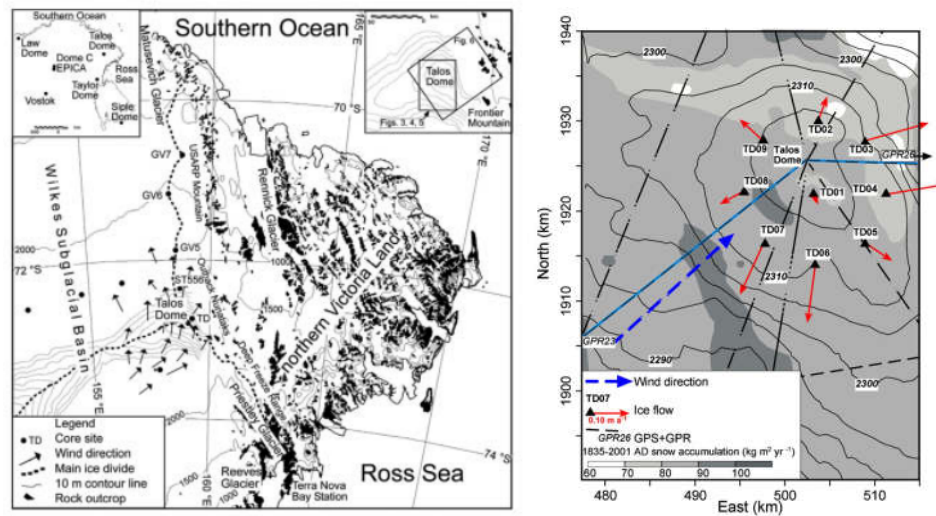
Figure 1.13: Left. Map of Talos Dome drainage system (contour every 500 m; contour every 10 m in Talos Dome area) from digital elevation model (Frezzotti et al., 2004). Right. Snow accumulation map (kg m^{-2} yr^{-1}) based on snow radar data (1835–2001 AD). Contour lines of surface topography (5 m interval) are reported in grey. Ice velocity vectors (red arrow) and wind direction (blue arrow) are shown (Urbini et al., 2008).

Talos Dome is characterized by relatively high accumulation rate, in average 80 mm water equivalent per year (w.e. year^{-1}) during the time period 1259-2004 AD (Stenni et al., 2002). Due to its semi-coastal position, it was selected as an ideal site to drill a new deep ice core to study at high resolution the response of near-coastal sites to climate change during the past 150-200 ka (Frezzotti et al., 2004; Urbini et al., 2006).

The ID1 site (159°11' E, 72°49'S, 2315 m a.s.l) was chosen to drill the deep TALDICE ice core, during the field seasons 2004-2008 (Buiron et al., 2011). ID1 is located at 5 km from the summit of Talos Dome, in an area characterized by continuous and horizontal internal layering. Deep drilling was performed using the 200-m LGGE[1] drilling system during the first year of campaign (2004-05) and then, the Berkner Island drilling system in the following seasons. The Berkner drill system is an electro-mechanical drilling equipment, designed and built for this project in collaboration with ENEA Brasimone, hung by a cable consisting of 7 conductors surrounded by 40 piano wires. The drill was lowered into the borehole of 130 mm in diameter, while the extracted ice core was 98 mm in diameter. The drilling was completed in the austral summer 2007-08, reaching a depth of 1620 m. At the beginning of the operations, the expected depth of the drilling has been estimated equal to 1500 m, but the actual ice core is longer (1620 m). This is due to fact that the drill missed (for less than 200 m) the intended target area over a plateau in the bedrock, perforating the ice that filled an unsurveyed deep gorge (1.6

---

[1] LGGE is now IGE (Institut des Géosciences de l'Environnement)

km wide) where the ice thickness is about 1795 m (*www.taldice.org*). Radargrams provided by the British Antarctic Survey (Figure 1.14) show that the deeper portion of the core lays in an area where the ice is not characterized by the presence of layers, but a shaded region is observed (Frezzotti, pers.comm.). Considering the proximity of the ice to the subglacial hill, the temperature of the borehole has been measured in the field down to 600 m depth and then modelled until the bottom of the core. The lowermost portion of the ice lies at a temperature of ~ -5°C, indicating the absence of melting processes due to geothermal flux (Frezzotti, *personal comm.*).
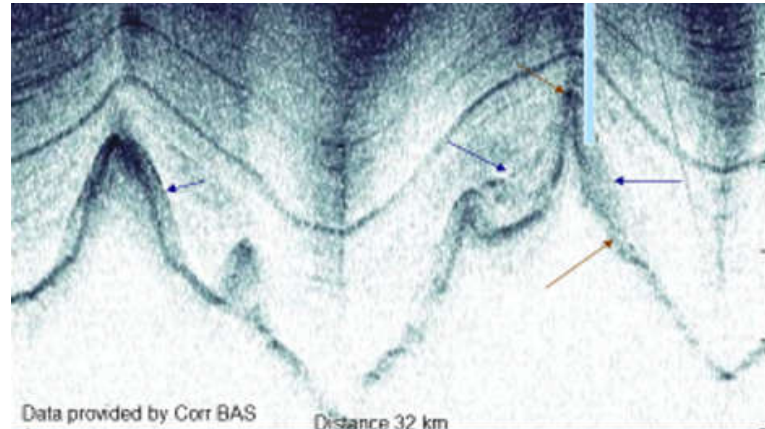
Figure 1.14: Radargram showing the TALDICE ice core drilling (light blue rectangle) and the ice unconformity (grey cloud) (courtesy of BAS).

1.3.3   TALDICE ice core

The TALDICE ice core is 1620 m long and, due to the unexpected drilling in the deep valley, the ice shows some particular features, especially in the lowermost portion. The shallower part of the core is characterized by horizontal internal layering and 59 visible volcanic markers between 1300 and 1528 m depth. However, below 1460 m depth the observed tephra layers are inclined. They indicate the presence of a shear stress component on the ice flow, as the coring site is located down the ridge from the dome summit, with an intensified contribution in the last 200 m of the core due to abrupt elevation changes of the bedrock (Montagnat et al., 2012). The observed ice properties (Figure 1.15) in the deeper portion of the core can be summarized as following:

a)   59 visible layers from 1300 m to 1528 m depth, mainly volcanic events;
b)   tilted layers from 1460 m to 1503 m (inclination from 5° to 30°);
c)   no visible layers from 1528 m;
d)   large grain size from 1590 m to the bottom (1620 m).
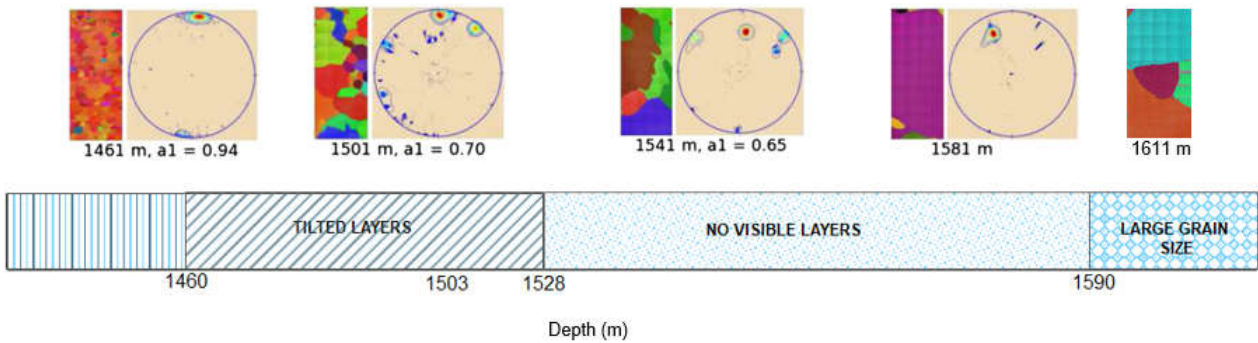
Figure 1.15: Schematic of the TALDICE ice core characteristics below 1460 m down to the bottom (1620 m depth). Microstructures in orientation colour-scale and Schmidt plots obtained from 1361 m to 1581 m depth are also reported from 1461 m depth down to 1611 m depth (Montagnat et al., 2012; Montagnat personal comm.).

Changes in the ice properties with depth appear also evident from the evolution of fabric and microstructures, as shown in Figure 1.15. Below 1411 m down to 1500 m depth an increasing number of grains show orientations departing from the single maximum. These orientations changes explain the progressive decrease of the fabric strength with depth, even if a strong single maximum orientation is still dominating. Below 1500 m a transition to very large grain size is observed (Figure 1.16) and no clear orientation could be identified due to the decreasing number of crystals (Montagnat et al., 2012).
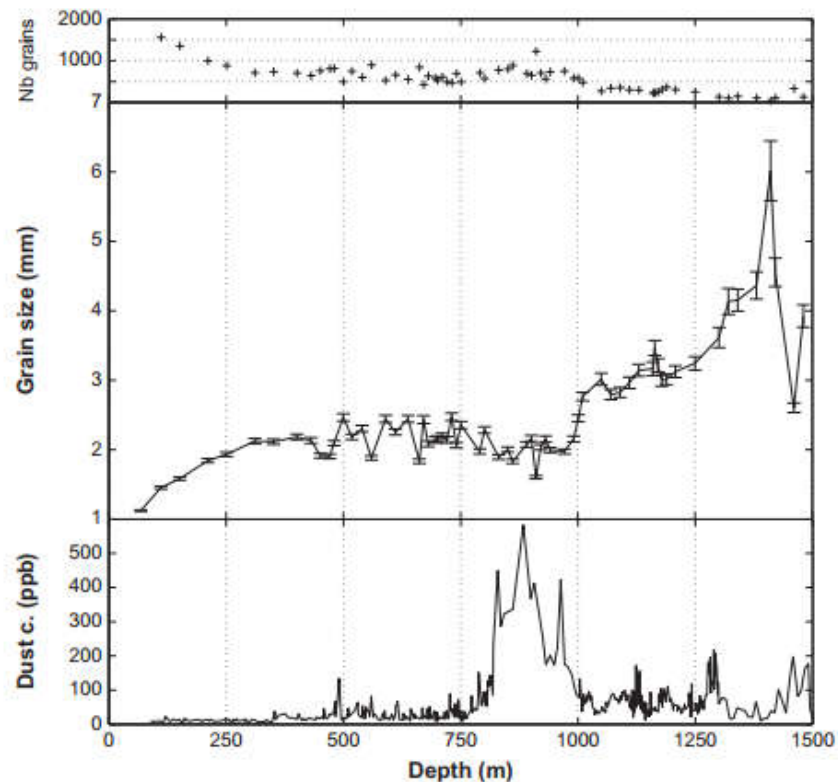
Figure 1.16: Dust content, average grain size and number of grains analysed (in each thin section), as a function of depth along the Talos Dome ice core (Montagnat et al., 2012).

1.3.4   TALDICE chronologies

The definition of an age scale for the TALDICE ice core needed three dating efforts due to the complex glaciological background and the peculiar ice features:

a) *TALDICE-1* is the first official age scale for the core defined by Buiron et al. (2011). It combines the glaciological modelling approach to the synchronization of TALDICE records with already dated ice cores from Greenland and Antarctica. Specifically, ice and gas tie points have been respectively chosen synchronizing TALDICE CH_4, $\delta^{18}O_{atm}$ and $\delta^{18}O_{ice}$ with EDC records on EDC3 chronology (EPICA community members, 2004) and composite records from Greenlandic cores on GICC05 age scale (Svensson et al., 2008). Tie points are then included in the Datice inverse model (Lemieux-Dudon et al., 2010), which provides the best estimation of gas and ice age. The TALDICE-1 gas chronology was built until 1428 m depth, corresponding to an age of ~141 ka due to the low resolution of the available $\delta^{18}O_{ice}$ and CH_4 records in the deepest part.

On the other hand, the ice age scale has been defined until 1558 m depth at ~290 ka. High uncertainties up to 2 ka for the gas chronology and 5 ka for the ice chronology have been estimated for the oldest portion of the core (Figure 1.17).
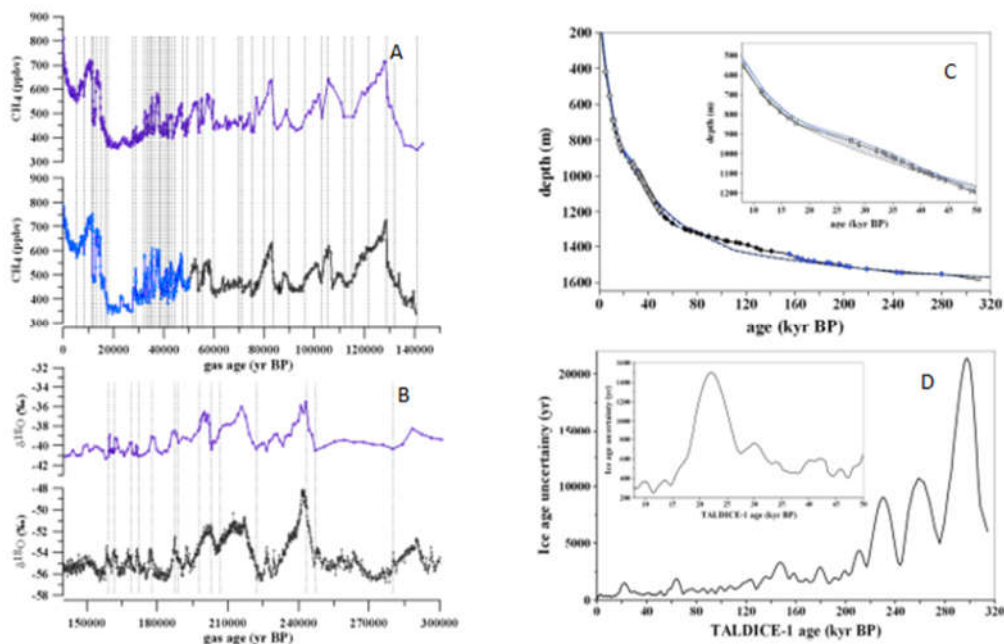
Figure 1.17: Left. (A) Synchronization of the TALDICE CH_4 record (purple curve) with the Greenland CH_4 composite on GICC05 age scale (blue curve) until 53 ka, and with the EDC CH_4 record (grey curve) on EDC3 age scale for ages older than 53 ka. (B) Synchronization of low resolution $\delta^{18}O_{ice}$ between TALDICE (purple curve) and EDC (grey curve) ice cores on the EDC3 age scale. Right. (C) TALDICE-1 age/depth relationship for the ice (blue a priori glaciological model - dashed lines- and after applying the inverse lines) and for the gas (black lines), from the a priori glaciological model (dashed lines), and after applying the inverse method (continuous lines), with a zoom on the period between 8 and 50 ka. (D) uncertainty associated with the chronology deduced from the inverse method and zoomed between 8 and 50 ka (Buiron et al., 2011).

b) *TALDICE 1-a* is the refined version of the TALDICE-1 gas chronology spanning the time window between 55 to 112 ka (1293-1380 m depth), proposed by Schüpbach et al. (2011), in order to reduce the uncertainties associated with the first TALDICE gas age scale. It is based on a simple synchronization approach between the new high-resolution methane data produced by Continuous Flow Analysis (CFA) with EDC CH_4 discrete record on EDC3 age scale (Loulergue et al. 2008; Parrenin et al. 2007). The new CH_4 measurements led to the reduction of the uncertainties associated with the gas age scale from up to 1.9 ka in TALDICE-1 to below 1.1 ka in the considered time interval.

c) *TALDICE AICC2012* represents the third improvement of the TALDICE timescale and included in the Antarctic Ice Core Chronology 2012, a multi-proxy and multi-site (EDC, Vostok, EDML and TALDICE) ice and gas orbital chronology, which spans the last 800 ka (Bazin et al., 2013; Veres et al., 2013) (Figure 1.18). TALDICE AICC2012 is based on the same dating strategy applied for TALDICE-1 (Datice model and records synchronization), but is improved with new gas measurements for all the involved cores. Regarding TALDICE, the novel $\delta^{18}O_{atm}$ and CH_4 data set of Buiron et al. (2011) between 1402 m down to 1553.95 m depth allowed to extend the chronology until 153 ka (gas age) at 1438 m depth with a 2 ka uncertainty. Despite the novel gas record, the poor resolution of data in the lowermost portion of the core and the complex glaciological background made impossible to extend the chronology further back in time.
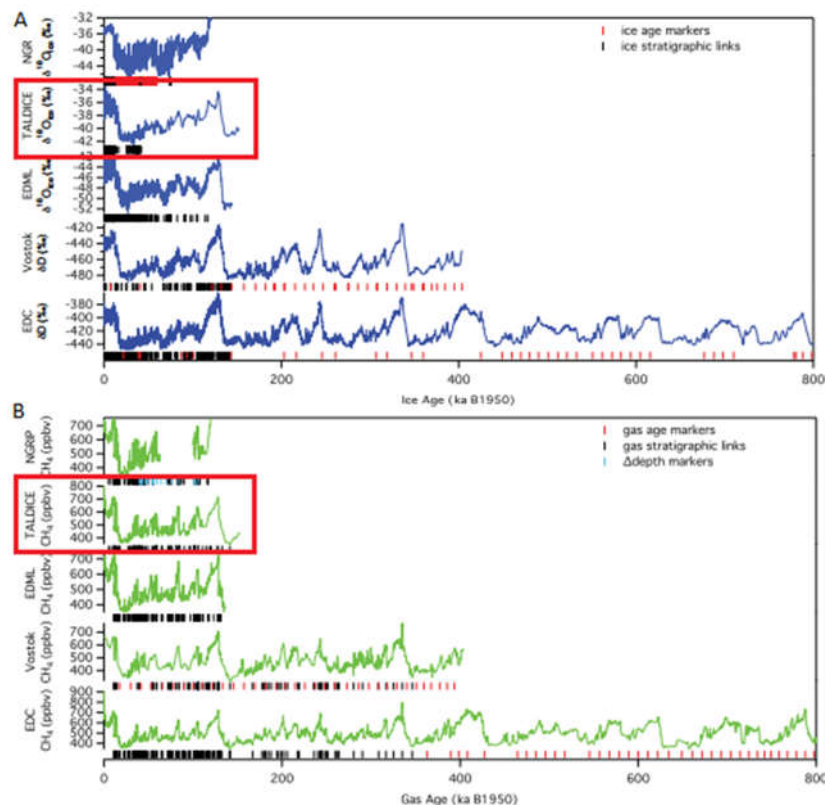
Figure 1.18: A. Water stable isotope records of NGRIP, TALDICE (in the red square), EDML, Vostok (Petit et al., 1999) and EDC) on the AICC2012 age scale. B. Methane records of NGRIP, TALDICE, EDML, and EDC (Loulergue et al., 2008) on the AICC2012 age scale. Stratigraphic links and age marker positions are displayed under each core (Bazin et al. 2013).

1.3.5 Past climate postcards from Talos Dome

The TALDICE ice core provides the first climatic record from a coastal position of Antarctica spanning back the past 150 ka. The peripheral position of the core, in association with the proximity to the Wilkes Subglacial Basin, makes the Talos Dome ice suitable to store information of a global signal superimposed on a local signal, related to the surrounding ocean and the dynamics of the East Antarctic Ice Sheet (EAIS) (Frezzotti et al., 2004). Several studies stressed the peculiarity and unicity of the climatic record enclosed in TALDICE through the comparison with other ice core signal, particularly during the Holocene and the LIG (Bradley et al., 2012, 2013; Masson Delmotte et al., 2011). This section consists in a short review of the major climatic and environmental changes deduced from the TALDICE proxy records spanning the Holocene and the LIG:

a) *Holocene (0-11.7 ka)* records from TALDICE undercover pictures of the past extension of sea ice and ice shelf in the Ross Sea. Albani et al. (2012) focused on the dust profiles of EDC and TALDICE (Figure 1.19), finding that the decreasing trend in dust deposition between 13 ka and 9 ka might be connected to a possible change in atmospheric pathways during the middle and late Holocene, with an increase in frequency of air masses transiting through the Ross Sea, making dust transport less favourable at TALDICE in response to the progressive opening of the Ross Sea embayment.
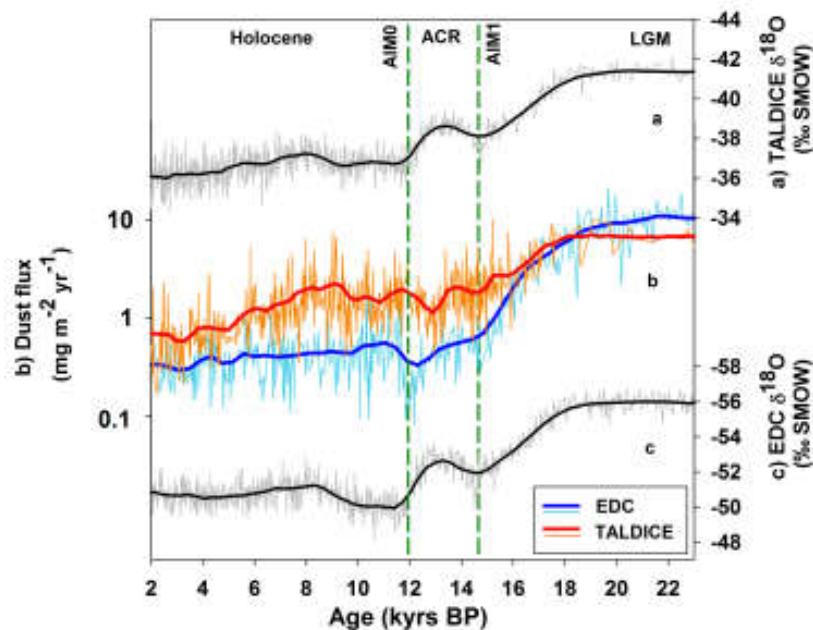
Figure 1.19: Comparison of TALDICE and EDC dust fluxes (1–5 μm) and $\delta^{18}O$ profiles. (a) TALDICE $\delta^{18}O$ record plotted on a reversed axis. (b) Profiles of EDC dust flux (light blue line) and TALDICE dust flux (orange line). Superimposed thick lines are the smoothed profiles of EDC (dark blue) and TALDICE (red), respectively. (c) EDC $\delta^{18}O$ ‰ s. EDC dust and $\delta^{18}O$ data are plotted using the new age scale by Lemieux-Dudon et al. (2010). Thin lines represent the original data, and superimposed thick lines mark the smoothed profiles (Albani et al., 2012).

This interpretation is also coherent with the comparison of TALDICE isotopic record with Taylor Dome $\delta^{18}O$ signal and *d*-excess in association with the sea salt sodium (ssNa) profiles (Figure 1.20) (Mezgec et al., 2017). Such comparison revealed that Taylor Dome $\delta^{18}O$ exhibits a decreasing trend during the whole Holocene, while TALDICE record shows an oscillating behaviour, which reaches minima at ~8 ka and during the last millennium. On the other hand, the TALDICE and Taylor Dome *d*-excess signals appear to be characterized by similar increasing trends over the entire Holocene. Regarding ssNa profiles of the two ice cores, they start diverging at 7 ka, as for the $\delta^{18}O$ records. Taylor Dome record exhibits a gradual increase towards older ages, while TALDICE ssNa record is stable over the same period. The differences observed in the $\delta^{18}O$ and ssNa record of TALDICE and Taylor Dome confirms the opening of the Ross Sea embayment starting from 7 ka.
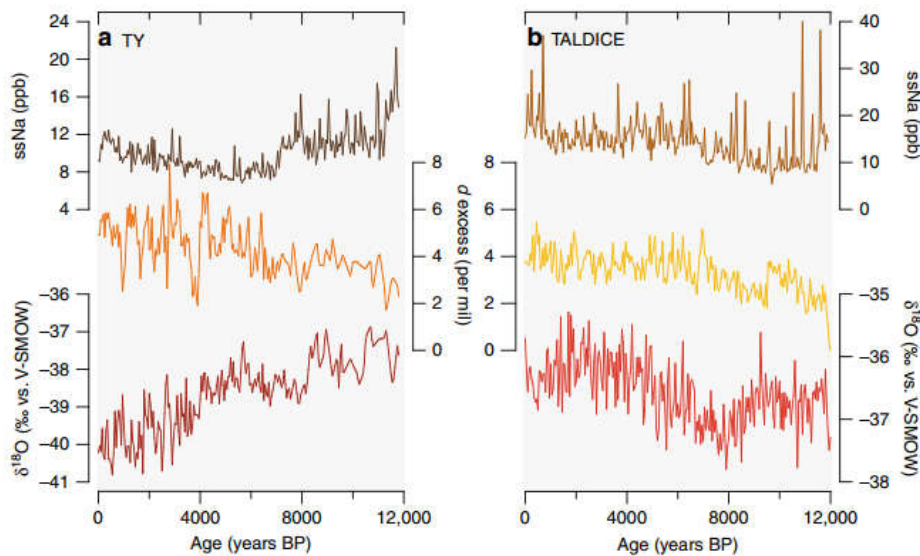
Figure 1.20: Holocene ice core records of Taylor Dome (TY) and TALDICE resampled with a 50-year time step. (a) sea salt sodium concentration (ssNa) in part per billion (dark brown line), deuterium excess (orange line) and $\delta^{18}O$ (dark red line) of Taylor Dome ice core. (b) sea salt sodium concentration in part per billion (brown line), deuterium excess (yellow curve) and $\delta^{18}O$ (red curve) in TALDICE ice core (Mezgec et al., 2017).

b) The *Last Deglaciation (9-21 ka):* the isotopic record of TALDICE shows a weaker cooling during the Antarctic Cold Reversal (13-16 ka), with respect to the other Plateau records. In addition, it shows a clear culmination of Antarctic Isotopic Maximum 1 (AIM1) at 14.7 ka, less defined at EDML, and an uninterrupted deglacial warming between 19 and 15 ka similar to the pattern at EDC (Figure 1.21). This weaker amplitude in the ACR may be interpreted as an increase in elevation of ~200 m at Talos Dome or by air-mass-trajectory changes due to the opening of the Ross Sea, a consequence of the grounding line retreat around 14 ka (Stenni et al., 2011). Moreover, the presence of the culmination of the AIM1, clearly visible in TALDICE and EDC (with a triangular shape) and less defined in the Atlantic Sector cores (Dome F and EDML) (with a squared shape), points to a reorganization of atmospheric circulation. Denton et al. (2010), in fact, indicated that during the Northern Hemisphere stadials a southward

displacement of the Southern Hemisphere westerlies might have occurred and warmed the Southern Ocean. In addition, Buiron et al. (2012) evaluated that during the AIM events of the MIS3 the rate of warming was two times smaller at TALDICE and EDC in comparison to EDML, suggesting a different expression of the bipolar see-saw in the two regions.
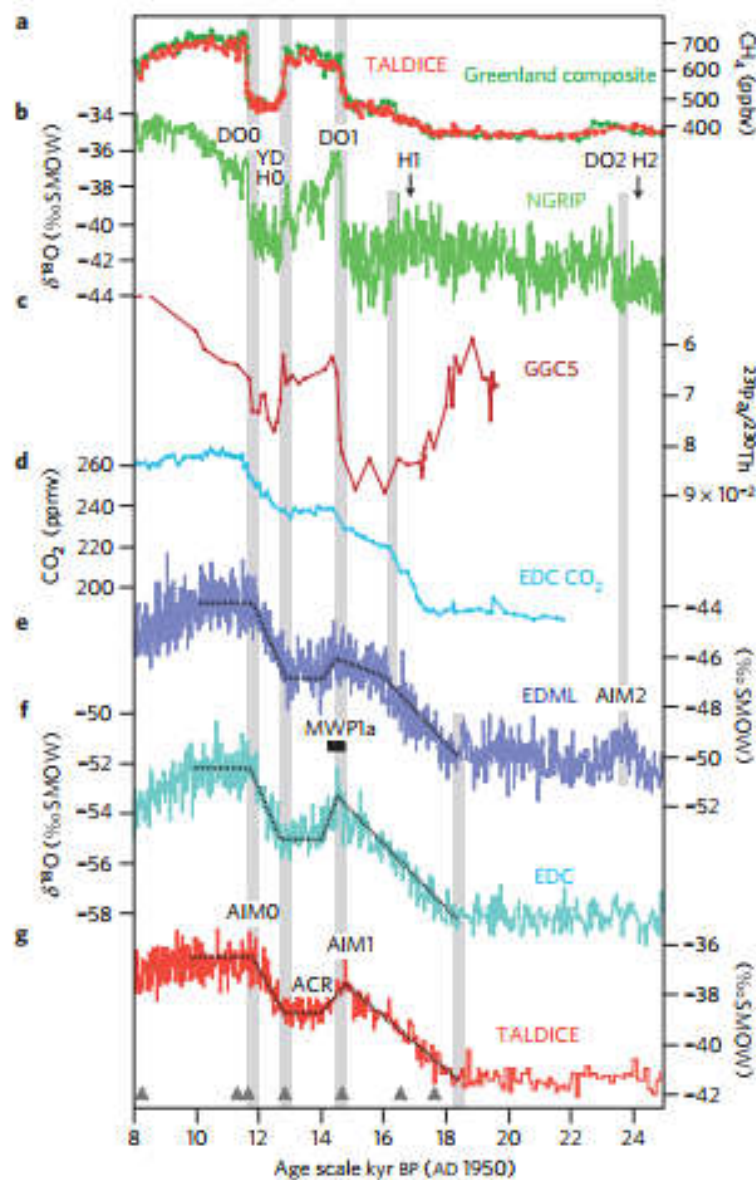
Figure 1.21: (a) CH_4 records of Greenland composite and TALDICE. (b) $\delta^{18}O$ record from NGRIP. (c) record of marine core GGC5, from Bermuda rise in the deep western subtropical Atlantic, taken as a proxy for Atlantic meridional overturning circulation strength. (d) CO_2 from EDC. (e) $\delta^{18}O$ record from EDML. (f) $\delta^{18}O$ record from EDC. (g) $\delta^{18}O$ record from TALDICE. EDML, EDC and TALDICE are synchronized on the GICC05, while GGC5 data are shown on their timescale (Stenni et al., 2011).

c) *Last Interglacial or MIS 5.5 (116-130 ka)* (or MIS 5.5) isotopic signature at TALDICE has gained the attention of several studies due to its peculiar shape. Masson Delmotte et al. (2011) at first identified TALDICE $\delta^{18}O$ signal as an outlier, due to an anomalous sustained increase of ~2‰ between ~127-119 ka, just before the glacial inception, while the other EAIS cores

display a decrease towards the glaciation (Figure 1.22). The combination of glacio-isostatic modelling with the observation of the isotopic record indicates that the distinct feature of TALDICE during the LIG might be the signature of the decrease in ice sheet thickness at Talos Dome due to the retreat of the marine-based ice sheet in the Wilkes Subglacial Basin (Bradley et al., 2013). In addition, the TALDICE (and EDML) $\delta^{18}O$ record shows an abrupt decrease of isotopic values at 118.5 ka not recorded in the plateau sites (EDC, Vostok and Dome Fuji). This peculiar isotopic feature may indicate that coastal sites are most sensitive to changes in the moisture origin or precipitation intermittency. Another hypothesis could connect the increased seasonal ice cover in the Ross Sea/Weddell Sea during the glacial inception and the increased distance between moisture source and the site, to a stronger isotopic depletion (Masson Delmotte et al., 2011).
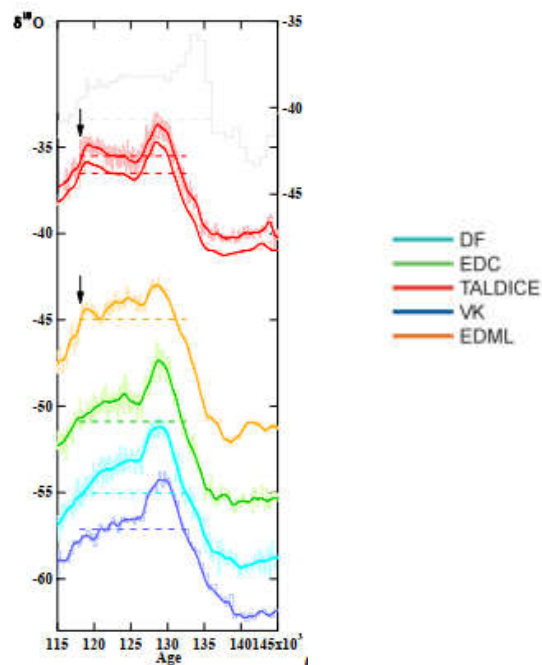
Figure 1.22: Water stable isotope records $\delta^{18}O$ from Dome Fuji (DF, light blue), Epica Dome C (EDC, grren), TALDICE, Vostok (VK, blue) and Epica Dronning Maud Land (EDML, orange) displayed on the EDC3 age scale for the Last Interglacial periods with the exception of TD on TALDICE-1 age scale (grey, left vertical axis with the same vertical scaling as for the right axis). All raw data (thin lines) and 5 points binomial filter 200 year re-sampled data are displayed (bold lines). The black arrows display the abrupt TALDICE and EDML $\delta^{18}O$ decrease observed at ~118 kyr (Masson Delmotte et al. 2011).

2 <u>Measured proxies and analytical methods</u>

The analysis of stable isotopes of water and gases trapped in air bubbles, represent two of the most common approaches to get paleoclimatic information from ice cores. Radioactive isotopes in air bubbles, on the other hand, are tools to obtain absolute dating of the ice. This chapter provides an overview of the stable and radioactive isotopes analysed in the framework of this thesis and the applied analytical methodologies.

2.1   Introduction on stable isotopes

2.1.1   Definition of stable isotopes

The term *isotope* derives from the greek ἴσος (*ìsos*, "same") and τόπος (*tòpos*, "place"). Isotopes are atoms whose nuclei accommodate the same number of protons, but a different number of neutrons and still occupy the same position on the periodic table. Isotopes official notation is written in the form $_n^m E$, where *m* is the mass number (i.e., sum of the number of protons and neutrons in the nucleus) and *n* denotes the atomic number. Each element may have a different number of isotopes, each of them with a specific abundance in nature, which could be stable or radioactive.
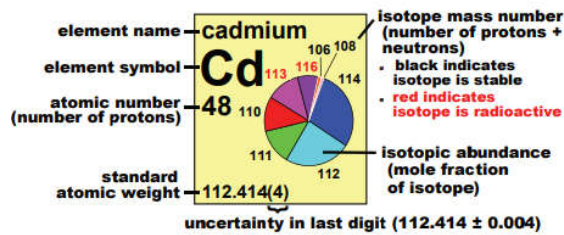
Figure 2.1: Cadmium and its isotopes (Holden et al., 2018).

A stable isotope is defined as an isotope that does not decay in another element. The stability of nucleides is governed by two main rules (Hoefs, 2015):

a) *The symmetry rule* states that in a stable nuclide with low atomic number, the neutron-to-proton ratio (N/Z) is approximately equal to unity. In stable isotopes with more than 20 protons or neutrons, the N/Z ratio is always larger than 1 and could reach the maximum value of about 1.5.

b) *The Oddo-Harkins rule* says that nuclides of even atomic numbers are more abundant than those with odd numbers.

2.1.2   Isotope fractionation processes

Variations in atomic mass of an element lead to differences in its chemical and physical properties. This phenomenon is called *isotope fractionation* and occurs when isotopes partition between two substances or two phases of the same substance with different isotope ratios.

The mass differences that characterize isotopic compounds (i.e. chemical compounds consisting of molecules containing different isotopes of the same element) lead to different behaviour of isotopic

23

molecules. In particular, heavier isotopic molecules are characterized by a lower mobility in comparison to the lighter ones, so they tend to diffuse slower and collide less frequently with other molecules. Moreover, heavier molecules generally have higher binding energies, so higher energy is needed to break chemical bonds of those molecules in comparison to the lighter ones.

Elements that undergo significant isotopic fractionation are the mostly studied and exhibit several common characteristics: (i) relatively low atomic mass, (ii) large mass difference between the rare (heavy) and abundant (light) isotope, (iii) chemical bonds that have a high degree of covalent character and (iv) relative abundance of the rare isotope to be detected by instrumentation (e.g. mass spectrometer) (Sharp, 2017).

2.1.2.1 Equilibrium fractionation

The equilibrium fractionation happens when the isotope distribution changes between different chemical substances, between individual molecules, or between different phases, without a net reaction. The equilibrium fractionation can be classified as a special case of general chemical equilibrium and can be written as:

$$aA_1 + bB_2 \leftrightarrow aA_2 + bB_1 \tag{2.1}$$

where A and B are the chemical species containing the light (1) or heavy isotope (2). The equilibrium constant K is expressed as following:

$$K = \frac{\left(\frac{A_2}{A_1}\right)^a}{\left(\frac{B_2}{B_1}\right)^b} \tag{2.2}$$

where the terms in parentheses are the molar ratios of different isotopic species. The magnitude of this equilibrium isotopic effect is related to the bonding environment of the phases involved. Moreover, the fractionation between two phases is only function of temperature and tends to be zero at very high temperatures (Hoefs, 2015).

2.1.2.2 Kinetic fractionation

Kinetic fractionation is an extremely common phenomenon in nature. Kinetic isotope effects are irreversible, and normally related to unidirectional and fast or incomplete processes like diffusion, dissociation reactions and evaporation. Kinetic fractionation connected to diffusion and evaporation may be explained by the different translational velocities owned by the different isotopic forms of molecules when they move across a phase boundary or through a phase. Those different velocities can lead to isotopic fractionation in many different ways. When diffusion happens, for example, isotopically light molecules will preferentially move out of the reservoir, leaving it enriched in heavy isotopes. During evaporation, isotopically lighter molecules cross the liquid surface and diffuse across a boundary

layer due the greater average translational velocities with respect to heavier molecules, generating isotopic fractionation between vapour and liquid (Sharp, 2017).

In the case of kinetic fractionation, the equilibrium constant K is expressed by the fractionation factor α:

$$\alpha = \frac{\left(\frac{A_2}{A_1}\right)}{\left(\frac{B_2}{B_1}\right)} \tag{2.3}$$

Where the numerator and denominator are the ratio of the numbers of isotopes in the different chemical compounds A and B.

2.1.2.3 The delta notation

The isotopic composition is expressed in delta units (δ). The delta notation has been introduced by McKinney et al. (1950) and is written as :

$$\delta = \left(\frac{R_x}{R_{std}} - 1\right) \times 1000 \tag{2.4}$$

where R is the ratio of the abundance of the heavy to the light isotope, x indicates the sample, and *std* is the standard. Delta values are expressed in per mil (‰) and might have both positive and negative values. A positive δ value indicates that the sample is enriched in the heavier isotope with respect to the standard, while a negative δ value means that the sample is depleted in the heavier isotope with respect to the standard.

2.2   Water stable isotopes

2.2.1   δD and δ¹⁸O in the hydrosphere

Water is the most abundant compound on Earth and plays an essential role in all life processes, in the formation and evolution of rocks and minerals, the development of physiographic features and meteorological patterns.
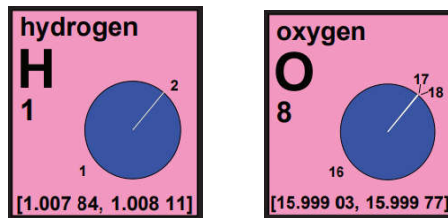
Figure 2.2: Hydrogen and Oxygen and their relative isotopic abundances (Holden et al., 2018).

As many other elements in nature, hydrogen and oxygen may exist in the form of different isotopes, each of them with a distinct abundance. Hydrogen has two stable isotopes, ^1H and ^2H (deuterium), with relative proportions of 99.9885 and 0.0115%, respectively. Oxygen atoms may have 8, 9, or 10 neutrons in their nucleus and so oxygen has three isotopes ^{16}O, ^{17}O, and ^{18}O. In nature, these

three stable isotopes shows different abundances: 99.757% (^{16}O), 0.038% (^{17}O), and 0.205% (^{18}O) (Hoefs, 2015).

Hence, water molecules may exist as nine possible isotopic combinations of H and O, with mass numbers spanning from 18 ($^{1}H_2^{16}O$) to 22 ($^{2}H_2^{18}O$). However, only four of those combinations are common, as water molecules containing two heavy isotopes are very rare, and important for paleoclimate reconstructions :$^{1}H^{2}H^{16}O$, generally written as HDO, and $^{1}H_2^{18}O$, $H_2^{16}O$ and $H_2^{17}O$.

Isotopomer of Water	Average Abundance (%)
$H_2^{16}O$	**99.73098**
$H2^{18}O$	**0.199978**
$H2^{17}O$	**0.037888**
$HD^{16}O$	**0.031460**
$HD^{18}O$	0.0000006
$HD^{17}O$	0.0000001
$D^{16}O$	0.00000002
$D^{17}O$	0.00000000001
$D^{18}O$	0.00000000005

Table 2.1: Average abundances of the nine isotopic combinations of water (Sharp, 2017).

Changes in isotopic composition follow the general rule that the isotopic composition of one element in a small reservoir varies largely, in comparison to the same element in a big reservoir, and by a quantity proportional to the relative dimensions of the reservoirs. The stable isotope composition of large water bodies like oceans and lakes, in fact, is subjected to small modifications over time. On the contrary, the isotopic composition of relatively modest amount of water, especially those from meteoric origin e.g. a cloud, fluctuates largely over time. Thus, in the hydrosphere the main variations in $\delta^{18}O$ and δD values are associated with phase change processes, as evaporation and condensation. Measurements of oxygen and hydrogen isotopic composition are reported against the international standard Vienna Standard Mean Ocean Water (V-SMOW), which carries a value of 0‰ for both $\delta^{18}O$ and δD.

Reservoir	Volume (%)	δD (‰) SMOW	$\delta^{18}O$ (‰) SMOW
Ocean	97.2	0±5	0±1
Deep Atlantic	+0.05		
Deep Pacific	-0.15		
Deep Antarctic	-0.40		
Ice Caps and Glaciers	2.15	-230 ± 120	-30 ± 15
Groundwater	0.62	-50 ± 60	-8 ± 7
Fresh surface water	0.017	-50 ± 60	-8 ± 7
Atmospheric water vapour	0.001	-150 ± 80	-20 ± 10

Table 2.2: Main water reservoirs on the Earth and their respective volumes and isotopic composition (Criss, 1999) .

2.2.2 Air masses journey towards Antarctica

This section focuses on the processes affecting air masses and their isotopic composition from their genesis until snow precipitation on the Antarctic ice sheet.

2.2.2.1 Sea water evaporation

The ice coring drilling sites in Antarctica are reached by moisture which originates in different ocean basins located at sub-tropical and mean latitudes of the Southern Hemisphere (Figure 2.3) (Sodemann & Stohl, 2009). The final $\delta^{18}O$ and δD composition of the precipitations reflect the thermal history during the water transport from evaporation source to the precipitation site (Lorius et al., 1969). However, the isotopic composition of vapour start changing right after the evaporation from the oceanic source.
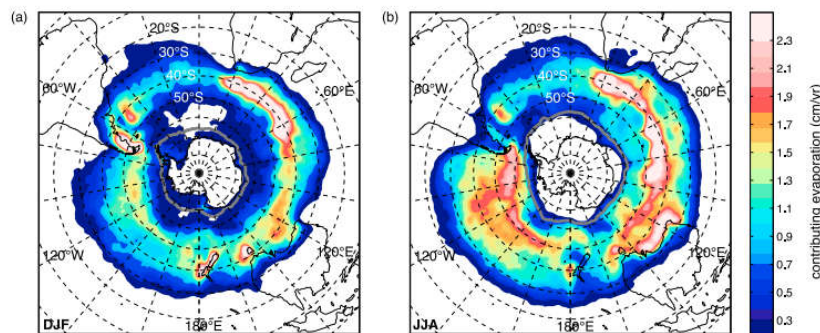
Figure 2.3: Map illustrating the seasonal mean moisture source areas for Antarctica during (a) summer (DJF) and (b) winter (JJA). Mean sea ice boundary is depicted by the grey line (Sodemann & Stohl, 2009).

Craig & Gordon (1965) developed the first general model to explain and predict fractionation during evaporation (Figure 2.4). Right after the evaporation from the ocean, the vapour isotopic composition is enriched in lighter isotopes (H and ^{16}O) as the lighter isotopologue molecules are characterized by higher vapour pressure in comparison to heavier molecules, composed by D and ^{18}O. The model represents the water-vapour interface as a series of discrete layers, each of them dominated by specific transport mechanism and equations to quantify the overall isotope fractionation as a function of humidity and the δ value of the free air. The δ value in the thin laminar liquid layer shows an increasing trend approaching the interface, due to preferential loss of the light isotopes to the vapour. The δ value of the vapour, on the other hand, decreases towards the free air away from the liquid-vapour interface. Despite its simplistic representation of evaporation processes at the water–air interface, the Craig and Gordon model is still considered to describe reasonably the isotopic composition of the evaporation flux (Horita et al., 2008).
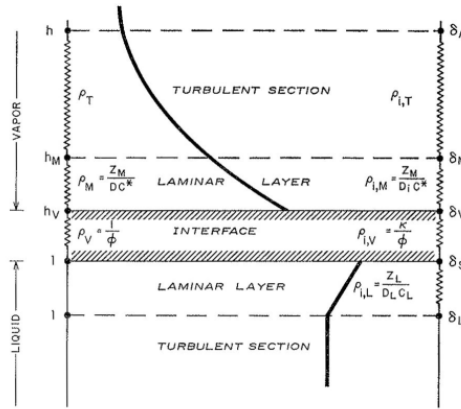
Figure 2.4: Craig and Gordon's 'laminar layer model' for evaporation of H2O into unsaturated air. The isotopic composition of the liquid and vapour layers are shown by the thick black lines (Craig & Gordon, 1965).

2.2.2.2 Transport and distillation models

Soon after water vapour leaves the ocean surface, it cools when it raises, and it forms clouds. When condensation occurs in the air mass and then a rain fall event happens, the isotopic composition of the air mass changes. The first theoretical approach to explain isotope variations in meteoric waters is based on the "closed" Rayleigh distillation model, which describes the partitioning of isotopes between two reservoirs as one reservoir decreases in size. However, such a model is quite limited and it can be applied only in those cases where rainout is the sole factor regulating the atmospheric-moisture budget (Dansgaard, 1964). The equations of the Rayleigh distillation model describe an isotope fractionation process where the condensate material (droplets) is continuously removed (rainfall) from the system (cloud) without back exchanges between the two phases. In a cloud, isotopically heavy water molecules are continuously lost as precipitation, since they easily pass from vapour to liquid state due to the lower vapour pressure in comparison to the ones containing lighter isotopes, thus, the δ value of remaining vapour becomes progressively more negative (depleted). With increasing degree of condensation, the δ value of rainfalls becomes proportionally lower (by the fractionation factor at the temperature of condensation). Rayleigh fractionation in an air mass can lead to very large depletions of the heavy isotopes in precipitation. In particular, considering an air mass originating at sub-tropical latitudes and travelling poleward, its isotopic composition will change from an initial value of $\delta^{18}O$ of -10‰, -15‰, to -50‰ while reaching Antarctica (Figure 2.5). The air mass isotopic composition turns in more negative values as it moves southwards due to cooling and precipitations, depleting the vapour of HDO and $H^{18}O$ molecules.
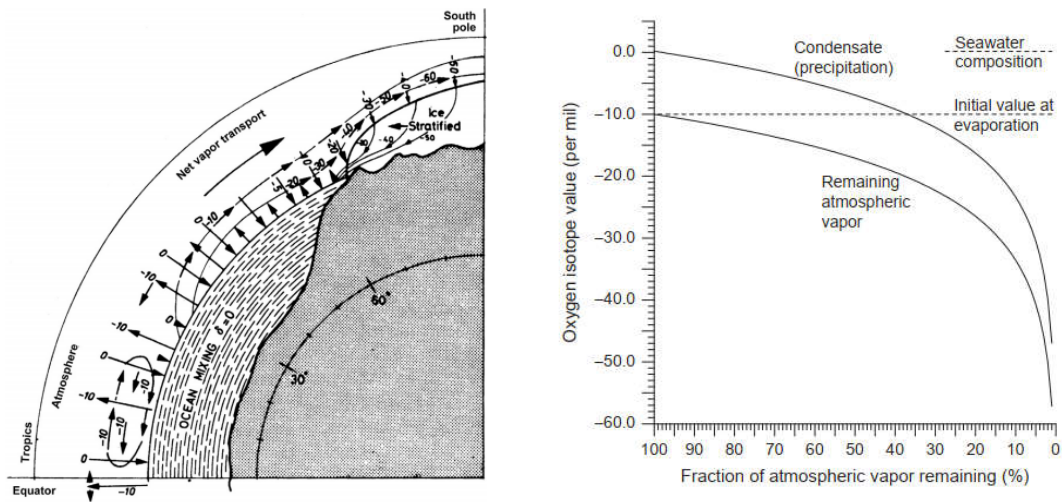
Figure 2.5: Left. Schematic diagram to illustrate isotopic depletion of water, with $\delta^{18}O$ values, while traveling from subtropical latitudes towards the Antarctic Ice Sheet (Bradley, 2015). Right. The relationships between isotopic composition of atmospheric vapour ($\delta^{18}O$) and precipitation relative to evaporation with an original composition of 10% and fractionation at a constant temperature of 15 °C (Rohling, 2013).

The simple Rayleigh distillation model, nevertheless, neglects the complexity of the dynamical processes involved in the formation of precipitations. To get closer to the real processes, models need to account for the complexity of cloud microphysics and its interplay with the various fractionation processes occurring at each phase change of the water in the atmosphere (Ciais & Jouzel, 1994).

One of the first improvement efforts of the Rayleigh distillation model was done by Jouzel & Merlivat (1984), through the introduction of the *isotopic kinetic effect* which governs the isotopic content together with the equilibrium isotopic effect during the vapour deposition leading to snow formation. When ice crystals are formed in a cloud, HDO and $H_2^{18}O$ molecules tend to condense more slowly than H_2O in a supersaturated environment. The Rayleigh Model including the isotopic kinetic effect (RMK) has been later ameliorated by the development of the vapour, liquid, and ice in the Mixed Cloud Isotopic Model (MCIM) (Figure 2.6c), characterized by a more refined description of the microphysical processes occurring at low temperature in the cloud (Ciais & Jouzel, 1994). The MCIM includes the coexistence of liquid droplets and ice crystals in a cloud and is based on the Bergeron-Findesein process (Bergeron, 1935). In mixed cloud containing both liquid water and ice for given range of temperatures, the crystals and the droplets will never be in isotopic equilibrium. In this case, the liquid droplets tend to evaporate, while vapour deposits directly onto the existing crystals by inverse sublimation and freezing of supercooled droplets. From an isotopic point of view, the Bergeron-Findesein process has to be taken into account in the MCIM model for polar precipitations because droplets will not be in isotopic equilibrium with respect to the vapour, which requires to consider the kinetic fractionation associated with the vapour-liquid transition.

29
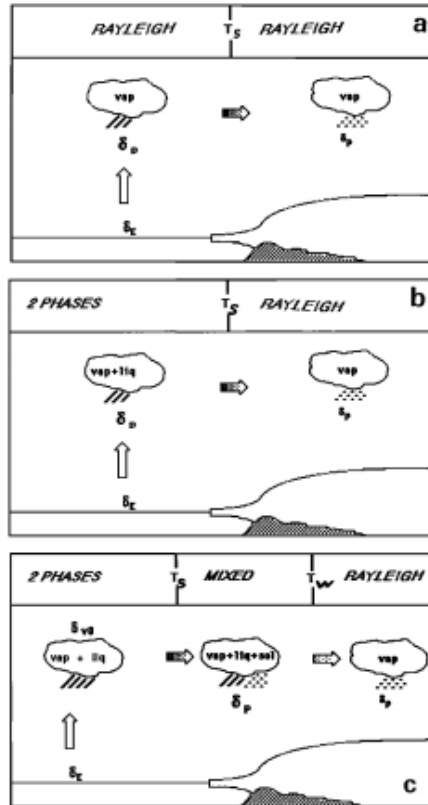
Figure 2.6: Three generations of one-dimensional isotopic models. (a) Classical Rayleigh distillation. (b) Rayleigh Model including the isotopic Kinetic effect (RMK) of Jouzel and Merlivat (1984).(c) Mixed Cloud Isotopic Model (MCIM) (Ciais & Jouzel, 1994). Figure from Ciais and Jouzel (1994).

However, one-dimensional isotopic models represent a simplification of reality as many other processes may affect the variation of isotopic composition in air masses traveling poleward. Several recent studies focus on the implementation of cloud isotopic models, incorporating the contribution of other phenomena affecting the fractionation process as: (i) presence of sea ice (Faber et al., 2017), (ii) contribution from multiple moisture sources (Sodemann et al., 2008), (iii) cloud condensation and changes in precipitation (Pausata & Löfverström, 2015) and (iv) re-evaporation of droplets (G. Hoffmann et al., 2000).

2.2.3   The Global Meteoric Water Line

One of the most exceptional correlations observed in the geochemistry of natural substances is the near linear relation existing between δD and $\delta^{18}O$ values for the most of waters of meteoric origin. Oxygen and hydrogen isotopic distribution are correlated in meteoric waters following the relationship defined by Craig (1961) known as Global Meteoric Water Line (GMWL):

$$\delta D = 8 \cdot \delta^{18}O + 10 \tag{2.5}$$

Assuming that oceans were characterized by different isotopic composition in the past and global atmospheric circulation patterns were similar to the ones of today, the past GMWL would have a similar slope to the modern one but a different intercept. The relationship between $\delta^{18}O$ and δD cannot

30

always be described by equation 2.5. Neither the numerical coefficient, 8, nor the 10, are really constant as both depend on local climatic processes. The GMWL is an equation which approximates the relationship existing between δD and δ¹⁸O at large spatial scale, thus, local variations of the GMWL may occur, introducing the concept of the local meteoric water lines (LMWLs) (Rozanski et al., 1992). The LMWLs slopes may assume values between 4.8 and 10.9 depending on the evaporative system (lakes or sea), and are a useful tool for evaluating hydroclimatic processes in isotope-enabled climate models (Putman et al., 2019).
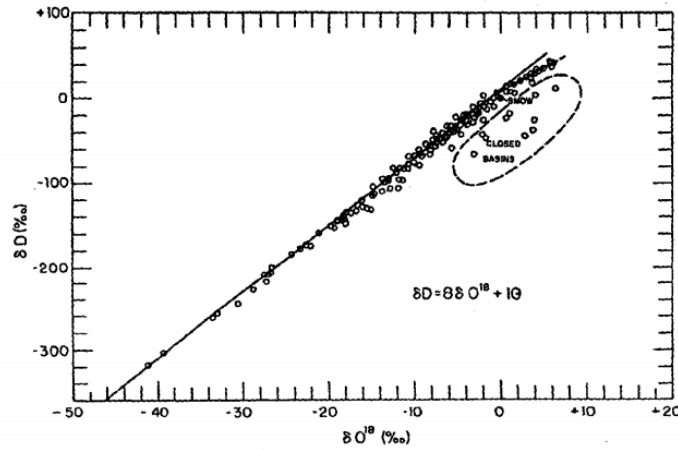
Figure 2.7: Deuterium (δD) and oxygen 18 (δ¹⁸O) variations in rivers, lakes, rain, and snow, expressed as per mill enrichments relative to "standard mean ocean water" (SMOW) (Craig, 1961).

2.2.4   *d*-excess

The *deuterium excess is a second order parameter*, which involves both δD and δ¹⁸O and follows the relationship:

$$d - excess = \ \delta D - 8 \cdot \delta^{18}O \tag{2.6}$$

The *d-excess* value of 10 is representative of mean modern worldwide meteoric water samples, but when *d-excess* values are far from 10, they fall above or below the Global Meteoric Water Line. The *d-excess* has firstly been interpreted as a parameter that contains information prevailing in the moisture source as sea surface temperature (SST), and relative humidity of the air compared to the saturation vapour pressure at the ocean surface (RH_{SST}). As the moisture sources can be spatially variable in time, the *d-exce*ss may also be considered as an integrated tracer of past hydrological cycles changes, providing information on variations in moisture transport, air masses trajectories and local temperature at the deposition site (Masson Delmotte et al., 2004; Stenni et al., 2010).

2.2.5   **The isotopic thermometer (δ¹⁸O-T_{site} relationship)**

When the air mass reaches high latitudes, after having travelled northwards/southwards, the remaining vapour is depleted of heavy isotopes and, due to the low temperature, the fractionation

becomes larger. The temperature is one of the control parameters of the meteoric water isotopic composition, because it constraints the amount of water lost by the air mass along its pathway.

Dansgaard (1964) has been the first who observed the existence of a relationship between the $\delta^{18}O$ in precipitations and mean annual temperature at collection site. Global correlations between $\delta^{18}O$, δD and mean annual surface temperature are described by the following equations:

$$\delta^{18}O = 0.69 \cdot T_{average} - 13.6 \text{‰} \tag{2.7}$$

$$\delta D = 5.6 \cdot T_{average} - 100 \text{‰} \tag{2.8}$$

Where T$_{average}$ is the mean annual temperature at precipitation site and 0.69 and 5.6 are the *spatial slopes* coefficients respectively for $\delta^{18}O$ and δD (Figure 2.8).
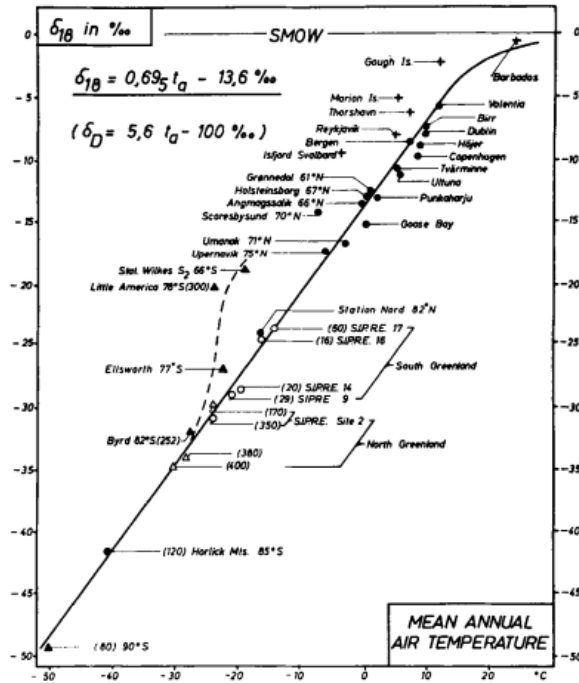
Figure 2.8: The annual mean $\delta^{18}O$ of meteoric precipitation function of the annual mean air temperature at surface (Dansgaard, 1964).

These first pioneering findings from Dansgaard have been followed by the work of Lorius & Merlivat (1975). They estimated the relationship between the isotopic composition in East Antarctic snow and site temperature along a traverse from Dumont D'Urville and Dome C, calculating the following relationship:

$$\delta D = 6.04 \cdot T_{average} - 51\text{‰} \tag{2.9}$$

However, the linear relationship between site temperature and isotopic composition of snow at a spatial scale represents a simplistic way to interpret this correlation. Starting from the 1980's, this pure experimental approach has been substituted with simulations performed with the use of General

Circulation Models (GCMs) equipped with stable water isotopes tracers. Those models simulate the fractionation and transport effects on the water isotopic composition along the hydrological cycle. From the very first step of evaporation from the ocean, they represent the contribution of evapotranspiration from the land surface, the transport and mixing in the atmosphere, the precipitation from clouds, and the return of water to the Earth's surface (Galewsky et al., 2016).

The existing relationship between water stable isotopic composition analysed in ice cores and site temperature can also be used to evaluate past temperature changes. Past site surface temperatures (T) are calculated by applying an estimated 'paleothermometer' gradient *a*:

$$a = \frac{\Delta(delta)}{\delta T} \tag{2.10}$$

Where δ (delta) is the isotopic variation in the ice record corrected for past changes in $\delta^{18}O$ seawater due to global ice volume (Bintanja et al., 2005) and δT is the variation of temperature over time. The $\Delta(delta)/\delta T$ slope can be estimated for past climate conditions, as glacial and interglacial periods, through the application of GCMs equipped with water stable isotopes. Recent studies suggest that the present-day spatial $\Delta(delta)/\delta T$ relationship for inland Antarctica can be used with good approximations for glacial to present-day changes (Jouzel et al., 2003; Werner et al., 2018). On the other hand, $\delta^{18}O$ appears to be less sensitive to temperature variations (0.34‰ °C^{-1}) for past interglacial conditions and future warming scenarios (Sime et al., 2008, 2009). In addition, past temperature variations at precipitation deposition site (T_{site}) and at the moisture source (T_{source}) can be reconstructed through the use of the *d*-excess record, following the method applied for EDC, EDML and Dome Fuji ice core (Landais et al., 2021; Stenni et al., 2010; Uemura et al., 2012), which takes into consideration the temperature changes in the moisture source regions (Figure 2.9). Additional methodologies can be used to reconstruct past temperature changes from ice cores:

a) *Temperature profiles of boreholes* conserve partial imprints of past temperature changes due to the heat diffusion from the surface to the depth of the ice sheets.

b) *Fluctuations in isotopic composition of atmospheric gases ($\delta^{15}N$, $\delta^{40}Ar$)* trapped in air bubbles could be used to estimate abrupt temperature changes as they cause thermal gas diffusion (Buizert et al., 2021; Kindler et al., 2014; Severinghaus & Brook, 1999).

Those techniques are usually not applied in Antarctica, due to the low accumulation rates at plateau sites. Isotopic anomalies in air bubbles cannot be applied as well, since central Antarctica did not experience abrupt temperature changes, which could be detected by variations in $\delta^{15}N$ and $\delta^{40}Ar$ isotopic composition (Jouzel et al., 2003). However, recently Buizert et al. (2021) reconstructed temperature variations in Antarctica during the LGM through borehole thermometry and firn properties (deduced from $\delta^{15}N$) in ice cores.
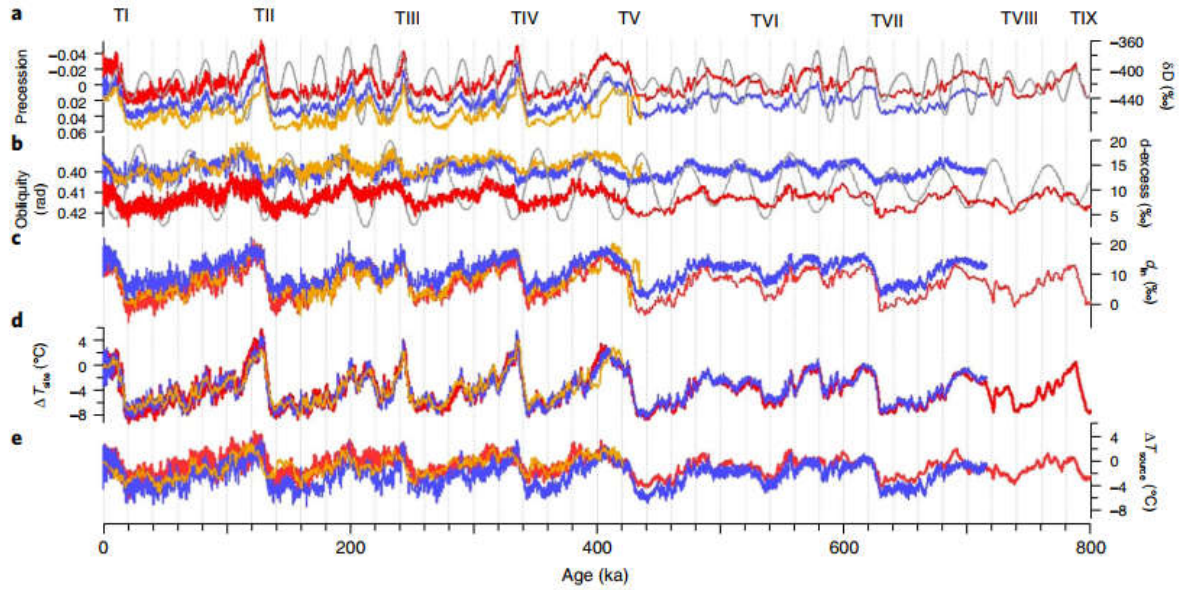
Figure 2.9: Deep Antarctic ice cores (EDC, Vostok and Dome F) water isotopic records and climate recontructions. a. δD and precession parameter on inverse scale (grey curve), b. *d*-excess and obliquity on inverse scale (grey curve), c. dLn, d. ΔT_{site} and e. ΔT_{source} series from the EDC (red), Vostok (orange), Dome F ice cores (Δ indicates the variation with respect to present-day values). The glacial terminations are numbered with roman numbers from TI to TIX.

2.2.6   Other factors controlling the isotopic composition in ice cores

Even if the temperature at the deposition site represents the main driver of the stable water isotopic composition in snow and then in glacier ice; other effects may contribute to the final signal. In this section some of the most common factors and their impacts on the isotopic composition are briefly described.

2.2.6.1 Continental effect

Precipitations become increasingly depleted in heavy isotopes as the air mass travels far away from the moisture source. When the air mass reaches the continent (which could be either Greenland or Antarctica), snow precipitations are already characterized by negative isotopic values in proximity of the coast (e.g. ~ -25‰ in coastal Antarctica). The more the air mass keep travelling towards the interior of the continent the more snow precipitations will have a negative isotopic composition. The continental effect is associated with the progressive depletion of heavier isotopes and the lack of moisture recharge on the way to the interior of the continent. In addition, in Antarctica the continental effect is also associated with the progressive temperature decrease from the coast to the interior, both contributing in determining the isotopic composition of snow precipitation.
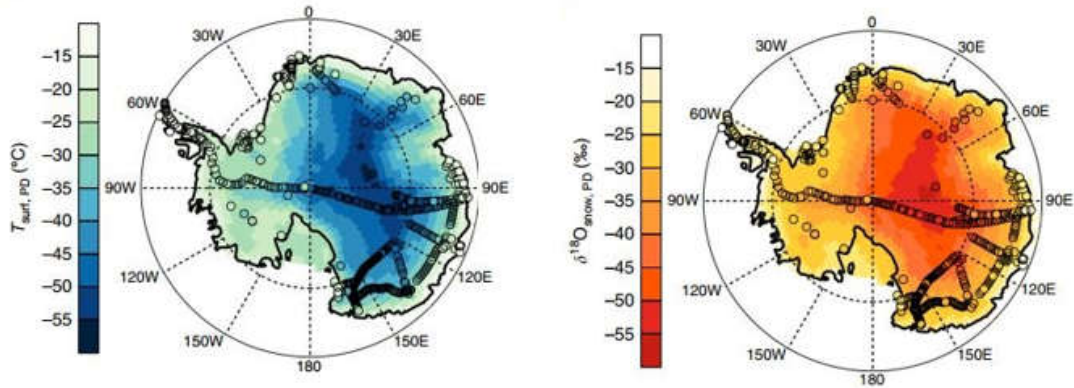
Figure 2.10: Left. Map of present-day Antarctic surface temperatures simulated by ECHAM5-wiso (background pattern) and field data (black circles). b Map of present day $\delta^{18}O$ in snow precipitations across Antarctica simulated by ECHAM5-wiso (background pattern) and field data (black circles) (Werner et al., 2018).

Observed and simulated annual average Antarctic surface temperatures range from -15°C in coastal areas to -60 °C in the plateau region. The continental effect is well depicted in the simulated $\delta^{18}O$ values distribution in surface snow ranges across Antarctica (based on traverse field data and modelled with atmospheric general circulation models equipped with stable water isotopes) since they mimic the temperature spatial pattern, with r=0.92, and are more negative in the interior of the continent as shown in Figure 2.10 (Werner et al., 2018).

2.2.6.2 Altitude effect

The isotopic composition of air masses becomes lighter with increasing altitude. When vapour is deviated upward by a mountain, it decompresses, cools adiabatically, and more precipitation occurs. The percentage of vapour remaining in the air mass will decrease rapidly if the elevation is high. Topography has a strong influence on the isotopic composition of snow precipitation. The altitude effect can be clearly observed in Figure 2.11. Highly negative correlation between altitude and $\delta^{18}O$ is evident along the two NS transects. In this specific case, elevation gradients are in the order of -1.3‰/100 m – -1.5‰/100 m (Becagli et al., 2004), however distinct areas in Antarctica are subjected to different altitude effects as the relationship depends also from other factors, like air masses provenance.
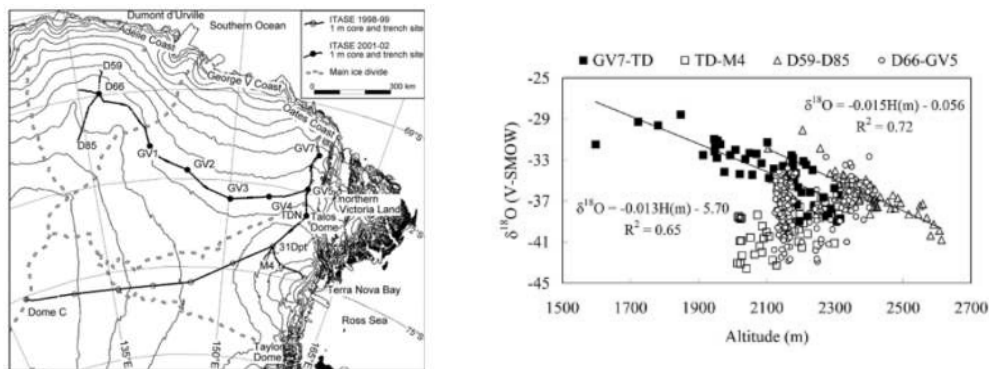
Figure 2.11: ITASE traverses for the years 1998-99 and 2001-02. Right: Snow δ18O values vs altitude for the different transects. The regression lines for the GV7–TD and D59–D85 transects are shown (black lines) (Becagli et al., 2004).

Generally, in Antarctica the isotopic records in snow, and then in ice, are mainly influenced by temperature at precipitation site as well as both latitudinal and continental effects depending on the ice core drilling site. Plateau ice cores records are characterized, in average, by more negative isotopic composition with respect to coastal sites due to colder temperatures, higher elevation and greater distance from moisture sources (Figure 2.12) (Masson Delmotte et al., 2011).
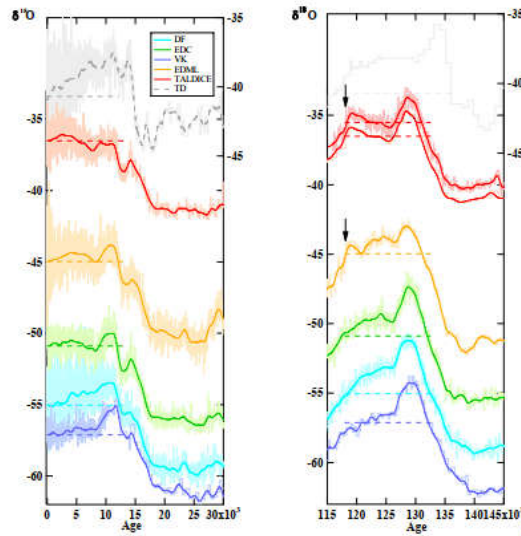
Figure 2.12: Water stable isotope records on the EDC3 age scale for Dome Fuji (DF), EPICA Dome C (EDC), Vostok (VK), EPICA Droning Maud Land (EDML) and TADICE during the Holocene (left panel) and Last Interglacial (right panel) periods. (Masson Delmotte et al., 2011).

2.2.7   Post depositional effects

When snow precipitation occurs on the ice sheet, the snowfall holds a certain isotopic composition which may be modified after the deposition due to several processes acting on snow during the climate signal archival process. It has been recently evidenced, thanks to new technological developments, that the isotopic composition of snow during summer in both Greenland and Antarctica is significantly affected by exchanges between snow and water vapour (Ritter et al., 2016; Steen-Larsen et al., 2014). The evolution of the snow isotopic composition after the deposition is most likely due to an exchange of molecules between the snow and the atmospheric vapour, causing an enrichment of the vapour and a depletion in the snow (Casado et al., 2018) (Figure 2.13). On the other hand, Ritter et al. (2016) estimate that during summer at Kohnen station (Antarctica) the isotopic composition in snow increases in the order of $\sim$ 3 ‰ for δD and $\sim$ 0.4‰ for $\delta^{18}O$, in phase with the diurnal cycle in the air.

In addition, snow metamorphism may as well influence changes in isotopic composition of deposited snow. During summertime, when snow metamorphism is strong, variations of $\delta^{18}O$ are estimated to experience changes up to 8‰ at Dome C. However, those changes in isotopic composition do not influence only surface snow but can be rapidly transferred to the subsurface. Those processes greatly influence the isotopic composition of snow deposited at the surface and weaken the correlation between isotopic composition in the snow and the temperature at site deposition, making complicated the reconstruction of temperature changes at seasonal scale at certain sites (e.g. Dome C) (Casado et al.,

2018; Münch et al., 2017). However, the isotopic composition is still valid to obtain past climate signal at multi-decadal and centennial time scales (Münch & Laepple, 2018).
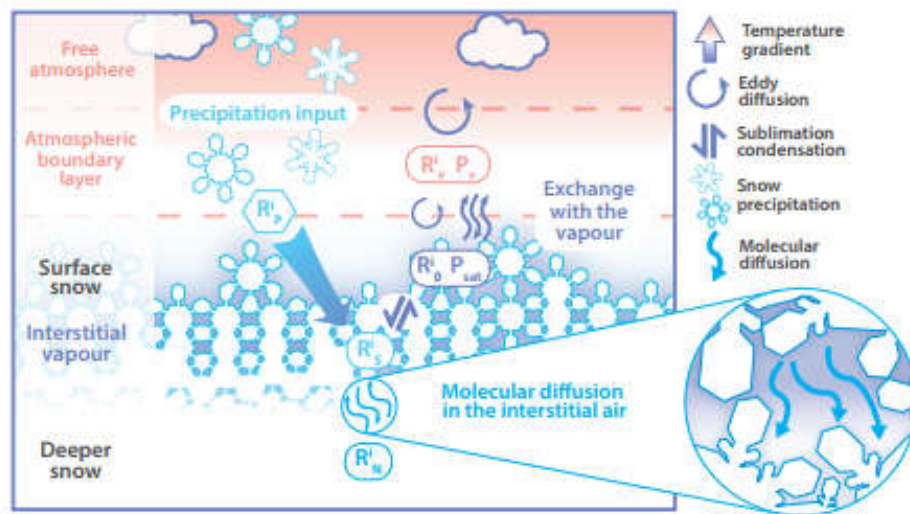
Figure 2.13: Schematic of the different processes that influence the snow isotopic composition (Casado et al., 2018).

In snow and firn layers, also the diffusion process act in modifying the isotopic signal. The air can move within the firn through pores, allowing water molecules to exchange between the vapour and solid phases. Diffusion may as well occur in solid ice beneath the firn layer. It is a slower process but, nonetheless, accounts for a significant amount of total diffusion as it happens over millennia (Jones et al., 2017). Diffusion acts as a low pass filter on the isotopic record archived in snow and ice, smoothing the signal (Figure 2.14). In ice cores records, diffusion has strong effect on power spectra, it tends to dampen high-frequencies, representative of annual and decadal signal, while centennial up to millennial low-frequencies are preserved (Casado et al., 2019).
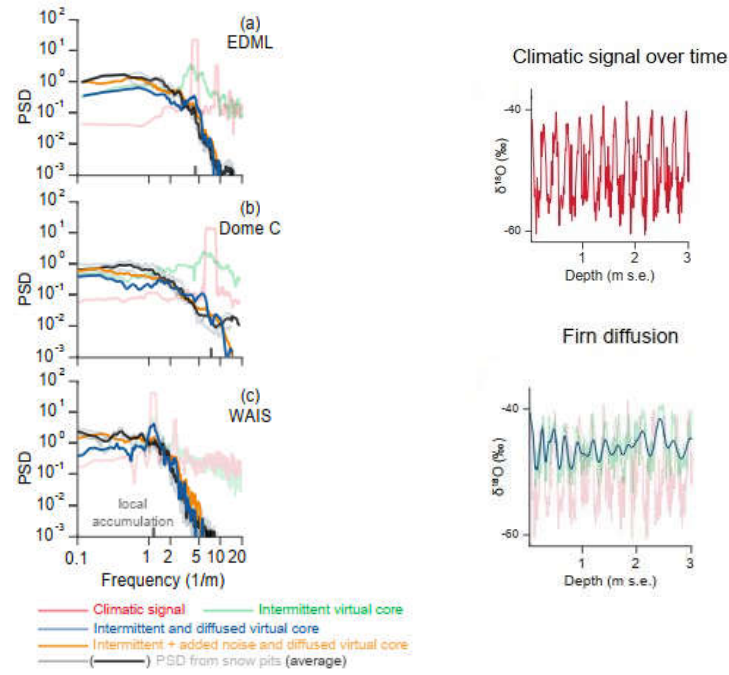
Figure 2.14: Left. Effects of precipitation intermittency and diffusion on spectral density of a virtual ice cores and real isotopes profiles from snow pits for (a) EDML, (b) Dome C, and (c) WAIS. In the graph are reported the climatic signal (light red), intermittent virtual core (light green), intermittent and diffused virtual core (light blue), intermittent + added noise and diffused virtual core (orange), snow pits from the sites (individual: grey, average: black). Right: Virtual climatic isotopic ($\delta^{18}O$) signal in a modelled ice core (top) only recording the climatic signal and modelled isotopic record introducing firn diffusion (bottom) (Casado et al. 2019).

2.2.8 Analytical methods for $\delta^{18}O$ and δD

In the framework of this thesis, the oxygen and hydrogen isotope composition of 3115 TALDICE samples has been analysed using the cavity-ring-down spectroscopy technique at the University of Venice (Italy) and at the Laboratoire des Sciences du Climat et de l'Environnement (LSCE, France). In this section the analytical methodology and the data calibration procedures are described.

2.2.8.1 Cavity Ring-Down Spectroscopy

Stable isotopes of water have been classically analysed on discrete samples with the isotope ratio mass spectrometry (IRMS) technique. Mass spectrometry may achieve high precision and accuracy. However, performing analysis with this technique requires long time since the isotopic composition of water molecules is not directly measured. For $\delta^{18}O$ analysis, the isotopic content of oxygen is measured after equilibrating the water sample with CO_2 (Epstein & Mayeda, 1953), while δD analysis commonly involves the reduction of water to hydrogen gas over hot uranium or chromium (Gehre et al., 1996; Vaughn et al., 1998), as well as the equilibration of water with H_2 gas in presence of a platinum catalyst (Horita et al., 1989).

Laser spectroscopy at the near- and mid-infrared (IR) regions has become a common alternative for water isotope analysis. In particular, the Cavity Ring Down Spectrometry (CRDS) holds numerous

advantages over IRMS, like a shorter time of analysis, direct injection of the vaporized sample in the optical cavity of the instrument and reduced costs (Gkinis et al., 2010).

The CRDS technology is based on the Lambert-Beer law, which states that at there is a linear relationship between the concentration and the absorbance of the solution (Ricci & Ditzler, 1994):

$$A = \varepsilon \cdot c \cdot l \hspace{8cm} (2.11)$$

Where A is the absorbance (adimensional), ε is the molar absorption coefficient ($M^{-1}cm^{-1}$), c is the molar concentration (M), and l is the optical path length (cm). The same principle could be applied to measure the isotopic composition of water ($\delta^{18}O$ and δD).

The analysis of $\delta^{18}O$ and δD composition in TALDICE samples (5 cm resolution) have been performed at University of Venice (Italy) and at LSCE with a Picarro L2130-i (Figure 2.15). A syringe held on an auto-sampler (a) collects the water and injects it in the vaporizer (b), which has a temperature of 120°C. The gas is then transferred to the instrument (c) thanks to a carrier gas (N_2). Once the sample reaches the optical cavity, equipped by three high reflectivity mirrors, a short single-frequency laser pulse enters in the cavity. The light is reflected back and forth inside the cavity among the three mirrors. Every time that the light is reflected, a small fraction of light leaks out of the cavity and produces a signal directly proportional to the intensity in the cavity. The CRDS measures the decay time of the light leaking out of the cavity, instead of the total intensity of the light. In this way the rate of absorption can be calculated, which is inversely proportional to the species concentration. The more the laser pulse is absorbed by the sample, greater is the concentration of certain chemical species in the sample, the shorter is the measured decay time (Berden et al., 2000). The measurements precision is $\pm$ 0.2 ‰ for $\delta^{18}O$ and $\pm$ 0.7 ‰ for δD.
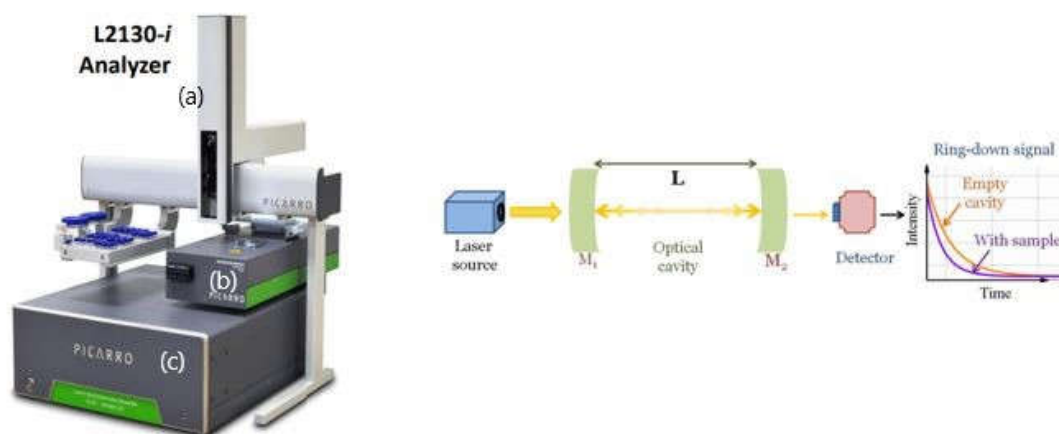
Figure 2.15: Picarro analyzer setup (L2130-i). Left. The instrument is made by an auto-sampler (a), a vaporizer (b) and an optical cavity with the detector (c). Right. Schematic diagram of CRDS, yellow arrows in the cavity depict the back and forth path of the light inside the cavity with a decreasing intensity after each pass. The signal is then collected by the detector and the decay time is recorded (www.picarro.com).

2.2.8.2 Laboratory standards

To analyse the $\delta^{18}O$ and δD in water samples is necessary to calibrate the raw data measured by the Picarro with laboratory standards. We choose three water standards whose isotopic composition is known and calibrated against the international standards provided by the International Atomic Energy Agency (IAEA): V-SMOW2 (Vienna Standard Mean Ocean Water 2) and SLAP2 (Standard Light Antarctic Precipitation 2). Their reference values are 0 ‰ and -55.50 ‰ for $\delta^{18}O$ and 0 ‰ and -427.5 ‰ for δD, respectively, on the V-SMOW-SLAP δ scales.

The laboratory standards used to calibrate TALDICE samples are waters collected in Antarctica (OC3 and Talos) and Greenland (NEEM), from surface snow. Generally, it is good practice to employ two standards covering a wide range of isotopic values (more and less negative, as OC3 and NEEM), and a third standard whose composition is similar to the one of the analysed samples (Talos). Standard isotopic composition values are reported in Table 2.3.

Standard	$\delta^{18}O$ (‰)	δD (‰)
OC3	-53.96	-423.20
Talos	-40.19	-313.60
NEEM	-33.50	-257.20

Table 2.3: Water standards used to calibrate TALDICE samples.

Those standards are placed in vials and analysed with the samples during the analysis run. Standards are placed at the first three positions in the tray and analysed 20 times each, while samples are analysed 7 times each. The analysis template is built as such: standards are analysed at first, then samples are analysed, and each 7 samples measured, the Talos standard is re-analysed. Then, Talos and NEEM standards are re-analysed at the end of the run 20 times each (Table 2.4). To avoid memory effects, only the last 4 values analysed for each standard and the last 3 values analysed for each sample are kept for the final calibration calculations.

1	2	3	4	5	6	7	8	9
OC3 x20	*Talosx20*	*NEEMx20*	Sample 1	Sample 2	Sample 3	Sample 4	Sample 5	Sample 6
10	2	11	12	13	14	15	16	17
Sample 7	Talosx7	Sample 8	Sample 9	Sample 10	Sample 11	Sample 12	Sample 3	Sample 14
2	18	19	20	21	22	23	24	2
Talosx7	Sample 15	Sample 16	Sample 1	Sample 17	Sample 18	Sample 19	Sample 20	Talosx7
25	26	27	28	29	30	31	2	32
Sample 21	Sample 22	Sample 23	Sample 24	Sample 25	Sample 26	Sample 27	Talosx7	Sample 28
33	34	35	36	37	38	2	39	40
Sample 29	Sample 30	Sample 31	Sample 32	Sample 33	Sample 34	Talosx7	Sample 36	Sample 37
41	42	43	44	45	2	3		
Sample 38	Sample 39	Sample 40	Sample 41	Sample 42	Talosx20	NEEMx20		

Table 2.4: Example of analysis template used for the Picarro at LSCE. Numbers in grey boxes indicates vials position on the tray. In white boxes the name of the respective samples, standards and the number of injections are reported.

2.3   Stable isotopes in air bubbles

This section focuses on the stable isotopes of oxygen and nitrogen in air bubbles trapped in ice cores. Processes happening in the firn as well as analytical method are described.

2.3.1   Air in the ice

The transformation of snow into glacial ice is an extremely important process as once the snow turns into ice, the air trapped in the pores gets sealed and creates a unique time capsule of the atmospheric composition at the closing-off time.
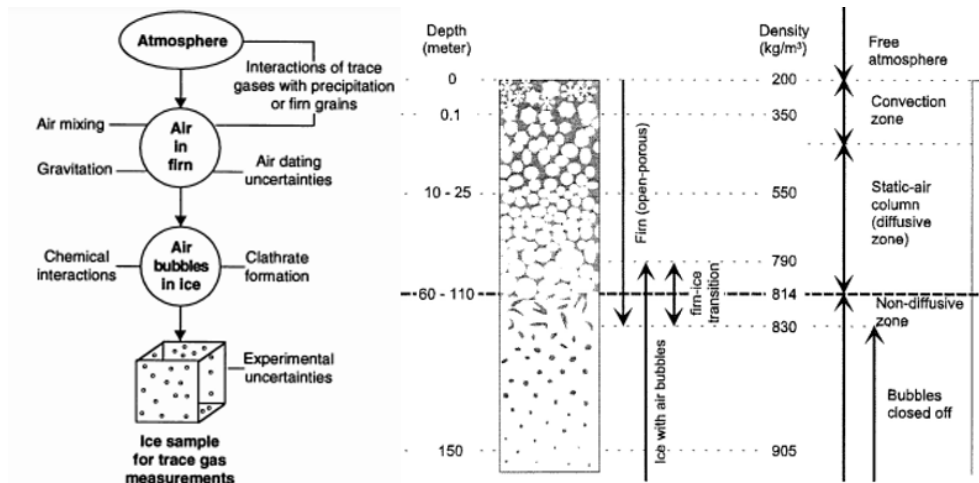
Figure 2.16: Left. Diagram of physical processes of snow-ice transformation and air trapping in the ice (Raynaud et al., 1993). Right. Schematic of the firn column and relative densities (Blunier & Schwander, 2000).

The continuous deposition of snow on ice sheets buries the previous snow layers, compacting the snow, increasing its density and decreasing its porosity. Snow slowly turns into glacial ice as the initial density keeps increasing, passing through an intermediate state called firn (Figure 2.16). Snow densification happens in three stages: settling, sintering and final transition into glacial ice (Herron & Langway, 1980). During the first stage, the initial snow density increases from 350 kg/m^3 to 550 kg/m^3 and snow transforms in firn. The metamorphism of snow into firn is dominated by the rearrangement of the snowflakes into firn grains, characterized by packing of the medium and porosity decrease. At this stage the air is still free to circulate in the firn pores and exchange with the free atmosphere. In deeper layers firn density increases slower with depth, while sintering and plastic deformation become the most important processes happening during the second stage.

However, the firn can be divided in three different layers based on different air circulation regimes: (i) convection zone, (ii) diffusive zone and (iii) non-diffusive zone (Sowers et al., 1992) (Figure 2.16). In the superficial convective zone, air circulating in the firn is well mixed and has a similar composition than the atmospheric air, due to the wind pumping. The thickness of the convective zone is influenced by wind strength, which moves air in the porous medium in response to atmospheric pressure

variations. Also other factors as surface topography, porosity, and grain size may influence this parameter. With the increasing of the depth, the firn is affected by decrease of porosity and of permeability which influences the airflow in the porous medium. In the diffusive zone, the wind pumping does not represent the main driver of the air movement, the air becomes static and its composition is mainly influenced by gravity, which attracts heavier gases towards the deepest portion of the firn. The bottom of the diffusive zone and the close-off depth are separated by a transition layer called "non-diffusive zone", where the most of gas transport does not happen due to the high density and little porosity. Here can be found the Lock-in-Depth (LID), which is defined as the depth at which the air stops diffusing as the porosity of the firn becomes too low (Buizert et al., 2013).

When the firn density reaches the critical value of 800 kg/m^3, the transition into ice happens. At the Close-off-Depth (COD) the intercommunicating passages become sealed and form bubbles in the ice, where no more exchanges are possible with the free atmosphere (Blunier & Schwander, 2000). The ice-firn transition zone could be identified between 60 m to 120 m below the surface, depending on the site condition (e.g. accumulation rate). After the bubble close-off, only further densification may take place deeper in the glacial ice. The progressive caging of air molecules inside the ice molecular structure leads to the formation of air hydrates in the deepest ice layers (Raynaud et al., 1993). The transition from air bubbles to air hydrates in polar ice sheets may take tens of thousands of years, and bubbles and hydrates coexist in layer called the bubble-to-hydrate transition zone, which could reach a thickness up to hundreds of meters (Ohno et al., 2004).
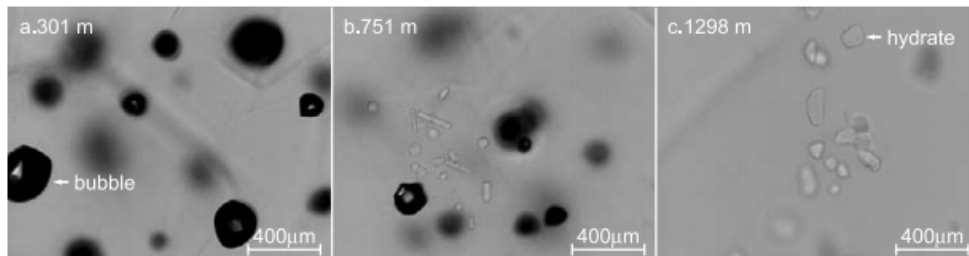
Figure 2.17: Micrographs of air inclusions in the Dome F ice core. Left. Air bubbles above the transition zone. Middle. Small clathrate-hydrates coexisting bubbles in the transition zone. Right. Hydrates below the transition zone (Ohno et al., 2004).

As the close-off happens later with respect to the snow deposition, the age of the air trapped in the bubbles is younger with respect to the surrounding ice. The difference between the ice age and the gas (phase) age at any given depth is called Δage. When the gas is locked-in as bubbles or hydrates, it does not change its position with respect to the surrounding ice over time (Parrenin et al., 2012). Snow accumulation and temperature represent the main driver of the Δage parameter. Sites characterized by high snow accumulation rate as Greenland, show Δage values in the order of 1-2 centuries, while in Antarctica, due to the low accumulation rate and colder temperatures, the typical values of Δage reach the order of millennia (Figure 2.18) (Blunier et al., 2007).
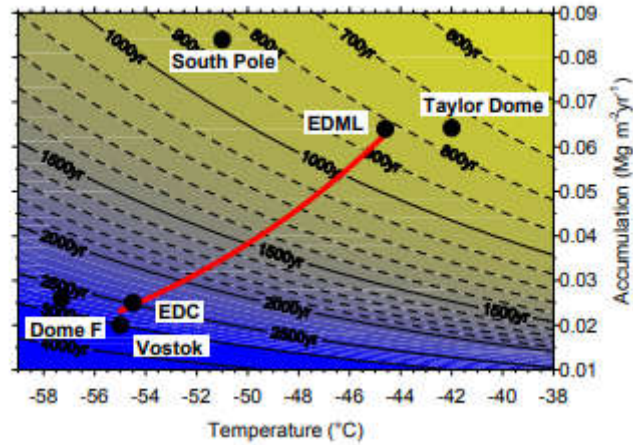
Figure 2.18: Δage as a function of temperature and accumulation rate. Black dots represent ice cores in Antarctica (Blunier et al., 2007).

2.3.2   Stable isotopes in air bubbles

In this thesis oxygen and nitrogen isotopes in air bubbles are analysed in the deeper portion of the TALDICE ice core. Their composition is then used mainly for dating purposes (Chapter 3). In this section the $\delta^{18}O_{atm}$, $\delta^{15}N$ and $\delta O_2/N_2$ parameters and their most common applications in ice core science are presented.
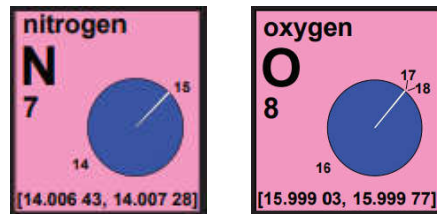
Figure 2.19: Nitrogen and oxygen and their relative isotopic abundances (Holden et al., 2018).

2.3.2.1 $\delta^{15}N$ of N_2

Nitrogen is the main component of atmospheric air (about 78%), ^{14}N is the most abundant isotope, 99.64%, and ^{15}N, the rare one, 0.35%. The isotopic abundance of nitrogen in the atmosphere is considered constant at global scale as its residence time is greater than 10^7 years (Sowers et al., 1989). The isotopic composition of nitrogen is expressed as $\delta^{15}N$. The isotopic composition of nitrogen trapped in air bubbles in ice cores should be constant over time, however processes acting in the firn may cause fractionation and generate deviation from the paleoatmospheric composition.

In this thesis the thickness of diffusive column is estimated with the application of the barometric equation on the new $\delta^{15}N$ data set for TALDICE ice core (Chapter 3). Moreover, $\delta^{15}N$ is also used to perform gravitational correction of other isotopes, as $\delta^{18}O_{atm}$ and $\delta^{40}Ar$ (Severinghaus & Brook, 1999).

2.3.2.2 $\delta^{18}O$ of O_2, $\delta^{18}O_{atm}$

As for water stable isotopes, the $\delta^{18}O$ of O_2 trapped in air bubbles ($\delta^{18}O_{atm}$) in ice cores is an important past climate tracer. Oxygen in the atmosphere is characterized by a turnover time of 1.2 ka (Bender et al., 1994) and its composition is homogeneous at global scale. In comparison to $\delta^{15}N$, $\delta^{18}O_{atm}$ is subjected to variations over past glacial/interglacial cycles in response to changes of the oxygen isotopic composition of seawater due to growth and collapse of ice sheets. The growth of ice sheets is usually accompanied by enrichment of oceanic water isotopic composition, as ice sheets are made by isotopically depleted waters due to cold temperatures and air masses fractionation processes. Such isotopic changes affecting seawater are then transmitted in the atmosphere by photosynthesizing organisms living on the oceans' surface (Sowers et al., 1993).

The $\delta^{18}O_{atm}$ signal is characterized by high complexity as it is not only representative of changes in global sea level, but it is also connected to low latitude water cycle and biosphere productivity (Bender et al. 1994). Several studies suggest that at millennial timescale $\delta^{18}O_{atm}$ variations are mainly driven by changes of the precession parameter (Dreyfus et al., 2007; Jouzel et al., 1996; Landais et al., 2010) (Figure 2.20). This correlation is explained by the fact that large scale monsoonal activity variations at millennial and orbital timescale are clearly modulated by precession changes, which cause shifts in the Inter Tropical Convergence Zone (ITCZ) position and consequently biosphere and hydrology variations at high latitudes, generating oscillations in the $^{18}O_{atm}$ composition over time (Extier et al., 2018; Landais et al., 2010).
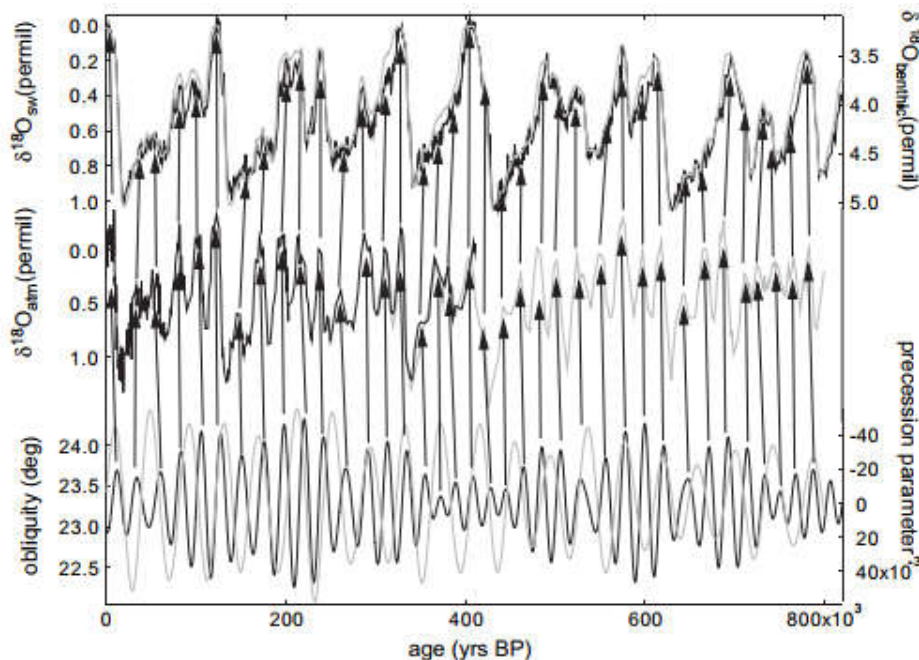
Figure 2.20: Orbital scale variations of $\delta^{18}O_{atm}$ Vostok ice core (black) and the Dome C ice core(grey) and relationships with $\delta^{18}O$ of sea water and $\delta^{18}O$ benthic (top) changes and precession parameter and obliquity (bottom) variations on EDC3 age scale. Arrows indicate the correspondence to precession extrema (Landais et al., 2010).

Due to the strong correlation between $\delta^{18}O_{atm}$ and the mid-June insolation curve at 65° N or precession, variations in oxygen isotopes in air bubbles have also been extensively used as an orbital dating tool in ice cores (Dreyfus et al., 2007; Jouzel et al., 1996; Petit et al., 1999). However, $\delta^{18}O_{atm}$ signal is not contemporary to orbital variations, but exhibits a lag of 5-6 ka which has to be taken into account when defining an ice core chronology (Bazin et al., 2013; Dreyfus et al., 2007). In addition, the $\delta^{18}O_{atm}$ can be used to synchronize ice cores over Antarctica, as done in this thesis work (Chapter 3), and archives from Antarctica and Greenland since it is a global signal (Sowers & Bender, 1995).

2.3.2.3 $\delta O_2/N_2$

A third parameter studied in air bubbles is the elemental ratio between oxygen and nitrogen. The $\delta O_2/N_2$ ratio has been proposed by Bender (2002) like an alternative orbital dating tool to $\delta^{18}O_{atm}$ The $\delta O_2/N_2$ signal shows analogous variations to those of the local 21st December insolation parameter at 78° S for the Vostok ice core between 160 and 400 ka. The Antarctic summer insolation may affect processes of surface snow metamorphism, which signal is then kept until the bubble close-off, as it governs the loss of O_2 (Fujita et al., 2009; Landais et al., 2012). The relationship between $\delta O_2/N_2$ and local summer insolation has also been spotted in the Greenland GISP2 ice core (Suwa & Bender, 2008). Chronologies of Antarctic ice cores like Dome F and Dome C have been refined using this new parameter (Figure 2.21), with the aim of reducing the uncertainty of the gas age scale (Bazin et al., 2013; Kawamura et al., 2007). The post coring gas loss fractionation that affects the $\delta^{18}O_{atm}$ record can be corrected with the $\delta O_2/N_2$. In this thesis the TALDICE $\delta O_2/N_2$ record is not applied as a dating tool, because samples are affected by severe gas loss, but only for $\delta^{18}O_{atm}$ data correction.
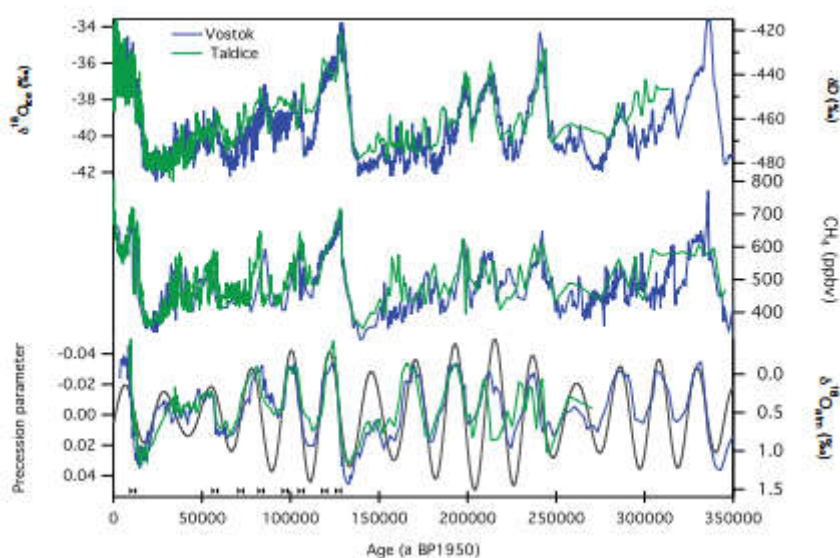
Figure 2.21: Comparison between Vostok (blue) and TALDICE (green) ice cores on the $\delta^{18}Oatm$ chronology (Bender, 2002) and TALDICE 1a age scale (Buiron et al., 2011)(Schüpbach et al., 2011), respectively. Top: δD and $\delta^{18}O$ in the ice matrix. Middle: CH_4 record at Vostok and TALDICE. Bottom: $\delta^{18}Oatm$ records: The grey curve is the precession parameter. Black markers indicate the position of stratigraphic links between TALDICE and Vostok deduced from $\delta^{18}O_{atm}$ data (Bazin et al., 2013).

2.3.3 Fractionation processes

Air composition in ice cores does not always reflect the original atmospheric composition. Several processes may act on the gases isotopic composition after snow deposition, in the firn layer as well as in the ice matrix.

2.3.3.1 Gravitational fractionation

Craig et al. (1988) showed that in the Greenland Dye 3 ice core, atmospheric gases enclosed in polar ice at the firn-ice transition zone are enriched in heavy isotopes of nitrogen and oxygen due to the gravity effect. The enrichment in heavy isotopes, called *gravitational fractionation*, depends on the mass difference between isotopes pair and is proportional to the depth of the diffusive firn column. The gravitational component of certain isotope can be calculated by the barometric equation:

$$\delta_{grav} = \frac{\Delta m g}{RT} \cdot Z \qquad (2.12)$$

Where Δm is the mass difference between the isotopes pairs, g is the gravitational constant (9.82 m s^{-2}), R the gas constant (8.31 J K^{-1} mol^{-1}), and T the mean firn temperature (K). Considering two well-known gases in the firn as Ar (^{40}Ar/^{36}Ar) and N (^{15}N/^{14}N), the gravitational fractionation scales with mass difference and affects δ^{40}Ar 4 times more than δ^{15}N (Severinghaus & Brook, 1999). When correcting isotopic data for gravitational fractionation, δ^{15}N is commonly used as the gravitational correction term.

2.3.3.2 Thermal fractionation

Thermal diffusion could be described as the process that drives isotopic fractionation in the firn when it is influenced by differences in temperature in the medium. In this case the diffusive mass transport is controlled by the thermal gradient, rather than by concentration gradient as for simple diffusion processes (Grachev & Severinghaus, 2003b). In the firn column, the isotopes of air trapped in the porous medium fractionate not only for gravitational settling, but also for thermal settling. In the firn affected by temperature gradient, heavier isotopes tend to move towards the colder and deeper section. The thermal fractionation component can be estimated as:

$$\delta_{therm} = \Omega \, \Delta T \qquad (2.13)$$

Where Ω is a laboratory constant called "thermal diffusion sensitivity" defined for each isotopic pair (Ar and N) (Grachev & Severinghaus, 2003b, 2003a), and ΔT is the temperature difference between the top and the bottom of the diffusive column (Severinghaus & Brook, 1999). When an abrupt climate warming event happens in Antarctica or Greenland, a temperature gradient takes place in the firn column and persists for several hundred years. In this case thermal fractionation takes place in the whole firn air column. As heat diffuses 10 times slower in the firn layer with respect to isotopes, the isotopes in the gas matrix fractionate well before the temperature equilibration along the column. Then, when the close-off happens at the bottom of the layer, bubble formation traps the isotopically modified air, recording the thermal event (Severinghaus et al., 1998) as displayed in Figure 2.22.
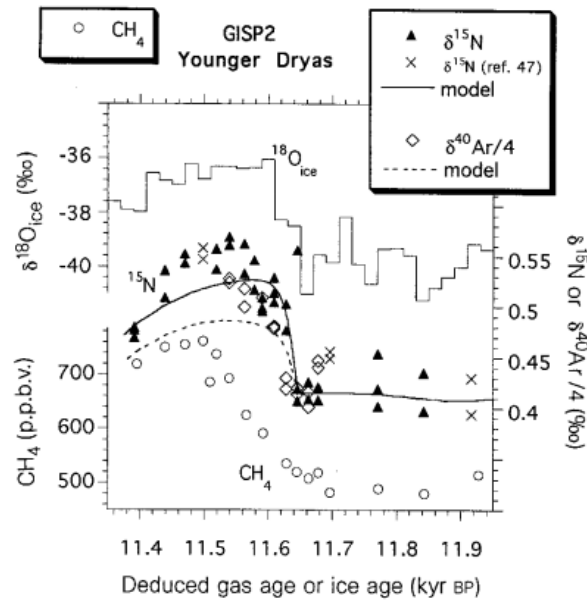
Figure 2.22: Isotopic ($\delta^{18}O$, $\delta^{15}N$ and $\delta^{40}Ar$) and CH_4 data plotted versus age (gas or ice) for the GISP2 core between 11.64 ka–11.68 ka. For comparioson $\delta^{15}N$ and $\delta^{40}Ar$ modelled profiles are shown (solid line and dashed line).

2.3.3.3 Gas loss

Once the bubbles are trapped in the ice, enclosed gas can still be affected by processes acting on the isotopic composition. Bender (2002) observed that in the Vostok ice core all samples are depleted in O_2, suggesting the selective exclusion of O_2 during the bubbles close-off process and/or the selective loss of O_2 in badly preserved ice samples. Another process has been observed by Landais et al. (2003) in the GRIP ice core from Greenland, as they notice a 3% (up to 8%) loss of O_2 between the new series of samples, analysed in 2003 and conserved at -20°C, and those previously analysed in 1997. They found that changes in $\delta O_2/N_2$ and $\delta^{18}O_{atm}$ isotopic composition are linearly correlated by a factor of 0.01. The gas loss process, during the core storage, driven by molecular diffusion from clathrate hydrates toward the ice-core surface through ice crystals, has been modelled by Ikeda-Fukazawa et al. (2005). They showed that the gas loss mainly affects $\delta O_2/N_2$ isotopic ratio, consequently the $\delta^{18}O_{atm}$ values, and is strictly connected to the storage temperature of samples as shown in Figure 2.23. The warmer is the storage temperature, the more pronounced is the gas loss effect over time. The dependence of gas loss fractionation with storage temperature and time has been confirmed by the $\delta O_2/N_2$ analysis of ice over time for the Antarctic cores of Dome Fuji (Kawamura et al., 2007) and Dome C (Extier et al., 2018; Kawamura et al., 2007).
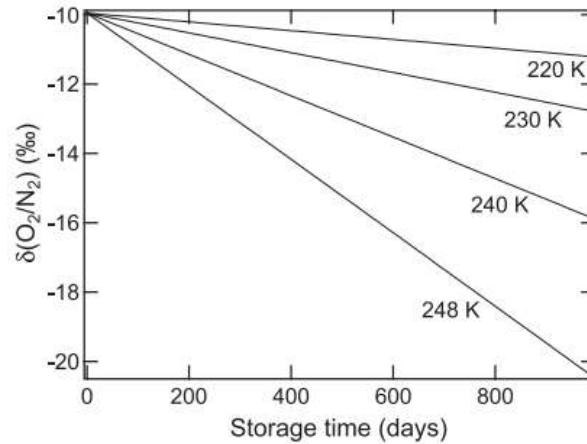
Figure 2.23: Variations of $\delta O_2/N_2$ ratio over time in ice samples at the storage temperatures of 248, 240, 230 and 220 K (Ikeda-Fukazawa et al., 2005).

2.3.4   Analytical methods

Air trapped in TALDICE ice core is extracted from 81 samples using the extraction line available at LSCE and then the $\delta^{18}O_{atm}$, $\delta^{15}N$ and $\delta O_2/N_2$ are analysed with mass spectrometer. In this section the extraction protocol, the analysis methodology and data correction procedure are described.

2.3.4.1 Air extraction method and protocol

The air extraction is performed using the semi-automated extraction line available at the LSCE. This extraction line represents an improved and automatized version of the first system developed by Sowers et al. (1989), improved by Landais et al. (2003) and then applied in other studies (Bazin et al., 2016; Capron et al., 2010; Extier et al., 2018). Ice samples of 40 gr each are cut every day in the cold room at -20°C. The external layers of ice are removed to avoid modern air contamination and samples are inspected to check the presences of fractures. Usually, each ice sample is split in two replicates, to obtain a more accurate measurement. However, TALDICE samples have not been split in two replicates due to the low amount of ice.

Figure 2.24: Left. Ice samples cut in the cold room. Right. Ice samples placed in the flasks before the melting step.

After the cutting procedure, every day 6 ice samples are placed in 6 glass flasks (Figure 2.24) that are connected to the extraction line along with 2 flasks containing external air used for measurements calibration. Every day the air is extracted from 6 ice samples and then analysed during the night with the mass spectrometer.

The extraction line is a vacuum system made by stainless steel tubing and valves (manual and automatic) connected to the flasks (Figure 2.25). The line is evacuated before and after the conclusion of the air extraction procedure thanks to 2 pumps (primary pump and turbo pump), to guarantee the lack of external air contamination. After the ice samples are melt, each air sample passes through the line one after the other and water and CO_2 are removed with the use of two cold traps. Then the air of each sample is transferred in a stainless steel multiport samples holder (also called "rosette"), which is made by 8 metal tubes created to accommodate the air samples, immerged in a liquid helium tank.
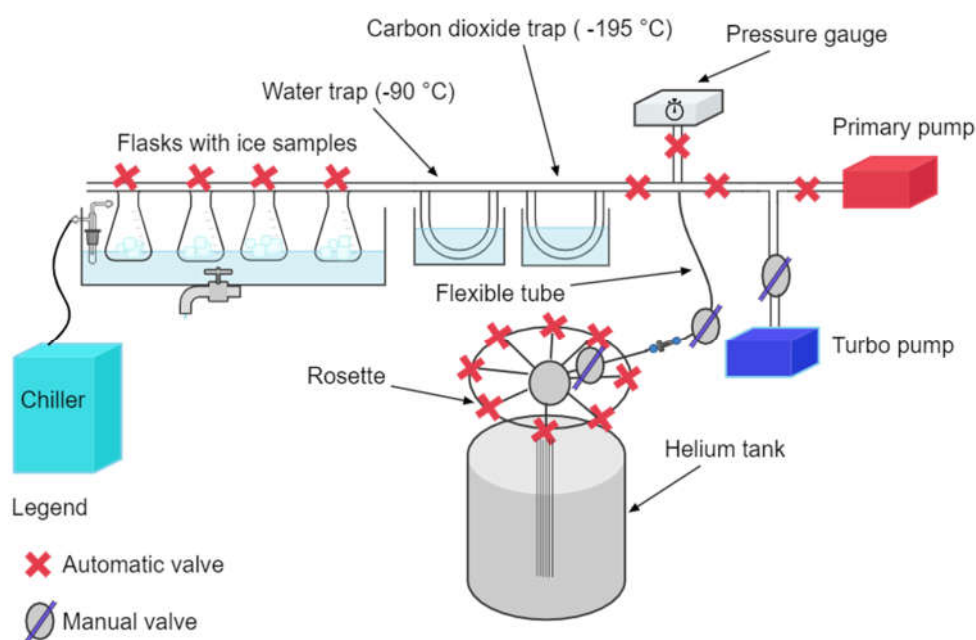
Figure 2.25: Simple schematic of the air extraction system at LSCE.

The extraction procedure follows a protocol applied to guarantee the quality and reproducibility of the measurements:

i. Six ice samples are shaved and decontaminated in the cold room and then placed in the glass bottles which have rested in the freezer all night long (Figure 2.24). The two air flasks are taken outside the building and filled with atmospheric air.

ii. The bottles containing the ice samples and external air flasks are connected to the line with the use of a rubber gasket (o-ring) and pinces to seal the bottles and avoid contamination with the atmospheric air. Bottles are immersed in a tank filled with ethanol at -20°C and kept at constant temperature with the use of a cold finger connected to a chiller, in order to prevent melting of the samples.

iii. The rosette multiport is cooled in liquid nitrogen for 5 minutes and then placed inside a helium tank at – 269 °C. Such a cold temperature is necessary to trap the air extracted from the samples inside the metal tubes during the air transfer procedure. The rosette is then connected to the line through a flexible tube and a manual valve.

iv. All the valves of the line, with the exception of the air flasks valves, are opened to remove the external air from the line. At first the air is extracted with the primary pump, when the pressure inside the line reaches the value of $1 \cdot 10^{-1}$ mbar the turbo pump is turned on to evacuate the line for 45 minutes and assure a complete cleaning.

v. When the line is evacuated, the valves connected to the glass bottles are closed and the ethanol is removed from the water tank and replaced with a water bath at room temperature (~20°C). The ice samples are let to melt for about 2 hours to assure that all the air trapped in ice bubbles is released in the bottles.

vi.   When the ice is completely melted, before starting the air transfer, the cold traps are prepared to remove water and CO_2 from the air samples. The water trap is immerged in a dewar full of cool ethanol at -95°C, while the CO_2 trap is immerged in a dewar full of liquid nitrogen at the temperature of -196°C. The nitrogen dewar is refilled each 10/15 minutes during the air transfer.

vii.   The air contained in air flasks and glass bottles is then transferred into the tubes of the rosette automatically thanks to a LabView program. Each sample is independently transferred inside one of the stainless steel tube of the rosette. The complete transfer of all samples needs 45 minutes.

viii.   When the transfer procedure is completed, the rosette is removed from the helium tank and warmed with a heat gun. The water bath is emptied and glass bottles are removed from the line which is vacuumed with the turbo pump for all the night.

Figure 2.26: Left. Picture of the extraction line at LSCE. Right. Rosette in the helium tank connected to the extraction line.

2.3.4.2 Mass spectrometry

The rosette containing the transferred air samples is left at room temperature for about 40 minutes to let the air equilibrate. Then, the multiport is ready to be connected to the mass spectrometer Delta V plus (Thermo) to analyse the air samples (figure 2.27) The spectrometer is equipped with 10 cups allowing the analysis at the same time of the following mass over charge ratios m/z = 28, 29, 30, 32, 33, 34, 36, 38, 40 and 44. It is important to highlight that the mass spectrometer works in vacuum conditions to analyse only the sample isotopic composition.
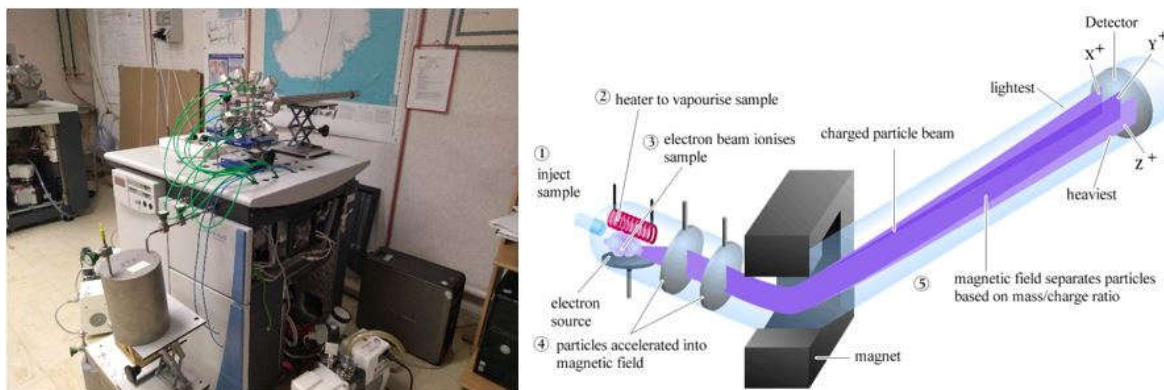
Figure 2.27: Left. Mass spectrometer Delta V at LSCE connected to the rosette during the analysis. Righ: Schematic of main components of a mass spectrometer (www.chem.ucalgary.ca).

Once the gaseous sample is introduced in the mass spectrometer it goes through the following steps to be analysed:

i.   *Sample and standard introduction:* The standard aliquot is introduced manually in the mass spectrometer. The aliquot is taken from the ST2 can (cylinder of dry atmospheric air without CO_2) connected to the mass spectrometer and let equilibrated in the line for 3 minutes to avoid fractionation. The gas is then expanded in the bellows before starting the analysis. Air samples are introduced in the bellows automatically from the mass spectrometer system for the analysis. The analysis is then performed automatically.

ii. *Ionisation:* The molecules of the gaseous sample are heated and vaporized at first in order to avoid any liquid presence in the instrument. The sample is then introduced in the ionization chamber, where an electron beam bombards the sample molecules generating positive ions (cations). The electrons are removed thanks to an electron trap made by a positively charged plate. Most of the generated positive ions carry a charge of +1, as it is difficult to remove additional electrons from a positive ion, and are directed towards the magnet thanks to a repeller, made of a metal plate slightly positively charged.

iii. *Acceleration*: ions are accelerated when they pass through three slits with a decreasing voltage (the last one carries 0 Volt). The ions are accelerated into a focused beam in which they all have the same kinetic energy.

iv. *Deflection*: the ion beam is accelerated and directed towards a magnet. The magnetic field deflects the ions depending on their mass-to-charge ratio (*m/z*), the lighter ions are more deflected in comparison to the heaviest ones. The strength of deflection is also related to the number of positive charges in the ion, the most charged ions are also the most deflected.

v.   *Detection:* the deflected ions then hit different cups (or detector) depending of their *m/z*. Each cup is located in a specific position to be hit by ions carrying a specific mass-to-charge ratio. As the employed mass spectrometer is equipped with 10 cups, the ions carrying different *m/z* ratios are deflected to their corresponding detectors through the modulation of the magnetic field, ions

with larger *m/z* need stronger magnetic field. When the ion hits the detector, its charge is neutralized by an electron which jumps from the metal of the cup onto the ion, leaving a space among the electrons in the metal. The cup is connected to an amplifier with a wire, in which electrons move towards the space created in the detector to fill it. The flow of electrons detected as an electric current pulse which is amplified. The more ions hit the cup, the greater is the intensity of the generated current. The mass spectrometer registers the abundance of ions detected with respect to the *m/z* parameter.

2.3.4.3 Measurement sequence

The analysis performed by the mass spectrometer follows a pre-defined sequence in which each sample is analysed twice and calibrated against atmospheric air. The analysed external air samples are used also to check that the measurements are not affected by drifting of the signal or other issues that can influence the samples measurements. Everyday two external air samples are analysed, but the first air sample measured is always discarded because of adsorption effects on the water trap. The sequence is made by 2 blocks of 16 measurements in dual inlet mode - 1 background measurement before the two blocks and one pressure adjust at the beginning of each block. Each measurement lasts 16 s per *m34/m32* measurement (as for *m29/m28*, *m32/m28*).

2.3.5 Corrections

The mass spectrometer provides measurements of mass over charge ratios *m/z* = 28, 29, 30, 32, 33, 34, 36, 38, 40 and 44. The final delta values used for this thesis are $\delta^{18}O_{atm}$, $\delta O_2/N_2$ and $\delta^{15}N$, obtained from the mass ratios 34/32, 32/28 and 29/28. The delta values obtained from the mass spectrometer measurements are corrected for pressure imbalance, chemical interferences of CO_2 and $\delta O_2/N_2$, and then calibrated against the mean exterior air values (Landais et al., 2003; Severinghaus et al., 2003). Secondly, $\delta^{18}O_{atm}$ and $\delta O_2/N_2$ data are corrected with $\delta^{15}N$ data for gravitational fractionation processes acting in the firn. In this section all the applied corrections are described.

2.3.5.1 Raw data corrections

Each sample is analysed twice and then the average delta value is calculated. Then each sample is raw value corrected for the following effects:

i.   *Pressure imbalance sensitivity (PIS):* is based on the principle that the measured delta values are sensitive to the difference of pressure existing between the standard and the sample bellows (Severinghaus et al., 2003). The initial part of measurements performed with the mass spectrometer involves the compression of the sample and the standard in the bellow to obtain an equal flow rate of gases into the measurement system (Bender et al. 1994). The PIS. correction is not constant and depends on the mass spectrometer settings as beam focusing. A new pressure imbalance correction is applied everyday on each analysis sequence. The pressure imbalance correction is applied on measured samples and is based on the assumption that the δ

deviation related to the pressure imbalance varies linearly with pressure imbalance (Bender et al., 1994) and that the PIS is stable during the analysis.

The PIS is calculated separately for $\delta^{15}N$, $\delta^{18}O_{atm}$ and $\delta O_2/N_2$ as following:

$$PIS = \frac{[\delta_{unbalanced} - \delta_{true}]}{\Delta p} \tag{2.14}$$

Where $\Delta p = [(V_{sample} - V_{standard} - 1) \cdot 10^3 ‰]$ is the difference of volume between the two bellows. Measured delta values of samples are corrected for the PIS effect with the application of the equation:

$$\delta_{PIS\ corr} = \delta_{measured} - PIS \cdot \Delta p \tag{2.15}$$

ii. *Chemical slope correction:* Mixtures of gases create additional problems in mass spectrometry measurements as isotopic ratios of a single element are susceptible to changes in the elemental ratios of the mixture (Severinghaus et al., 2003).

Delta values corrected for the pressure imbalance sensitivity are then subjected to correction for the chemical interference of CO_2 and $\delta O_2/N_2$ (Landais et al. 2003). Due to gas ionisation happening in the mass spectrometer, the CO_2 molecule could be turned into the ion CO^+, which has a mass of 28 or 29. The presence of this ion having a similar mass of the nitrogen molecule creates some issues is estimating the correct $\delta^{15}N$ value. The ratio O_2/N_2 may as well influence the measurement of $\delta^{15}N$ as its value strictly depends on the ratio. To correct the $\delta^{15}N$ value, two different types of calibration are performed. A standard with known $\delta^{15}N$ is enriched with known aliquots of CO_2 or O_2 and then the delta value is measured. The variation of $\delta^{15}N$ value is measured in function of the added aliquots. The slope calculated between the measured $\delta^{15}N$ and $\delta O_2/N_2$ (or $\delta CO_2/N_2$) and O_2 (or CO_2) aliquots is used to correct the delta values and is called *chemical slope*. Based on the same principle of chemical interferences, also the $\delta^{18}O_{atm}$ measured values are corrected for the interference of $\delta O_2/N_2$ and $\delta CO_2/N_2$, while $\delta O_2/N_2$ is corrected for the interference of $\delta CO_2/N_2$. Experiments to calculate the chemical slope are performed before starting the analysis campaign and when settings or components of the mass spectrometer are changed. In general, the delta value corrected for the chemical slope effect ($\delta_{chem.slope\ corr}$) is expressed with the following equation:

$$\delta_{chem.slope\ corr} = \delta_{PIS\ corr} - m \cdot \delta_{ratio} \tag{2.16}$$

Where $\delta_{PIS\ corr}$ is the (considered) delta value corrected for the Pressure Imbalance, m is the chemical slope and δ_{ratio} is the measured delta value of the ratio that generates the interference.

iii. *Calibration to external air:* all data corrected for pressure imbalance and chemical slope are then normalized with respect to atmospheric air (Landais et al. 2003; Severinghaus et al. 2003). Every day the isotopic composition of two external air samples is measured and the first sample is always discarded because of adsorption effects on the water trap.

The isotopic composition of the atmospheric air samples measured during the analysis campaign are averaged (δ_{air}) and used to correct the extracted samples delta values:

$$\delta_{air\,corr} = \delta_{PIS,chem.slope} - \delta_{ext.air} \qquad (2.17)$$

Where $\delta_{PIS,\,chem.slope}$ is the sample delta value corrected for the pressure imbalance and $\delta_{air\,corr}$ is the final isotopic ratio for the air sample after the correction for atmospheric air.

2.3.5.2 Gravitational and gas loss corrections

The measured values of $\delta^{18}O_{atm}$ and $\delta O_2/N_2$ of trapped air in ice need to be corrected for gravitational effect. The Earth gravity field causes the phenomenon of fractionation in the firn to be equivalent to the mass difference between the studied isotopes: 1 g/mol for the $^{15}N/^{14}N$ ratio; 2 g/mol for $^{18}O/^{16}O$ ratio and 4 g/mol for the O_2/N_2 ratio (Craig et al., 1988; Extier et al., 2018; Severinghaus et al., 1998). The $\delta^{15}N$ value measured in each air sample is used to gravitationally correct the $\delta^{18}O_{atm}$ and $\delta O_2/N_2$ measured values for the same sample, as the $\delta^{18}O_{atm}$ is affected twice by gravitational fractionation with respect to $\delta^{15}N$ and the $\delta O_2/N_2$ 4 times. The $\delta^{18}O_{atm}$ and $\delta O_2/N_2$ values (after applying all the corrections described in the previous section) are gravitationally corrected as following:

$$\delta^{18}O_{atm\,grav\,corr} = \delta^{18}O_{atm} - 2 \cdot \delta^{15}N \qquad (2.18)$$

$$\delta O_2/N_{2\,grav\,corr} = \delta O_2/N_2 - 4 \cdot \delta^{15}N \qquad (2.19)$$

The last correction performed on isotopic composition of the air is the correction for the gas loss fractionation. The $\delta^{18}O_{atm}$ value need to be corrected for the gas loss fractionation due to the long storage times. The TALDICE $\delta^{18}O_{atm}$ data set published by Buiron et al. (2011) and Bazin et al. (2013) are corrected applying the linear relationship introduced by Landais et al. (2003):

$$\delta^{18}O_{atm\,gas\,loss\,corr} = \delta^{18}O_{atm} + (\delta O_2/N_2 + 10) \cdot 0.01 \qquad (2.20)$$

In this thesis the $\delta^{18}O_{atm}$ is measured in 81 ice samples that have been stored for about a decade at the relatively high temperature of -30°C. Due to this reason, several samples show extremely negative $\delta O_2/N_2$ values down to -124‰, which affect the gas loss correction. At first, equation 2.20 is applied to correct data for gas loss fractionation, which is usually employed to correct samples with $\delta O_2/N_2$ values of about -30‰ (Landais et al., 2003). However, TALDICE $\delta^{18}O_{atm}$ values carrying very negative $\delta O_2/N_2(<-50‰)$ corrected with equation 2.20 appear to not fit properly with the previously published data set (Bazin et al., 2013; Buiron et al., 2011) (green stars in Figure 2.28).

In order to perform a more accurate gas loss correction tailored on the very negative TALDICE $\delta O_2/N_2$ values, a new gas loss equation has been formulated (eq. 2.21). We explored the EPICA Dome C raw data obtained in Extier et al. (2018) and extracted the neighbouring samples with differences of $\delta O_2/N_2$ larger than 40‰. Samples with $\delta O_2/N_2$ values greater than -50‰ are corrected applying eq. 2.20,

while samples showing values more negative than -50‰ are corrected with the following equation (red stars in Figure 2.28):

$$\delta^{18}O_{atm\ gas\ loss\ corr} = \delta^{18}O_{atm} + (\delta O_2/N_2 + 10) \cdot 0.007 \tag{2.21}$$

A complete explanation regarding the calculation of the new gas loss coefficient (0.007) is presented in the Appendix A of the manuscript in Chapter 3.
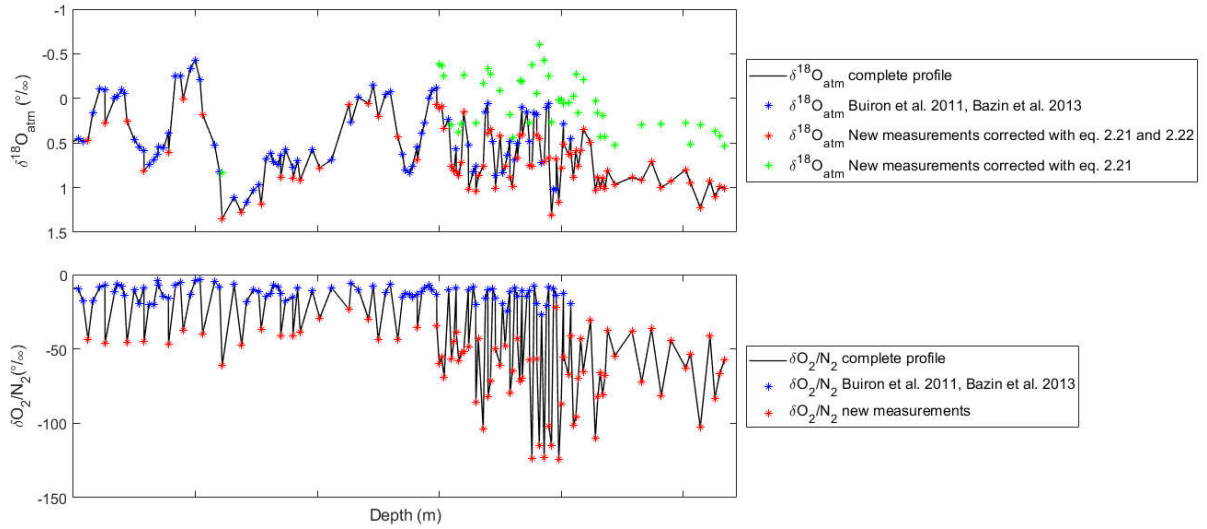
Figure 2.28: $\delta^{18}O$ and $\delta O_2/N_2$ new and published measurements for TALDICE ice core. Data published by Buiron et al.(2011) and Bazin et al.(2013) (blue stars) are plotted with the new data set. $\delta^{18}O_{atm}$ data characterized by <-50‰ $\delta O_2/N_2$ values corrected with eq.2.21 (green stars) show over corrected values in comparison to the same data corrected with eq. 2.22 (red stars).

2.4 Radioisotopes in air bubbles

2.4.1 Definition of radioisotopes

In opposition to stable isotopes, radioisotopes are unstable atoms which undergo spontaneous radioactive decay by the loss of nuclear particles (α- or β-particles), and, they might transform into a new element. Stable and unstable atoms exist on the Earth since its formation, about 5 billion years ago. The major share of unstable atoms has been radioactively disintegrated and achieved stability, however, in nature radioactive atoms are still present and divided in three main categories:

a) Radioisotopes with a long half-life: those isotopes had not enough time to decay completely since their formation, due to their long life as Uranium-238 (4.5 billion years) and Potassium-40 (1.3 billion years).

b) Radioactive descendants of radioisotopes: radioisotopes originate from the natural decay of other radioisotopes. For example, radium-226 is formed by the disintegration of uranium-238 and then it slowly turns into the radioactive gas radon-222.

c) Radioisotopes formed by the interaction with cosmic radiation: those are radioisotopes generally formed in the atmosphere, as ^{14}C.

2.4.2 Radioisotopes as a dating tool in ice cores

One of the most relevant properties of the radioisotopes is that the decay rate into its daughter product is constant for each isotope species. Knowing the actual concentration of the product isotopes allow one to calculate the age of the sample. This is the principle on which the radioisotope "clock" is based and the amount of time that a half of the original radioactive material needs to decay is called *half-life* (τ).

Radioactive isotopes employed for dating should possess several properties as:

a) The radioisotope and its daughter product should occur in measurable quantities and distinguishable from other isotopes.

b) The decay rate must be measurable.

c) The half-life should be suitable for the time window needed to date.

d) The initial concentration of the parent radioisotope should be known.

Radio-dating techniques have been applied to date ice cores because, in comparison to wiggle matching or synchronization methods, they provide an absolute age. However, in the ice core field radio-dating still represents a side tool since stratigraphic techniques are the mostly employed. The most common analysed radio isotopes in ice cores are ^{14}C, ^{10}Be, ^{36}Cl, ^{81}Kr and ^{39}Ar (Figure 2.29).
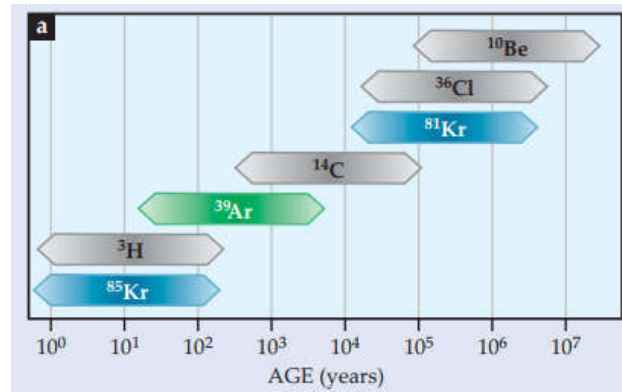
Figure 2.29: Plot of the age ranges covered from different radio isotopes for dating purposes (Lu, 2013).

The analysis of ^{14}C represents the golden standard of the radio-dating methods, however radiocarbon dating is less employed in ice core science. As alpine glaciers are located close to urban areas and carbonaceous particles deposited in the snow and in ice could be dated with the ^{14}C technique (Sigl et al., 2009). Such methodology could is generally applied only to ice cores drilled at medium latitudes and to date relatively recent samples, as the half-life of ^{14}C is ~5.7 ka (Fang et al., 2021; Hoffmann et al., 2018). However, for such recent cores the layer counting technique is usually applied. Ice cores from Greenland or Antarctica could not be dated with the use of this technique due low concentration of carbonaceous particles, since sources are distant from the deposition site and samples age does not fit the ^{14}C half-life.

The cosmogenic isotopes ^{36}Cl and ^{10}Be are produced in the Earth's atmosphere due to the spallation reaction of ^{36}Ar and ^{14}N or ^{16}O atoms respectively with the galactic cosmic rays particles (Muscheler et al., 2005). Their production is controlled by the variation of solar activity and the geomagnetic field. The record of ^{10}Be and ^{36}Cl in ice cores is modulated by variations of the solar wind, which could be observed in its 11-year cycles signal (Abreu et al., 2013). Inland Antarctica represents one of the best location to study the variations of ^{10}Be and ^{36}Cl as they quickly attach on atmospheric aerosols and fall on the ice sheets through wet deposition in 1 or 2 years-time (Horiuchi et al., 2008). However, ^{10}Be and ^{36}Cl do not provide an ideal chronometer as meteorological conditions and snow accumulation changes influence the concentration of radioisotopes in snow and ice (Berggren et al., 2009). Moreover, past peaks in cosmogenic isotopes are related to large geomagnetic excursions, thus those records may be used as stratigraphic tools to date ice cores rather than as pure radio-dating tools (Horiuchi et al., 2008) The applications of ^{81}Kr dating method and the ^{40}Ar methods are discussed in details respectively in Chapter 3 and Chapter 5.

2.4.3 ^{81}Kr as ice dating method
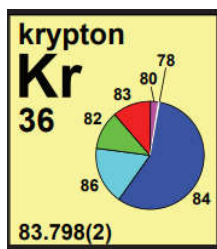
Figure 2.30: Krypton and its relative isotopic abundances (Holden et al., 2018).

The history of krypton dating started at the University of Bern (Switzerland), when Loosli and Oeschger (1969) observed the decay of ^{81}Kr in natural gas extracted from the atmospheric air. The ^{81}Kr isotope is naturally produced in the upper atmosphere by cosmic-ray induced spallation and neutron activation of stable krypton (Loosli & Hoeschger, 1969; Lu et al., 2014) and has an half-life of 229 ka (Lu et al., 2014). Due to its chemical stability, this isotope is characterized by a long residence time in the atmosphere and it is also well mixed, with an average concentration of 1.10 ppmv (Aoki & Makide, 2005). A little portion of atmospheric krypton, including ^{81}Kr, dissolves in water or is trapped in ice, and thus this radioisotope can be found in environmental samples. In nature there are no significant ^{81}Kr sources except for the radioactive decay, making this isotope ideal for radio-dating.

Krypton dating was applied at first to estimate the age of old groundwater in Australia (Collon et al., 2000). About 15 years after this first application, Buizert et al. (2014) used the ^{81}Kr dating technique to obtain the age of ancient air trapped in ice samples collected at Taylor Glacier (Antarctica) as shown in Figure 2.31. They proved that this method works for dating air bubbles trapped in ice in the 30-1300 ka age range, also for cores affected by disturbed stratigraphy or discontinuous records. The new dating approach has then been applied on ice samples collected from the Guliya Ice Cap, Tibetan Plateau (Tian et al., 2019).

One of the main issues related to the first application of krypton dating technique is the great sample size. The typical weight for the initial study is about 40-80 kg of ice, from which 5-10 μL of krypton can be extracted for the analysis with the Atom Trap Trace Analysis (ATTA) method (Jiang et al. 2012, Lu et al., 2014). However, recent developments of the ATTA machine reduced the sample size down to 1 μL of krypton, which can be extracted from about 10 kg of Antarctic ice (Jiang et al., 2020; Tian et al., 2019). In this thesis we present the results for the first application of the ^{81}Kr dating technique to define an ice core age scale with the application of the new developments of the ATTA machine, that allow us to use less than 10 kg of ice per sample. Details on the TALDICE chronology construction with krypton dating are provided in Chapter 3.

Figure 2.31: Ice samples from Taylor Glacier (Antarctica) devoted to [81]Kr dating (Lu, 2013).

2.4.4 Analytical methods

In this thesis three samples have been analysed with the application of the [81]Kr dating methodology. In this section air extraction and Kr purification methods, analysis method and the age calculation are described.

2.4.4.1 Samples preparation

Samples devoted to [81]Kr dating were stored at the EuroCold facility at the University of Milano-Bicocca (Italy) at constant temperature of -30°C (Figure 2.32). Three depth layers are selected to perform the dating in deepest portion of the core, where no stratigraphic constraints are available. Three samples, covering 4-5 m depth each and belonging to 13 1-m-long bags of TALDICE CUT B (54 x 55 mm) are chosen between 1560 and 1617 m depth (Table 2.5).

Samples	Depth layers (m)	Samples weight (kg)
Sample 1	1559 - 1563	9.6
Sample 2	1573 - 1575 1577 - 1578	5.4
Sample 3	1613 - 1618	9.5

Table 2.5: Depths and weight (after cleaning) of the three TALDICE samples devoted to [81]Kr dating.

Samples are cut in the cold room at University of Milano-Bicocca (Italy) at -20 °C. The ice inspected to check the presence of fractures and/or melted layers and removed. The ice is then shipped to LSCE (France) with a controlled temperature transport (-20°C).

Figure 2.32: Left. [81]Kr dating samples preparation at the EuroCold facility at the University of Milano-Bicocca. Right. Cut ice samples ready for the air extraction at LSCE (France).

At LSCE (France), the ice samples are decontaminated and cut before performing the air extraction in the cold room at the temperature of -20°C. At first the external layers of ice are removed to avoid modern air contamination and then samples are again inspected to remove fractures and melted layers. As final step, the ice is cut in smaller sticks and placed in the stainless steel chamber (Figure 2.32).

2.4.4.2 Air extraction method and protocol

The air extraction system for [81]Kr ice samples is a manual extraction system set up at LSCE. The system and the extraction protocol employed are the same described in Tian et al. (2019) (Figures 2.33 and 2.34).
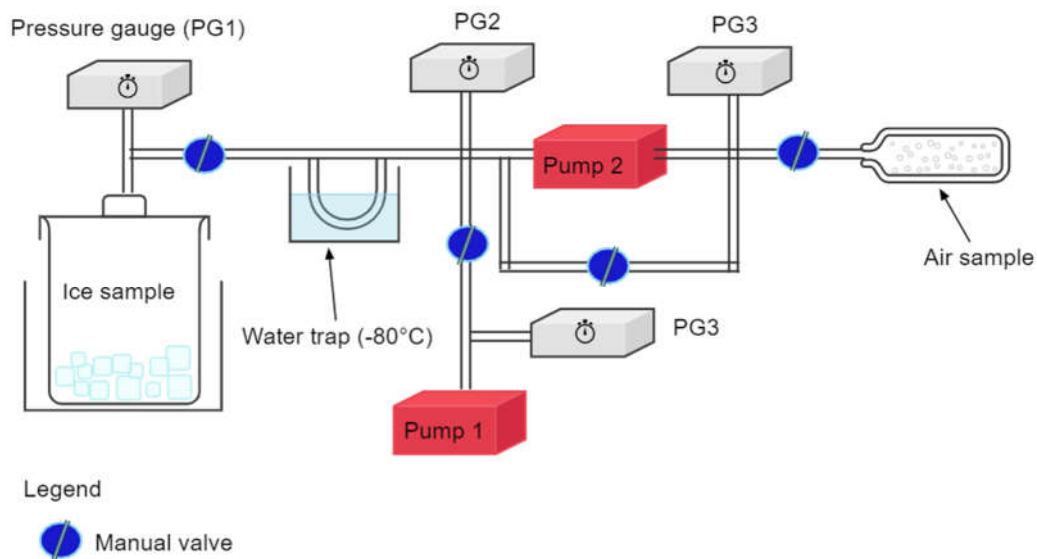
Figure 2.33: Schematic of the air extraction system for [81]Kr dating samples at LSCE as described by Tian et al. (2019).

The air extraction system is composed of a large stainless steel tank in which the ice sample is placed and then melted, after having created vacuum conditions (Figure 2.34). The air released from bubbles is kept inside the chamber and pumped into a water trap to remove vapour. Then the air is transferred to a stainless steel cylinder, sealed after having completed the air transfer. The air sample is ready to be sent to Hefei University (China) to perform Krypton extraction and analysis. In opposition to the $\delta^{18}O_{atm}$ extraction line, which allows us to perform air transfer of 6 samples in parallel, with this methodology each sample is treated separately due to the large size.

The air extraction is performed following the above protocol to guarantee the quality and reproducibility of the measurements:

i. After the ice sample decontamination in the cold room at -20°C and the cutting in smaller sticks, all the ice belonging to one sample is placed into the big stainless steel chamber as well placed in the cold room. The chamber is closed with a heavy lid sealed with an o-ring to prevent external air contamination. The chamber is transferred to the laboratory at ambient temperature and placed inside a large tank.

ii. The atmospheric air in the chamber is removed pumping (with pump 1 and 2) the air for 30 minutes. The removed air passes through a water trap, placed in ethanol cooled at -80°C with liquid N_2, to protect the pumps from the water vapour produced by the sublimated ice.

iii. After having completed the evacuation of atmospheric air from the chamber, it is isolated from the rest of the line closing the manual valve attached to the lid. The ice is melted adding warm water in the tank in which the chamber is placed. During the melting, the rest of the line is continuously pumped to flush away the water vapour still in the line.

iv. When the ice is completely melted and all the air trapped in the bubbles is released in the chamber, the manual valve close to chamber is opened and the air sample is transferred through the line. The air passes through the water trap and then is compressed into a stainless steel sample cylinder. After about 10 minutes of compression, the increase of the pressure in the cylinder slows down and after additional 5 minutes, the sample cylinder is closed with a manual valve. As the cylinder volume is known, the air content of the sample is determined reading the final pressure on the pressure gauge.

Figure 2.34: Picture of the [81]Kr air extraction at LSCE.

2.4.4.3 Kr purification method and protocol

One of the first Kr purifications system was developed by (Yokochi et al., 2008) to work with large gas volumes up to 125 L and employed cryogenic distillation technique with titanium gettering and gas chromatography. Then, a similar system was developed for samples with smaller volumes between 1 and 20 L (Tu et al., 2014). Following those new developments, Yokochi (2016) replaced the cryogenic distillation system with a fractionating desorption system at -135 °C.

The three stainless steel bottles containing air samples extracted from deep layers of the TALDICE ice core were sent to the University of Science and Technology of China (USTC) to extract ^{81}Kr and ^{85}Kr from air. In this thesis work is employed the new developments of the previous krypton purification systems. Dong et al. (2019) set up an automated system for dual separation of argon and krypton, which combines a first step of titanium getter, followed by gas chromatography (GC) separation, which can be used for samples with volumes of less than 1 L (Figures 2.35 and 2.36). The purification system extracts the Kr gas then analysed with the ATTA machine.
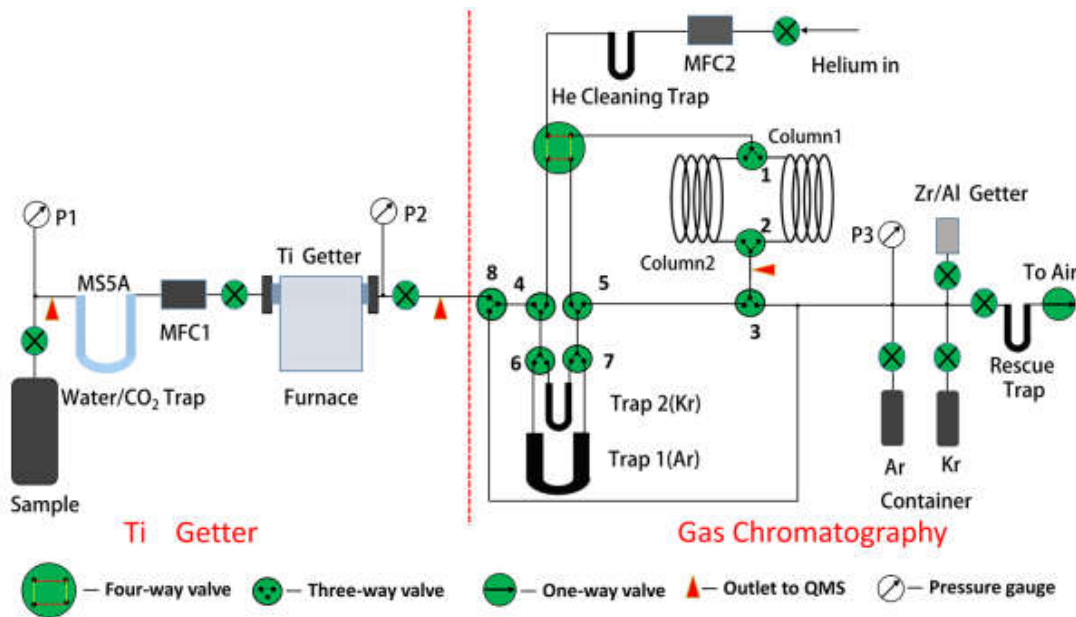
Figure 2.35: Schematic of the Kr/Ar separation system composed by a Ti getter part and a gas chromatography part (Dong et al., 2019).

The Kr purification system and protocol steps are described below:

i.   The air sample contained in the bottle at first passes through a U-shaped trap filled with molecular sieve 5A (MS5A) which removes CO_2 and water vapour at room temperature.

ii.   The dry air flows into the titanium getter. The getter is made by pipe heated by an oven at 900 °C and filled with titanium sponge which traps N_2 and O_2, while it decomposes CH_4. The remaining H_2 is absorbed by the edge of the titanium getter, characterised by a temperature of 25°C.

iii.   The remaining gas sample is mainly composed of Ar, Kr and Ne. It flows inside the U-shaped trap 1 filled with activated charcoal at -196°C which captures respectively Ar and Kr. Neon is not trapped and is not detected during gas chromatography cycles.

iv.   Kr and Ar are then separated via gas chromatography at room temperature, where He is used as a carrier gas. The gas chromatography columns are made of stainless steel tubes filled with MS5A mesh. Three gas chromatographic cycles are necessary to reduce the presence of Ar in the sample, as after the gettering step Ar fraction is 4 order of magnitude larger with respect to krypton. During the first cycle, trap 1 is heated at 150°C to liberate the trapped Ar and Kr and the gas flows into the column 1 f the GC. The gas then circulates towards trap 1, which is ready to collect Ar but not Kr, since there are traces of Ar captured by the clean trap 2. The Ar purification step is completed.

v.   The second GC cycle starts when Kr is collected on trap 2 and the trap is heated at 150°C. Then, the trap is cooled again at -196°C and a third cycle with the GC is repeated to further purify the krypton fraction. When the U-trap is cooled the residual He and H_2 are pumped away while both trap 1, containing Ar, and trap 2, containing Kr, are kept at low temperatures.

vi.   To finally release the Kr fraction, trap 2 is heated at 150°C. The gas flows inside a Zr/Al getter to remove the tracers of the remaining gases and the purified krypton, ~1 μL, is finally collected in a small stainless steel sample holder filled with activated charcoal at -196°C.

vii.   The Ar fraction, on the other hand, is already purified and is transferred directly to a small volume bottle. In this thesis the air samples are purified to analyse the krypton fraction, while the argon share is not considered.
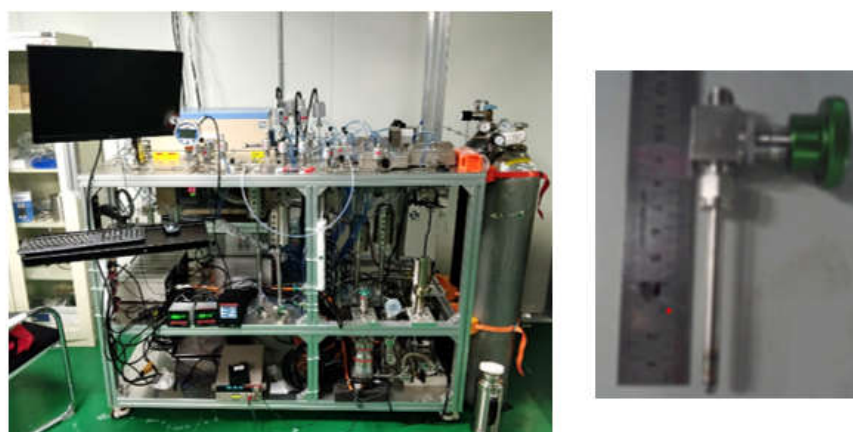
Figure 2.36: Left. Kr purification system at the USTC. Right. Kr sample holder (courtesy of F. Ritterbusch).

2.4.4.4 Atom Trap Trace Analysis (ATTA)

Analysis of isotope traces for dating purposes have been performed for decades using the well-developed methods of accelerator mass spectrometry (AMS) and low-level counting (LLC). Chen et al. (1999) developed the Atom Trap Trace Analysis (ATTA) methodology to perform isotope traces analysis. The set-up of the ATTA-3 instrument (Jiang et al., 2012) at the Argonne National Laboratory

(U.S.A.) allowed the [81]Kr analysis to be available for the geoscience community by November 2011. The ATTA instrument employed in this thesis work (Figures 2.37 and 2.38) is the one available at USTC (China) and developed in collaboration with the Argonne group (Cheng et al., 2010; Yang et al., 2013).
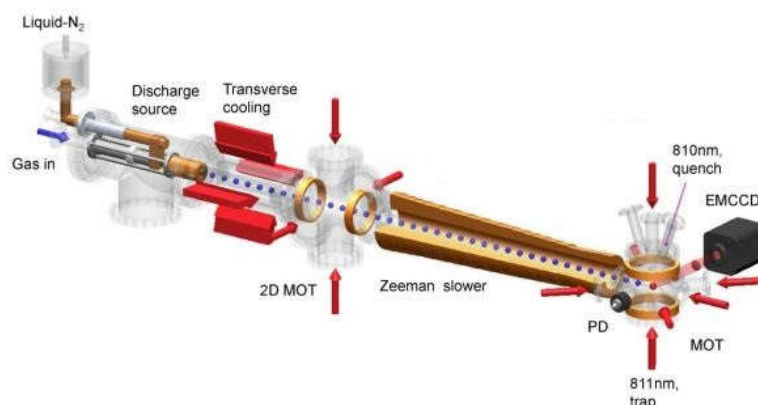
Figure 2.37: Schematic of the ATTA instrument at the USTC laboratories (Yang et al., 2013).

The ATTA is an atom counting method based on laser technology and determines the abundance of rare isotopes for a given sample by measuring simultaneously the single atom counting rate of [81]Kr and the stable isotope ([83]Kr). The instrument at USTC is represented in Figure 2.38. When the Kr aliquot flows inside the system, a radio-frequency-driven discharge inside a ceramic tube cooled by liquid-N_2 produces Kr atoms in a metastable state (Kr*). Then a laser light transversely cools the Kr* beam, which is then focused on the two-dimensional magneto-optic trap (2D-MOT) and later slowed by Zeeman slower. The beam is trapped in another MOT, where about 10 cold atoms of abundant Kr can be hosted simultaneously, while [81]Kr atoms are trapped individually due to their low abundances. Images of trapped atoms are recorded by an electron-multiplying charge-coupled device (EMCCD).

As the trapping efficiency is affected by drifts over time due to variations of the experimental conditions, it is necessary to normalize the atom counting rate by the stable [83]Kr trap loading rate, measured with a "quench-and-capture" process (Cheng et al., 2013). In this process, stable Kr isotopes contained in the trap are excited by an 810 nm laser beam from the metastable state Kr* to the ground state through spontaneous decays. This method allows to remove the metastable atoms when the laser beam is turned on. When the laser is off, stable [83]Kr atoms are captured and their number shows a linear increase. The number of trapped atoms can be estimated through the measurement of the fluorescence emitted by stable atoms during the linear increase. The loading rate of the stable Kr is then determined and applied to normalize the [81]Kr counting rate, to obtain the final [81]Kr/Kr isotope ratio.
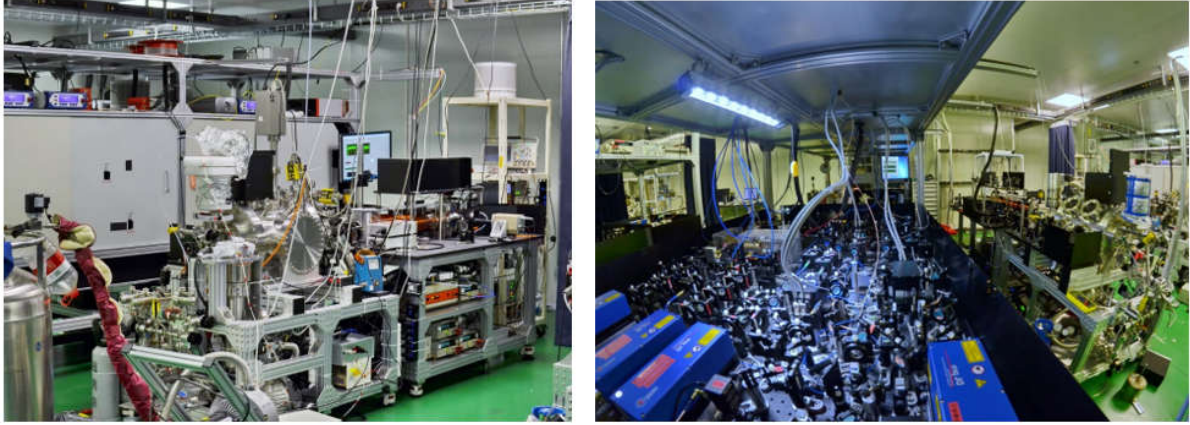
Figure 2.38: ATTA instrument at USTC (China) (Courtesy of F. Ritterbusch).

2.4.4.5 ^{81}Kr-age calculation

To estimate the samples ages, the ^{81}Kr abundance (R_{81}) is determined in the sample by the number of ^{81}Kr atoms in comparison to the atmospheric reference. Assuming that the ^{81}Kr abundance in the atmosphere have been constant in the past, the ^{81}Kr-age can be calculated through the following equation:

$$^{81}Kr - age = -\tau_{\frac{1}{2}}/\ln(2) \cdot \ln(R_{81}) \tag{2.22}$$

where $t_{1/2}$ = (229 ± 11 ka) is the half-life of ^{81}Kr.

However, the ^{81}Kr abundance in the atmosphere has not been completely constant in the past. Such changes are connected to variations of the cosmic ray flux on the Earth, which lead to a potential difference in the ^{81}Kr-age of up to 4% (Buizert et al. 2014, Zappala et al. 2020). Through reconstructions of the geomagnetic field intensity, the ^{81}Kr atmospheric input over the past 1.5 Ma has been calculated by Zappala et al. (2020) and applied when calculating the ^{81}Kr-age (Figure 2.39).
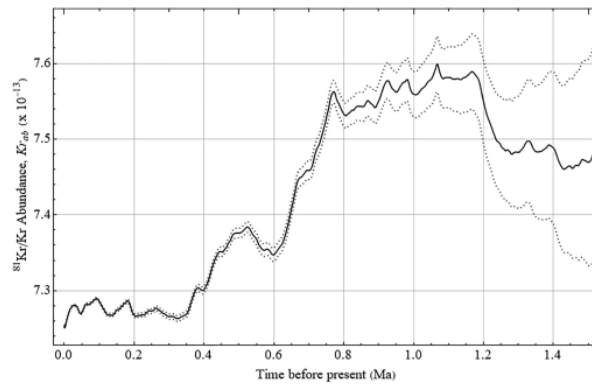
Figure 2.39: Isotopic abundance of 81Kr in the atmosphere over the past 1.5 Ma (back curve). Production rates two standard deviations are represented by the dotted lines (Zappala et al., 2020).

Then, the error associated with the ^{81}Kr measured abundance, given by the statistical error of atom counting, is calculated. This error propagates in the calculation of the Kr-age determination and is also summed to the error of the Kr half-life. In addition, the final uncertainty of the Kr age depends also on the ice amount and on the Kr sample size. The larger is the amount of used ice (from 6 to 10 kg) and the volume of the extracted Kr, the smaller would be the dating uncertainty. Considering TALDICE ice amount, samples size and their estimated age, they are characterized by 4% of uncertainty on the final ^{81}Kr age (Figure 2.40).
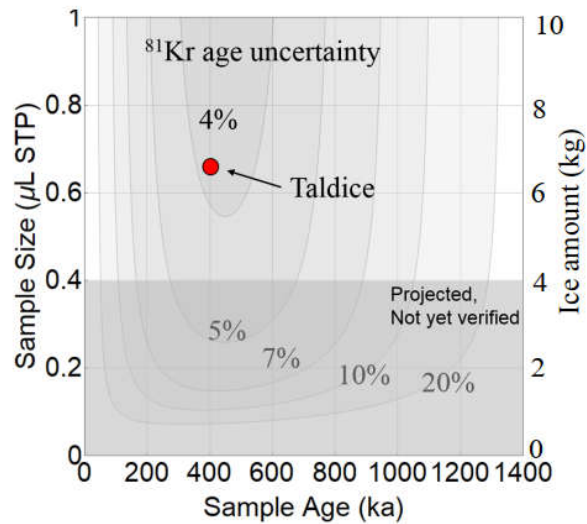
Figure 2.40: ^{81}Kr age uncertainty depending on the ice amount and on Kr sample size. TALDICE samples (red dot) fall in the region of 4% uncertainty on the final Kr-age (Ritterbusch et al., 2020) .

3 **The TALDICE deep1 age scale**

3.1 **Introduction**

One aim of this thesis consists in defining a chronology for the portion of the TALDICE ice core below 1438 m depth. As mentioned in Chapter 1, several previous studies (Bazin et al., 2013; Buiron et al., 2011; Schüpbach et al., 2011) focused on building an age scale for the TALDICE ice core. The most recent published work refines the age-depth relationship for TALDICE from the top of the core until 1438 m depth, at ~150 ka (Bazin et al., 2013).

This chapter presents my article "An extension of the TALDICE ice core age scale reaching back to MIS 10.1" published in the journal *Quaternary Science Review* (Crotti et al., 2021), as an invited paper. The paper is available in open access at the following link https://www.sciencedirect.com/science/article/pii/S0277379121002857. This work gathers all the efforts to extend the chronology of the TALDICE ice core below 1438 m depth. In this original work, I conducted most of laboratory analysis to improve the original data set. In the article, the results related to the definition of the TALDICE-deep1 age scale, are presented.

My contribution consists in the analysis of 1335 δD ice samples with the CRDS technique as well as samples cutting, air extraction and mass spectrometer measurements of $\delta^{18}O_{atm}$, $\delta O_2/N_2$ and $\delta^{15}N$ of 81 ice samples. All the analytical techniques are described in detail in Chapter 2. In addition, I participated to the first application of the ^{81}Kr dating techniques to build an ice core chronology, cutting the ice and performing the air extraction on 2 of the 3 samples. The ^{81}Kr purification and ATTA analysis were performed by the Hefei University research team (China), which provided the final results.

I also performed the synchronizations shown in the paper, produced the background chronology and the final age-depth relationship with the application of the IceChrono1 model (Parrenin et al., 2015) with the help of the co-authors. I wrote the whole text and designed all the graphs and tables.

In this original work, the new TALDICE δD high resolution (5cm) profile below 1438 m depth and the new $\delta^{18}O_{atm}$, $\delta O_2/N_2$ and $\delta^{15}N$ profiles are presented. The paper focuses of the following points: (i) display of the new data set and results of the δD and $\delta^{18}O_{atm}$ synchronization with the EDC profiles, (ii) definition of the background scenario, (ii) chronology construction with the IceChrono1 probabilistic model, (iii) evaluation of the age-depth scale and discussion of the ^{81}Kr dating results, (iv) discussion on the peculiarities of the δD profile during past interglacials.

3.2   An extension of the TALDICE ice core age scale reaching back to MIS 10.1

Ilaria Crotti [1,2], Amaelle Landais [2], Barbara Stenni [1,6], Lucie Bazin [2], Frédéric Parrenin[3], Massimo Frezzotti [4], Florian Ritterbusch[5], Zheng-Tian Lu [5], Wei Jiang [5], Guo-Min Yang [5], Elise Fourré[2], Anais Orsi[2], Roxanne Jacob[2], Bénédicte Minster [2], Frédéric Prié [2], Giuliano Dreossi [6], and Carlo Barbante [1,6]

[1]Department of Environmental Sciences, Informatics and Statistics, Ca' Foscari University, Venice, 30172, Italy

[2]Laboratoire des Sciences du Climat et de l'Environnement LSCE/IPSL, CEA-CNRS-UVSQ, Université Paris-Saclay, 91191 Gif-sur-Yvette, France

[3]University Grenoble Alpes, CNRS, IRD, IGE, 38058, Grenoble, France

[4]Department of Science, Roma Tre University, Rome, 00154, Italy

[5]University of Science and Technology of China, Hefei, 230026, China

[6]Institute of Polar Sciences (ISP), CNR, Venice, 30172, Italy

Abstract

TALDICE (TALos Dome Ice CorE) is a 1620 m deep ice core drilled at Talos Dome, an ice dome located at the edge of the East Antarctic Plateau in the Ross Sea Sector. The Antarctic Ice Core Common Chronology (AICC2012) extended the age scale of the core until ~150 ka (1438 m depth) (Bazin et al., 2013), while no age scale was available below 1438 m depth. In this work we present the new TALDICE-deep1 chronology using the new measurements of $\delta^{18}O_{atm}$, δD and ^{81}Kr as well as the inverse model IceChrono1. The TALDICE-deep1 chronology stops at 1548 m, as the portion below this depth is probably affected by mixing processes. The new age scale extends the climate record for the Ross Sea Sector of the East Antarctic Ice Sheet back to MIS 10.1 ~343 ka (1548 m depth) and identifies both MIS 7 and 9 warm stages, which show specificities in the δD signal. However, it is not possible to recover the isotopic record beyond stage 10.1 as the signal shows a quasi-flat shape. Thereby, the new chronology TADICE-deep1 doubles the extension of the previous age scale as it covers the three past glacial/interglacial cycles.

3.2.1   Introduction

Because of ice thinning from the top to the bottom of the ice-sheet, the deepest sections of ice cores store most of the paleoclimatic information. However, phenomena acting in the lowermost layers of ice-sheets, such as strong diffusion and physical layer mixing, may affect the quality of the record and its interpretation (NEEM community members, 2013; Tison et al., 2015). Improving dating techniques for the deeper sections of ice cores, as well as extending climate records further back in time, represents one of the major challenges of the ice core science community, which is now involved in the quest of the oldest ice core (Lilien et al., 2021; Parrenin et al., 2017).

The low accumulation rates of ice core drilling sites on the East Antarctic plateau prevent annual layer counting. Consequently, deep ice cores need the employment of dating strategies based on various approaches combining age markers of gas and ice phases (e.g. volcanic tephra) with ice flow modelling

(Parrenin et al., 2007; Bazin et al., 2013). Some tracers provide absolute or orbital dating constraints, i.e., dating constraints for each individual ice core, while other tracers provide relative dating constraints, i.e., stratigraphic tie points, to adjust the timescale of one ice core relative to another ice core age scale.

Air trapped in polar ice cores has the unique property of containing global tracers of the atmosphere, which record the variations of atmospheric composition over time at different drilling sites in both hemispheres (Loulergue et al., 2008; Petit et al., 1999; Raynaud et al., 1993). The $\delta^{18}O$ of atmospheric O_2 ($\delta^{18}O_{atm}$) and CH_4 represent two signals well suited to define relative age scales for different ice cores through records synchronization. $\delta^{18}O_{atm}$ is characterized by an atmospheric turnover time on the order of 1000-2000 years and can be used to provide tie points on millennial and multi-millennial timescales (Capron et al., 2010), while CH_4 is characterized by a much shorter residence time (5 to 10 years) and is used for synchronisation on multidecadal to millenial timescales if sampling resolution and width of the age distribution allows for.

In addition to gas synchronization tools, some independent absolute constraints can be obtained. Radiometric dating, based on the well-known radioactive decay of certain isotopes, represents an alternative and complementary dating technique. Recent instrumental developments have enabled the use of ^{81}Kr (229,000 years half-life) for dating ice cores. Its dating range of 0.03-1.3 Ma (million years) perfectly fits the expected age range of Antarctic ice. As a noble gas isotope, it is not involved in complicated geochemical reactions and it is well mixed in the atmosphere (Lu et al., 2014). Moreover, the anthropogenic ^{85}Kr can be measured simultaneously with ^{81}Kr to quantify any contamination with modern air.

However, absolute dating and gas records cannot not be employed alone to construct ice core age scales and they are frequently associated with glaciological modelling to build robust chronologies (Barnola, et al., 2007). The most common modelling approach for Antarctic ice cores is based on the application of Bayesian tools such as, the Datice or IceChrono1, respectively developed by Lemieux-Dudon et al. (2010) and Parrenin et al. (2015), which compute the best compromise between markers (absolute and relative) and prior estimation of the ice and gas chronologies (background scenario). The background scenario consists in the estimation of depth-profiles of three glaciological quantities: accumulation rate, thinning function and Lock-In-Depth (LID). The LID corresponds to the lowermost depth where air can diffuse in the firn (Buizert et al., 2013; Landais et al., 2006). The calculation of the LID is essential for dating purpose, as it provides a tool to link gas and ice chronologies. A first determination of this depth can be estimated from a firn densification model adapted to the surface characteristics of the site of interest (e.g. Arnaud et al., 2000; Breant et al., 2017). Measurements of $\delta^{15}N$ of molecular N_2 also provide constraints on the LID: because of the effect of gravity, $\delta^{15}N$ in the firn air, and thus enclosed in air bubbles, is proportional to the LID at the time of depth enclosure in absence of any abrupt mean temperature change (Severinghaus et al., 1998). An ice flow model (e.g. Parrenin et

al., 2004) provides an estimation of the thinning function using scenario of past temperature and accumulation rate as well as temperature profile in depth. δD or $\delta^{18}O$ profiles are used to calculate the accumulation rate (Parrenin, Dreyfus, et al., 2007).

TALDICE (TALos Dome Ice CorE) is a 1620 m deep ice core drilled at Talos Dome, an ice dome located on the edge of the East Antarctic plateau, about 290 km from the Southern Ocean, 250 km from the Ross Sea, 275 km from the Italian Mario Zucchelli Station, 550 km North of Taylor Dome, 1500 km NW of Siple Dome, and 1100 km East of Dome C (Frezzotti et al., 2004). The drilled core is longer than expected since the target area was missed by less than 200 m and the bedrock was not reached. The drilling reaches a 1.6 km wide valley, not noticed in the low-resolution radar profiles available at that time and spotted later in high resolution radar surveys (Figure 1b). The ice thickness at the drilling site is ~ 1795 m, surrounded by subglacial hills at about 1550 m (Jordan et al., 2008).

The first official age scale for the TALDICE core, TALDICE-1, is defined by Buiron et al. (2011), combining glaciological modelling to CH_4 and $\delta^{18}O_{atm}$ records synchronization with already dated ice cores from Antarctica and Greenland. The dating method is based on the Datice tool (Lemieux-Dudon et al., 2010). The TALDICE-1 chronology is built only until 1428 m depth, corresponding to a gas age of ~141 ka (thousands of years before present) due to the low resolution of the available $\delta^{18}O_{ice}$ and CH_4 records (Buiron et al., 2011). In order to reduce the uncertainties associated with the first age scale, Schüpbach et al. (2011) propose TALDICE 1-a, a refined age scale covering the time span between 55 to 112 ka (1293-1380 m depth), based on new high-resolution methane data produced by Continuous Flow Analysis (CFA). The new CH_4 measurements allow the reduction of the uncertainties associated with the age scale from 1.9 ka in TALDICE-1 to 1.1 ka in the considered time interval. Then, the TALDICE chronology is improved a third time and included in the AICC2012 (Antarctic Ice Core Chronology 2012) framework (Bazin et al., 2013; Veres et al., 2013), a multi-proxy and multi-site ice and gas orbital chronology which spans the last 800 ka. AICC2012 is based on the same dating strategy applied for TALDICE-1 (Datice model and synchronization), including several new gas measurements for all involved cores. For TALDICE, new $\delta^{18}O_{atm}$ measurements extend the record of Buiron et al. (2011) from 1402 m down to 1553.95 m depth. Despite the novel gas record, the poor resolution of both methane and $\delta^{18}O_{atm}$ data in the deeper part of the core do not allow to extend the chronology beyond ~150 ka (gas age) at 1438 m depth. Moreover, the complexity of the glaciological background in the lowermost portion of the TALDICE ice core makes the definition of a preliminary age scale based on the pure glaciological modelling hard to obtain. Indeed, the ice flow dynamics are complex at Talos Dome site. The ice stream surges on the two sides of the dome, either through the small outlets located in the Transantarctic Mountains, or through Wilkes Land, near an efficient ice stream (Masson Delmotte et al., 2011). The internal layering below the dome is detectable only up to 1400–1500 m. Below that limit reflecting horizons are irregular and discontinuous (Frezzotti et al., 2004). In addition, stratigraphic markers in the deeper portion of the ice core, such as volcanic layers (tephra and sulphates peaks), are

not detected below 1400 m depth (Delmonte and Severi, *personal comm.*). To expand the age scale back in time, Bazin et al. (2013) point out that new $\delta^{18}O$ (or δD) and $\delta^{18}O_{atm}$ records at higher resolution are necessary in the deep part of the core, to improve synchronization with other ice core records and to assess the stratigraphic integrity of the ice.

In this work we present the new age scale, named TALDICE-deep1, for the TALDICE ice core between 1438 m and 1548 m depth based on the combination of classical and new dating techniques. We base our chronology on new measurements of gas phase parameters ($\delta^{18}O_{atm,}$ $\delta^{15}N$ and $\delta O_2/N_2$) and δD for the ice phase. In addition, considering the complicated glaciological background and the lack of climatic signal below 1548 m depth, we integrate the dating approach with the application of the novel ^{81}Kr dating technique on three different depth intervals. We build the new age scale with the use of the IceChrono1 probabilistic model (Parrenin et al., 2015), which requires the selection of gas markers, ice markers and the definition of a background scenario for the accumulation rate, thinning function and LID. We use a similar strategy to the one employed by Bazin et al. (2013), however we adapt it to the complicated conditions of the deepest portion of TALDICE. In particular, we define gas and ice age markers through the comparison of TALDICE with only EDC $\delta^{18}O_{atm}$ and δD records, avoiding a multicore approach, due to high uncertainties associated with the background scenario. We do not include the CH_4 record in our synchronization strategy since the available data set (Buiron et al., 2011; Schüpbach et al., 2011) below 1438 m depth has not the necessary high resolution needed for comparison with other cores. Moreover, because of the centennial variability of CH_4, this tracer cannot be used to check the integrity of the stratigraphy. In addition to $\delta^{18}O_{atm}$, considering the absence of stratigraphic markers (e.g. volcanic layers) in this portion of the core, we define ice markers from water isotopes profiles synchronization.

This work is structured as follows: we provide new gas and ice data set, as well as ^{81}Kr dating results, from 1438 m to the bottom, synchronization results, background chronology definition and the inverse method approach to construct the TALDICE-deep1 chronology. Results, uncertainties and a posteriori evaluation of the ^{81}Kr dating method are discussed in section 3.2.6, along with a preliminary climatic interpretation of the new δD record.
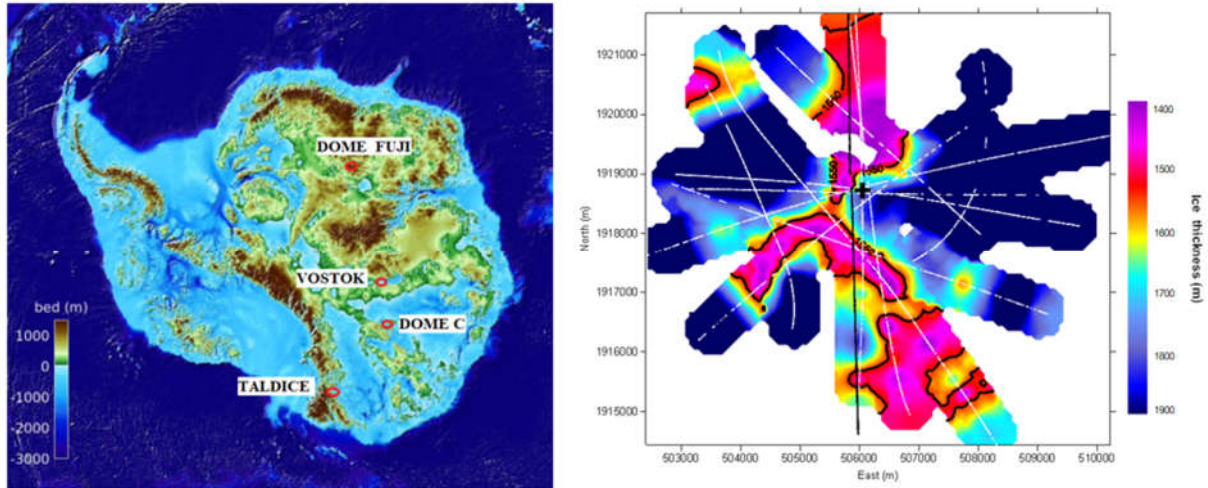
Figure 3.1: Location of East Antarctic deep cores on bed topography map (a) (BedMachine, Morlighem et al., 2020) and radar survey in the Talos Dome area (b). In figure (b) black line indicates depth and contours of subglacial hills and the black cross indicates the TALDICE drilling site (Jordan et al., 2008).

3.2.1.1 New data set for $\delta^{18}O_{atm}$, $\delta O_2/N_2$ and $\delta^{15}N$

Buiron et al. (2011) and Bazin et al. (2013) report the isotopic and the elemental composition of trapped air ($\delta^{18}O_{atm}$, $\delta^{15}N$ and $\delta O_2/N_2$) for the TALDICE core in 228 samples between 583 m and 1553 m depth with a mean resolution of 1.5 ka. To increase the resolution of the available data set and to obtain a complete record down to the bottom of the core, 81 new data points are added. Ice samples of ~40 g each, stored at -20 °C, are decontaminated and handled following the procedure described in Extier et al. (2018). The extraction of air trapped in the ice is performed at LSCE, using a semi-automatic extraction line (Capron et al., 2010), and $\delta^{18}O_{atm}$, $\delta^{15}N$ and $\delta O_2/N_2$ of air are measured using a dual inlet Delta V plus (Thermo Electron Corporation) mass spectrometer. To produce the final dataset, several corrections are applied on raw data, taking into account instrumental sensitivity and processes acting in the firn as described in Extier et al. (2018). Lastly, the $\delta^{18}O_{atm}$ record is corrected for gas loss fractionation using $\delta O_2/N_2$ data.

The new $\delta O_2/N_2$ dataset is characterized by low values, i.e. on average - 62 ± 25 ‰ with values down to -124 ‰ (Figure 3.2a, b). The typical values of $\delta O_2/N_2$ for ice analysed shortly after drilling and not affected by gas loss are around -10 ‰ at Dome C (Extier et al., 2018), and such values were also previously observed at TALDICE (Figure 3.A.1). Due to the gas loss, our new $\delta O_2/N_2$ results cannot be directly used for dating purposes, but they are still useful to correct $\delta^{18}O_{atm}$ data as in previous studies (Extier et al., 2018; Severinghaus et al., 2009). For samples showing $\delta O_2/N_2$ values more negative than -50‰ (i.e. much more negative than values measured before in ice cores affected by gas loss), the equation proposed by Extier et al. (2018) does not correct properly the $\delta^{18}O_{atm}$. We thus propose an alternative gas loss correction equation tailored for samples affected by extreme gas loss, based on EDC $\delta^{18}O_{atm}$ and $\delta O_2/N_2$ data set. Detailed gravitational and gas loss correction calculations are described in Appendix 3.A.

The new $\delta^{18}O_{atm}$ data set fits well with the available profile of TALDICE (Buiron et al., 2011, Bazin et al., 2013), validating our measurements and gas loss correction approach. The extended and corrected $\delta^{18}O_{atm}$ and $\delta O_2/N_2$ datasets between 1350 m depth and the bottom are shown in Figure 3.2. Due to the small size of the available samples, measurements in replicates are not possible. The 1σ uncertainty associated with the measurements is calculated on 30 replicates of air samples and is equal to ± 0.04‰ for the $\delta^{18}O_{atm}$ data set, ± 1.24‰ for $\delta O_2/N_2$ measurements and ± 0.02‰ for $\delta^{15}N$ data. The combined $\delta^{15}N$ record is also used to estimate the LID.

3.2.1.2 *^{81}Kr dating*

Krypton is a noble gas present in the atmosphere with a concentration of 1.10 ppmv (Aoki & Makide, 2005). Its ^{81}Kr isotope, with an atmospheric abundance of $9.3 \cdot 10^{-13}$ (Zappala et al., 2020), is naturally produced in the upper atmosphere by cosmic-ray induced spallation and neutron activation of stable krypton (Loosli & Oeschger, 1969; Lu et al., 2014). ^{81}Kr has a long residence time in the atmosphere and, due to its chemical stability, is well-mixed. Buizert et al. (2014) suggests that ^{81}Kr might be applied as a dating tool for ancient air trapped in polar ice, in the 0.03-1.3 Ma age range, also for cores affected by disturbed stratigraphy or discontinuous records.

^{81}Kr dating represents a new dating approach in ice cores. Until now it has been successfully applied only on outcropping old ice from Taylor Glacier, Antarctica (Buizert et al., 2014) and Guliya Ice Cap, Tibetan Plateau (Tian et al., 2019). The typical sample size for the initial study is about 40-80 kg of ice, from which 5-10 µL STP of krypton can be extracted for the analysis with the Atom Trap Trace Analysis (ATTA) method (Jiang et al. 2012, Lu et al., 2014). However, recent developments of the ATTA machine reduces the sample size down to 1 µL STP of krypton, which can now be extracted from about 10 kg of Antarctic ice (Jiang et al., 2020; Tian et al., 2019).

In order to provide an absolute dating of three different depth intervals in the lowermost part of the TALDICE core and to assess the integrity of ice stratigraphy, three samples covering consecutively 4-5 m core length each and weighing from 5.5 to 9.5 kg, are selected between 1560 and 1617 m depth. The chosen samples belong to 13 1-m-long bags of TALDICE CUT B (54 x 55 mm), stored at the European Cold Laboratory Facilities (University of Milano-Bicocca, Italy) at -30 °C. We ship the bags to LSCE (France) with a dedicated transport at constant temperature of -20 °C and then store in the cold room at the same temperature for several weeks. We carry out samples cutting, decontamination and air extraction at LSCE, following the protocol described in Tian et al. (2019). We extract air from TALDICE samples and collected in three stainless steel cylinders that we send to the University of Science and Technology of China (USTC) for krypton purification and ^{81}Kr analysis with the ATTA method, as described by Jiang et al.(2012) and Dong et al.(2019). The anthropogenic ^{85}Kr is measured simultaneously with ^{81}Kr to quantify any contamination with modern air. The ice sample details and krypton dating results are reported in Table 1. For all three samples the measured ^{85}Kr activity is below

the detection limit, so no correction for contamination with modern air is necessary. For the calculation of the [81]Kr-ages, the changes in the past atmospheric [81]Kr abundance due to variation of the cosmic ray flux on the Earth (Zappala et al., 2020) are taken into account. The age uncertainty calculation is based on the statistical error of the atom counting. The detailed [81]Kr data analysis can be found in Appendix 3.B.

Depth (m)	Air Extracted/ Ice Weight (mL STP/kg)	Sample Used (µL STP, Kr)	[85]Kr (dpm/cc)[a]	[81]Kr (pMKr)[b]	[81]Kr-Age (ka)	Systematic error (ka)
1559 - 1563	700 / 9.6	~ 0.7	< 0.3	30.5 ± 1.6	397 ± 18	± 19
1573 - 1575	550 / 5.4	~ 0.6	< 0.8	24.9 ± 3.5	470 ± 54	± 23
1577 - 1578						
1613 - 1618	760 / 9.5	~ 0.8	< 0.1	29.4 ± 1.5	410 ± 19	± 20

Table 3.1: Ice sample details and radiokrypton dating results. Reported errors are 1-σ errors. Upper limits have a 90% confidence level. The average [85]Kr activity in the northern hemisphere has been ~75dpm/cc at the time of sample processing. The measured [85]Kr concentrations are below the detection limit, verifying that no relevant contamination with modern air has occurred. Additional to the statistical error on the [81]Kr-age from atom counting, a systematic error due to the uncertainty in the half-life of [81]Kr has to be taken into account. This error would shift all [81]Kr ages up or down together. [a] dpm/cc= decay per minute / cubic centimetre STP of krypton, [b] pMKr =percent modern Krypton.

3.2.1.3   δD of water

The complete record of hydrogen isotopic composition (δD) in the TALDICE ice core at 1-m resolution is published in Stenni et al. (2011). The 1-m record is characterized by a resolution of 128 years/m during the LIG, when the AICC2012 chronology ends. Here we present new continuous δD dataset at 5 and 10 cm resolution starting at 1438 m down to the bottom, which aims at increasing the record resolution. Discrete samples at 10 cm-resolution between 1438 m and 1486 m depth are measured at the University of Venice using a Thermo Fisher Delta Plus Advantage mass spectrometer coupled with a HDO device. The precision of δD measurements is ± 0.7‰ (1σ). Below 1486 m depth, discrete 5 cm-resolution analyses are carried out the University of Venice and LSCE using the Cavity Ring Down Spectroscopy technique (CRDS). Analysis are performed using a Picarro isotope water analyser (L2130-i version) for both laboratories. The data are calibrated using a linear calibration with three lab-standards periodically calibrated vs V-SMOW. Intercomparison of standard waters are performed between the two laboratories over the analysis period. A comparison of our new δD TALDICE record with the previous data set published by Stenni et al. (2011) is shown on Figure 3.2c.
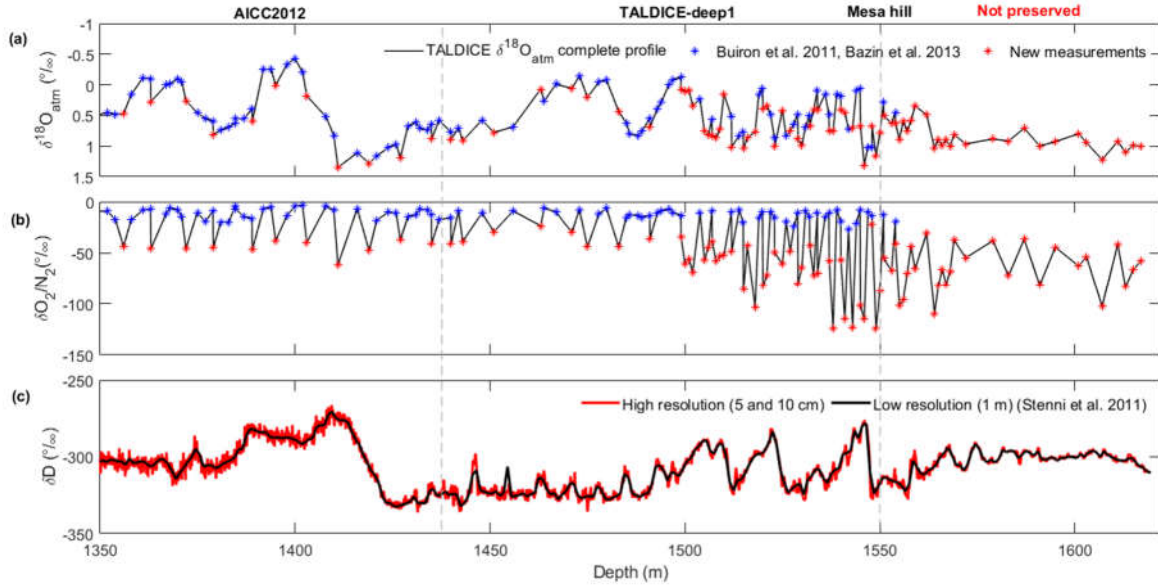
Figure 3.2: New data set for deep portion of the TALDICE ice core. $\delta^{18}O_{atm}$ (a) and $\delta O_2/N_2$(b) record between 1350 m and 1620 m depth, new measurements presented in this study (red stars) and measurements published by (Bazin et al., 2013; Buiron et al., 2011) (blue stars). δD record between 1350 m and 1620 m depth (d), the new high resolution δD profile (red curve) (10 cm between 1438 m and 1486 and 5 cm resolution below 1438 m depth to the bottom) is superimposed on 1-m resolution δD record (black curve) (Stenni et al. 2011). The core is divided in three sections on the basis of the chronology. From the top until 1438 m TALDICE is dated by the AICC2012 chronology, between 1438 m depth and 1548 m depth we define the TALDICE-deep1 age scale. Below 1548 m depth the climatic signal is not preserved. The mesa hill is depicted at 1550 m depth.

3.2.2   Synchronization and age markers definition

Ice flow modelling for dating the ice, as well as the identification of dated volcanic horizons (e.g. tephra layers, sulphate spikes) and orbital tie points represent the main classical strategies to define the ice chronology. The deep part of TALDICE ice core, unfortunately, does not provide suitable conditions to employ any of the above mentioned approaches. We decide to apply a dating strategy which involves the use of the new $\delta^{18}O_{atm}$ TALDICE profile as a stratigraphic tool, synchronizing it with the dated EDC signal (Extier et al., 2018) in parallel with the alignment between TALDICE and EDC δD signals (EPICA Community Members, 2004). The synchronization between δD records is based on the principle that large climatic variations observed in the stable water isotopes records are synchronous in all Antarctic cores. The δD matching becomes an essential tool, in our case, to find the best visual matching scenario and to provide markers to define the ice age scale.

3.2.2.1   *$\delta^{18}O_{atm}$ synchronization*

The new TALDICE $\delta^{18}O_{atm}$ profile allows the synchronization of the record below 1438 m depth with the extended $\delta^{18}O_{atm}$ data set published for the EDC ice core (Extier et al., 2018) on the AICC2012 gas age scale (Bazin et al., 2013). We select the EDC dataset spanning the time window from Termination III to Termination IV at relatively high resolution: ~160 years for Termination III and ~700 years for Termination IV (Extier et al., 2018). Due to the relatively low resolution of our TALDICE $\delta^{18}O_{atm}$ record (1.55 m, ~ 2620 years), we cannot apply any automatic matching algorithm for synchronization. We employ the manual wiggle-matching technique to choose TALDICE tie points.

When possible, we define tie points at mid-slope, however maxima and minima are selected as well. We perform several sensitivity tests increasing and decreasing the number of tie points and verifying the degree of agreement between the two records. After several visual experiments we define 22 gas age markers between 1455.92 m and 1548 m depth (Table 3.2), which represent the minimum number of data points allowing superimposition of the two curves with the maximum degree of agreement (r= 0.81) (Figure 3.3). Within these 22 tie points, 15 are located at slope breaks (50%, 25% or 75% of the transition) in the TALDICE record, 6 points at maxima and 1 at a minimum.

Then, we associate with each tie point a corresponding AICC2012 age from the EDC $\delta^{18}O_{atm}$ record (Figure 3.3a). The final age of each TALDICE tie point is calculated as the mean age obtained from five different possible visual matchings between the two records, following a similar approach applied by Capron et al. (2010). The uncertainty (reported in Table 3.2) is calculated adding the uncertainty of the visual matching between TALDICE and EDC $\delta^{18}O_{atm}$ records (difference between the maximum and the minimum estimated EDC AICC2012 age for one single TALDICE tie point), TALDICE $\delta^{18}O_{atm}$ resolution on the initial TADICE-1 age scale (Buiron et al., 2011) and the uncertainty associated with AICC2012 gas age scale for EDC. Detailed uncertainty calculations are reported in Appendix 3.C. As expected, the synchronization result shows a good agreement between the two $\delta^{18}O_{atm}$ records in the time span 158-252 ka (r=0.86), the TALDICE record displays a signal similar to the EDC one in terms of shape and intensity. On the other hand, between 252 and 280 ka the matching between the two profiles appears less clear (r=0.60) due to the relative higher values of the TALDICE $\delta^{18}O_{atm}$ record (average of ~ 0.70‰) with respect to the EDC ones (average of ~ 0.48‰), and the lack of the ~260 ka peak in our data set, attributable to the low resolution. For the part older than 280 ka, a good agreement (r= 0.62) between the two data set is visible until Termination IV (~343 ka). In order to refine the synchronization during this time period we perform 7 new $\delta^{18}O_{atm}$ measurements on the EDC core in the time interval between 335 ka and 337 ka (2587.20-2594.90 m depth), which improves the resolution over the ~336 ka excursion just at the start of the deglaciation (Figure 3b). This short event is also visible in the TALDICE profile, and it allows the synchronization of the two records with a high degree of confidence until 335 ka. Below 1548 m depth, corresponding to a gas age of 336 ka, the synchronization is more difficult due to the lower variability of $\delta^{18}O_{atm}$ and we do not select additional tie points (Figure 3.2a).

The uncertainty associated with the $\delta^{18}O_{atm}$ records synchronization spans from a minimum of 2.7 ka to a maximum of 7.9 ka, and its evolution along with the depth is variable and strictly influenced by the uneven sampling of TALDICE $\delta^{18}O_{atm}$ data points (see Table 3.2). However, our simple synchronization provides a uniform evolution of the gas age scale as a function of depth and allows for identification of a preserved $\delta^{18}O_{atm}$ signal down to 1548 m depth.

Depth TALDICE (m)	Depth EDC (m)	Gas age (ka)	Uncertainty (±ka)
1447.92	1930.08	158.8	4.9
1455.92	1919.42	163.1	4.3
1483.00	1991.81	179.8	4.0
1492.95	2041.79	190.3	6.2
1498.95	2068.01	195.7	5.8
1503.87	2089.34	199.7	2.7
1509.00	2143.21	209.3	5.0
1510.00	2181.61	215.9	7.7
1511.92	2221.86	224.0	5.4
1518.00	2256.98	233.7	6.5
1519.90	2284.32	239.7	3.7
1521.93	2298.62	242.2	3.0
1525.00	2331.01	248.7	3.9
1527.95	2352.46	256.6	5.2
1528.92	2364.23	261.0	7.9
1529.00	2391.71	270.6	7.7
1533.00	2426.71	282.9	3.8
1536.93	2460.24	293.2	5.4
1538.92	2500.29	308.1	4.6
1541.00	2513.95	314.0	6.8
1545.00	2580.40	334.4	3.5
1548.00	2589.72	336.3	3.0

Table 3.2: Tie points defined by $\delta^{18}O_{atm}$ record synchronization between TALDICE and EDC ice cores on the AICC2012 gas age scale.
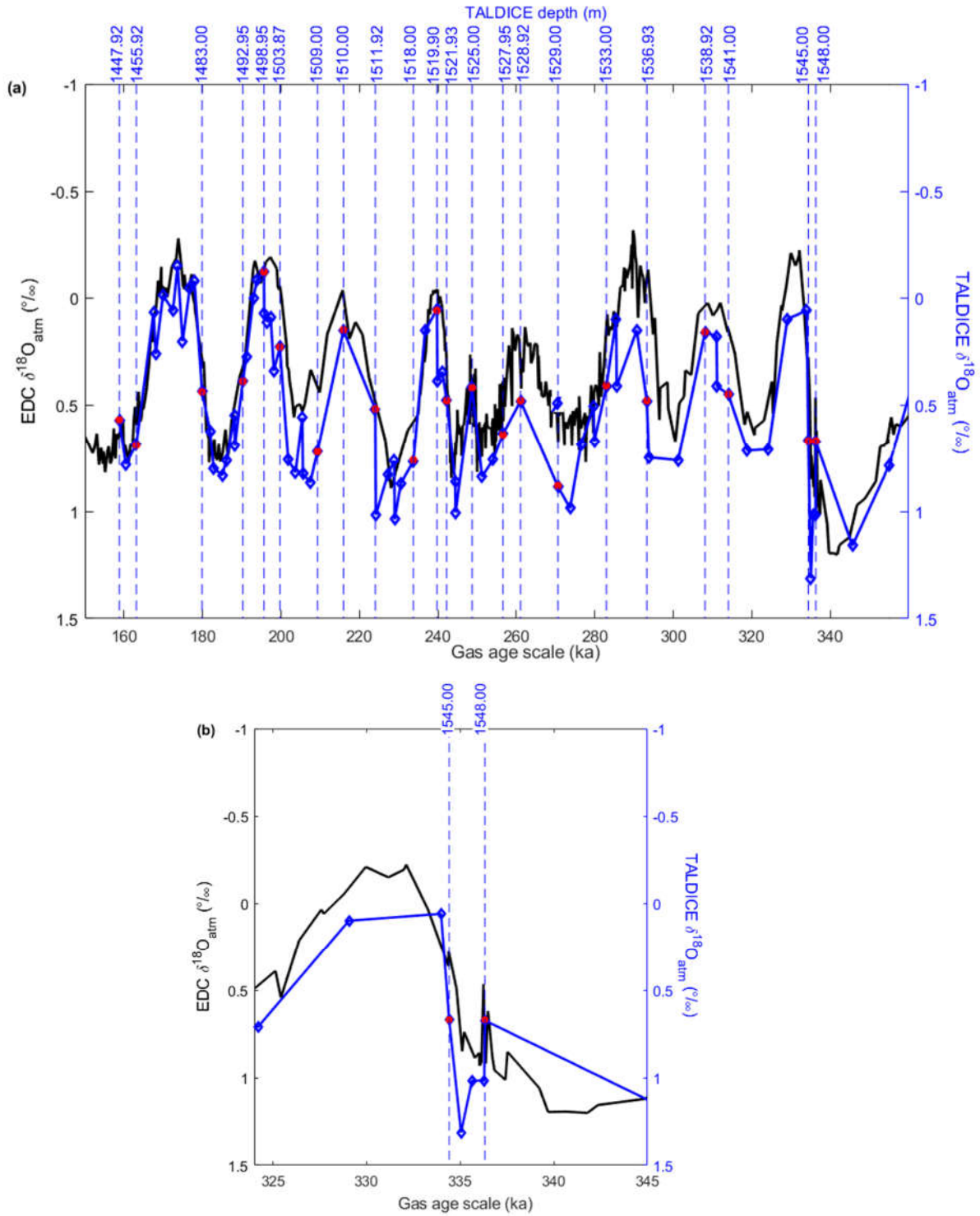
Figure 3.3: Synchronization of TALDICE and EDC $\delta^{18}O_{atm}$ records between 150 and 336 ka. (a) TALDICE (blue curves) $\delta^{18}O_{atm}$ record and gas tie points (red dots) synchronized on EDC (black curve) (Extier et al.; 2018 and new measurements) drawn on the AICC2012 gas age timescale (Bazin et al. 2013) (b). Focus on new event detected before Termination IV in both cores.

3.2.2.2 *Water isotopes synchronization*

We define ice age markers through the synchronization between the new TALDICE δD profile below 1438 m depth and the EDC δD profile (55 cm resolution) (EPICA community members, 2004) drawn on AICC2012 ice age scale, which covers the last 800 ka (Bazin et al., 2013). For matching purposes, we select the EDC δD portion of the profile spanning from 150 ka to 450 ka, with a mean data resolution of ~ 250 years for Termination III and ~ 340 years for Termination IV. The preliminary estimation of the temporal resolution of TALDICE water isotopes below 1438 m depth, obtained from the δD synchronization, is ~127 years for Termination III and ~190 years for Termination IV. We employ the same visual synchronization approach applied for the $\delta^{18}O_{atm}$ record, but here we mainly select mid-slopes points thanks to the high-resolution of both EDC and TALDICE records.

The choice of tie points has fallen on the minimum number of points (18), which provides the highest degree of agreement between the two records (r=0.91), with the purpose of better constraining the synchronization over the interglacial periods MIS 7.5 and 9.3. The result of the δD visual matchings are displayed in Figure 3.4. The complete list of the selected tie points and the associated uncertainties are reported in Table 3.3. Each marker point has an associated uncertainty, called cumulative uncertainty, and its calculation is explained in details in Appendix 3.C. The synchronization effort exhibits a good agreement between the two isotope profiles between ~174 and ~249 ka (r=0.88), as during MIS 7 sub-stages are well constrained. The uncertainties of the tie points in this age window are almost constant and set around the average value of ~3.5 ka. In contrast, the portion older than ~ 249 ka, is characterized by larger uncertainties up to 6 ka when constraining the MIS 9, since the TALDICE isotope profile show a second interglacial peak around ~330 ka which is not identified in the EDC δD signal. However, the synchronization provides a high degree of agreement (r=0.95) between the two records down to the depth of 1547.65 m, where the estimated ice age is ~ 343 ka. Below 1548 m depth we cannot observe any similarity between TALDICE and EDC δD records, concluding that no climatic signal is preserved in this portion of the core. The δD signal below the last tie point does not show any significant variability, similarly to what is observed in the $\delta^{18}O_{atm}$ profile (Figure 3.2d).

Depth TALDICE (m)	Depth EDC (m)	Ice age (ka)	Uncertainty (ka)
1470.05	1951.07	174.2	3.0
1483.95	1976.48	180.0	2.7
1500.90	2065.91	198.3	3.6
1506.30	2102.32	204.4	2.6
1508.00	2125.53	209.2	4.0
1511.10	2196.59	220.8	3.9
1512.80	2220.68	227.1	3.5
1516.20	2253.90	236.0	3.7
1524.40	2312.42	246.6	3.1
1529.85	2381.50	270.4	5.8
1531.25	2410.21	280.7	2.9
1535.60	2448.49	292.3	3.5
1538.45	2486.11	305.4	3.0
1540.20	2502.06	312.2	6.3
1543.50	2556.84	330.7	5.3
1545.95	2579.17	335.8	3.4
1547.40	2595.56	340.4	4.4
1547.65	2602.60	343.8	3.2

Table 3.3: Tie points defined by δD record synchronization between TALDICE and EDC ice cores on the AICC2012 ice age scale.
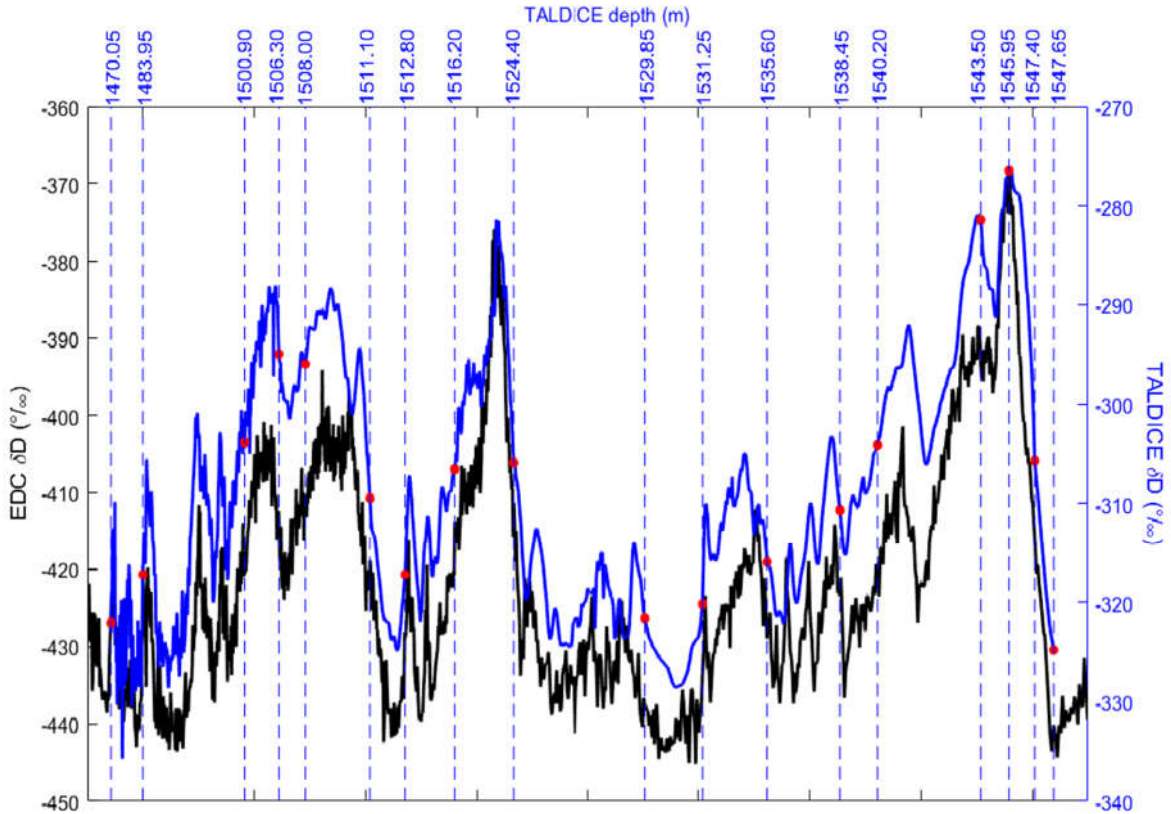
Figure .3.4: Synchronization of TALDICE and EDC δD records between 150 and 350 ka. TALDICE (blue curves) δD record and ice tie points (red dots) synchronized on EDC (black curve) (EPICA community members, 2004) drawn on the AICC 2012 ice age timescale (Bazin et al. 2013).

3.2.3 Background scenario

To build the TALDICE-deep1 age scale we employ the inverse model IceChrono1 (Parrenin et al., 2015), which provides the best compromise between a background chronology (based on ice flows and snow densification simulations) and observations (ice and gas stratigraphic links between cores and absolute ages). The background scenario is defined by three profiles in function of depth for the following glaciological parameters: thinning function, accumulation rate and LID. The background scenario is usually computed by firn densification and ice flow models; however, the LID can be calculated from the application of the firnification model as well as from the barometric equation using $\delta^{15}N$ data. In the following two sub-sections we describe how we define the background scenario associated with the deep portion of the TALDICE ice core, integrating previous estimation of glaciological parameters from Buiron et al. (2011) with our new $\delta^{15}N$ data set.

3.2.3.1 *Accumulation rate and thinning function*

In order to build the TALDICE-deep1 age scale we use the accumulation rate and thinning function estimated by Buiron et al. (2011) for the TALDICE-1 age scale until 1597 m depth, while we estimate a new LID profile from novel $\delta^{15}N$ measurements. Our choice is driven by the fact that no new data set of field measurements is available for the TALDICE ice core for the accumulation rate and the thinning function, estimated with the 1-D ice flow model (Parrenin et al., 2007).

Input parameters for the 1-D model are past accumulation rate and temperature changes. Those quantities are derived from the hydrogen isotopic content of the ice (δD) through the following equations:

$$T = T_0 + \Delta\delta D corr \alpha \tag{3.2}$$

$$A = A^0 \exp(\beta\Delta\delta Ds_{mo}) \tag{3.3}$$

where T^0 and A^0 are the current surface temperature (°C) and accumulation rate (cm of ice equivalent per year) at the ice core site. $\Delta\delta D_{corr}$ is the temporal deviation to the present-day hydrogen isotopic content of precipitation at the site, corrected for past $\delta^{18}O_{sw}$ variations derived from the marine benthic stacks (Lisiecki & Raymo, 2005). Due to the lack of the complete TALDICE δD profile, Buiron et al. (2011) calculate the record multiplying by 8 the available $\delta^{18}O$ data set (Stenni et al., 2011). We decide to use the Buiron et al. (2011) data set as well, even if the 5 and 10 cm δD profile is now available, as it would not impact on the background scenario. $\Delta\delta D_{smo}$ is a 50-yr average of $\Delta\delta D_{corr}$, α represents the spatial slope present-day isotopic thermometer (Frezzotti et al., 2004; Magand et al., 2004) and β is related to the glacial-interglacial amplitude of accumulation rate changes, tuned for the best fit of age markers for the TALDICE-1 chronology (Buiron et al. 2011). All the coefficients applied in the 1-D model are reported in Buiron et al. (2011). Unfortunately, the model contains poorly-constrained parameters and a simplistic description of the ice flow, generating errors in the estimation of the thinning function and accumulation rate profile with respect to the depth, especially in the lowermost portion of the core (below 1500 m depth). For such reason, we define high relative uncertainties as constant values and larger with respect to the pure values of thinning function and accumulation rate, respectively equal to σ=1 and σ=0.5.

3.2.3.2 *LID estimation from the new $\delta^{15}N$ data set*

The LID can be estimated either from firnification model (Goujon et al., 2003) or from the isotopic composition ($\delta^{15}N$) of gases trapped in the ice (Landais et al., 2006).

Taking into account the firn density increase from the surface to the depth where air stops diffusing, the firnification model defines the LID as:

$$LID = \int_0^{LID} D(y, t)dy \tag{3.4}$$

where D is the density of the material at the time *t* and at vertical coordinate *y* (Parrenin et al., 2012).

The LID (m) can also be estimated independently from the firnification model, and based on the $\delta^{15}N$ profile, through the application of the barometric equation (Sowers et al., 1992):

$$\delta^{15}N = \Delta m g LID/RT \tag{3.5}$$

where Δm is the mass difference between ^{15}N and ^{14}N (gmol^{-1}), g is the gravitational acceleration (ms^{-2}), R the gas constant (JK^{-1}mol^{-1}) and T the mean firn temperature (K). T is calculated following equation 2 reported in section 4.1. The Lock-in-Depth in Ice Equivalent (LIDIE) is then calculated multiplying the LID by 0.7, the compaction factor typical of modern conditions on the East Antarctic Plateau (Herron and Langway, 1980; Parrenin et al., 2012), as no firn density profile is available for the deeper portion of TALDICE. For the definition of TALDICE-1 age scale, Buiron et al. (2011) estimate the LIDIE until 1597 m depth through the application of the firnification model. Here, we calculate the LIDIE profile for the portion of the core between 1356 and 1597 m depth from our new $\delta^{15}N$ data set for the definition of the TALDICE-deep1 chronology.

The uncertainty associated with our $\delta^{15}N$-LIDIE estimation is described in Appendix C. In figure 3.5, we compare the two LIDIE estimations and we observe that the firnification model estimates a quasi-constant LIDIE of ~ 62 m over the depth range of interest (1438–1597 m depth), while the LIDIE deduced from the $\delta^{15}N$ data set (smoothed red curve, figure 5a) shows an increasing trend with depth, from ~ 48 m at 1438 m depth to ~65 m at 1597 m depth. We also calculate the difference between the two estimated quantities (Figure 3.5b) and we find out that it decreases over depth. At 1438 m the LIDIE calculated with the firnification model exceeds the LIDIE obtained from the barometric equation by ~16 m, while at ~1574 m depth the two parameters converge on the common value of ~60 m. Below that depth, down to 1597 m, the LIDIE deduced from $\delta^{15}N$ data becomes larger of about 5 m with respect to the modelled one.
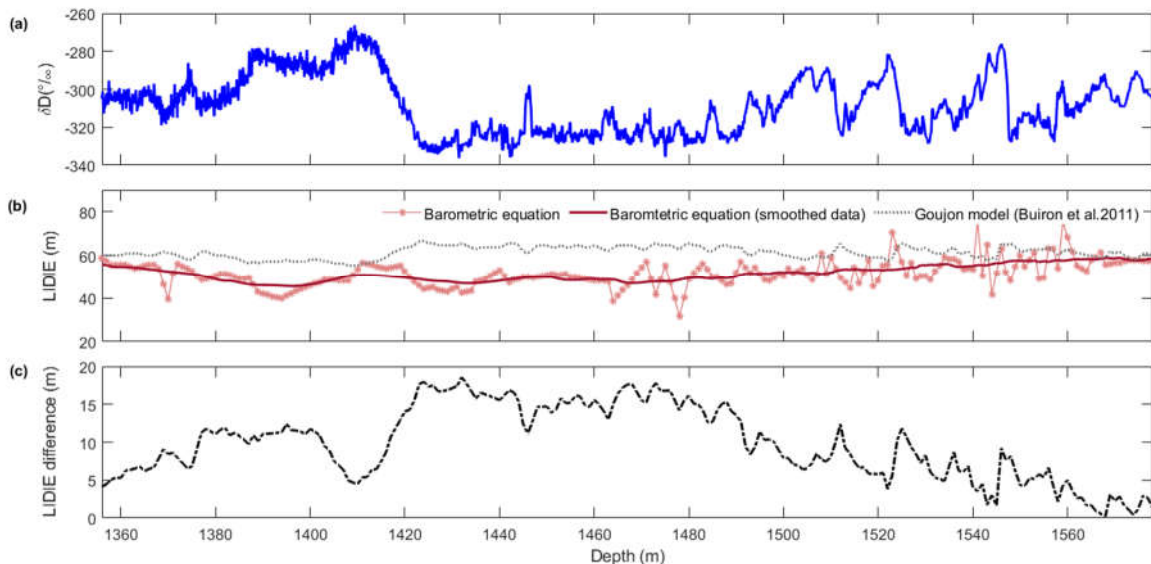
Figure 3.5: LIDIE for the deep portion of the TALDICE ice core. New δD profile (‰) (a). LIDIE estimated with the Goujon model (grey curve) applied for the TALDICE-1 age scale (Buiron et al. 2011) and LIDIE calculated from barometric equation with our new δ15N data set (dark red curve with star markers) and smoothed data (red curve) (b), both profiles are function of depth. Difference between LIDIE defined from firnification model and the LIDIE calculated from the barometric equation (m) in function of depth (c).

3.2.4   TALDICE-deep1 age scale based on a probabilistic model

IceChrono1 is an inverse model based on a similar approach to the Datice tool (Lemieux-Dudon et al., 2010), which is used to build both the TALDICE-1 age scale (Buiron et al., 2011) and the TALDICE AICC2012 age scale (Bazin et al., 2013), but including mathematical, numerical and programming improvements. The dating strategy of IceChrono1 is based on finding the best compromise between the background scenario and observations (absolute ages, stratigraphic links between cores, orbital ages and reference horizons) of several cores. It combines different sources of information, mathematically described as probability density functions (PDF), which are supposed to be independent (prior and observation) and are combined using a Bayesian framework to obtain the most probable scenario. This scenario provides *a posteriori* estimation of the background parameters and the ice and gas chronologies (Parrenin et al., 2015).

To construct the TALDICE-deep1 chronology we adopt a simplified approach, avoiding the multi-cores comparison strategy as in IceChrono1, and synchronize the TALDICE ice and gas records only with the EDC core data. Below 1438 m depth the background scenario (thinning function and the accumulation rate parameters) is poorly constrained and the multi-core synchronization effort would not improve the age scale quality. We use the following parameters as input files for IceChrono1 model: (i) the background scenario, which consists in accumulation rate, thinning function and LIDIE quantities defined with respect to depth; (ii) gas stratigraphic links (tie points) between TALDICE and EDC $\delta^{18}O_{atm}$ profiles; (iii) ice stratigraphic links (tie points) between TALDICE and EDC δD signals (Severinghaus et al., 2003); (iv) absolute ages obtained from ^{81}Kr dating. In addition, we define the relative uncertainties associated with all the elements of the background scenario and the cumulative uncertainties related to gas and ice tie points. Uncertainties are carefully estimated and calculations are detailed in Appendix 3.C. All the input files are defined until 1578 m depth, which corresponds to the last ^{81}Kr age that we consider to be coherent with our gas synchronization results.

3.2.5   Results and discussion

3.2.5.1   *The TALDICE-deep1 age scale and added value of ^{81}Kr dating results*

The combination of our different observations for the portion of the TALDICE ice core below 1438 m depth (absolute ages, gas stratigraphic links and ice stratigraphic links) with the previous data sets published by Buiron et al. (2011) and Bazin et al. (2013) extends the core chronology beyond the limits set by the AICC2012 age scale. The TALDICE-deep1 gas and ice age-depth relationships, defined from our background scenario on which we applied the inverse model IceChrono1, are shown in Figure 6a, b. In particular, the TALDICE-deep1 age scale exhibits a double-feature evolution as the trend appears coherent with the AICC2012 curve until ~1500 m depth, while below this depth we observe a change in behaviour and the curve shows an extremely steep shape, indicating the presence of enhanced thinning until 1550 m depth.

The inverse model also calculates uncertainty in the chronology, which is influenced by the errors associated with tie points and dated horizons. Figure 6c shows the uncertainty related to the age-scale at different ages. The youngest portion of the chronology, from ~150 ka to 170 ka, shows a relatively high error of about ~4 ka. This result is influenced by the uncertainty defined over the oldest portion of the AICC2012 age scale, around 150 ka, and the presence of a limited number of markers for both ice and gas matrices. Then, the uncertainty decreases down to an average value of ~2 ka between 170 and 343 ka due to the large number of both ice and gas tie points, which improves the constraints on the chronology.

This study includes the first application of ^{81}Kr analysis on small ice samples (<10 kg) as a tool to assist an ice core chronology. Previous applications of ^{81}Kr dating are performed on 40-80 kg of ice blocks or shallow cores from margin sites. In this application, we date three layers below 1548 m depth to assess the preservation of the stratigraphic order. Indeed, the first ^{81}Kr dated sample is located between 1559 and 1563 m depth and provides an absolute ^{81}Kr age estimation of 397±19 ka. The age depth relationship evolution below 1564 m is driven by the ^{81}Kr dated horizon between at 1573-1578 m, 470±54 ka and the error curve exhibits a sharp increase caused by the high uncertainty associated the two shallower Kr dated layers (Figure 3.6c). The deepest ^{81}Kr age constraint at 1613-1618 m depth carries a comparable age (410±20 ka) with respect to the upper samples; indicating the presence of processes that induce an alteration of the stratigraphic order, as folding and/or mixing. This finding indicates that ^{81}Kr dating can be applied to date deep ice when no other constraints are available to verify the preservation of the stratigraphy.

We stop the TALDICE-deep1 chronology at 1548 m depth, corresponding to an age of 343 ka. This choice is driven by the absence of climatic variability in the δD and $\delta^{18}O_{atm}$ profiles below this depth and the exponential increase of the age scale uncertainty (Figure 3.6). In addition, the ^{81}Kr results indicate that below 1548 m depth the stratigraphic order might be compromised. We suggest that the position of the drilling site, located inside a deep gorge and close to a mesa hill at 1550 m depth (Urbini et al., 2008) might cause disturbances of the ice flow and/or folding of the ice at deeper depths or act as holder for stagnant ice (Lilien et al., 2021).
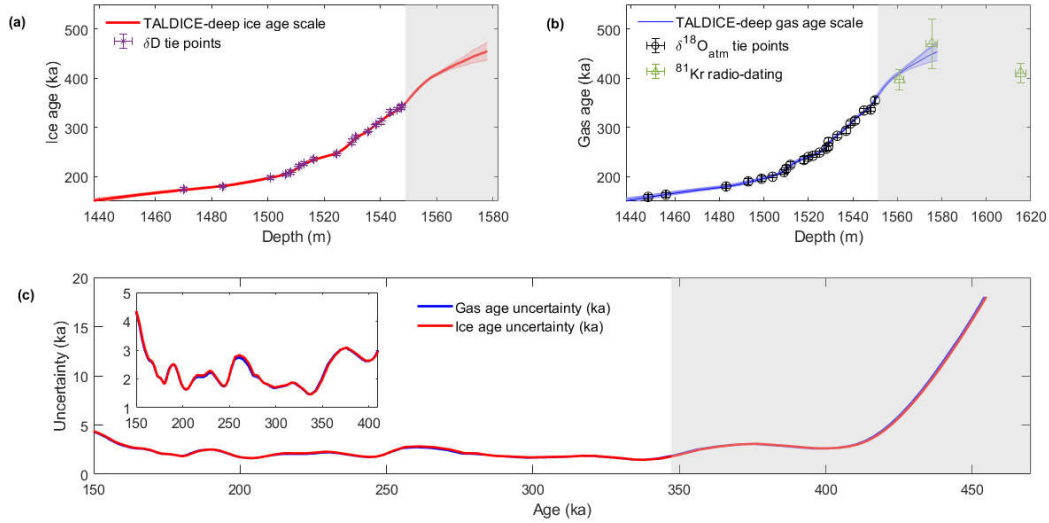
Figure 3.6: TALDICE-deep1 age scale for both gas and ice matrix with the respective uncertainties. TALDICE–deep age/depth relationship for the ice matrix (a) and for the gas matrix (b) superimposed on their respective age markers obtained from the synchronization between TALDICE and EPICA δD and δ18Oatm profiles and 81Kr dated horizons (green triangles). Uncertainty in ka associated to the TALDICE-deep1 ice (red curve) and gas (blue curve) chronology (c). The chronology stops at 1548 m depth (343 ka), below that depth we cannot extend the age scale (shaded area).

3.2.5.2   *A posteriori evaluation of the thinning function*

The thinning function presented here for the core portion below 1438 m, relies on ice, gas markers and comparison with the EDC timescale because glaciological constraints are not available. Interestingly, Montagnat et al. (2012) observe that grains with orientations departing from the single maximum appear below ~1410 m down to 1500 m depth hence suggesting a complex glaciological behaviour. Below a depth of 1500 m the increase of crystals size does not allow any statistical analysis (Montagnat, *personal comm*).

Due to the poor glaciological constraints, we associate the background thinning function defined by Buiron et al. (2011) for the TALDICE-1 age scale with high uncertainties (σ=1) to let the ice and gas markers shaping the final thinning function. As shown in figure 7a, the inverse method computes a thinning function for the deep portion of the ice core which does not agree with the respective *a priori* estimation. The *a posteriori* thinning function is characterized, as the curve defined by the AICC2012 chronology, by the presence of "bumps". These "bumps" are generally the expression of upstream or temporal variations of ice thickness at the deposition site (Parrenin et al., 2004; Parrenin, Dreyfus, et al., 2007). The TALDICE-deep1 thinning function shows only one bump, visible at 1473 m depth (~175 ka), associated with a value of 0.04, and followed by a sharp decrease in the function down to a value of ~0.01 until 1510 m depth (~220 ka). Considering the large deviation of the *a priori* thinning function from the calculated one (factor of 2) and the complex glaciological background in the deeper portion of TALDICE, this bump can be interpreted as the manifestation of irregular ice flow in those deep layers as observed in the EDC ice core at 500 m from the bottom (Dreyfus et al., 2007).

Between 1510 m and 1551 m depth the function shows a quasi-constant behaviour set on the value of 0.005; while between 1551 m and 1578 m the thinning function tends to join the *a priori* curve as only few constraints (age markers) are defined (Bazin et al., 2013) (Figure 3.7b). In particular, it is characterized by a steep slope below ~ 1100 m, as it reaches small values at relatively shallow depths. Similar small values are observed in the Dome Fuji core and are connected to very small basal melting rate (Parrenin, Dreyfus, et al., 2007). EDC shows a similar behaviour to the TALDICE thinning function, with a "bump" close to the bottom and a *quasi-vertical* shape in the deepest portion of the core. However, for the lowermost portion of the core the thinning function shows values close to 0.05, which are associated with basal melting (Parrenin, Dreyfus, et al., 2007). On the other hand, the Vostok core shows higher value of the thinning function in comparison to the other cores, close to 0.1 at the bottom. Such different feature at Vostok might be connected to the presence of melting conditions at the bottom due to the influence of the subglacial lake (Parrenin et al., 2004)

The small thinning value below 1500 m indicates that, compared to the other Antarctic cores, TALDICE does not experience melting. The absence of melting processes is also confirmed by the modelled temperature profile with the depth, as the average temperature at the bottom is estimated to be -6 °C (Frezzotti, *unpublished data.*).
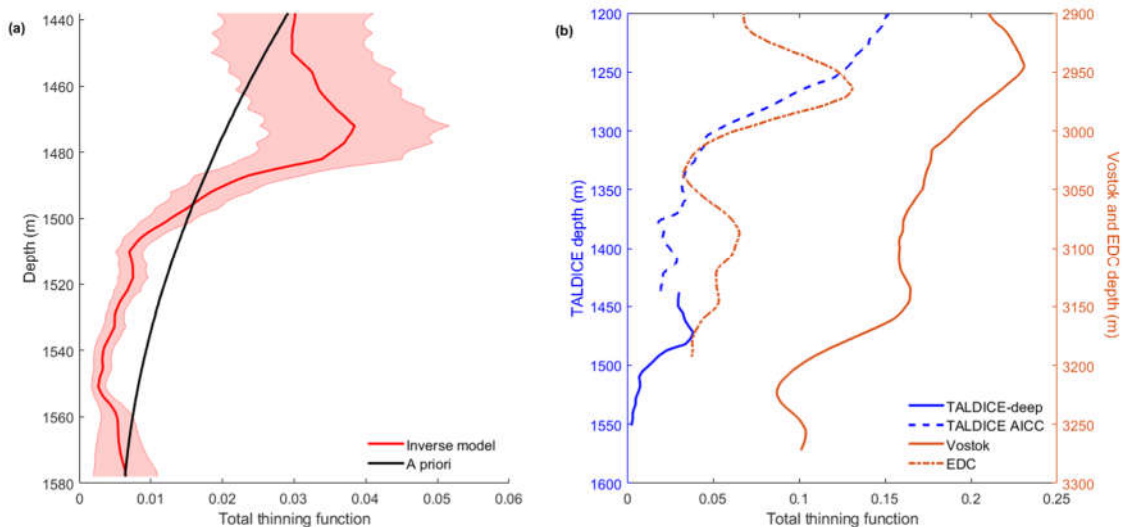
Figure 3.7: Thinning functions for TALDICE, Vostok, and EDC. Comparison between the thinning function obtained from the a priori ice flow model (black curve) and the one calculated by the inverse model (red line) with the associated uncertainty (red shade) for the deep portion of TALDICE ice core(a). Total thinning functions deduced from the inverse method for Vostok (red curve) and EDC (red dashed curve) (Bazin et al. 2013) and the composite thinning for TALDICE core derived from the inverse model applied to construct the AICC2012 age scale (blue dashed curve) (Bazin et al. 2013) and TALDICE-deep1 chronology versus depth (m) (b).

3.2.6 TALDICE δD unique behaviour during interglacial periods

The TALDICE-deep1 age scale extends the core chronology beyond the previous AICC2012 age scale (~150 ka, 1438 m depth) (Bazin et al., 2013) up to ~343 ka (at 1548 m depth). In addition, taking into account the peripheral and coastal position of Talos Dome (Frezzotti et al., 2004), the

TALDICE ice core provides the unique chance to investigate the past climate and environmental changes in the Ross Sea sector spanning the last three glacial/interglacial cycles. Our new δD profile drawn on the TALDICE-deep1 age scale makes possible to identify a well preserved climatic record and to study glacial and interglacial main events and sub-events back to MIS 10.1 (1548 m, ~343 ka) (figure 3.8a), which are not identified in other studies (Stenni et al., 2011). The $\delta^{18}O_{atm}$ signal appears as well to be preserved until Termination IV (Figure 3.8b).
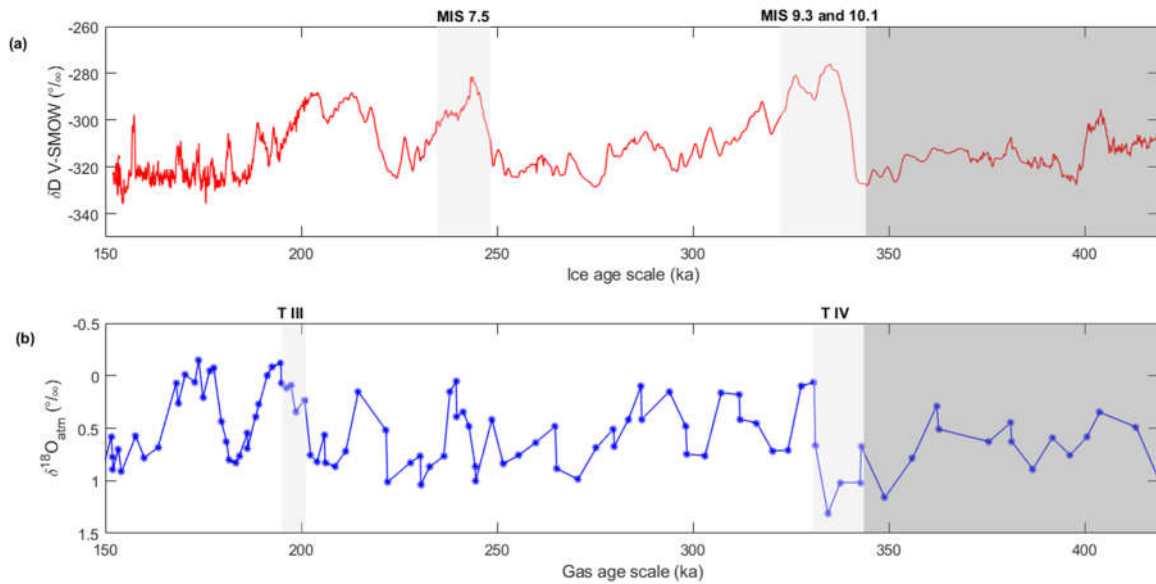
Figure 3.8: New δD and $\delta^{18}O_{atm}$ data set on the TALDICE deep-age scale. New δD record of TALDICE ice core on the TALDICE-deep1 age scale (red curve) for the last 343 ka (a). Warm stages 7.5 and 9.3 are highlighted (light grey shading). while the isotopic signal is not preserved on the oldest portion of the core (dark grey shaded area). New $\delta^{18}O_{atm}$ profile (blue curve with stars) on the TALDICE-deep1 chronology (b). Termination III and IV are highlighted (light grey shading). The isotopic signal (δD and $\delta^{18}O_{atm}$) is not preserved below 1548 m depth (dark grey shaded area).

Masson-Delmotte et al. (2011) identify TALDICE as an outlier, in comparison to the other plateau sites, as it shows a different behaviour of the isotopic profile during the LIG at ~118 ka, prior to the glacial inception. Our aim is to study if the TALDICE δD signal shows the same unique behaviour for the older warm periods. We thus perform the same comparison exercise for the oldest interglacial periods MIS 7.5 (240.8-245.8 ka) and 9.3 (324.6-338.8 ka) with Vostok, EDC and Dome Fuji δD records (EPICA community members, 2004; Petit et al., 1999; Uemura et al., 2018) on AICC2012 age scale (Bazin et al., 2013) (Figure 3.9).

The TALDICE signal is coherent with the Vostok, EDC and Dome Fuji profiles during the culmination of the deglaciation for both MIS 7.5 (~ 243 ka) and 9.3 (~335 ka), showing a clear shaped peak. On the other hand, prior to the glacial inception, the TALDICE δD curve does not display a monotonous decrease as in the other cores but is characterized by a plateau between 235 and 240 ka for MIS 7.5 and by a second peak during MIS 9.3 (~335 ka) as for MIS 5.5.

Our results confirm that TALDICE appears to record a different climatic and/or environmental signal during interglacials of the past 350 ka in comparison to the other cores drilled in the Antarctic Plateau. Masson-Delmotte et al. (2011) hypothesize that the peculiar behaviour of the water isotopes signal during MIS 5.5 in TALDICE might be connected to elevation changes and/or variations of sea ice extent or changes in the regional high latitude moisture transport. On the other hand, Bradley et al. (2012) explain the same anomaly in the δD signal observed during MIS 5.5 as consequence of a fall in surface elevation along the eastern edge of the Ross Sea over this period. Considering the unique position of the Talos Dome site, located close to the Ross Sea and at the border between the Transantarctic Mountains and Wilkes Subglacial Basin, all hypotheses appear intriguing and further investigation is needed.
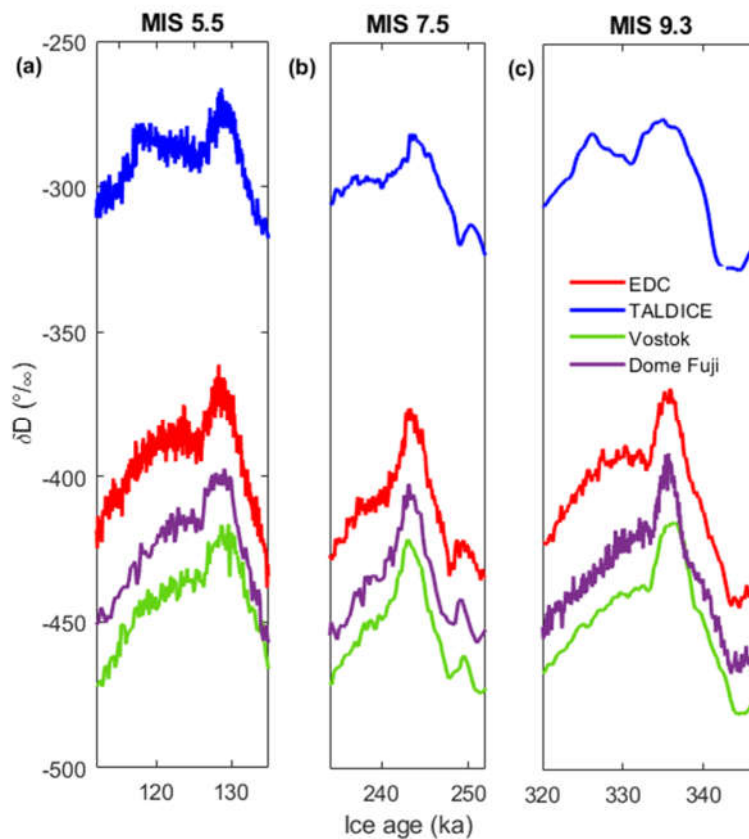
Figure 3.9: Comparison of TALDICE water stable isotope record (δD) on AICC2012 (MIS 5.5.) and TALDICE-deep1 (MIS7.5 and 9.3) age scale with other deep Antarctic ice core records. TALDICE δD profile (blue curve) is compared with EDC (red curve), Vostok (green curve) and Dome Fuji ice (purple curve) cores during MIS 5.5 (a), MI 7.5 (b) and MIS 9.3 (b). TALDICE MIS 5.5 (Masson Delmotte et al., 2011), EDC (EPICA community members, 2004), Vostok (Petit et al., 1999) and Dome Fuji (Uemura et al., 2018) profiles are drawn on the AICC2012 age scale (Bazin et al., 2013).

3.2.7 Conclusions

In this study we define the chronology called TALDICE-deep1 for the lowermost and less investigated portion of the TALDICE core, providing an extension back in time of the previous dating efforts (Bazin et al., 2013; Buiron et al., 2011; Schüpbach et al., 2011).

The age scale is built through the application of the IceChrono1 inverse model, which provides the best compromise between a background chronology and observations (tie points). We define gas matrix tie points for the oldest part of the core through the classic approach of manual wiggle matching between the new $\delta^{18}O_{atm}$ record of TALDICE and the $\delta^{18}O_{atm}$ profile of EDC. On the other hand, due to the absence of ice stratigraphic markers (e.g. volcanic tephra), we are forced to employ a non-conventional dating strategy, which includes the definition of ice age markers from TALDICE and EDC δD records for synchronization. In addition, we constrain the chronology through the application of the novel ^{81}Kr dating on three ice samples. Our study represents the first application of ^{81}Kr dating of about 5-10 kg of ice from a deep ice core to constrain the chronology. The dating effort for the deep portion of TALDICE demonstrates that the ice stratigraphy is preserved until 1548 m depth at an age of ~343 ka, i.e. in a zone where the thinning function reaches value close to 0, a value rarely observed in other deep ice cores. We cannot extend the chronology below 1548 m depth due to the lack of climatic variability in both δD and $\delta^{18}O_{atm}$ profiles. In addition, the ^{81}Kr dated samples indicate that below 1548 m the stratigraphy might be disturbed by mixing/folding process or by the presence of stagnant ice, as recently observed at Little Dome C (Lilien et al., 2021).

The TALDICE ice core can be now divided in three main sections: (i) between the top and 1438 m depth where the core age is defined by the AICC2012 chronology (Bazin et al., 2013), (ii) between 1438 m depth and 1548 m where the TALDICE-deep1 chronology applies and (iii) below 1548 m depth to the bottom (1620 m depth) a proper age scale cannot be defined due to lack of a clear preservation of the climatic signal

Our new δD and $\delta^{18}O_{atm}$ records below 1438 m depth, provides the unique chance to investigate climate and environmental changes back to MIS 10.1 (~343 ka, 1548 m depth) in the Ross Sea sector of the EAIS. The comparison with other records from Plateau sites during interglacial periods identifies the existence of a different behaviour in the TALDICE δD record during MIS 7.5 and 9.3, as already observed for MIS 5.5 (Masson Delmotte et al., 2011). Further research is needed to investigate this unique pattern.

Appendix

Appendix 3.A. Gravitational and gas loss corrections

Gases and isotopes in the firn layer above the ice are mainly affected by gravitational separation above the ice (Craig et al., 1988). To correct $\delta^{18}O_{atm}$ measurements for the gravitational effect we use the $\delta^{15}N$ values obtained for the same samples applying the following formula:

$$\delta^{18}O_{atm\,corrected} = \delta^{18}O - 2 \cdot \delta^{15}N \tag{3.A.1}$$

The factor of 2 arises from the fact that the gravitational effect is proportional to the mass difference between the two isotopes, meaning that it is two times larger for $\delta^{18}O$ ($^{18}O/^{16}O$) as for $\delta^{15}N$ ($^{15}N/^{14}N$)

(Craig et al., 1988). $\delta O_2/N_2$ values are corrected as well for gravitational fractionation effects using $\delta^{15}N$ but with a factor of 4 as in the following equation (Extier et al., 2018):

$$\delta O_2/N_{2\ corrected} = \delta O_2/N_2 - 4 \cdot \delta^{15}N \tag{3.A.2}$$

It has been demonstrated that the O_2/N_2 ratio of the ice sample decreases over time when ice is stored at temperatures higher than -50°C, since O_2 is preferentially lost from clathrate hydrates through ice crystal after the coring in comparison to N_2 (Ikeda-Fukazawa et al., 2005; Kawamura et al., 2007; Landais et al., 2012).

The gas loss correction for $\delta^{18}O_{atm}$ is based on the measured $\delta O_2/N_2$ (Extier et al., 2018; Landais, et al., 2003a; Landais; Severinghaus et al., 2009) and follows the linear relationship:

$$\delta^{18}O_{atm\ corrected} = \delta^{18}O_{atm} + (\delta O2/N_2 + 10) \times 0.01 \tag{3.A.3}$$

This correction is estimated in two different ways. In Landais et al. (2003b), $\delta^{18}O_{atm}$ and $\delta O_2/N_2$ values are measured on neighboring Vostok ice core samples that are stored over different time periods. The second set of ice samples is stored 10 years longer at -20°C than the first set of samples and an increase of $\delta^{18}O_{atm}$ by 0.3‰ is observed between the two series in parallel with a decrease of $\delta O_2/N_2$ of 30‰. In Severinghaus et al. (2009) and Extier et al. (2018), samples at the same depth are measured for $\delta^{18}O_{atm}$ and $\delta O_2/N_2$ with differences in $\delta O_2/N_2$ reaching 30‰. From paired difference plot for the $\delta^{18}O_{atm}$ vs $\delta O_2/N_2$, the same slope of 0.01 for variations of $\delta^{18}O_{atm}$ vs $\delta O_2/N_2$ due to gas loss are obtained. In the Extier et al. (2018) dataset, the $\delta O_2/N_2$ measurements from the EPICA Dome C ice core are performed in 2017 at the latest, i.e. after 13 years of storage at -20°C. The $\delta O_2/N_2$ values measured for this series are on average -38±18‰ with the most extreme value being a $\delta O_2/N_2$ of -78‰.

In our new dataset for the TALDICE samples, $\delta O_2/N_2$ are on average - 62 ± 25‰ with values down to -124‰ (figure 3.A.1). This is significantly less than what is observed for the EPICA Dome C or Vostok ice cores previously, and we can wonder if the same correction should be applied by extrapolating the results observed over variations of $\delta O_2/N_2$ over 30‰. Actually when we compare the new dataset obtained in 2020 and corrected with equation (3.A.3) with data obtained in 2011 and 2012, corrected with the same equation and published in Bazin et al. (2013), we observe a huge scatter. We hypothesize that the gas loss correction extrapolated from Extier et al. (2018) to values of $\delta O_2/N_2$ lower than -100‰ is too strong. We calculate a mean decrease of about 7.30‰ between 2011 and 2012 series and of 48.88‰ between 2011 and 2019 series. In order to revise this correction for low $\delta O_2/N_2$ values, we thus explore again the EPICA Dome C raw data obtained in Extier et al. (2018) extracting the neighboring samples and showing differences of $\delta O_2/N_2$ larger than 40‰ (Table 3.A.1). It is not possible to have neighboring samples with exactly the same depth with such a high $\delta O_2/N_2$ difference, but we find high $\delta O_2/N_2$ difference for EDC samples with a depth difference of less than 2 m. Comparison of $\delta^{18}O_{atm}$ and $\delta O_2/N_2$ values between samples taken at less than 2 m depth difference is justified by the

fact that natural $\delta^{18}O_{atm}$ and $\delta O_2/N_2$ variations occur on long-time (orbital) scale while our samples are chosen on a depth range where 1 m records less than 500 years of climatic history.

The slope for these EDC samples that experienced extreme gas loss is only 0.007, thus only 70% of the classical slope for more moderate gas loss (0.01) (Equation 3.A.3). For TALDICE samples associated with a $\delta O_2/N_2$ lower than -50‰, we thus apply the following equation instead of the classical one:

$$\delta^{18}O_{atm\ corrected} = \delta^{18}O_{atm} + (\delta O_2/N_2 + 10) \times 0.007 \qquad (3.A.4)$$

Depth (m)	$\delta O_2/N_2$ (‰)	$\delta^{18}O_{atm}$(‰)	Ratio $\Delta\delta^{18}O_{atm}$ vs $\Delta\delta O_2/N_2$
2315.473	-8	1.70	-0.009
2316.628	-52	2.11	
2352.873	-7	1.41	-0.006
2353.450	-66	1.79	
2357.850	-57	1.60	-0.007
2358.923	-8	1.26	
2346.823	-9	1.51	-0.006
2346.850	-56	1.77	
2433.750	-45	1.24	-0.008
2435.373	-5	0.91	
2334.750	-52	1.88	-0.006
2335.273	-12	1.65	
2363.350	-58	1.52	-0.005
2364.423	-7	1.25	
Average slope $\Delta\delta^{18}O_{atm}$ vs $\Delta\delta O_2/N_2$ = -0.007			

Table 3.A.1: EPICA Dome C raw data obtained in Extier et al. (2018) extracting the neighboring samples showing differences of $\delta O_2/N_2$ larger than 40‰. Data comparison allows the calculation of the average slope equal to 0.007 to correct $\delta^{18}O_{atm}$ data with $\delta O_2/N_2$ values lower than - 50‰.
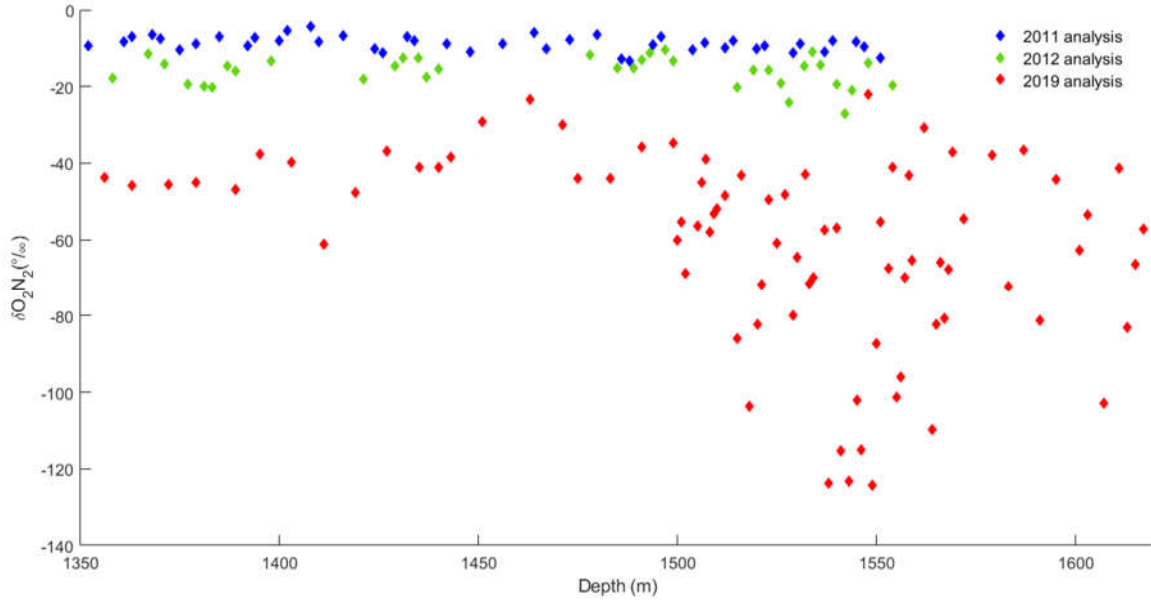
Figure 3.A.1: $\delta O_2/N_2$ measurements for the TALDICE core between 1350 m and 1620 m depth performed in 2011 (blue diamonds), 2012 (green diamonds) and 2019 (red diamonds).

Appendix 3.B. ^{81}Kr and uncertainty calculation

The ^{81}Kr abundance R_{81} in the sample is determined by the number of counted ^{81}Kr atoms in the sample as compared to the atmospheric reference. If ^{85}Kr is found to be present in the sample, indicating contamination of modern krypton, then correction must be applied to the measured ^{81}Kr abundance. The measured ^{85}Kr activity in the TALDICE samples is below the detection limit, so no correction is applied. If the ^{81}Kr abundance in the atmosphere had been constant in the past, the ^{81}Kr-age would simply be:

$$^{81}Kr - age = -t_{1/2}/\ln(2)\ln(R_{81}) \tag{3.B.1}$$

where $t_{1/2} = (229 \pm 11$ ka) is the half-life of ^{81}Kr. However, the ^{81}Kr abundance in the atmosphere has not been completely constant in the past due to variations of the cosmic ray flux on the earth which lead to a potential difference in the ^{81}Kr-age of up to 4% (Buizert et al. 2014, Zappala et al. 2020). As the atmospheric ^{81}Kr abundance of the past 1.5 Ma can be calculated based on reconstructions of the relative geomagnetic field intensity, the atmospheric ^{81}Kr input history can be taken into account when calculating the ^{81}Kr-age. This is done for the ^{81}Kr-ages of the TALDICE samples given in Table 3.1.

The error of the measured ^{81}Kr abundance is given by the statistical error of the atom counting. This error propagates to the ^{81}Kr-age, also taking into account the ^{81}Kr input history. Due to this reason, and because the relation between the ^{81}Kr-age and the ^{81}Kr abundance is not linear, the error of the ^{81}Kr-age can be asymmetric. Due to the uncertainty of the ^{81}Kr half-life, there is an additional systematic error on the ^{81}Kr-age. This systematic error would affect all the ^{81}Kr-ages in the same way, so that they would shift up or down together.

Appendix 3.C. Uncertainties calculation on IceChrono1 model input files

In this section we describe how we calculate the uncertainties associated with the background scenario quantities and with the air-ice stratigraphic links. Our background scenario is made by the thinning function and the accumulation rate quantities defined by Buiron et al. (2011) with 1D ice flow model, while the LID is derived from the new $\delta^{15}N$ data set.

Considering the difficulties encountered in the definition of the background scenario for the deep portion of TALDICE core, due to the poorly constrained 1D ice flow model, we choose to define relative uncertainties as constant values and larger with respect to the values of thinning function and accumulation rate, hence respectively equal to $\sigma=1$ and $\sigma=0.5$. This strategy, already applied by Bazin et al. (2013), allows the IceChrono1 model to base the output chronology on the stratigraphic links and on the LIDIE, rather than on the glaciological quantities. On the other hand, the LIDIE relative uncertainty is carefully calculated at each depth level. At first we calculate the uncertainty as the absolute difference between the LIDIE obtained for the TALDICE-1 background chronology (Buiron et al. 2011) and then we transform it in relative uncertainty (*ru*), which is calculated through the following formula:

$$ru = \ln[(x + \sigma)/(x - \sigma)]/2 \qquad (3.C.1)$$

where x is value of LIDIE associated with a certain depth and σ is its uncertainty.

We compute the uncertainties for the gas and ice stratigraphic links (tie points) as well. We calculate for each tie point the cumulative uncertainty (*cu*), which follows the equation above:

$$cu = (\sigma_{ID}^{2} + res^{2} + \sigma_{ref}^{2})^{1/2} \qquad (3.C.2)$$

where σ_{ID} is the difference between the maximum and the minimum age associated with the single tie point, *res* is the a priori temporal resolution of the record estimated from theTADICE-1 age scale and σ_{ref} is the uncertainty associated with AICC2012 gas or ice age scale for the EDC core.

3.3   Conclusions

In this article the TALDICE deep1 chronology is presented. This age scale extends the previous AICC2012 age scale back to 343 ka (MIS 10.1) at 1548 m depth, including two more interglacial periods MIS 7.5 and MIS 9.3 which were not included in the previous chronology. Thanks to this extended chronology TALDICE carries the oldest climate record from a coastal area in Antarctica.

The climatic signal in the TALDICE ice core is well preserved until 1548 m, where both δD and $\delta^{18}O_{atm}$ profiles can be compared to the EDC signals. Below 1548 m depth EDC and TALDICE δD and $\delta^{18}O_{atm}$ profiles start to diverge and the TALDICE records assume a quasi-flat shape in the deepest part below ~1570 m depth. To better study this portion and understanding the mechanism acting below 1548 m depth, three layers are dated using the ^{81}Kr technique. The dating results show that below 1548 m depth the three dated layers have a similar age of about 450 ka, indicating that mixing and folding processes, probably due to the adjacent subglacial hill, may have disturbed the ice stratigraphy. Further studies are necessary to understand which mechanisms have modified the deep ice layers.

The definition of the new TALDICE deep1 age scale is also fundamental to extend the climatic record back in time. The new high-resolution δD profile covers two additional glacial/interglacial cycles reaching back MIS 10.1 at 343 ka. Interestingly, the isotopic record reveals some intriguing features during the interglacial periods MIS 7.5 and MIS 9.3. The signal shows a different behaviour in comparison to other Antarctic records as EDC, Dome Fuji and Vostok, consisting in a plateau for MIS 7.5 and a peak for MIS 9.3 before the glacial inception, when all the other cores display a monotonous decrease. Such unique behaviour was already detected for MIS 5.5 by Masson-Delmotte et al. (2011), as they noticed a different isotopic behaviour around 118 ka. Several hypotheses may explain this peculiar feature in the δD record, as site elevation changes and/or variations of sea ice extent or changes in the regional high latitude moisture transport. Additional research efforts to investigate TALDICE isotopic behaviour and to reveal which climatic and environmental processes generate this interglacial pattern are presented in Chapter 4.

4 Interpretation of the TALDICE isotopic signal during past Interglacial periods

4.1 Introduction

The definition of the TALDICE deep1 chronology represents a first step to extend and investigate the climatic record archived in the TALDICE ice core. The new age scale allows to study the climatic record back to ~343 ka and to identify the interglacial periods MIS 7.5 and 9.3 in the novel 5cm - $\delta^{18}O$ record. Masson Delmotte et al. (2011) showed that during the Last Interglacial (LIG or MIS 5.5) the TALDICE isotopic record displays a different shape in comparison to the other plateau cores (EDC, Vostok and Dome Fuji). This unique isotopic signature has been initially interpreted as a response to ice thickness variations at Talos Dome (Bradley et al., 2012), however this topic is still matter of debate (Golledge et al., 2021; Sutter et al., 2020). Thanks to the new high resolution $\delta^{18}O$ record, the TALDICE isotopic signal can be investigated also for the older interglacial periods MIS 7.5 and MIS 9.3.

This chapter presents my manuscript submitted to the journal *Nature Communications*. This work combines new isotopic and chemistry data with a record from the marine sediment core U1361A (Wilson et al., 2018) and the GRISLI ice sheet model outputs (Quiquet et al., 2018), in order to interpret the TALDICE isotopic signal during past interglacials. I performed the isotopic laboratory analysis on the TALDICE ice core and applied the multiproxy approach in this original manuscript.

My contribution consists in the analysis of $\delta^{18}O$ ice samples with the CRDS technique and the calculation of the *d*-excess parameter for the past interglacials (MIS 5.5, 7.5 and 9.3). The CRDS analytical technique is described in detail in Chapter 2. In addition, I collaborated to the modelling effort, defining the ice sheet model experiments set up and interpreting the outcomes. I also participated in the refinement the U1361A sediment core record age model and produced the whole text and most of the graphs and tables.

In this original work the new TALDICE $\delta^{18}O$ (5 cm resolution) profile below 1438 m depth and the new d-excess and ssNa$^+$ flux records during interglacial 5.5, 7.5 and 9.3 are presented. In addition, the TALDICE data set is compared to the U1361A sediment core record and GRISLI ice sheet model simulations. The paper focuses on the interpretation of the new TALDICE $\delta^{18}O$ signal during the past interglacials and includes the following points: (i) comparison of the new $\delta^{18}O$ data set with the new ssNa$^+$ flux and d-excess profiles, (ii) calculation of the elevation changes at Talos Dome from the $\delta^{18}O$ record and from 6 sensitivity experiments, (iii) comparison of the TALDICE glaciological data and GRISLI modelling results with the U1361A sediment core record, (iv) results discussion and future expectations.

4.2   Response of the Wilkes Subglacial Basin Ice Sheet to Southern Ocean Warming During Late Pleistocene Interglacials

Ilaria Crotti[1,2], Aurélien Quiquet[2,3], Amaelle Landais[2], Barbara Stenni[1,8], David J. Wilson[4], Mirko Severi[5,8], Robert Mulvaney[6], Frank Wilhelms[7], Carlo Barbante[1,8] and Massimo Frezzotti[9]

[1]Department of Environmental Sciences, Informatics and Statistics, Ca' Foscari University, Venice, Italy

[2]Laboratoire des Sciences du Climat et de l'Environnement LSCE/IPSL, CEA-CNRS-UVSQ, Université Paris-Saclay, Gif-sur-Yvette, France

[3]NumClim Solutions, Palaiseau, France

[4]Institute of Earth and Planetary Sciences, University College London and Birkbeck, University of London, London, UK

[5]Department of Chemistry Ugo Schiff, University of Florence, Florence, Italy[6]British Antarctic Survey, Cambridge, United Kingdom

[6]British Antarctic Survey, Cambridge, United Kingdom

[7]Department of Geophysics and Glaciology, Alfred Wegener Institute for Polar and Marine Research, Bremerhaven, Germany

[8]Institute for Polar Sciences (ISP), CNR, Venice, Italy

[9]Department of Science, Roma Tre University, Rome, Italy

Abstract

The response of the East Antarctic Ice Sheet to past intervals of oceanic and atmospheric warming is still not well constrained, but is critical for understanding both past and future sea-level change. Furthermore, the ice sheet in the Wilkes Subglacial Basin, which is characterized by a reverse-sloping bed, appears to have undergone thinning and ice discharge events during recent decades. By combining new glaciological evidence on ice sheet elevation from the TALDICE ice core with offshore sedimentological records and ice sheet modelling experiments, we reconstruct the ice dynamics in the Wilkes Subglacial Basin over the past 350,000 years. Our results indicate that the Wilkes Subglacial Basin experienced an extensive retreat 330,000 years ago and a more limited retreat 125,000 years ago. These changes coincided with warmer Southern Ocean temperatures and elevated global mean sea level during those interglacial periods, confirming the sensitivity of the Wilkes Subglacial Basin ice sheet to ocean warming and its potential role in sea-level change.

4.2.1   Introduction

The growth and decay of polar ice sheets exert important controls on regional and global climate, while their future behaviour is a key uncertainty in predicting sea-level rise during and beyond this century (Edwards et al., 2021). Over the last decade, it has been observed that excess basal melting in Antarctica, arising from ocean heat supply, has increased the dynamic mass loss of grounded ice shelves bordering the Southern Ocean (SO) (Adusumilli et al., 2020). This observation has implications for future ice sheet stability, and also suggests that ocean warming may have played a role in controlling past ice sheet dynamics in Antarctica. The largely marine-based West Antarctica Ice Sheet, which could contribute up to 4-5 m to Global Mean Sea Level (GMSL) (Rignot et al., 2019), is well known for its past and future vulnerability to a warming climate (Pollard & DeConto, 2009; Turney et al., 2020).
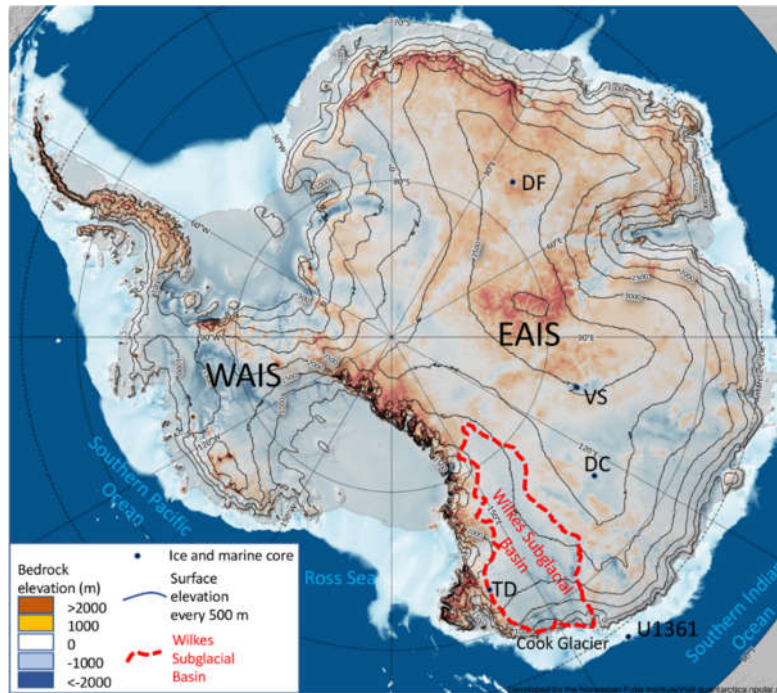
Figure 4.1: Location of the Antarctic ice cores main drilling sites and the U1361A marine sediment core. The map shows the subglacial bedrock elevation above sea level (m) and the Antarctic ice sheet present-day surface elevation above sea level (m)(Fretwell et al., 2013). The main ice cores drilling sites are Talos Dome (TD), Dome C (DC), Vostok (VK) and the marine sediment core U1361A are indicated with blue dots. The studied area of the Wilkes Subglacial Basin is delimited by the red dashed contour.

In contrast, past stability of the much larger East Antarctic Ice Sheet (EAIS), which is characterized by a total potential contribution to GMSL of 53 m (Fretwell et al., 2013), of which around one-third is marine-based ice, is still under debate (Blackburn et al., 2020; Golledge et al., 2021; Sutter et al., 2020; Wilson et al., 2018). The Wilkes Subglacial Basin, which contains 3 to 4 m sea-level equivalent (Rignot et al., 2019), is characterized by a reverse-sloping bed with an elevation below sea level (Figure 4.1). Ice that is grounded below sea level is vulnerable to intrusions of warm modified Circumpolar Deep Water (CDW) across the continental shelves into ice shelf cavities (Morlighem et al., 2020; Rignot et al., 2019; Roberts et al., 2018). An initial grounding line retreat into deeper water may then lead to a marine ice sheet instability condition, which would be followed by increased ice discharge, inland thinning, and a rapid contribution to GMSL (Schoof, 2007).

Satellite altimetry and images reveal that the Cook Glacier, which drains a large proportion of the Wilkes Subglacial Basin, has experienced thinning of 33 ± 12 cm/a (year) over the past 25 years (Schröder et al., 2019), following near-complete loss of the Cook West Ice Shelf between 1973 and 1989 that resulted from intense oceanic warming during the middle of the 20th century (Frezzotti et al., 1998; Miles et al., 2018). Model simulations suggest a modest sensitivity of the Wilkes Subglacial Basin ice sheet to oceanic warming (Golledge et al., 2015, 2017) and margin retreat controlled by the presence of a coastal "ice plug" (Mengel & Levermann, 2014). However, projected atmospheric and oceanic warming could soon lead to the crossing of tipping points in Antarctica, and hence the destabilization

of marine-based sectors of the ice sheet (DeConto & Pollard, 2016; Shen et al., 2018). In light of this potential vulnerability, future predictions of the Wilkes Subglacial Basin ice dynamics should be refined by studying previous occurrences of instabilities during past warm climatic periods when temperatures were comparable to, or warmer than, modern conditions.

Here we explore the past ice dynamics of the Wilkes Subglacial Basin during the recent interglacial Marine Isotopic Stages (MIS) 5.5, 7.5, and 9.3 of the last 350 ka. These warm periods can be considered similar, in terms of atmospheric warming and GMSL increases, to a range of near-future climate projections (DeConto & Pollard, 2016; Dutton et al., 2015). Our approach is based on interrogation of the new isotopic data (δ^{18}O and *d*-excess) from the TALDICE ice core at Talos Dome, which is sensitive to grounding line retreat in the Wilkes Subglacial Basin (Frezzotti et al., 2004; Sutter et al., 2020), in comparison to the EDC ice core record at Dome C, which is representative of East Antarctic plateau conditions under the influence of the Southern Indian Ocean (Figure 4.1). We compare estimated elevation changes at Talos Dome with simulations of local ice thickness variations and Wilkes Subglacial Basin ice dynamics from experiments conducted with the GRISLI ice sheet model (Quiquet et al., 2018) in order to identify past instability events. To provide a comprehensive picture of the ice sheet behaviour in the Wilkes Subglacial Basin during past warm interglacials, we also integrate our glaciological data and simulation results with late Pleistocene sedimentological and geochemical records from the marine core U1361A offshore Wilkes Subglacial Basin (Wilson et al., 2018) (Figure 4.1).

Our results suggest that neither changes in air mass trajectories nor variations in sea-ice extent can explain the unique TALDICE δ^{18}O signal recorded during late MIS 5.5, 7.5, and 9.3. Instead, we propose that the interglacial anomalies in the isotopic record have been produced by lowering of the site elevation at Talos Dome due to ice loss and inland retreat of the Wilkes Subglacial Basin grounding line in response to intrusion of warmer ocean waters. The GRISLI ice sheet simulation that best fits with our elevation data suggests a 10% reduction of the Wilkes Subglacial Basin ice volume during MIS 5.5, and a loss of up to 25% for MIS 9.3. Hence, these findings depict a highly dynamic ice sheet in the Wilkes Subglacial Basin and provide insights into the future response of the EAIS in a warmer world.

4.2.2 Results

4.2.2.1 TALDICE isotopic records over past interglacial periods

The EDC and TALDICE water isotopic records are both influenced by precipitation originating mainly from the Southern Indian Ocean (Scarchilli et al., 2011). The site of EDC on the East Antarctic plateau is believed to be predominantly representative of past climatic variations at a hemispheric scale (Bradley et al., 2013), while the TALDICE isotopic record is also sensitive to localised sea-ice extent in the Ross Sea (Holloway et al., 2016; Mezgec et al., 2017; Noone, 2004) and local elevation changes (Bradley et al., 2013; Goursaud et al., 2020; Sutter et al., 2020). During the current and last interglacial (LIG) periods, TALDICE and the plateau ice cores (EDC, Vostok, Dome F) share common isotopic

maxima (δ^{18}O and δD), between 12 and 9 ka (thousands of years ago) in the Holocene and at 128 ka during the LIG (Masson-Delmotte et al., 2011). The LIG isotopic maxima indicate Antarctic atmospheric temperatures 2-4.5 °C warmer than the Holocene (Jouzel et al., 2007; Uemura et al., 2018; Vimeux et al., 2002), probably arising from the operation of the bipolar seesaw mechanism during deglaciation of the Northern Hemisphere ice sheets (Masson Delmotte et al., 2011; Rohling et al., 2019; Stenni et al., 2011). However, during the late stage of MIS 5.5, the TALDICE isotopic record has a δ^{18}O peak at 117 ka followed by an abrupt decrease towards the glacial inception, and such features are not recorded in the cores from the plateau (Masson Delmotte et al., 2011).

Here we compare our new TALDICE δ^{18}O data (measured at 5 cm resolution) from MIS 5.5 (V. Masson Delmotte et al., 2011), MIS 7.5 and 9.3 with the published EDC δ^{18}O record (Fischer et al., 2007; Wolff et al., 2006), which is representative of a common Antarctic signal (Landais et al., 2021), in order to investigate TALDICE isotopic patterns during previous late Pleistocene interglacials (Methods). Interestingly, the TALDICE δ^{18}O record from MIS 9.3 exhibits a double-peak shape that is similar to the one observed for MIS 5.5, but which is not seen in EDC (Figure 4.2c). Both cores display a common interglacial isotopic peak at 335 ka, but from 331 ka the TALDICE signal diverges from the EDC signal, showing a sustained increase of about 1.5‰ until 326 ka followed by a steep decrease, while the EDC record declines gradually across this entire interval. During MIS 7.5, there is also some divergence between the two records, but the differences are smaller (Figure 4.2c). The TALDICE δ^{18}O record exhibits a second late and muted rise of ~0.8‰ between 240 ka and 237 ka, rather than the well-defined late peak observed for MIS 5.5 and MIS 9.3, while the EDC δ^{18}O record decreases towards the glacial inception. We explore three main hypotheses that could explain the discrepancies between the EDC and TALDICE water isotopic records, namely (i) differences in moisture sources, (ii) changes in sea-ice extent in the Ross Sea, and (iii) a local decrease of elevation at Talos Dome.

Differences in moisture sources between EDC and TALDICE can be explored using the deuterium excess (*d*-excess = δD - 8·δ^{18}O) thanks to the new TALDICE *d*-excess profile (5 cm resolution) for MIS 5.5, 7.5 and 9.3. This second-order parameter is an indicator of climate conditions in the vapour source regions, and is therefore sensitive to changes in the source regions or changes in air mass trajectories towards the sites(Jouzel et al., 2013; Masson Delmotte et al., 2008; Stenni et al., 2010). Our comparison shows no clear differences between the TALDICE and EDC (Landais et al., 2021) *d*-excess profiles, which exhibit coherent patterns during all interglacials (Figure 4.2b). In particular, the absence of peculiarities in the *d*-excess during the intervals with δ^{18}O anomalies at TALDICE suggests that there are no significant variations of moisture sources (Masson Delmotte et al., 2005; Stenni et al., 2010) that could explain the TALDICE isotopic behaviour.

The hypothesis of a change in sea-ice extent can be addressed using published sea-salt sodium (ssNa$^+$) fluxes in TALDICE for MIS 1 (Mezgec et al., 2017) and 5.5 (Schüpbach et al., 2013), and new

data for MIS 7.5 and 9.3, as a proxy for sea-ice coverage in the western sector of the Ross Sea and in the southern Indian Ocean facing the Wilkes Subglacial Basin (Mezgec et al., 2017). The high-resolution (7-8 cm) TALDICE ssNa$^+$ flux record for MIS 5.5 (Schüpbach et al., 2013), 7.5 and 9.3 agrees well with the EDC record (Fischer et al., 2007; Wolff et al., 2006) and no site-specific differences are identifiable (Figure 4.2a). Note that the peak in the TALDICE ssNa$^+$ record during MIS 7.5 at 240 ka is not interpreted as being climate-driven, but rather as artifacts from chemical weathering processes in the deep ice layers (Baccolo et al., 2021; Traversi et al., 2009). The overall coherence between the EDC and TALDICE ssNa$^+$ records indicates that sea-ice variations in the Ross Sea or southern Indian Ocean cannot explain the double-peak shape of the $\delta^{18}O$ record at Talos Dome, and hence the second hypothesis can also be discounted.
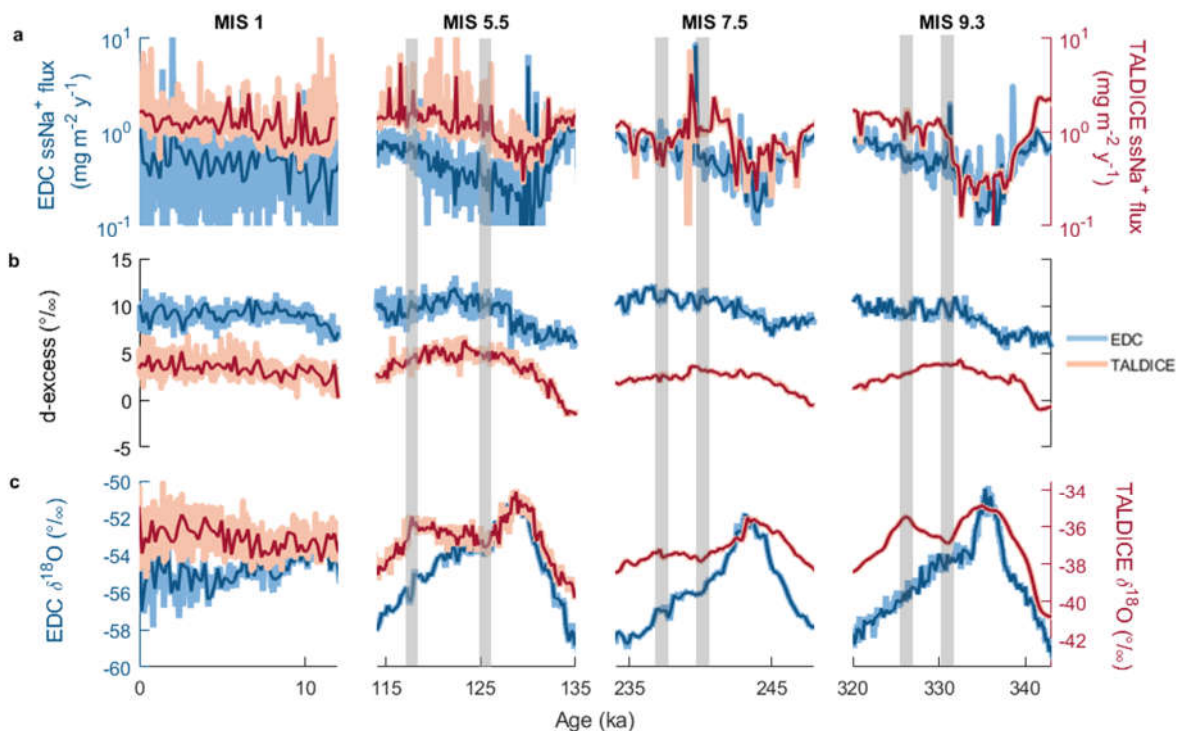
Figure 4.2: Compilation of TALDICE and EDC sea-salt sodium fluxes, d-excess, and $\delta^{18}O$ records over the last four interglacial periods. For all the proxies, the resampled records at 200 years (blue curves for EDC and red curves for TALDICE) are superimposed on the raw signals (light blue curves for EDC and pink for TALDICE). a. EDC (Fischer et al., 2007; Wolff et al., 2006) and TALDICE (Mezgec et al., 2017; Schüpbach et al., 2013) ssNa$^+$ fluxes on logarithmic scale. TALDICE ssNa$^+$ fluxes for MIS 7.5 and 9.3 are from this study. b. EDC (Landais et al., 2021) and TALDICE (Mezgec et al., 2017) d-excess records. TALDICE d-excess profiles for MIS 5.5, 7.5 and 9.3 are from this study. c. EDC (Fischer et al., 2007; Landais et al., 2021; Wolff et al., 2006) and TALDICE (Masson Delmotte et al., 2011; Stenni et al., 2011) $\delta^{18}O$ records. The TALDICE $\delta^{18}O$ data for MIS 7.5 and 9.3 are from this study. The anomalies in the TALDICE $\delta^{18}O$ record are identified by grey shaded bars (marking the start and end of the anomalous increase in $\delta^{18}O$ values).

In summary, our multi-proxy comparison (Figure 4.2) indicates that neither changes in air mass trajectories nor in sea-ice extent can explain the unique interglacial $\delta^{18}O$ excursions recorded at Talos Dome. In the following sections we therefore interpret the isotopic anomalies as an indication of

elevation changes at this site, and estimate the magnitude of changes that are required to explain the anomalies.

4.2.2.2   *Interglacial elevation changes at Talos Dome from δ¹⁸O records*

The relationship between $\delta^{18}O$ values and ice sheet elevation has recently been investigated to reconstruct EAIS dynamics during the Last Glacial Maximum (LGM) and LIG (Goursaud et al., 2020; Sutter et al., 2020; Werner et al., 2018). To estimate the imprint of elevation changes at Talos Dome during the LIG, Sutter et al. (2020) applied a $\delta^{18}O$-elevation relationship of -0.53‰/100 m, based on multiplying the present day lapse rate of -0.8°C/100 m by the local $\delta^{18}O$ isotope-temperature relationship of 0.66‰/°C estimated from the atmospheric general circulation model ECHAM5-wiso equipped with an isotope module (Werner et al., 2018). In contrast, Goursaud et al. (2020) obtained a relationship of -0.93‰/100 m for the LIG, based on the simulated isotopic response to idealised changes in Antarctic ice sheet elevation in the isotope-enabled coupled ocean-atmosphere-sea-ice general circulation model HadCM3 (Tindall et al., 2009). As a third approach, we directly compute the isotope-elevation relationship from present-day snow-pit $\delta^{18}O$ data collected along the traverse from GV7 site to Talos Dome (Magand et al., 2004), which takes into account the provenance of air masses reaching Talos Dome (see details in Methods). This method leads to an estimate of the modern isotopic lapse rate for Talos Dome of -1.35 ‰/100 m.

We use the three different $\delta^{18}O$ lapse rate estimates for TALDICE to calculate the elevation changes required to explain the observed anomalies in the isotopic signal ($\Delta\delta^{18}O$) (see Methods) for MIS 5.5, 7.5, and 9.3 (Table 4.1). The periods of MIS 5.5 and MIS 9.3 were apparently subjected to the largest elevation changes, with similar magnitude for the two periods, while only around half of this elevation decrease is invoked to explain MIS 7.5 signal. Applying the isotopic lapse rates of -1.35‰/m (Magand et al., 2004) and -0.93‰/m (Goursaud et al., 2020), we obtain a decrease in elevation of about 100-200 m during MIS 5.5 and 9.3. On the other hand, using the lapse rate of -0.53‰/m (Sutter et al., 2020) would imply larger elevation variations (~300 m) for those intervals. Hence, while subject to uncertainty from the choice of lapse rate, we conclude from the TALDICE isotopic record that the Talos Dome site was subjected to elevation changes on the order of 100-300 m during MIS 5.5 and 9.3 (Table 4.1). We further note that, due to signal smoothing at the centennial resolution of the record in the deep portion of the ice core (Crotti et al., 2021; Jones et al., 2017), the $\Delta\delta^{18}O$ anomaly during MIS 9.3, and consequently the ice thickness variation inferred for this interglacial, could be under-estimated.

4.2.2.3   *Sensitivity tests with the GRISLI ice sheet model*

To further explore possible elevation changes at Talos Dome, as well as Wilkes Subglacial Basin grounding line displacements, we perform numerical experiments of the Antarctic ice sheet dynamics over the last 400 ka with the GRISLI ice sheet model (Quiquet et al., 2018), using the same setup as Quiquet et al.(Quiquet et al., 2018). The model is forced by near-surface air temperatures over

Antarctica deduced from the EDC δD record (Jouzel et al., 2007) and by ocean temperatures derived from the ODP 980 benthic temperature record from the North Atlantic Ocean (Waelbroeck et al., 2002). Due to the lack of a continuous proxy record of sub-oceanic conditions around Antarctica covering the past 400 ka, changes in the temperature of North Atlantic Deep Water are assumed to influence the temperature of upwelled waters in the SO (Quiquet et al., 2018), which affects the sub-shelf melting rate at the grounding line. However, this simplified approach does not account for the influence of local sea-ice changes (Holloway et al., 2016) or freshwater capping (Golledge et al., 2014; Rohling et al., 2019) on sub-surface temperatures around Antarctica, or for variability in Circumpolar Deep Water upwelling or cross-shelf transport (Nakayama et al., 2019). Considering the simplified SO conditions employed, we modify the original oceanic forcing to test the response of the Wilkes Subglacial Basin ice sheet to variations of the oceanic conditions.

We present 6 sensitivity experiments, varying (i) the initial state of the Antarctic ice sheet at 400 ka, and (ii) the sub-shelf melting rate. The GRISLI experiments labelled IS (Interglacial Start) adopt an Antarctic ice sheet simulated for the present day as the initial condition at 400 ka, while the GS (Glacial Start) experiments use a Last Glacial Maximum (21 ka) initial state (Quiquet et al. 2018). These initial ice sheet states are simulated as in Quiquet et al.(2018). For both IS and GS initial states, we present three GRISLI simulations forced by different ocean sub-surface conditions (see Methods): (i) the sub-shelf melting rate signal applied by Quiquet et al. (2018) and derived from the ODP 980 benthic record (Waelbroeck et al., 2002), (ii) the signal defined by Quiquet et al.(2018) increased by 5%, and (iii) the signal defined by Quiquet et al.(2018) increased by 10% over the past 400 ka (Table 4.1). The GRISLI experimental results include elevation changes at Talos Dome, ice volume variations in the Wilkes Subglacial Basin, grounding line displacements, and the contribution of grounded ice above flotation to GMSL.

The ice thickness results from the GS and IS sensitivity experiments are compared to ice thickness variations calculated from the isotopic record at Talos Dome (Table 4.1 and Figure 4.3), with simulation GS-5 (i.e. Glacial Start and +5% oceanic forcing) showing the best agreement with the elevation changes deduced from the ice core record. For MIS 5.5, simulation GS-5 predicts an elevation decrease at Talos Dome on the order of 100 m (Figure.4.3c, Table 4.1), an average of ~100 km grounding line retreat into the Wilkes Subglacial Basin between 133 ka and 115 ka (Figure 4.4a), and loss of 10% of its ice volume (Figure 4.3d). The main grounding line retreat during MIS 5.5 is seen earlier in the model (128 ka) than what is suggested by TALDICE isotopic signal (117-127 ka) (Table 4.1). We however do not expect a perfect synchronicity between the two series because of uncertainties in relative timescale and in the ice sheet time response. Moreover, the elevation change at Talos Dome may not be completely connected to the grounding line retreat, and could also be influenced by a change in accumulation rate during interglacials at the site.

	MIS 5.5	MIS 7.5	MIS 9.3
Time interval of δ^{18}O anomaly (ka) at TALDICE	117-127	237-240	326-331
δ^{18}O max and δ^{18}O min (‰)	(-35.45)-(-37.13)	(-37.19)-(-37.87)	(-35.46)-(-36.89)
$\Delta\delta^{18}$O (‰)	1.68	0.68	1.42
Lapse rate (‰/100m)	**Elevation changes (m)**		
-0.53 (Sutter et al. 2020)	-317	-128	-268
-0.93 (Goursaud et al. 2020)	-180	-73	-153
-1.35 (Magand et al. 2004)	-124	-50	-105
	MIS 5.5	**MIS 7.5**	**MIS 9.3**
Ocean forcing	**GRISLI elevation changes at Talos Dome (m)**		
Time interval for max elevation anomaly at TALDICE (ka)	115-128	233-241	321-332
IS — Quiquet et al. (2018)	-132	-103	-749
IS-5 — Quiquet et al. (2018) +5%	-126	-101	-720
IS-10 — Quiquet et al. (2018) +10%	-750	-87	-714
GS — Quiquet et al. (2018)	-126	-85	-134
GS-5 — Quiquet et al. (2018) +5%	-116	-89	-473
GS-10 — Quiquet et al. (2018) +10%	-152	-103	-754

Table 4.1: Isotopic anomalies and elevation changes calculated and modelled for Talos Dome during interglacial MIS 5.5, 7.5, and 9.3. Isotopic anomalies are calculated from the δ^{18}O record resampled at 200 years intervals. Elevation changes are calculated from the isotopic anomalies using the lapse rate estimates of Sutter et al. (2020), Goursaud et al.(2020), and Magand et al. (2004). IS and GS elevation changes are modelled for 6 sensitivity tests performed with the GRISLI ice sheet model, varying the Antarctic ice sheet initial conditions and the SO temperature forcing. IS simulations are initialized with Antarctic interglacial initial conditions at 400 ka and GS simulations are initialized with Antarctic glacial initial conditions at 400 ka. Elevation variations at Talos Dome are calculated for interglacial time intervals when the simulated GRISLI ice thickness variations are maximized.

For MIS 7.5, GS-5 predicts no grounding line displacement and only a very limited reduction in ice thickness at Talos Dome, in agreement with the TALDICE isotopic record (Figure 4.3b-c, table 1). For MIS 9.3, GS-5 simulates a more dynamic ice sheet response in the Wilkes Subglacial Basin, with an average of ~330 km grounding line retreat between 339 ka and 318 ka (Figure 4.4b) leading to the loss of ~25% of its ice volume (Figure 4.3d). The modelled elevation at Talos Dome exhibits an abrupt decrease of ~470 m between 332 ka and 321 ka (Figure 4.3c), synchronous with the TALDICE isotopic anomaly (Figure 4.3b). However, the ice thickness variations simulated at Talos Dome during MIS 9.3 are much greater than those calculated from the isotopic record (~100-250 m) (Table 4.1). The TALDICE lower temporal resolution (~200 years/5 cm) below 1530 depth probably leads to smoothing of the isotopic signal (Crotti et al., 2021; Jones et al., 2017), which could be responsible for a muted $\Delta\delta^{18}$O signal during MIS 9.3. Overall, the modelled contribution from grounded ice above flotation in the Wilkes Subglacial Basin to GMSL increase is estimated to be +0.5 m during MIS 5.5 and +0.9 m

during MIS 9.3 for the GS-5 experiment. The former value is supported by the changes in the TALDICE ice core isotopic record, while the latter value may be an upper estimate, depending on the extent of signal smoothing in the TALDICE record during MIS 9.3.

The results of these IS experiments depict a highly-unstable ice sheet in the Wilkes Subglacial Basin, which is inconsistent with the elevation changes deduced from the TALDICE $\delta^{18}O$ record and with evidence from previous studies (Blackburn et al., 2020; Golledge et al., 2021).A ~700 m elevation reduction at Talos Dome is simulated over MIS 9.3, while a Wilkes Subglacial Basin collapse is simulated in the IS-10 experiment but not the other IS simulations for MIS 5.5 (Table 4.1). An increase of 10% in the oceanic warming forcing seems to represent a tipping point that triggers deglaciation of the Wilkes Subglacial Basin ice sheet in both IS and GS experiments during 9.3 and in IS simulations during MIS 5.5 (Table 4.1). We suggest that this tipping point was not passed during those intervals (Figure 4.3).
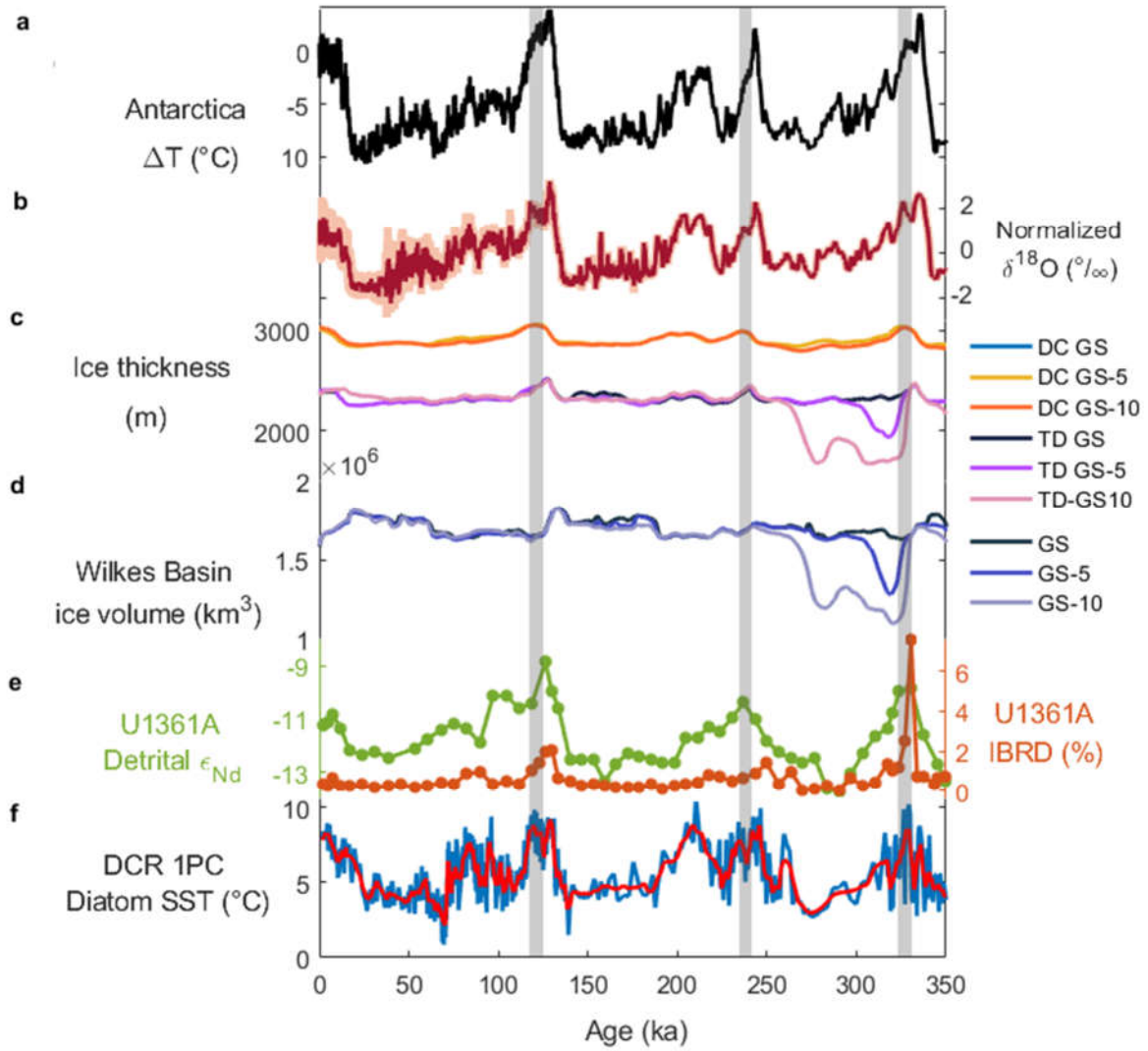
Figure 4.3: Comparison of the TALDICE isotopic record and GRISLI simulations to sedimentological data from sediment core U1361A and Antarctic atmospheric and oceanic temperature records since 350 ka. a. Antarctic ice core temperature difference (ΔT, difference from mean values of the last millennium) derived from δD at EDC (Jouzel et al., 2007) plotted on the AICC2012 age scale (Bazin et al., 2013). b. TALDICE normalized δ^{18}O record (data centred and scaled to have mean 0 and standard deviation 1) (measured, pink; resampled at 200 years intervals, red). Holocene data are from Stenni et al. (Stenni et al., 2011) and MIS 5.5 record is from Masson-Delmotte et al. (2011). The MIS 7.5 and MIS 9.3 isotopic data are from this study. c. Talos Dome (TD) and Dome C (DC) elevation from GS simulations, based on the original oceanic forcing used by Quiquet et al. (2018) (blue curve), and the original forcing increased by 5% (yellow) and by 10% (orange). d. Wilkes Subglacial Basin ice volume evolution from GS simulations. e. Core U1361A Nd isotope record (plotted as ϵ_{Nd}; green curve with dots) and iceberg-rafted debris (IBRD) % (brown curve with dots) (Wilson et al., 2018) on AICC2012 age scale (see Methods). f. Diatom-based sea-surface temperatures (SST) from core DCR-1PC (blue curve), and smoothed data with 5-point moving average (red curve) (Shukla et al., 2021). Grey bars highlight the intervals with a unique isotopic signal in the TALDICE ice core compared to the EDC record.
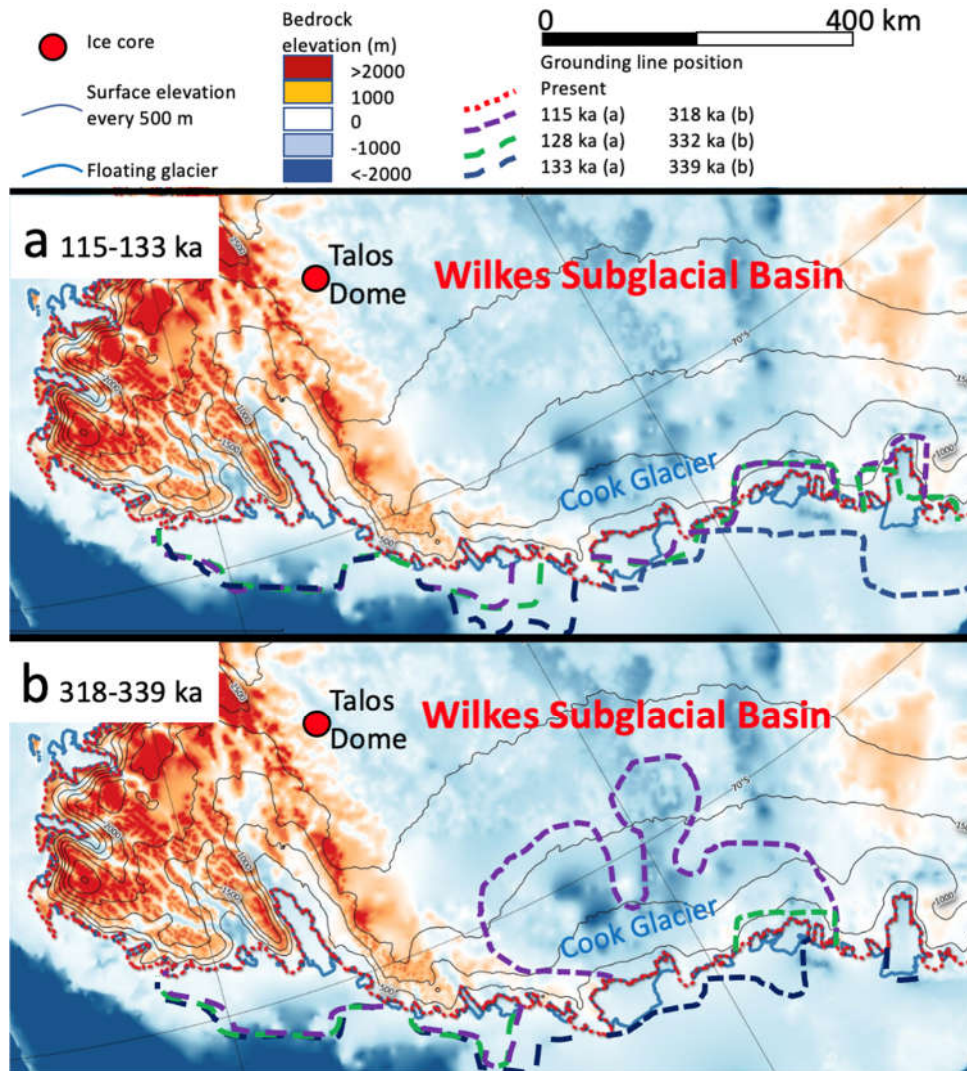
Figure 4.4. Interglacial grounding line retreat of the Wilkes Subglacial Basin ice sheet simulated by the GRISLI GS-5 experiment at three different time intervals at 40 km resolution. a. Grounding line displacement during MIS 5.5 between 115 ka and 133 ka. b. Grounding line displacement during MIS 9.3 between 318 ka and 339 ka. The map shows the subglacial bedrock elevation above sea level (m), the Antarctic ice sheet present-day surface elevation above sea level (m) and the present day grounding line position (Fretwell et al., 2013).

4.2.2.4   Comparison to the U1361A marine sediment core record

The Antarctic ice sheet loses the majority of its mass via iceberg calving and sub-ice-shelf melting (Rignot et al., 2013). Past retreat of the ice shelves and ice sheet in the vicinity of the Wilkes Subglacial Basin is therefore expected to have left geochemical and sedimentological signatures in the nearby marine sediments. The sediment core U1361A (64.41°S, 143.89°E, 3,454 m water depth) (Escutia et al., 2011), recovered from the continental rise adjacent to the Wilkes Subglacial Basin (Figure 1), provides a near-continuous archive of Pliocene to Pleistocene variability of this marine EAIS margin (Cook et al., 2013; Patterson et al., 2014; Wilson et al., 2018). Specific events of iceberg-rafted debris (IBRD) discharge can indicate dynamic ice loss, while Nd isotopes (ε_{Nd}) provide a provenance indicator for changes in subglacial erosion and transport that could reflect ice sheet retreat (Cook et al., 2013; Patterson et al., 2014; Wilson et al., 2018) (Figure 4.4). To enable a direct comparison of the TALDICE

isotopic record and GRISLI simulations with the U1361A record, we refined the original U1361A chronostratigraphy to achieve consistency with the AICC2012 framework (see Methods).

The prominent IBRD and Nd isotope peaks during MIS 5.5 and 9.3 are interpreted as evidence of ice loss from the margins of the Wilkes Subglacial Basin (Wilson et al., 2018). Interestingly, the IBRD peaks, which record transient events of ice discharge and iceberg calving, and the Nd isotope maxima, representing inland erosion, coincide with the onset of the TALDICE $\delta^{18}O$ anomalies at ~125 ka during MIS 5.5 and at ~330 ka during MIS 9.3 (Figure 4.4b and 4.4e). In addition, the duration of the TALDICE isotopic anomalies are consistent with the sustained high Nd isotope values during the later stages of MIS 5.5 and MIS 9.3, suggesting a prolonged interval of inland glacial erosion and relative increase of iceberg calving. Furthermore, the highest IBRD content in the U1361A record (~7.5%) occurred at ~330 ka, indicating a significant ice loss event and potentially a more dynamic Wilkes Subglacial Basin ice sheet during MIS 9.3 in comparison to MIS 5.5, for which the IBRD peak was less pronounced (~2%) (Figure 4.4e). A more dynamic behaviour during MIS 9.3 than MIS 5.5 is also supported by the GRISLI modelling results (Figure 4.4c-d).

In contrast, the interglacial periods of MIS 1 and MIS 7.5 are characterized by only minor IBRD occurrences and more muted Nd isotope maxima in core U1361A (Figure 4.4e), indicating a more stable ice sheet. Similarly, the TALDICE isotopic anomaly is less pronounced at these times (Figure 4.4b), and the GRISLI simulations also indicate a muted response in the Wilkes Subglacial Basin during those interglacials (Table 4.1). As such, evidence from these independent datasets and approaches appears to converge on a consistent picture of the differential response of the ice sheet in the Wilkes Subglacial Basin to the subtly different climate forcing of individual late Pleistocene interglacials.

4.2.3 Discussion

By combining the TALDICE $\delta^{18}O$ record with GRISLI ice sheet model outputs and records from marine sediment core U1361A, we propose that the TALDICE isotopic anomalies during late Pleistocene interglacials reflect a reduction in elevation at Talos Dome arising from accumulation rate changes, ice loss, and grounding line retreat in the Wilkes Subglacial Basin. Our results from the GRISLI GS-5 simulation suggest that even a small increase of the SO sub-shelf melting rate of 5%, which we attribute to the intrusion of warm water at the grounding line depth was enough to trigger significant margin retreat (although not complete collapse) of the ice sheet in the Wilkes Subglacial Basin during the warmest late Pleistocene interglacials. Notably, our simulated Talos Dome elevation changes during MIS 5.5 are consistent with recent studies (Golledge et al., 2021; Sutter et al., 2020), while GRISLI GS-5 depicts a larger retreat at the margin of the Wilkes Subglacial Basin in closer accordance with the U1361A record (Wilson et al., 2018).

Since the SO Polar Front and Subantarctic Front probably shifted polewards during MIS 5.5, the more southerly and warmer Antarctic Circumpolar Current could have induced a dynamic response

in the EAIS sectors with reverse-sloping subglacial basins (Chadwick et al., 2020; Fogwill et al., 2014). A comparable scenario can also be anticipated for MIS 9.3. Interestingly, a new late Pleistocene Subantarctic sea surface temperature reconstruction from the Indian sector of the SO (core DCR-1PC) shows that both MIS 5.5 and MIS 9.3 were characterized by a double warming phase (Shukla et al., 2021). The first warming phase corresponded to the interglacial optimum, which was followed by a cooling phase attributed to feedbacks from the Antarctic Ice Sheet, and then a second late warming phase before the glacial inception (Shukla et al., 2021) (Figure 4.4f). Over time, the two long warming phases probably contributed to the destabilization of the ice shelves and outlet glaciers of the Wilkes Subglacial Basin, leading to inland retreat of the grounding line. Our evidence also points to an ice sheet in the Wilkes Subglacial Basin that was particularly susceptible to local SO warming and/or CDW intrusion during MIS 9.3 (Shukla et al., 2021), which may suggest that the ice sheet remained in a relatively unstable state following the proposed ice sheet collapse during MIS 11 (Blackburn et al., 2020; Wilson et al., 2018).

Finally, sea-level reconstructions for MIS 5.5 and MIS 9.3 are also consistent with our reconstruction of the Wilkes Subglacial Basin ice dynamics during the late Pleistocene. Data from corals and other sea-level proxies indicate a late peak in GMSL during MIS 5.5 at ~119 ka of ~6 to 9 m above present (Dutton et al., 2015; O'Leary et al., 2013). For MIS 9, a stacked GMSL reconstruction based on various proxies indicates a sea-level highstand of ~9 m above modern(Spratt & Lisiecki, 2016). The GS-5 experiment indicates that the grounding line in the Wilkes Subglacial Basin may have retreated by several hundred kilometres during those interglacials, leading to contributions of approximately +0.5 m and +0.9 m to the GMSL increases during MIS 5.5 and MIS 9.3, respectively (Methods). These instabilities of the Wilkes Subglacial Basin ice sheet appear to have been driven mainly by increases in SO temperatures and/or CDW intrusion during past interglacials. Despite the qualitative agreement between the ice core data, marine sediment core proxies, and the ice sheet modelling results, it will be essential to better assess quantitative differences between the data and models, as well as the relative roles of atmospheric and oceanic warming in triggering ice sheet instabilities (Golledge et al., 2017), in order to improve our understanding of EAIS dynamics during past interglacial intervals and on a future warming Earth.

4.2.4 Methods

4.2.4.1 TALDICE $\delta^{18}O$ and δD records

In this study we focus on the oxygen and hydrogen isotopic composition ($\delta^{18}O$) and d-excess ($d = \delta D - 8 \times \delta^{18}O$) new and published profiles measured at high resolution (5 cm) in the TALDICE ice core during interglacials. Here we present the published $\delta^{18}O$ bag resolution profile (1 m) for the Holocene(Stenni et al., 2011), the published profile for MIS 5.5 (Masson Delmotte et al., 2011) and new 5 cm resolution profiles MIS 7.5, and MIS 9.3. For the d-excess, we show the published bag resolution signal (1 m) for MIS 1 (Mezgec et al., 2017) and the new 5cm resolution signal or the oldest interglacials.

We draw data from MIS 1 (0-20 ka) and MIS 5.5 (~115-132 ka) on the AICC2012 age scale (Bazin et al., 2013). The new data for δ^{18}O and *d*-excess during MIS 7.5 (~240-246 ka) and MIS 9.3 (~324-339 ka) are plotted on the TALDICE-deep1 age scale (Crotti et al., 2021).

The 5 cm samples were analysed in Italy (University of Venice) and France (LSCE) using the Cavity Ring Down Spectroscopy (CRDS) technique. Analyses were performed using a Picarro isotope water analyser (L2130-i version for both laboratories). The data were calibrated using a three-point linear calibration with three lab-standards that were themselves calibrated versus Standard Mean Ocean Water (SMOW). Intercomparisons between the two laboratories have been performed over the analysis period. The average precision for the δ^{18}O and δD measurements is 0.1 and 0.7‰, respectively.

In this work we compare δ^{18}O and *d*-excess records from TALDICE and EDC cores (Landais et al., 2021), which are characterized by different temporal resolution, mostly due to differences in the sampling interval, snow accumulation and thinning function at different depth (Table 4.2).

		MIS 1 (0-20 ka)	MIS 5.5 (110-140 ka)	MIS 7.5 (234-252 ka)	MIS 9.3 (320-345 ka)
TALDICE	Sample length (cm)	1 m	5 cm	5 cm	5 cm
	Resolution (years/5 cm)	-	32	95	192
	Resolution (years/m)	24	630	1891	3843
EDC	Sample length (cm)	55 cm	55 cm	55 cm	11 cm
	Resolution(years/sample length)	22	53	116	33
	Resolution (years/m)	40	96	212	301

Table 4.2: Comparison of temporal resolution for TALDICE and EDC δ^{18}O samples during interglacial periods. We calculated the sample resolution based on the original sample length (5 cm for TALDICE, 55 cm or 11 cm for EDC). We also calculated the average temporal resolution for each metre of the core.

4.2.4.2 *Identification of change-points and calculation of anomalies*

To identify differences between the TALDICE and EDC isotopic records, we assessed changes in slope and intercept in the data sets. We first normalized both records (data centred and scaled to have mean 0 and standard deviation 1) and resampled them at the same time step of 200 a. We then searched for changes using the MATLAB task *find change points* with a maximum of 3 or 4 change points (Killick et al., 2012). The software identifies points with changes in slope (derivative) and intercept (Figure 4.5). Isotopic anomalies were then calculated as the differences between values in the resampled record between the two change points (Table 4.1).
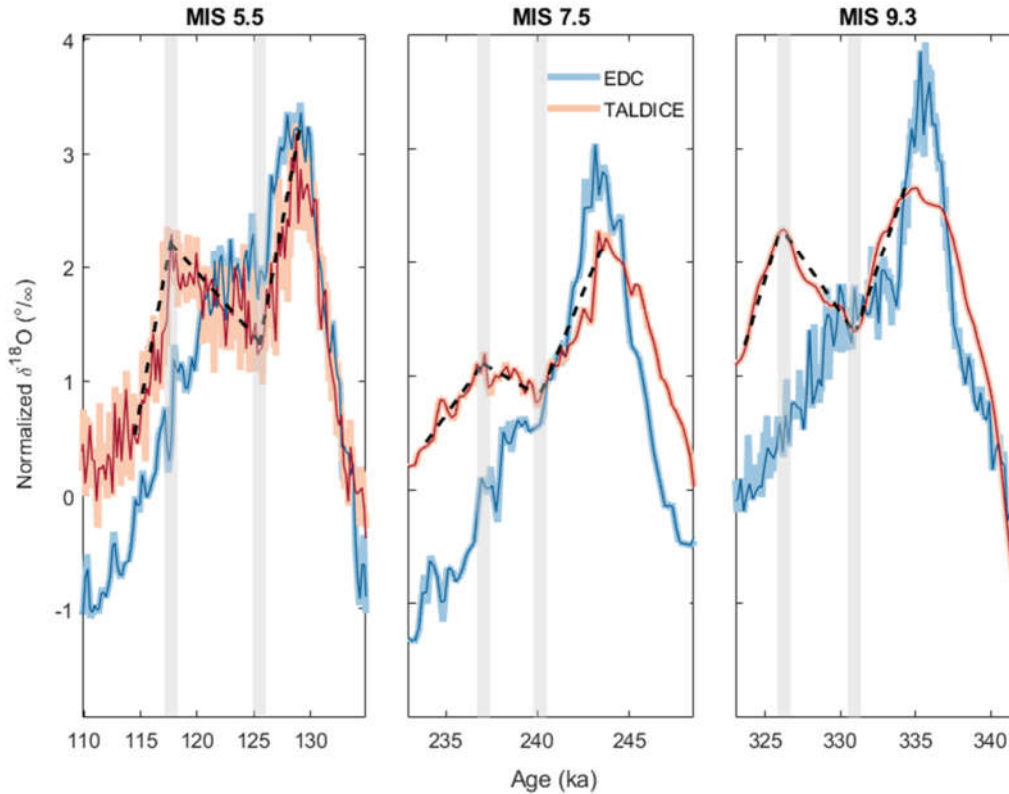
Figure 4.5: Identification of change points and anomalies in the TALDICE ice core in comparison to EDC. Original TALDICE and EDC δ¹⁸O records were normalized (pink and light blue, respectively) and then re-sampled at a 200 years time step (red and dark blue, respectively). Change points in the TALDICE record (grey bars) are identified where the record shows a change in slope (dashed black lines). Anomalies are calculated based on the differences in values in the resampled record between the two change points.

4.2.4.3 Lapse rate calculation for TALDICE

In the modern day, Talos Dome receives 50% of its total precipitation from the west (Southern Indian Ocean), 30% from the east (Ross Sea and Southern Pacific Ocean), and approximately 15% from the interior (Scarchilli et al., 2011). In contrast, at EDC the modern precipitation is mainly from the western Southern Indian Ocean (85%), with a small amount coming from the east via the Ross Sea and Transantarctic Mountains (15%).

The isotopic lapse rate expresses the variation in the oxygen isotopic composition (δ¹⁸O) in permil (‰) for every 100 m change in altitude. Here we calculate the isotopic lapse rate for TALDICE using the ITASE traverse dataset (Magand et al., 2004). We take into account the δ¹⁸O values of snow between GV7 and Talos Dome sites sampled every 5 km and the altitude profile from GV7 site to Talos Dome. This approach seems reasonable, given that the air masses travelling to Talos Dome mainly originate from the Southern Indian Ocean at 60°S and likely follow a similar path to the traverse once they reach Antarctica (Scarchilli et al., 2011). The calculated isotopic lapse rate is -1.35‰/100 m.

4.2.4.4   TALDICE ssNa⁺ fluxes

In this study we show the sea-salt sodium (ssNa$^+$) flux measured in the TALDICE ice core during MIS 1 (1 m resolution) (Mezgec et al., 2017), MIS 5.5 (1cm resolution) (Schüpbach et al., 2013), an new data for MIS 7.5 and MIS 9.3 (8 cm resolution). The concentrations of ssNa$^+$ were measured by classical ion chromatography on discrete samples collected using a melting device connected to an auto-sampler for the MIS 1, MIS 7.5 and MIS 9.3 whereas Continuous Flow Analysis (CFA) was applied for MIS 5.5 samples (Schüpbach et al., 2013). The total deposition ssNa$^+$ flux was calculated multiplying the measured ice concentration of ssNa$^+$ by the reconstructed accumulation rate. The accumulation rates were derived from the AICC2012 age scale (Bazin et al., 2013) for the upper part of TALDICE (until 1438 m depth), while for the deepest part (1438-1578 m) depth accumulation rates were obtained from the TALDICE-deep1 age scale (Crotti et al., 2021).

4.2.4.5   Refined age model for core U1361A

To compare the sedimentological and geochemical records from core U1361A with the TALDICE ice core isotopic records, we needed to define a common chronostratigraphy. The original chronology for the U1361 composite splice (U1361A and U1361B) was based on biostratigraphic and magnetostratigraphic data and one radiocarbon date (Escutia et al., 2011; Tauxe et al., 2012; Wilson et al., 2018). The TALDICE chronology is based on the AICC2012 age scale until ~150 ka (Bazin et al., 2013), built with a multi-site approach including both Greenland and Antarctic ice cores, while for the older part it is based on TALDICE-deep1 chronology (Crotti et al., 2021). Here we use the AICC2012 ice core chronology (Bazin et al., 2013) as a reference curve in order to compare the late Pleistocene sediment core data from U1361A to the TALDICE ice core record. Specifically, we refine the existing U1361A age model through the alignment of barium/aluminium (Ba/Al) ratios from XRF-scanning (Wilson et al., 2018) with the EDC δD record on the AICC2012 age scale. Glacial-interglacial cycles are clearly expressed in the U1361A Ba/Al record, with higher ratios reflecting warmer conditions and reduced sea-ice extent during interglacials (Wilson et al., 2018). As such, and similar to the EDC δD record, the Ba/Al record reflects a combination of local forcing and global climate boundary conditions. We apply a conservative tuning strategy to align the two records, using tie points (derived by visual matching) only at the mid-points of the major glacial terminations I-V, where large and rapid signals are recorded in both U1361A Ba/Al and EDC δD records. Such transitions are likely to be synchronous in the two records, at least at the multi-ka sample resolution of the U1361A marine record, whereas there is greater uncertainty in the exact timing and progression of productivity changes during the steps from interglacial to glacial periods. Over the interval of interest for the present study (i.e. ~100-350 ka), the new age model for core U1361 differs by only 0 to 6 ka compared to the previous age model in which the sedimentation rate was assumed to be constant (Wilson et al., 2018). The temporal resolution of the U1361A record is on the order of several ka for the time period from 0 ka to 345 ka. Specifically, the mean resolution of the record is 5.9 ka for IBRD, 6.5 ka for Nd isotopes, and 3.4 ka for Ba/Al ratios.

4.2.4.6   GRISLI ice sheet model

The GRISLI (Grenoble ice sheet and land ice) model is a large-scale three-dimensional thermomechanical ice sheet model. In this work, we use the GRISLI version 2.0 (Quiquet et al., 2018), which is the latest revision, to model changes of the Antarctic ice sheet between 100 ka and 400 ka, since it is mostly designed for multi-millennial integrations. The model combines an inland ice model with an ice shelf model, extended to the case of ice streams considered as dragging ice shelves (Ritz et al., 2001). The latest release includes a better representation of grounding line migration and a sub-glacial hydrology model. The model uses finite differences on a Cartesian grid at 5 to 40 km resolution depending on the application. Here we use a 40 km grid to take advantage of the model calibration performed in Quiquet et al. (2018). Given its low numerical cost at this resolution, Quiquet et al. (2018) performed an ensemble of 600 simulations to calibrate the mechanical parameters. We use the ensemble member of Tsai et al. (2015) for the formulation of the flux at the grounding line, since it best reproduces the glacial-interglacial transitions. This ensemble member is labelled AN40T213 in Quiquet et al. (2018). Note that, due to the relatively coarse resolution (40 km) applied here, fine-scale structures such as individual ice streams might not be properly represented. The model setup used to perform the transient paleo ice sheet simulations is identical to that used by Quiquet et al. (2018).
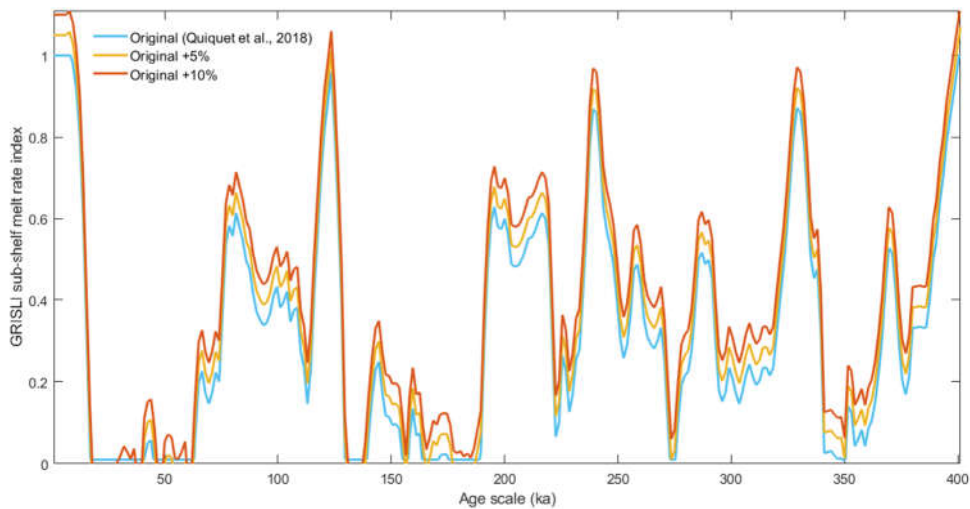
Figure 4.6: Oceanic forcing prescribed in our GRISLI simulations over the past 400 ka. This forcing is used as a percentage change from the present-day sub-shelf melt rate. The original forcing is derived from the North Atlantic benthic temperature reconstruction of Waelbroeck et al. (2002) (blue curve), with the other versions increased by 5% (yellow curve) and by 10% (red curve).

Because there are some slow feedbacks that affect the Antarctic ice sheet (e.g. glacial isostasy, internal temperature), the simulated state of the ice sheet for a given interglacial largely depends on the preceding glacial cycles. For this reason, we performed two different families of sensitivity tests in which we changed the initial state of the Antarctic ice sheet (i.e. glacial or interglacial) at 400 ka.

The oceanic forcing is the main driver for glacial-interglacial grounding line migration. However, since glacial-interglacial ocean temperature changes around Antarctica are poorly constrained, this forcing represents an important source of uncertainty for the ice sheet evolution.

To account for past changes in oceanic forcing, Quiquet et al. (2018) used a paleo-index to modify the present-day sub-shelf melt rates. This index is based on a record of deep water temperature in the North Atlantic Ocean (Waelbroeck et al., 2002), which is assumed to correlate with temperature variations of the waters upwelling in the Southern Ocean, and is therefore applied as a proxy for past Antarctic sub-shelf melt rate changes. We scaled the temperature change so that sub-shelf melting is virtually suppressed during the Last Glacial Maximum (100% reduction but with a minimum melt rate of 1cm/year) but remains unchanged for the present-day. Given that the oceanic forcing represents a large source of uncertainty, we perform sensitivity simulations with the oceanic forcing increased by 5% and by 10% (Figure 4.6). As well as ice thicknesses and elevation at Talos Dome, we calculate the ice volume evolution of the Wilkes Subglacial Basin over the past 400 ka from the GRISLI IS and GS simulation results. The drainage basin boundaries are from IMBIE2, extended offshore for the ISMIP6 project (Nowicki et al., 2016).
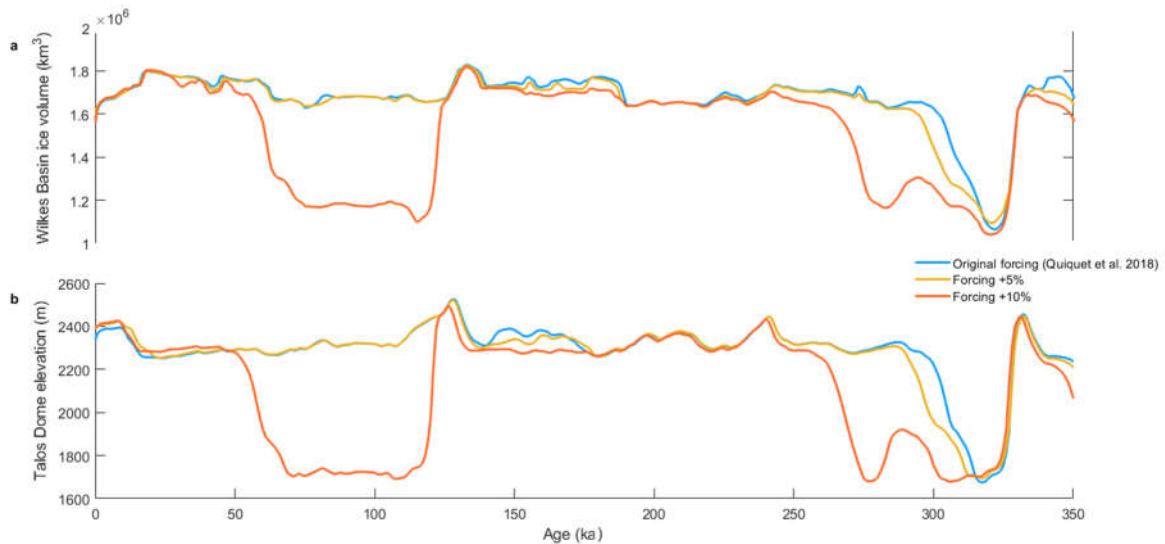
Figure 4.7: GRISLI IS simulations during the past 350 ka. a. Wilkes Subglacial Basin ice volume evolution. b. Talos Dome elevation. We applied the original oceanic forcing from Quiquet et al. (2018) (blue curve), and the original forcing increased by 5% (yellow) and 10% (red).

In Figure 4.7 we show the Wilkes Subglacial Basin ice volume changes and the Talos Dome elevation variations over the past 350 ka for the GRISLI IS simulations. The IS simulations have been disregarded due to the modelled collapse of the Wilkes Subglacial Basin ice sheet during MIS 9.3, which is inconsistent with the TALDICE record. Hence, only the GS simulations are shown in the main paper. We also compute the contribution of the Wilkes Subglacial Basin grounded ice above flotation to GMSL increase during past interglacials for all the GS and IS experiments (Figure 4.8), which was not shown in the main text.
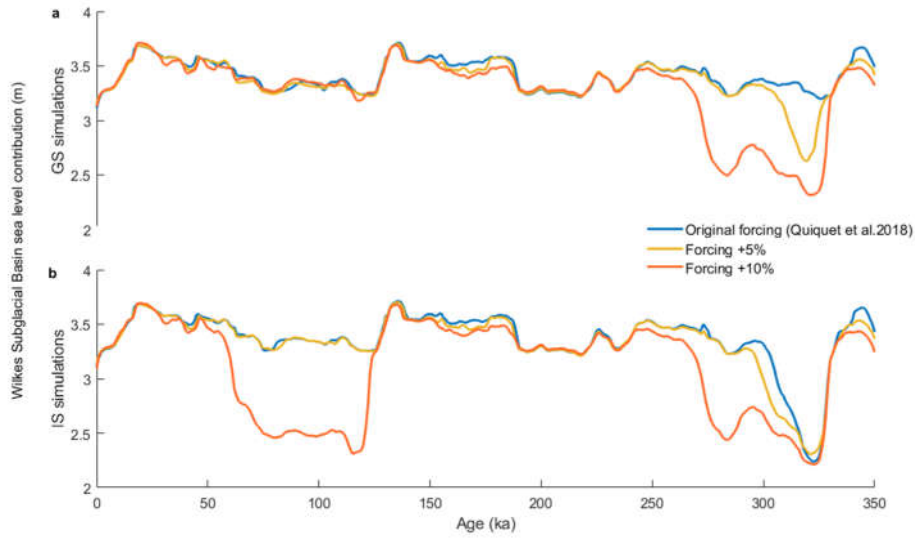
Figure 4.8: Contribution of Wilkes Subglacial Basin grounded ice above flotation to GMSL during the past 350 ka, simulated by the GRISLI model. a. GS experiment. b. IS experiment. We applied the original oceanic forcing from Quiquet et al. (2018) (blue curve), and the original forcing increased by 5% (yellow) and by 10% (red).

4.3   Conclusions

In this manuscript the interpretation of the TALDICE isotopic record during past interglacials (MIS 5.5, 7.5 and 9.3) is presented. The new high-resolution $\delta^{18}O$ record (5 cm resolution) during MIS 7.5 and 9.3 shows a "double-peak" shape, similar to the one observed by Masson Delmotte et al. (2011) during MIS 5.5. Through the comparison of the TALDICE $\delta^{18}O$ data set with d-excess and ssNa$^+$ flux profiles during past interglacials, we infer that this unique isotopic signal is probably caused by temperature changes at Talos Dome site, connected to elevation variations caused by Wilkes Subglacial Basin grounding line migrations.

To better explore this hypothesis, this manuscript presents a multiproxy approach and modelling sensitivity experiments. The comparison between the TALDICE $\delta^{18}O$ data set with d-excess and ssNa$^+$ flux profiles reveals that nor sea-ice variations, nor changes in moisture sources may have generated the isotopic anomaly. The temperature variations due to Talos Dome site elevation changes appear to better explain the isotopic anomalies. To explore deeper this hypothesis, the Talos Dome site elevation changes are computed from the isotopic anomalies and compared with the site elevation variations obtained by 6 sensitivity experiments performed with the GRISLI ice sheet model. The incorporation of these two different approaches reveals that the Talos Dome site has probably undergone elevation variations of 100-400 m order during the past interglacials. In particular, during the MIS 9.3 the Wilkes Subglacial Basin ice sheet appears to have experienced a great margins retreat, which has probably caused an ice thickness variation at Talos Dome of about 400 m. During MIS 5.5, on the other hand, a 100 m elevation changes at Talos Dome might be associated to a combination of Wilkes Subglacial Basin grounding line displacement and variation in snow accumulation rate.

To validate these hypotheses, the modelling sensitivity experiments and the TALDICE isotopic record are matched with the U1361A sediment core record. The ice rafted debris record (IBRD) and the neodymium isotopes signal interestingly show that, during MIS 5.5 and MIS 9.3, the Wilkes Subglacial Basin ice sheet has been subjected to ice discharge events. The major ice discharge events appear to have happened during MIS 9.3 and minor events seems to have characterized the MIS5.5, in agreement with our interpretation. In addition, new sediment core records from the Southern Ocean (Chadwick et al., 2020; Shukla et al., 2021) suggest a double phase ocean warming during interglacials might have contributed to the Wilkes Subglacial Basin ice sheet margin retreat and to the Talos Dome elevation variations. Further efforts would be necessary to better illustrate the past response of the Wilkes Subglacial Basin ice sheet to atmospheric and oceanic warming, in order to predict its behaviour in a future warmer world.

5. <u>Implementation of Argon dating technique</u>

Different techniques can be applied for ice cores dating, but often they require a great amount of ice. Large sample size, as for [81]Kr dating shown in chapter 2 and 3, does not always represent the best solution to date ice cores due to lack of large ice amount and the need for multiple measurements. This chapter focuses on new developments of the Ar dating technique *(copper method)* applied on air trapped in ice cores, which aims at reducing the sample size down to ~65 g, to obtain a reasonable compromise between amount of required ice and dating uncertainty. Then, to validate the new technique, a "classic" *getter method* is applied on neighbouring samples.

5.1 Introduction on Ar dating

5.1.1 Ar isotopes
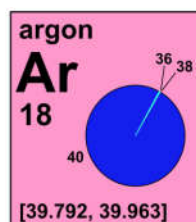
Figure 5.1: Argon and its isotopes (Holden et al., 2018).

The argon is a chemically a noble gas, inert by definition, and constitutes the 0.93% of the atmospheric air. Argon has three natural isotopes with masses 36, 38 and 40. The most abundant Ar isotope in nature is [40]Ar, which makes about the 96% of the total share, followed by two minor isotopes [38]Ar, 4%, and [36]Ar, 2%.

The [40]Ar stable isotope is produced in nature by the radioactive decay of [40]K, which is characterized by half-life of $4.5 \cdot 10^9$ years. The [40]K isotope is contained in the Earth's Upper and Lower Mantle and in the continental crust, when it decays is replaced by the [40]Ar (Allègre et al., 1996).
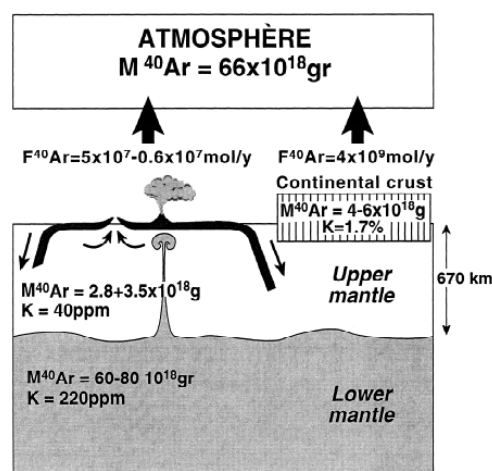
Figure 5.2: Schematic of model distribution of [40]K and [40]Ar in the Earth system (Allègre et al., 1996).

The stable ^{40}Ar accumulates in the solid Earth and then is released in the atmosphere. The outgassing is controlled by several process, from chemical weathering of the continental crust to the direct degassing from the lower and upper mantle by volcanism (Bender et al., 2008). The less abundant isotopes ^{36}Ar and ^{38}Ar are stable and not produced by radioactivity processes. The ^{36}Ar isotope can be produced in tiny amounts by rare reactions such as the β−radioactive decay of ^{36}Cl yielding ^{36}Ar, while ^{38}Ar is produced by cosmic-ray bombardment of rocks and soils and is usually applied to reconstruct erosion rate and exposure history of rocks. Besides such minor productions, the ^{36}Ar and ^{38}Ar isotopes have been produced in stars even before solar system formation and may carry a message about the processes that occurred at and before planetary formation.

5.1.2 Principles of Ar dating

The Ar isotopes in ice cores are measured in air bubbles. The Argon paleo-chronometer is based on the principle that ^{36}Ar and ^{38}Ar isotopes have been essentially constant throughout recent geologic time, but ^{40}Ar has been slowly increasing in the atmosphere as a result of the decay of ^{40}K (Yau et al., 2016).
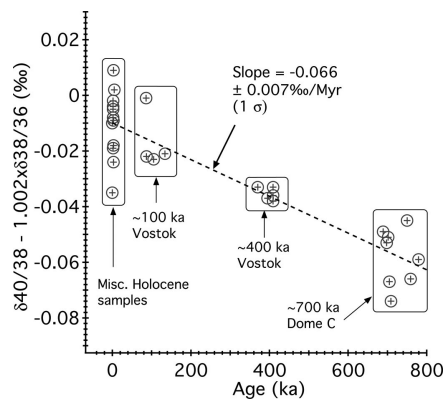
Figure 5.3: $\delta^{40/38}$Ar ratio in Vostok and EDC cores plotted versus age (Bender et al., 2008).

Bender et al. (2008) measured the isotopic ratios $\delta^{40/38}$Ar and $\delta^{38/36}$Ar in Vostok and EDC ice cores in different samples spanning the past 800 ka. They assume that the measured ratios of $\delta^{40/38}$Ar needs to be corrected for gravitational enrichment to best estimate the past $\delta^{40/38}$Ar in the atmosphere at the time it was trapped in ice bubbles, following the equation below:

$$\delta^{40/38}Ar_{paleotmosphere} = \delta^{40/38}Ar_{sample} - 1.002 \cdot \delta^{38/36}Ar_{sample} \qquad (5.1)$$

where 1.002 is the ratio of the mass difference between $^{40/38}$Ar and $^{38/36}$Ar. The latter one is considered to be constant over time.

They observed that the $\delta^{40/38}$Ar paleoatmospheric ratio in air bubbles increases linearly over time, estimating a rate of change of 0.066 ± 0.007‰/Ma (Figure 5.3). The determination of the rate of change in the $\delta^{40/38}$Ar provides a great tool for dating ice cores analysing Argon isotopes trapped in bubbles.

5.1.3 Two Ar extraction methodologies

In the past 20 years several efforts have been performed to develop different Ar extraction methodologies from ice core samples. Two different methods are available for ice and are commonly named copper and getter method.

a) The copper method for Ar, N_2 and Kr isotopes is developed by Kobashi et al. (2008) and based on the getter method presented by Severinghaus et al. (2003). In this method the getter part of the extraction line is substituted by a copper oven. This method preserves the $\delta^{15}N$ it in the sample. Small ice samples (50-100 g) are placed in in glass flasks cooled with ethanol, while extracting the outside air. Once the vacuum is created inside the flask, the sample is melted and the released air passes through a water trap, a CO_2 trap and a copper oven to remove O_2 and other reactive gases. The final gas sample is then collected in a stainless steel metal tube and then analysed with the mass spectrometer. Each sample is analysed in 2 replicates.

b) The getter method, used to extract Ar from bigger ice samples (500-800 g), is based on the initial work of Severinghaus et al. (2003) (Figure 5.4) and the following developments by Bender et al. (2008) and Yau et al.(2016). The ice sample is placed in a cooled chamber to extract all the outside air. Once the chamber is evacuated, the sample is melted and the air extraction and purification process starts. At first the air passes through a cooled water trap, then the air sample is collected in a stainless-steel metal tube. The air in dip tube is injected in the line to remove N_2, O_2 and impurities through the getter. The purified gas sample is then analysed with the mass spectrometer.
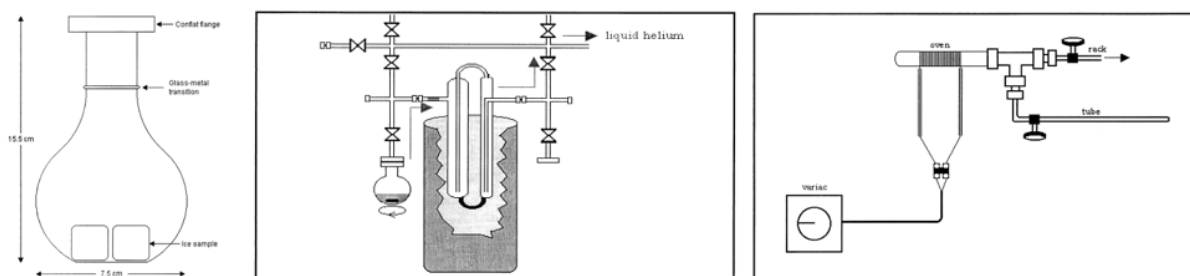
Figure 5.4: The first experimental setup of the getter method for Ar samples (Severinghaus et al., 2003). Left: vacuum extraction flask with ice samples. Middle: water trap at -100°C using water vapour as a carrier gas. Right: oven made by Zr/Al (SAES) getter in a quartz oven to absorb the N_2, O_2, and other reactive gases.

5.1.4 Aim of this chapter

The aim of this chapter consists in illustrating the copper method developed at LSCE, the laboratory protocols and the mass spectrometer setup that have been developed and improved to analyse TALDICE ice samples. Raw data correction and final age calculations are also shown. To evaluate the final dating results obtained with this technique, we use the getter method, which is considered a reliable Ar extraction technique, on bigger TALDICE ice samples. In addition, to provide a final overview of

both techniques a final comparison of the Ar dating results and the TALDICE AICC2012 (Bazin et al., 2013) and TALDICE deep1 age scales (Crotti et al., 2021) is presented.

5.2 The copper method at LSCE

In this section we show the developments applied on copper method for Ar dating. The aim of those improvements is to reduce the sample size down to ~65 g (per replicate) while achieving a sufficient precision to perform the Ar dating. Here the air extraction and purification protocol, the details of the mass spectrometer analysis and the data treatment procedure are shown. The age calculation of the analysed samples and the comparison with the TALDICE published chronologies are also displayed.

5.2.1 Analytical methods

5.2.1.1 Air samples preparation

The analysis of the isotopic composition of modern air is essential for this technique. The air analysis results are used during the beginning of the line testing campaign to assess the reproducibility of the purification technique and of the mass spectrometry analysis methodology. In addition, air values are necessary to normalize to the ice data with respect to atmosphere (Severinghaus et al., 2003). While carrying on ice samples campaign analysis, 2 air samples are usually processed one day per week. The modern (outside) air is stored in a glass bottle attached to the extraction line. The bottle is refilled with new outside air when necessary (Figure 5.5). The bottle is taken on the rooftop of the LSCE, where the air is well mixed and far from polluting sources, and is filled with outside air with the help of a tubing system attached to a pump. As a good practice, the whole system is not exposed to direct sunlight. The water in the air is removed with the use of a trap placed in an ethanol and cooled with liquid N_2 at the temperature of -100°C. The filling procedure takes 10 minutes, then the bottle is sealed, moved to the lab and attached to the line.
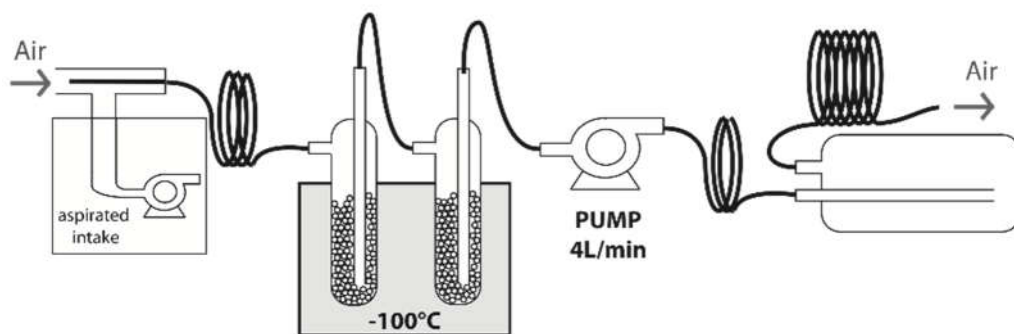
Figure 5.5: External air sampling setup at LSCE (courtesy of A. Orsi).

5.2.1.2 Air samples purification and transfer protocol

The wet extraction line at LSCE is a vacuum system made of stainless steel tubing, glass traps and an oven filled with copper wool. An aliquot from the air bottle is transferred in the line and the flux is manually regulated by stainless steel bellows sealed valves (SS-4H Swagelok valves) and one flux

controller spherical stem stainless steel bellow sealed valve (SS-4WT Swagelok, valve 10) (Figures 5.6 and 5.7). The pressure is continuously checked using a 10 Torr baratron gauge and a 1 Torr baratron gauge. The passage of the sample through the line allows to remove components and gases that are not needed for Ar dating. In particular, CO_2 is removed thanks to 2 traps immerged in liquid N_2 at the temperature of -195°C. The O_2 in the sample is then removed by an oven made by a heating ceramic cylinder filled with copper wool. When the copper is heated, it reacts with O_2 in the line and oxidizes, trapping the molecule. After the purification the air sample is collected in a stainless-steel sample holder (dip tube) placed inside a liquid He tank at the temperature of -270°C. The line is evacuated before and after the conclusion of the air transfer and purification procedure thanks to 2 pumps (fore vacuum pump and turbo pump), to guarantee the lack of external air contamination.
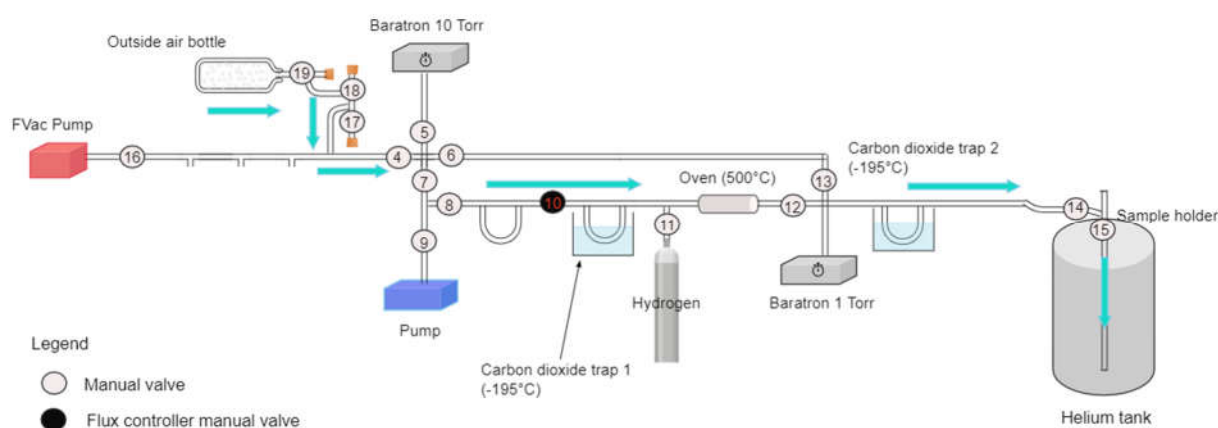
Figure 5.6: The copper method setup for air samples at LSCE.

The extraction procedure follows a protocol to guarantee the quality and reproducibility of the measurements:

i.   The oven is turned on and set at the temperature of 500°C early in the morning. It needs about 1h to reach the desire temperature and to completely degas.

ii.   The dip tube, evacuated during the night, is cooled in the liquid N_2 tank for 5 min before being inserted in the liquid He tank. At the top of the tube 5 cm margin are left to lower the tube later.

iii. The oven is isolated closing the surrounding valves (4, 8, 12) to keep it clean and avoid contamination from laboratory air.

iv.   The dip tube is connected to the line through the flexible tube opening the valves 14 and 13. As such connection introduces laboratory air in the line, valves 6, 7 and 9 towards the pump are open to remove the air. When the pressure inside the line reaches the value of 0.01 mbar, valves 4, 8, 12 and 16 are opened to evacuate all the line for 10 min. The air bottle valve (17) and the dip tube valve (15) are kept close at this stage.

v.   At the end of the 10 min, 2 dewars are filled with liquid N_2 at -195°C and placed below the CO_2 traps.

vi.   Valve 9 is closed to check if there are leaks in the line. If the pressure does not increase more than $1 \cdot 10^{-4}$ per min, no relevant leaks can be detected.

vii.   An aliquot of external air stored in the bottle is prepared. Valve 18 is opened and then valve 19 connected to the bottle is opened for 5 s and then closed. Valve 18 is closed again to isolate the aliquot.

viii.   Now the line is ready to proceed with air aliquot transfer. Valve 9 is closed with the oven bypass valves (6 and 13) and the flux controller valve (10).

ix.   To start the transfer, valve 10 is slowly opened and the dip tube valve (15) is opened soon after. The air flux that goes from the aliquot flask to the dip tube is manually controlled opening slowly valve 10 and keeping the pressure rising constantly without exceeding 0.5 mbar threshold until valve 10 is fully opened. It usually takes about from 5 to 10 min. The dewars need to be refilled every 10 min during the whole transfer, which takes 40 min.

x.   5 min after, valve 10 is fully opened and the dip tube is lowered in the helium tank.

xi.   40 min after the beginning of the transfer, the pressure is checked and when it reaches the value of 0 mbar the transfer is over. Valve 15 is closed to seal the air sample in the dip tube and the residual pressure is noted in the lab notebook. The residual pressure has to be lower than $0.2 \cdot 10^{-3}$ mbar to assure that the whole sample has been transferred, then valve 9 to the pump can be opened. If the pressure increases after valve 15 closure, the sample transfer is probably not completed. In this case valve 15 need to be opened again until the transfer is completed and the residual pressure is below $0.2 \cdot 10^{-3}$ mbar.

xii.   Valves 10, 12, 4 and 8 are closed to isolate the oven and the other portion of the line that need to avoid contamination with outside air. The dewar below CO_2 trap 2 can be removed and valve 14 is closed.

xiii.   As the first sample transfer procedure is over, the second dip tube can be cooled in the liquid N_2 tank for 5 min when the first sample holder is removed from the He tank.

xiv.   Once the second dip tube is placed in the He tank, it is connected to the line through the flexible tube opening valve 14. When the pressure reaches values below 0.01 mbar, all the valves are opened to vacuum the line for 10 min before starting the transfer of the second air sample.

xv.   When all the samples are transferred, the copper wool needs to be regenerated for the following lab day. Valves 4, 14 and 9 need to be closed to let H_2 react with the copper. A little amount of H_2, less than 10 mbar, is injected in the line opening valve 11 while the oven is still at the temperature of 500°C. The H_2 reacts with CuO formed on the surface of the copper wool, which assumes a brown colour. CuO is reduced by H_2, H_2O is released and captured by trap 1, which is refilled with fresh liquid N_2 every 10 minutes. The H_2 is let to react with the copper for at least 10 minutes. When the copper wool colour turns to pink again, the oven regeneration is completed. If the copper wool colour is not pink, additional H_2 needs to be injected in the line.

xvi.   When the pressure diminishes, the pump valve 9 is opened to flush the residual H_2.

xvii. The dewar below the second CO_2 trap is removed and all the line valves are opened, including the valves 18 and 17 to let the bottle connection clean overnight. Three dip tubes are connected to the line and evacuated all night long to be ready for the following day.
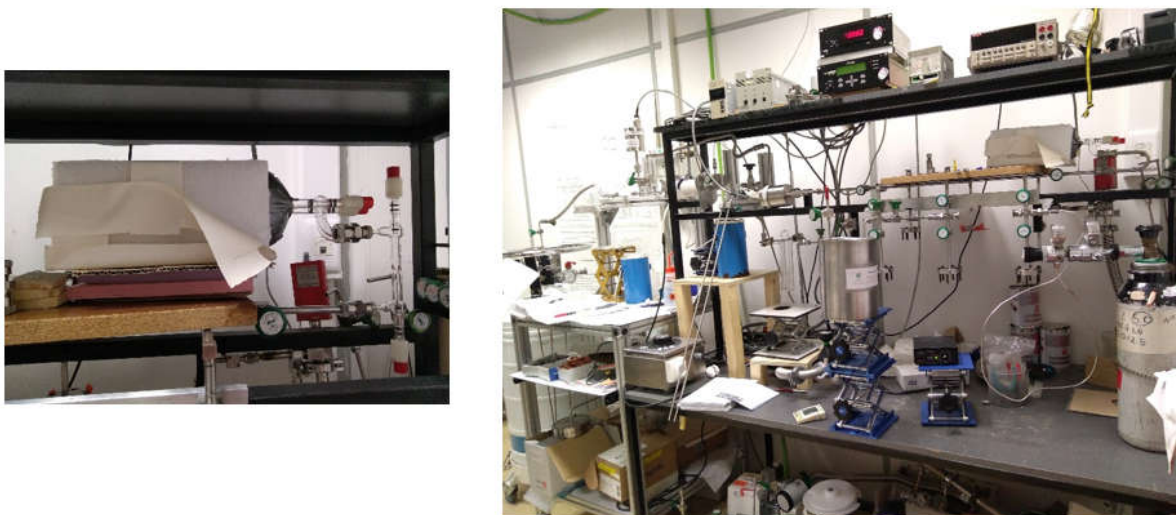
Figure 5.7: Left: External air bottle attached to the line. Right: Extraction line setup of the copper method when performing air transfer.

5.2.1.3 Ice samples preparation in the cold room

Every day the ice samples need to be prepared in the cold room at -20°C for the analysis. Glass vessels and stir bars that have been placed overnight in the freezer are carried in the cold room. In the cold room ice samples are shaved with a ceramic knife to remove the external 3-5 mm layer which could be affected by atmospheric air contamination. Ice is also inspected in order to remove cracks and melted layers which could modify the composition of the air trapped in the ice. Each ice sample is then split in two replicates of ~65 g each (Table 5.1). Each replica is then cut in small pieces to fit in the glass vessel. A stir bar is also inserted in each flask.

Figure 5.8: Ice samples for Ar dating performed with copper method. Left. Ice weighting in the cold room. Right. Ice in the glass flask ready to be evacuated.

Top depth (m)	Bottom depth (m)	Weight (g)	Total weight (g)
218	218.175	63.7	
218	218.175	69.5	133.2
442	442.18	76	
442	442.18	76.5	152.5
545	545.18	63	
545	545.18	66.3	129.3
1356.05	1356.25	71.8	
1356.05	1356.25	69.7	141.5
1363.05	1363.25	66.7	
1363.05	1363.25	68.1	134.8
1372.05	1372.25	63	
1372.05	1372.25	61.5	124.5
1443.05	1443.25	68.3	
1443.05	1443.25	68.6	136.9
1491.05	1491.25	64.1	
1491.05	1491.25	64.4	128.5
1499.05	1499.25	65.8	
1499.05	1499.25	58.9	124.7
1548.1	1548.25	69.3	
1548.1	1548.25	64.9	134.2
1566.05	1566.25	58.9	
1566.05	1566.25	58.5	117.4
1579.05	1579.25	54.6	
1579.05	1579.25	58.3	112.9
1591.05	1591.25	65.5	
1591.05	1591.25	64.7	130.2
1607.05	1607.25	64.5	
1607.05	1607.25	70.5	135
1611.05	1611.25	56.7	
1611.05	1611.25	59.6	116.3

Table 5.1: TALDICE samples extracted with the copper method. The weight refers to the weight of each replicate after shaving, while the total weight indicates the weight of the two replicates.

5.2.1.4 Ice samples purification and transfer protocol

The extraction line follows the same setup as the one of the air samples with two main changes. The first consists in the presence of 2 or 3 vessels installed on the line containing ice samples and the placement of a dewar containing ethanol cooled with liquid N_2.

The extraction and the purification procedures follow the protocol described here:

i. The oven is turned on at the temperature of 500°C and is let warm during the samples preparation in the cold room.

ii. Ice samples are shaved and cut in the cold room as described above and placed in the glass flasks. Vessels are carried in the lab inside a cooled box.

iii. The vessels are connected to the line below valves 1, 2 and 3 (Figure 5.9). Before the vessels connection, dewars filled with ethanol at the temperature of -25°C (not colder than -30°C) are placed below each vessel to keep them cool and avoid ice melting during the evacuation.

iv. A new copper gasket is placed on each vessel. To mount the flasks on the line, the upper part of the vessels needs to be properly mated with the flange and then bolts are tightened gradually with the help of a wrench until they are completely locked. Then ethanol levels in the dewars are checked and adjusted to properly cover the ice.

v. When the vessels are all properly mounted, the main connections to the line (valves 6 and 8) are closed to isolate the clean part of the line and valve 9 and the black valve close to the pump are closed.

vi. At this stage the vessels need to be evacuated to remove the external air. The valve 1 to the first vessel is opened and then the valve 16 is slowly opened to remove most of the air with the help of the high vacuum pump (FVac pump) until the baratron show values less than 1 Torr. Valve 1 is closed and the same procedure is repeated for the other vessels. Then valve 16 is closed.

vii. When all the vessels are evacuated with the high vacuum pump, all the vessels valves (1, 2 and 3) are opened again with the valve 9 and the black valve to the pump.

viii. The vessels are evacuated for 10 min and then the vapour pressure over ice is measured. The vessel valves, except one, and the valve 9 are closed. The pressure shown on the baratron is noted (it should fall in the range between 0.500 and 1.000 mbar) and the temperature of the ethanol should be around -25°C, and not higher than -15°C. Otherwise the ethanol needs to be cooled with liquid N_2. If the pressure is higher or keeps increasing there might be a leak. Bolts need to be tightened in this case.

ix. After the measurement of the vapour pressure over ice, all the vessels' valves are opened (valve 9 as well). The vessels are evacuated for another 20 min. When 20 min are elapsed the vessel valves are closed.

x. The dewar below the first sample is removed and the sample is let to melt with the help of a small amount of lukewarm water placed below the sample. During the melting, the line needs

to be prepared for the transfer and purification. An evacuated dip tube is cooled for 5 min in the liquid N_2. The clean portion of the line needs to be kept as it is, so valves 4, 8, 12 are closed. The dip tube is inserted in the He tank and is connected to the line opening valves 14, 13 and 6, then the flexible tube connection is evacuated for 10 min opening valve 9 to the pump.

xi.   In the meantime, the water trap is prepared adding liquid N_2 to -20°C cold ethanol until the temperature of -100°C is reached. The dewar is placed below the water trap (trap 1).

xii.   When 10 min are elapsed, 2 dewars are filled with liquid N_2 and placed below the CO_2 traps.

xiii.   When some small pieces of ice are left in the vessel, the transfer can start. Is important that the water temperature is around 0°C at the beginning of the transfer and it never exceeds the room temperature (~21°C). In the meantime, dewars with N_2 need to be refilled every 10 mins.

xiv.   The line is prepared for the transfer. The magnetic stirrer is turned on and valves 9,10, 6 and 13 are closed. The vessel valve (1) and the dip tube valve (15) are opened.

xv.   To start the transfer, the flux controller valve (10) is opened slowly to let the pressure increase gently in the line and to not exceed 0.5000 mbar until the valve is fully opened. It usually takes from 10 to 15 min. The CO_2 traps need to be refilled every 10 min and the water trap temperature has to be kept below -100°C.

xvi.   After 5 min from the beginning of the transfer, the dip tube is lowered in the He tank. The transfer should take from 40 to 50 min and is ended when the pressure in the line is equal to 0.000 mbar.

xvii.   At the end of the transfer, the stirrer is turned off and the vessel valve (1) and dip tube valve are closed with valves 4, 8 and 12.

xviii.   The CO_2 trap is removed and the connection with the dip tube (valve 14) is closed and the dip tube is extracted from the He tank.

xix.   A new dip tube is cooled in the liquid N_2 tank for 5 min and then inserted in the He tank and connected to the line with the flexible tube. Valves 14, 13 and 6 are opened and the line is evacuated for 10 min.

xx.   To transfer the second sample, the whole procedure needs to be repeated from point vi.

xxi.   At the end of the lab day, the vessels are dismounted, cleaned and dried in the oven to be ready for the following day.

xxii.   The copper wool is regenerated following the procedure described in Section 5.2.1.2, the water trap is dismounted during the regeneration (with valves 8 and 10 closed) and substituted with a dry one.

xxiii.   The CO_2 trap is removed and the dip tubes are connected to the line. All the valves are opened and the line and the dip tubes are evacuated overnight.
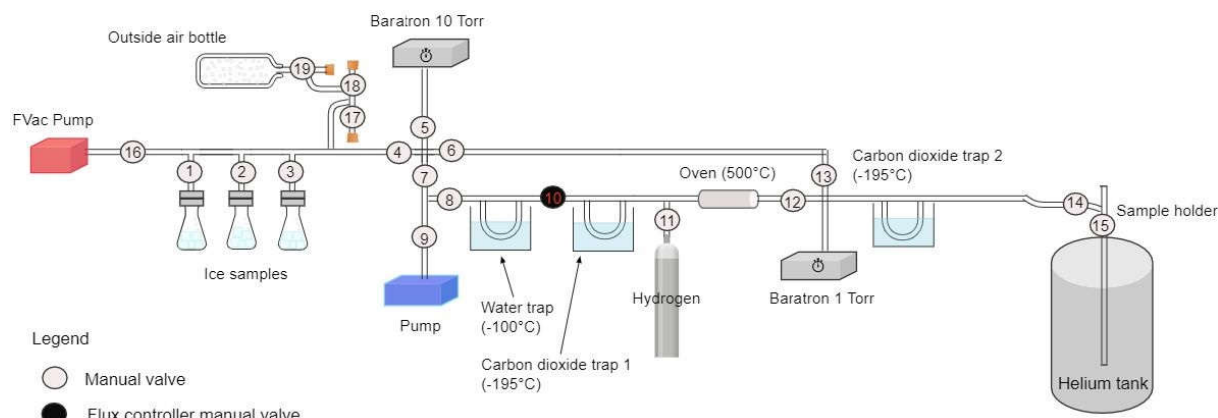
Figure 5.9: The copper method line setup for ice samples at LSCE.

5.2.2 Mass spectrometer analysis

The gas samples in the dip tubes are analysed, after the transfer and purification with the mass spectrometer.

5.2.2.1 The mass spectrometer

The analyses are performed on a dual inlet Thermo Fischer Scientific 253 Plus. The dip tube containing the sample is directly connected to one of the inlets, while the working standard is attached on the other inlet. The mass spectrometer is equipped with 10 cups allowing the analysis of Ar, N_2, Kr and O_2 isotopes for the mass over charge ratios m/z = 28, 29, 32, 33, 34, 36, 38, 40, 82, 84 and 86. The basics regarding the general principles of operation of a mass spectrometer are described in Chapter 2. Some changes are introduced in the mass spectrometer set-up at the beginning of the analysis campaign (modern air samples), to improve in the quality of the analysis.

The analytical precision of multi-collection mass spectrometry applied to analyse small ion beams is limited by the detection system (amplifiers). Ion beams in isotope analyses can be small if the abundance of the isotope measured is low or because the amount of sample is low (Koornneef et al., 2014). To increase the amplification of the signal, precision and accuracy for Ar and N_2 isotopes analysis while decreasing the ice sample size, we substituted the default 10^{11} Ohm resistors with high 10^{12} and 10^{13} Ohm resistors to design the 2020 Configuration (Table 5.2). Before performing the analysis, we modified the resistors configuration moving high 10^{12} and 10^{13} Ohm resistors to the amplifier housing channel of Ar and N_2 (2020 configuration). Those changes improve the amplification of the signal since, for example, the 10^{12} Ohm amplifiers have a 3 times higher signal to noise ratio compared to the default 10^{11} Ohm resistors (Wieser & Schwieters, 2005).
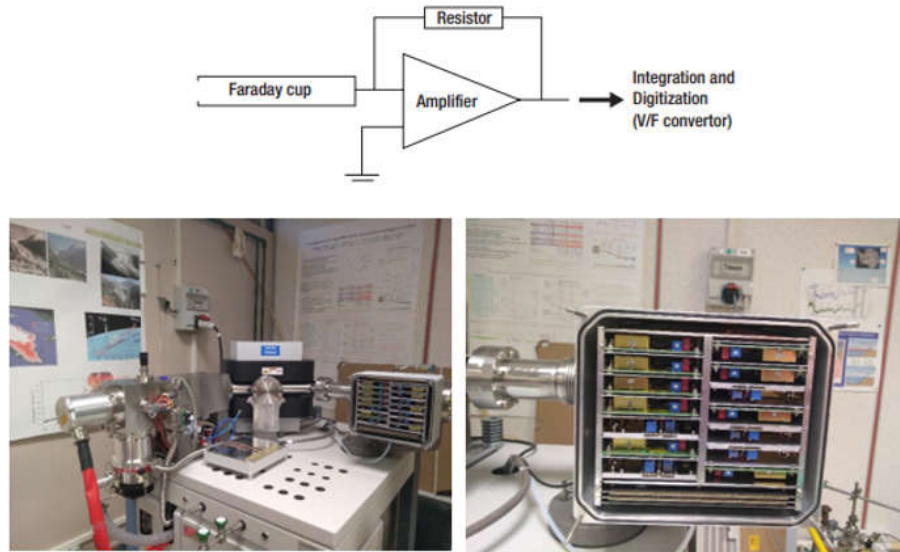
Figure 5.10: Top. Schematic representation of the Faraday cup detection system. The Faraday cup is connected to electrical ground via an amplifier that is equipped with a resistor. The amplified signal is converted to volts by a V/F converter. Bottom. Amplifier housing of Thermo Fischer Scientific 253 Plus at LSCE.

Amplifier housing channel	CUP	Gases/Masses	2018 config. (Ω)	2019 config. (Ω)	2020 config. (Ω)
1	1	O_2 32 N_2 28	$3 \cdot 10^8$	$3 \cdot 10^8$	$3 \cdot 10^8$
2a	2	Ar 36	$1 \cdot 10^{11}$	$1 \cdot 10^{11}$	$\underline{1 \cdot 10^{12}}$
2b		-	Not used	$1 \cdot 10^{12}$	$1 \cdot 10^{12}$
3a	3	N_2 33	$3 \cdot 10^{11}$	$1 \cdot 10^{13}$	$\underline{3 \cdot 10^{11}}$
3b	-	-	Not used	$1 \cdot 10^{12}$	$1 \cdot 10^{12}$
4a	4	Ar 38	$3 \cdot 10^{11}$	$1 \cdot 10^{12}$	$\underline{1 \cdot 10^{13}}$
4b		Kr 82 N_2 29	$3 \cdot 10^{10}$	$3 \cdot 10^{10}$	$3 \cdot 10^{10}$
5	5	Kr 84 Xe 132	$1 \cdot 10^{13}$	$1 \cdot 10^{13}$	$1 \cdot 10^{13}$
6a	6	Ar monitor	$1 \cdot 10^{13}$	$1 \cdot 10^{13}$	$1 \cdot 10^{13}$
6b		Xe 129 O_2 34	$1 \cdot 10^{11}$	$1 \cdot 10^{12}$	$\underline{1 \cdot 10^{11}}$
7a	7	Ar 40	$1 \cdot 10^{13}$	$1 \cdot 10^9$	$\underline{1 \cdot 10^{13}}$
7b		Kr 86	$3 \cdot 10^8$	$1 \cdot 10^{12}$	$\underline{3 \cdot 10^9}$
8a	8	Xe 136	$1 \cdot 10^{13}$	$1 \cdot 10^{13}$	$1 \cdot 10^{13}$
8b		-	Not used	$1 \cdot 10^{13}$	$1 \cdot 10^{12}$

Table 5.2: Resistors configuration changes performed on Thermo Fischer Scientific 253 Plus. The configuration 2020 is the one applied to analyse TALDICE samples with the copper method. Changed resistors in 2020 configuration are underlined in black.

5.2.2.2 Sample introduction

After the air transfer is completed, the dip tube containing the gas sample is connected to the mass spectrometer with ultratorr fittings. The mass spectrometer has two inlet bellows to allow the alternative introduction of standard and sample. The N_2-Ar-Kr standard is prepared in the laboratory with roughly air composition, and its exact calibration will be performed by measuring modern air samples, as modern air is our ultimate reference.
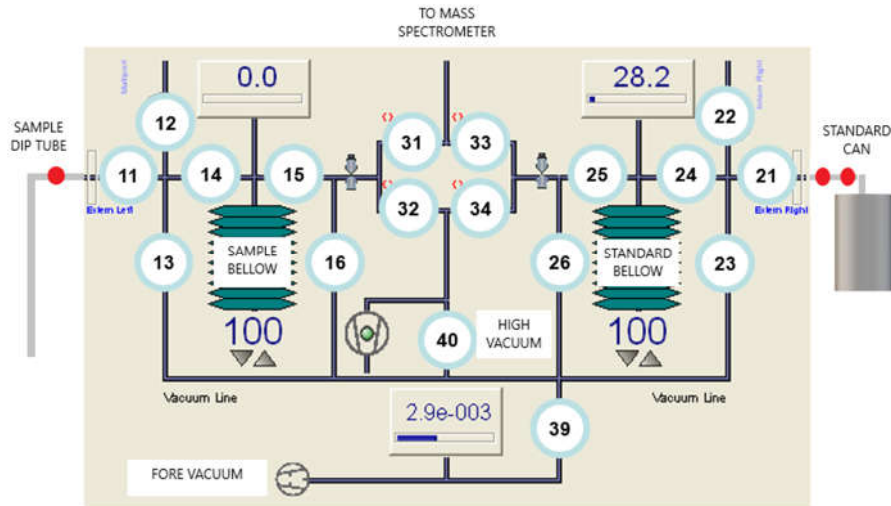
Figure 5.11: Scheme of the dual inlet system on Isodat interface.

Once the dip tube and the standard are connected, the dual inlet system (Figure 5.11) is evacuated at least for 10 min and the bellows need to be completely open. The control of the valves to introduce the sample and the standard is performed by the user through the Isodat software interface. After opening the valve on the dip tube manually, the sample is introduced in the left bellow after closing valves 13, 16 and 12 and let to equilibrate for 5 min. On the right side, a standard aliquot is let to equilibrate on the space between the two valves on the standard can arm, and then is introduced in the right bellow and let to again equilibrate for 5 min. The gas pressure on both sides is noted and then the bellows volume is adjusted to ~100 mbar to help the automatic adjustment. The mass spectrometer is ready to start the analysis.

5.2.2.3 Analysis sequence

The mass spectrometer measures the isotopic ratios of $\delta^{40/36}Ar$, $\delta^{38/36}Ar$, $\delta^{40/38}Ar$, $\delta^{15}N$ and the elemental ratios $^{36}Ar/^{28}N_2$, $^{84}Kr/^{36}Ar$ and $^{32}O_2/^{36}Ar$. The mass spectrometer analysis follows a sequence provided by the user. For this thesis, the used sequence is displayed in Figure 5.12. The sequence consists in 31 lines, called blocks. Each block starts with a peak centre during which the ion beam is adjusted in the centre of the cup by the electric field, a background measurement and a bellow adjustment. The gas contained in the standard bellow is injected into the source for 10 s of stabilization and 16s of integration. An identic injection is then performed from the sample side. The standard-sample cycle injection and measurement is repeated for 10 times and the raw delta value is computed by the mass spectrometer. Each block analysis takes about 12 minutes to complete. The raw isotopic delta value is computed for each block as following:

$$\delta^{n/m}A = \frac{\left(\frac{n_A}{m_A}\right)_{sample\ i}}{\frac{0.5 \cdot {}^{n}A_{standard\ i-1} + 0.5 \cdot {}^{n}A_{standard\ i+1}}{0.5 \cdot {}^{m}A_{standard\ i-1} + 0.5 \cdot {}^{m}A_{standard\ i+1}}} \qquad (5.2)$$

Where $^{n/m}A$ is the selected isotope and i is the number of integrations. The measured delta value of a single integration is averaged on the previous and following integration.

To analyse the elemental ratios, the magnet needs to change its parameters in order to measure the elements. At first, a peak centre is performed and the mass spectrometer counts the first element in the sample and in the standard. Then the magnet parameters are changed to perform the peak centre and the second element in the sample and in the standard is counted. Each block of peak jump consists in 4 measurements for each element. The final sequence is then composed of 5 blocks of Ar isotopes analysis, 3 blocks for N_2 isotopes and 3 peak jump blocks for $^{36}Ar/^{28}N_2$, $^{84}Kr/^{36}Ar$ and $^{32}O_2/^{36}Ar$. This sequence represents the regular one for day-time analysis as it takes about 4 hours to complete. The complete sequence, usually used for night-time analysis, includes Pressure Imbalance Slope (PIS) blocks for Ar, N_2, $^{36}Ar/^{28}N_2$, $^{84}Kr/^{36}Ar$. Each PIS block is repeated 5 times with different level of pressure imbalance between the sample and standard bellows.

Figure 5.12: Complete analysis sequence applied to measure the TALDICE samples to perform the Ar dating with the copper method.

5.2.3 Data correction and calibration

Raw data need to be corrected for several processes that influence the isotopic ratio during the mass spectrometer analysis. In this section all the applied corrections are described in association with the improvements of the data set quality. The TALDICE samples were analysed in two different campaigns, the first one was followed by the second one after several months. The mass spectrometer

was turned off for several weeks between the first and the second analysis campaign, causing the change of several parameters in the instrument.

5.2.3.1 Background correction

During the analysis campaign a drift is noticed while performing the high voltage scan on external air and standard samples on the mass 38 (Figure 5.13). The background is not flat but affected by a slope (in the red rectangle), which might influence the final delta Ar results for ice samples. Failure to properly correct for this dynamical background might create significant errors in final isotope abundances, thus it essential to carefully monitor and correct for this effect (Bernasconi et al., 2013). For this reason, the correction for the background effect is the first correction performed on the data (both air and ice) and aims at removing this artifact produced by the mass spectrometer.
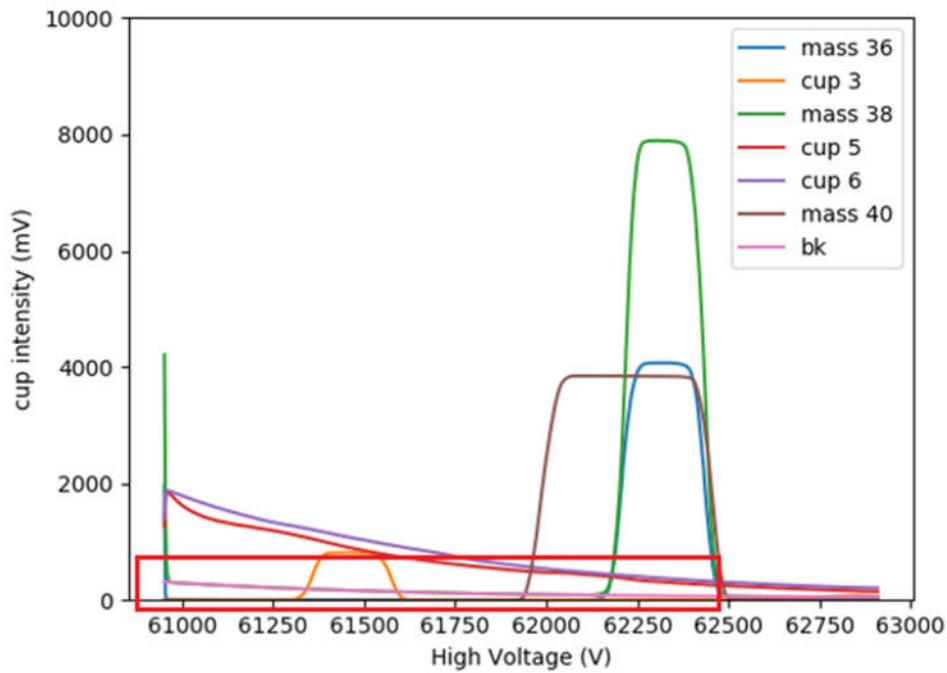
Figure 5.13: HV scan of an air sample. The mass 38 (green curve) is affected by a drift in the background (pink curve 'bk' in the red rectangle).

This background (*bk*, pink line in Figure 5.13) is related to the intensity measured on neighbouring cup 5 or cup 6 through a linear regression of all of the scans collected over several weeks for the measurements of modern air samples and the air standard.

The background effect is computed by the following equations for cups 5 and 6:

$$Bk5 = a_5 \cdot I_{cup\ 5} + b_5 \tag{5.3}$$

$$Bk6 = a_6 \cdot I_{cup\ 6} + b_6 \tag{5.4}$$

Where Bk5 and Bk6 are the background computed respectively for cup5 and cup6, *a* and *b* are the slope and the intercept of the background for each cup and *I* is the intensity measured by each cup. Once the

parameters of equation are found (slope and intercept), they are applied to correct the ice samples raw data for this effect (Table 5.3). The background correction is performed for the mass 38 using both equations for cup 5 and cup 6. In Figure 5.14 we show the background equations for both cups and for the two air samples series.
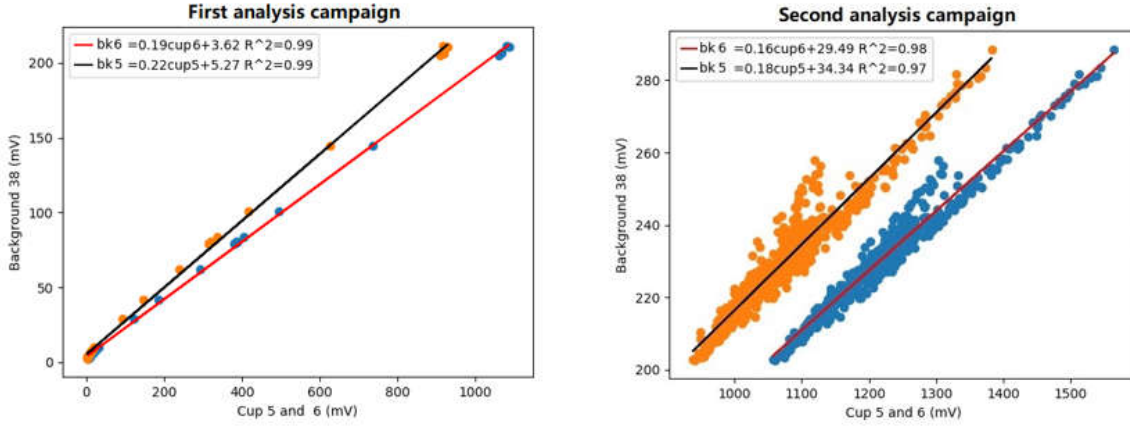
Figure 5.14: Correlation between the cup 5 and cup 6 signal and the background signal for the first and second set of air samples. The equations of the background corrections for both cups are reported for cup 5 and cup 6.

	Cup 5 slope	Cup 5 intercept	Cup 6 slope	Cup 6 intercept
First analysis set	0.22	5.27	0.19	3.62
Second analysis set	0.18	34.34	0.16	29.49

Table 5.3: Cup 5 and cup 6 slopes and intercept values obtained from the linear regression of the background values for the first and second measurements campaigns.

The quality of the correction for both cup 5 and 6 is assessed by looking at the residual of the determination of the background with the above equations:

$$R_{bk5} = bk_{measured} - (a_5 \cdot I_{cup\ 5} + b_5) \tag{5.5}$$

$$R_{bk6} = bk_{measured} - (a_5 \cdot I_{cup\ 6} + b_6) \tag{5.6}$$

Where bk$_{measured}$ is the intensity of the measured background by the mass spectrometer, when a scan is performed (e.g. Figure 5.13). The residuals calculated for both cup 5 and cup 6 are reported in Figure 5.15 and the quality of the correction is assessed by looking at the residuals calculated with the equations 5.5 and 5.6 (Figure 5.15). We choose to correct the raw data for the background measured by cup 6 as it minimizes the residuals. The correction for the background effect is finally applied on the mass 38 intensity subtracting the background of cup 6 to the raw intensity as following:

$$I_{38} = I_{38\ raw} - Bk6 \tag{5.7}$$

Where I_{38} is the intensity for the mass 38 corrected for the background effect and $I_{38\ raw}$ is the raw intensity.
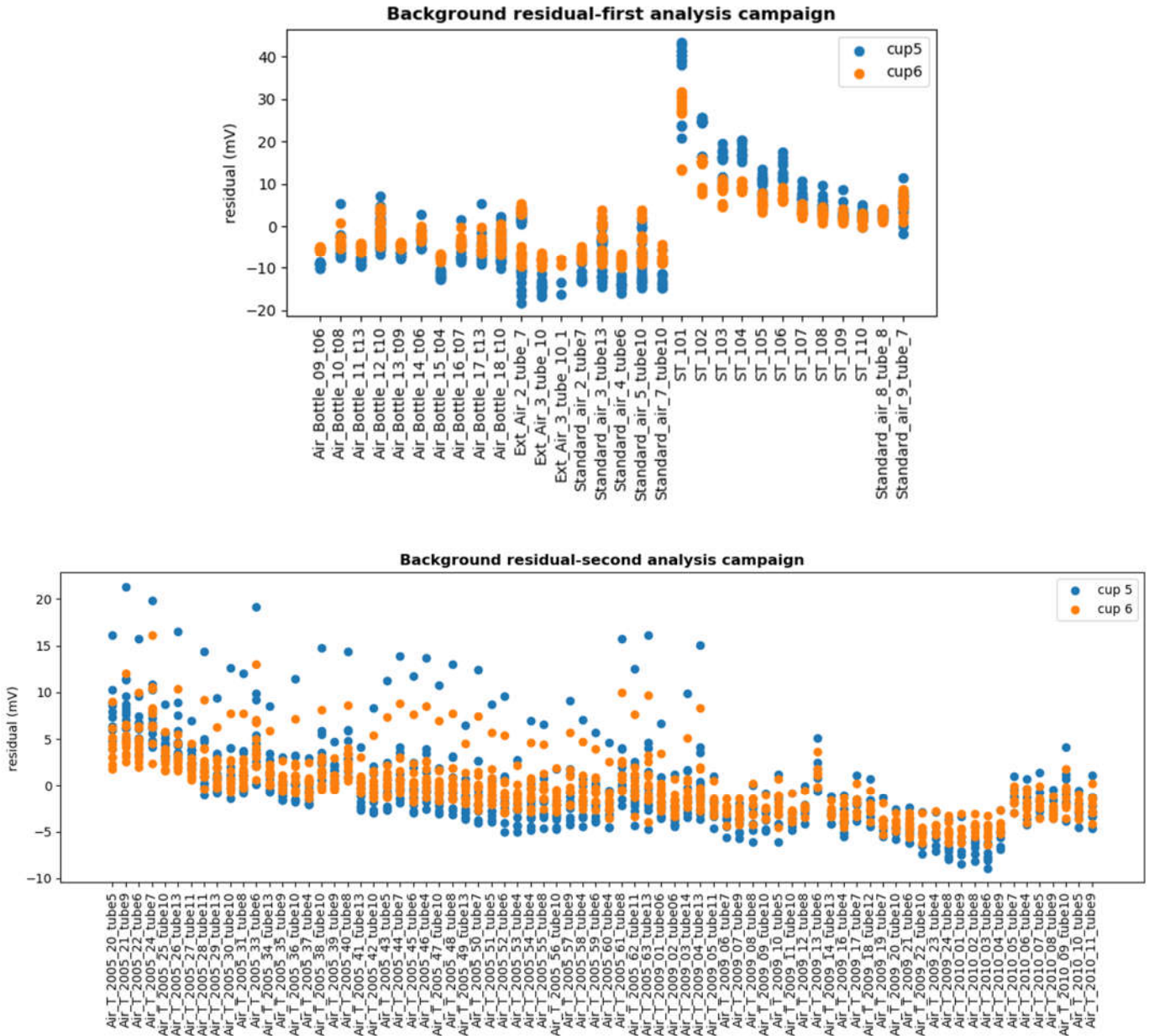
Figure 5.15: Background residuals calculated for both cup 5 and cup 6. Top. Background residuals computed for the first analysis campaign of external air and standard samples for cup 5 (blue dots) and cup 6 (orange dots). Bottom. Background residuals computed for the second analysis campaign of external air and standard samples for cup 5 (blue dots) and cup 6 (orange dots).

5.2.3.2 Pressure imbalance sensitivity

To the Ar ratios and $\delta^{15}N$ we apply the pressure imbalance sensitivity correction for both air and ice samples, following the same equations reported in Chapter 2 (equations 2.14 and 2.15). The pressure imbalance correction is based on the principle that the measured delta values are sensitive to the difference of pressure existing between the standard and the sample bellows (Severinghaus et al., 2003).
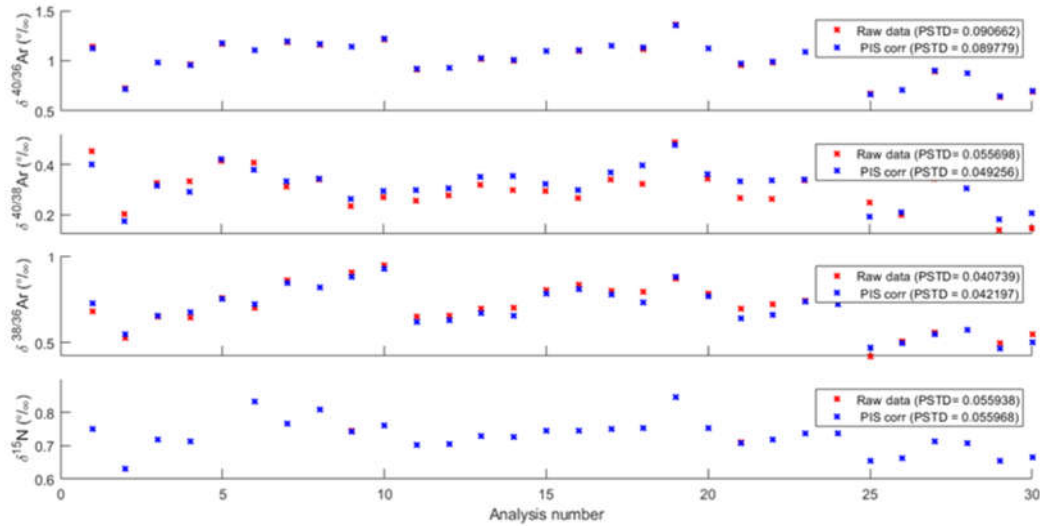
Figure 5.16: Comparison of $\delta^{40/36}$Ar, $\delta^{40/38}$Ar, $\delta^{38/36}$Ar and δ^{15}N before (red crosses) and after PIS correction (blue crosses) on TALDICE ice samples. Analysis numbers corresponds to the progressive number of samples analysed over time.

The PIS blocks are run usually overnight and each PIS block, which is repeated 5 times for each different element or element ratio, consists in 21 integrations. The pooled standard deviation is calculated for ice samples replicates (PSTD) for each isotope ratios for both raw and PIS corrected data (Figure 5.16). The PSTD for PIS corrected data is generally lower than raw data, however the PIS correction improvement could not be fully appreciated as some replicates are low quality (their difference exceed the 2*PSTD threshold) and need to be removed from the data set. The data cleaning step is presented in section 5.2.4.2. On the other hand, the PIS correction effect can be clearly observed looking at the mean standard deviation of block-averaged δ values within a sequence for all the samples (Table 5.4).

	$\delta^{40/36}$Ar (‰)	$\delta^{40/38}$Ar (‰)	$\delta^{38/36}$Ar (‰)	δ^{15}N (‰)
Mean std raw data	0.0249	0.0964	0.0806	0.0017
Mean std PIS corr	0.0172	0.0323	0.0342	0.0016

Table 5.4: Mean standard deviations calculated before and after PIS correction applied on Ar isotopes ratios and δ^{15}N.

5.2.3.3 Chemical Slope

Isotopic ratios of a single element measured in a mixture of gases are usually sensitive to variations in the elemental ratios of the mixture (Severinghaus et al., 2003). The gas introduced in the mass spectrometer (from air and ice samples) is a mixture of N_2 (~99%) and Ar (~1%) with an extremely low amount of Kr. When the gas sample is ionized, the relative ionization efficiencies of ^{40}Ar and ^{36}Ar are affected by differences in sample and standard N_2/Ar ratios, probably caused by the charge transfer between Ar and N_2 in the source (Severinghaus et al., 2003). The Ar measurements need to be corrected for this effect called chemical slope. The chemical slope is defined through a set of measurements of standard samples in which the amount of pure aliquot N_2 is progressively increased.

The chemical slope (CS) for Ar is defined through the following equation:

$$CS = \frac{\Delta \delta Ar_{PIS\ corr}}{\Delta \delta Ar/N_2}$$

(5.8)

The chemical slope is applied on samples corrected for the pressure imbalance sensitivity as following:

$$\delta^{40}Ar_{CS\ corr=}\ \delta Ar_{PIS\ corr} - CS \cdot \delta Ar/N_{2\ measured}$$

(5.9)

For the TALDICE data set we add aliquots of 0%, 5%, 10%, 15% and 20% of pure N_2 to standard samples. The chemical slope is measured twice because we performed two ice analysis campaign and the mass spectrometer has been turned off between the analysis of the two set of samples (Figure 5.17). The chemical slope correction produces greater isotopic values for both $\delta^{40/36}Ar$, $\delta^{40/38}Ar$, while smaller values for $\delta^{38/36}Ar$ (Figure 5.18).
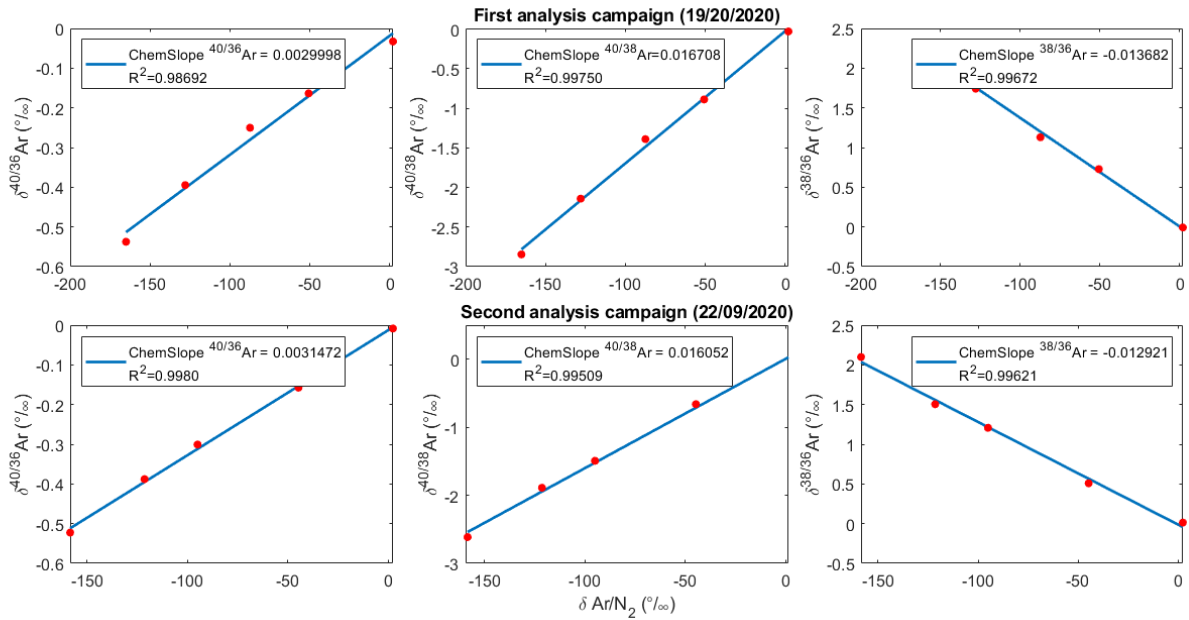
Figure 5.17: Chemical Slope applied for corrections on $\delta^{40/36}Ar$, $\delta^{40/38}Ar$ and $\delta^{38/36}Ar$ isotopic ratios. We use the chemical slope at the top to correct the TALDICE samples measured during the first analysis campaign the one at the bottom to correct the TALDICE samples measured during the second analysis campaign.
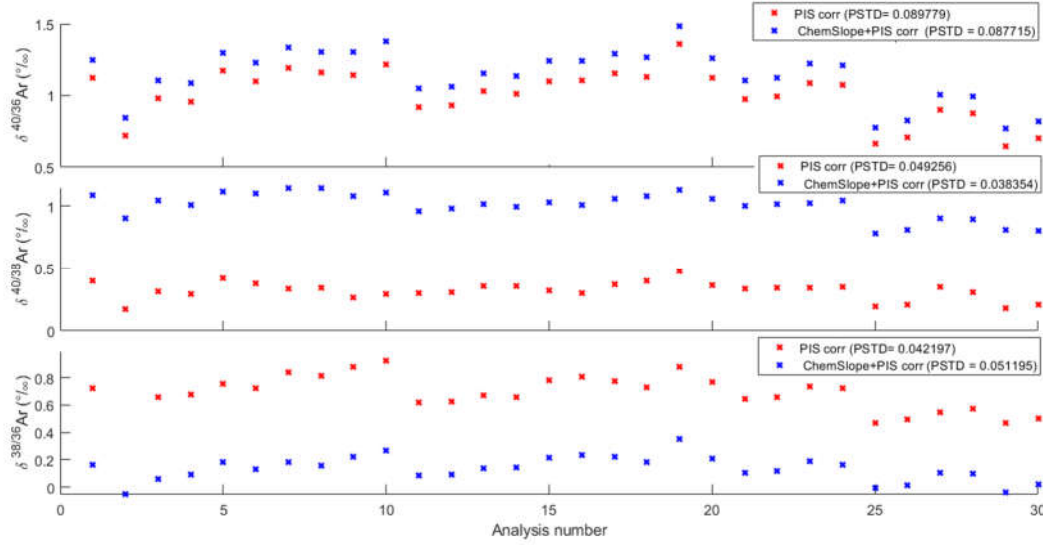
Figure 5.18: Comparison of $\delta^{40/36}$Ar, $\delta^{40/38}$Ar, $\delta^{38/36}$Ar and δ^{15}N corrected for PIS (red crosses) and for PIS and Chemical Slope (blue crosses) on TALDICE ice samples. Analysis numbers correspond to the progressive number of samples analysed over time.

5.2.3.4 Calibration to the outside air

All the ice samples data corrected for pressure imbalance and chemical slope are then normalized with respect to atmospheric air (Landais et al. 2003; Severinghaus et al. 2003). To perform the air calibration, we analysed 18 air samples before the first TALDICE ice measurement campaign and 76 air samples before the second measurement campaign. The air samples used for the calibration come from a bottle filled with modern (outside) air, which is transferred and purified following the protocol described in section 5.2.1.1. The air values are corrected for the background effect, the PIS and the chemical slope (except for δ^{15}N which is only corrected for the PIS) as described in the previous sections. From the entire air data set we choose 9 samples from the first campaign analysis and 6 from the second, to calibrate the ice samples for the outside air. We select the air samples data set that guarantee the best reproducibility of the air data, with comparable isotopic values and the lowest standard deviations (Table 5.5 and Figure 5.19).

Permill (‰)	$\delta^{40/36}$Ar (mean)	$\delta^{40/36}$Ar (std)	$\delta^{40/38}$Ar (mean)	$\delta^{40/38}$Ar (std)	$\delta^{38/36}$Ar (mean)	$\delta^{38/36}$Ar (std)	δ^{15}N (mean)	δ^{15}N (std)
1st analysis campaign	-0.4042	0.0128	0.2330	0.0163	-0.6352	0.0157	0.3659	0.0040
2nd analysis campaign	-0.3987	0.0056	0.2326	0.0170	-0.6331	0.0184	0.3678	0.0039

Table 5.5: Air bottles isotopic mean values for $\delta^{40/36}$Ar, $\delta^{40/38}$Ar, $\delta^{38/36}$Ar and δ^{15}N used for air calibration of the ice samples.
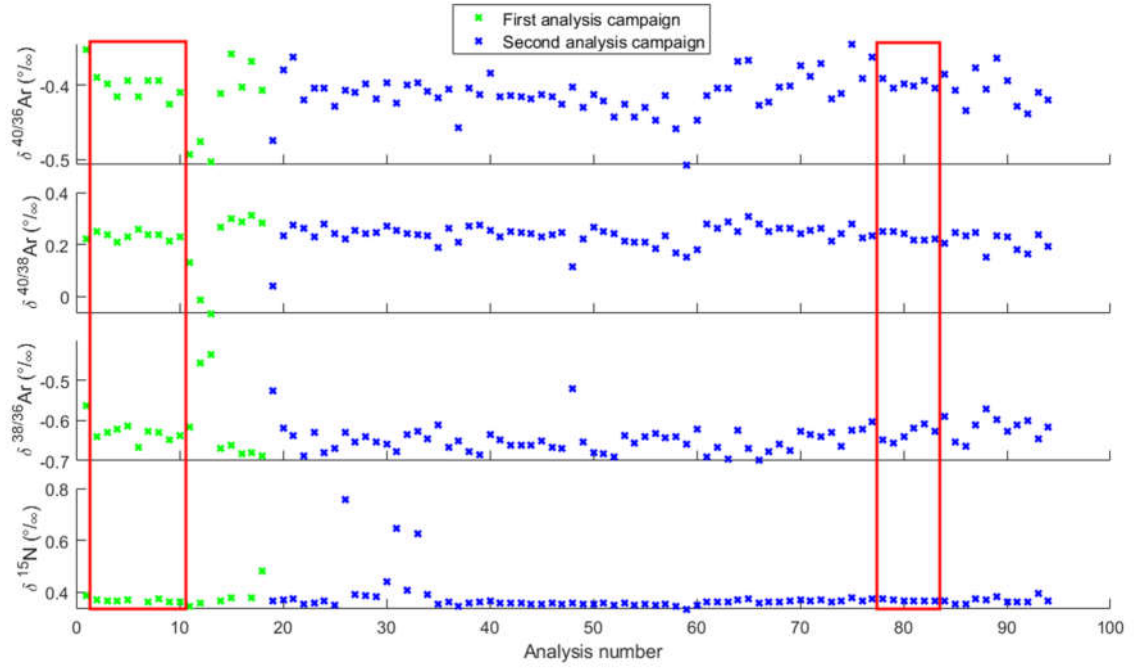
Figure 5.19: Outside air samples isotopic values data set for $\delta^{40/36}$Ar, $\delta^{40/38}$Ar, $\delta^{38/36}$Ar and δ^{15}N corrected for PIS and chemical slope of the first (green) and second (blue) analysis campaign. The data in the red box are used to calibrate the TALDICE ice samples.

The delta values of each campaign are averaged (δ_{air}) and used to correct the ice samples delta values as shown in Figure 5.20:

$$\delta_{air\ corr} = (\frac{\frac{\delta_{PIS,chem.slope}}{1000}+1}{\frac{\delta_{ext.air}}{1000}+1} - 1) * 1000 \qquad (5.10)$$
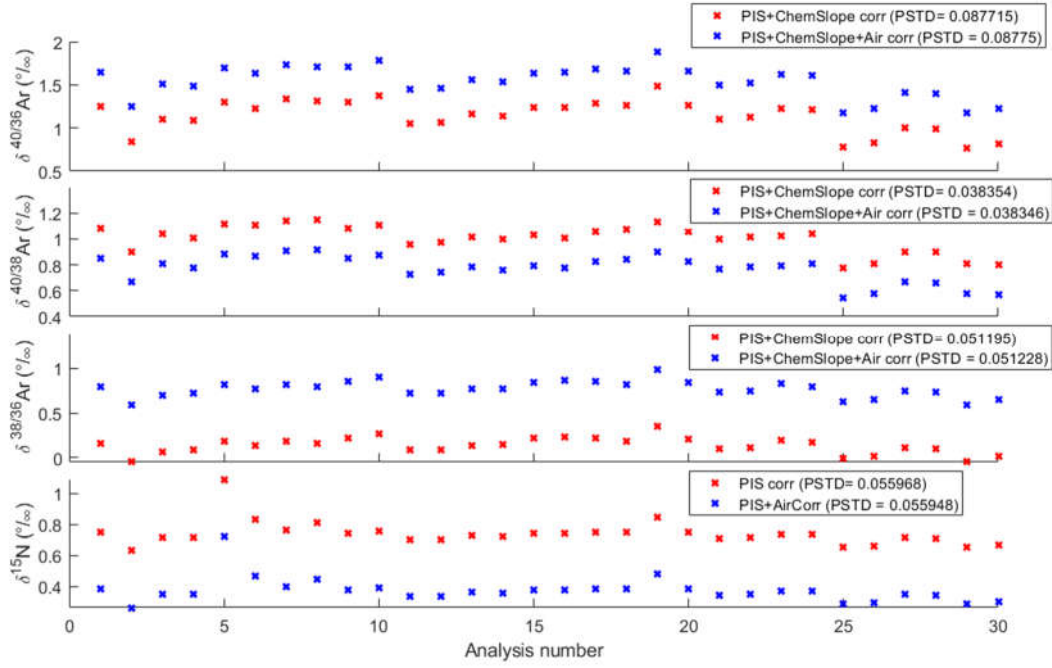
Figure 5.20: Comparison of $\delta^{40/36}$Ar, $\delta^{40/38}$Ar, $\delta^{38/36}$Ar and δ^{15}N corrected for PIS and chemical slope (red crosses) and for PIS, chemical slope and outside air (blue crosses) on TALDICE ice samples. Analysis numbers correspond to the progressive number of samples analysed over time.

5.2.4 Gravitational and gas loss correction

We analysed a total of 15 TALDICE ice samples, each of them in two replicates. In this section we show the ice data set and the applied gravitational and gas loss corrections.

5.2.4.1 38 background excess

The $\delta^{38/36}$Ar and $\delta^{40/38}$Ar values should be almost equal for the same sample as they are characterized by mass difference of 2. However, the mass spectrometer analysis introduces an extra background on the mass 38 observed during the analysis, that we have only imperfectly corrected with Equation 5.7. Since $\delta^{38/40}$Ar is principally affected by gravitational fractionation, we can infer this excess on the background by:

$$\text{Bckg 38 excess} = (\delta^{38/36}Ar/2 \ - \delta^{15}N \ ) \tag{5.11}$$

This background excess is used to correct the final Ar$_{\text{paleoatmosphere}}$ for the $\delta^{40/38}$Ar$_{\text{paleoatmoshere}}$ calculations as shown in section 5.2.5.

5.2.4.2 Data cleaning

In order to detect the presence of outliers in the TALDICE data set, we perform a first data check to observe if some samples need to be removed before the application of the gravitational and gas loss corrections. We routinely controlled the quality of the data and we identify as outliers the samples showing replicates difference of δAr and δ^{15}N isotopic values greater than 2 PSTD. From our results samples 1356, 1579 and 1611 are labelled as outliers (Figure 5.22). The bad quality of the outliers is

caused by issues occurring during the sample purification. We observed that leakage occurred while transferring sample 1611 and the oven was degassing during transfer of samples 1357 and 1592.
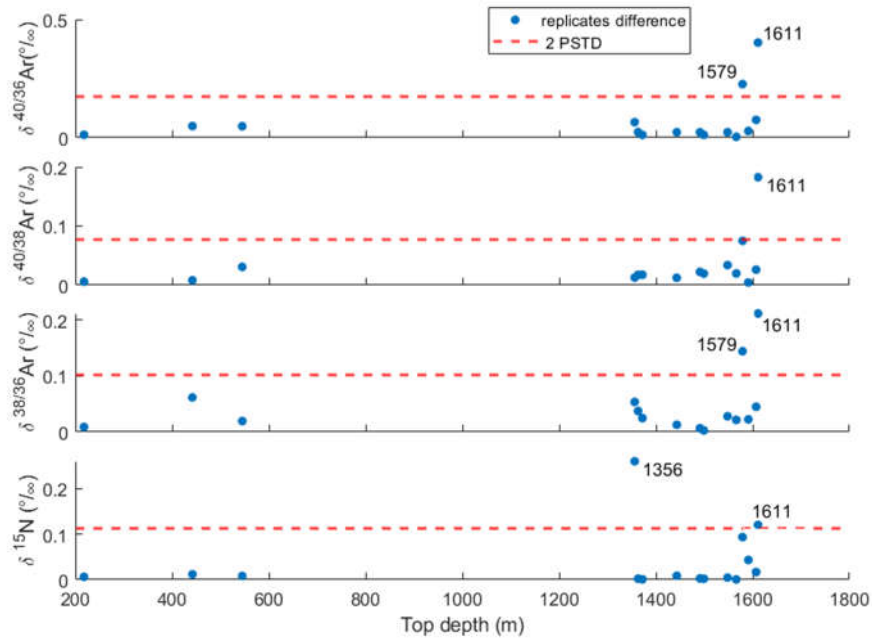
Figure 5.22: Replicate differences for $\delta^{40/36}Ar$, $\delta^{40/38}Ar$, $\delta^{38/36}Ar$ and $\delta^{15}N$ (blue dots) of TALDICE samples are compared to the 2*PSTD threshold (red dashed line). Samples which replicate difference exceed the 2*PSTD threshold are classified as outliers. Samples 1356, 1579 and 1611 are identified as outliers.

In addition, before performing the gravitational correction, which need $\delta^{15}N$ data, we check the quality of $\delta^{15}N$ values (Figure 5.23). Due to the same mass difference, each sample should exhibit similar isotopic values of $\delta^{15}N$ and $\delta^{38/36}Ar/2$. In particular, one of the replicates at depth 1356.05 m shows too high $\delta^{15}N$ value. We decide to remove the samples of 1611.05 m depth and 1579.05 m depth from our data set. Regarding the sample at 1356.05 m depth, as it shows only anomalous $\delta^{15}N$, we correct it for gravitational effect using the ratio $\delta^{38/36}Ar/2$.
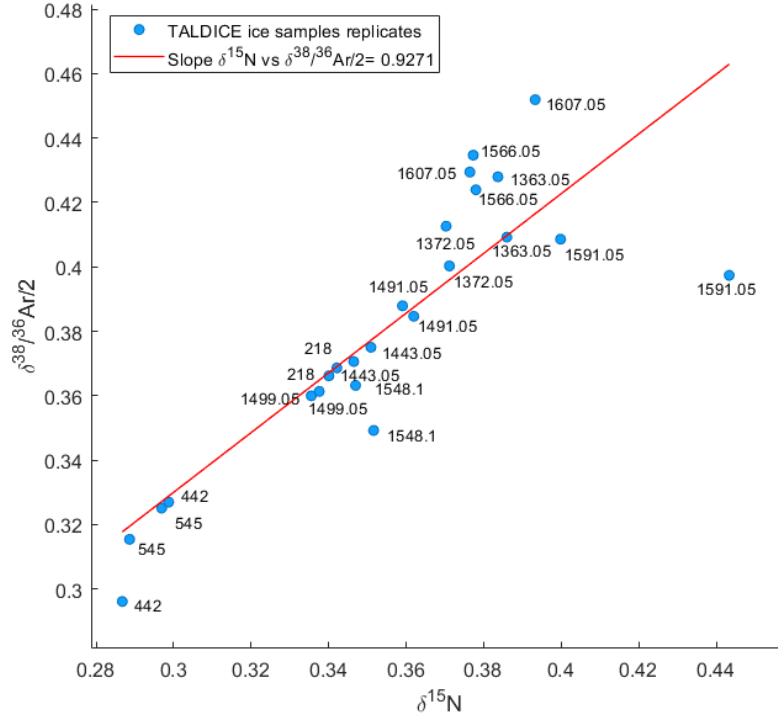
Figure 5.23: TALDICE samples δ ^{15}N isotopic values compared to δ$^{38/36}$Ar/2 values (blue dots). Outliers can be easily observed also on this plot. One of the replicates of the sample at 1356.05 m depth display an anomalous δ ^{15}N value.

5.2.4.3 Gravitational correction

The measured values of isotopic ratios in trapped air in the ice need to be corrected for the gravitational effect because the Earth gravity field causes fractionation in the firn to be equivalent to the mass difference between the studied isotopes: 1 g/mol for the ^{15}N/^{14}N ratio; 2 g/mol for ^{40}Ar/^{38}Ar and ^{38}Ar/^{36}Ar ratio, 4 g/mol for the ^{40}Ar/^{36}Ar ratio and 12 g/mol for the ^{36}Ar/^{28}N$_2$ (Craig et al., 1988; Severinghaus et al., 1998). The measured isotopic values (after applying all the corrections described in the previous section) are gravitationally corrected using the δ^{15}N ratio as reference for all samples, excluding 1356.05 m depth samples:

$$\delta^{40/36}Ar_{grav\ corr} = \delta^{40/36}Ar - 4 \cdot \delta^{15}N \tag{5.12}$$

$$\delta^{40/38}Ar_{grav\ corr} = \delta^{40/38}Ar - 2 \cdot \delta^{15}N \tag{5.13}$$

$$\delta^{38/36}Ar_{grav\ corr} = \delta^{38/36}Ar - 2 \cdot \delta^{15}N \tag{5.14}$$

$$\delta Ar/N_{2\ grav\ corr} = \delta Ar/N_2 - 12 \cdot \delta^{15}N \tag{5.15}$$

The replicate of 1356.05 m depth sample showing anomalous δ^{15}N value is gravitationally corrected using δ$^{38/36}$Ar as following:

$$\delta^{40/36}Ar_{grav\ corr} = \delta^{40/36}Ar - 2 \cdot \delta^{38/36}Ar \tag{5.16}$$

$$\delta^{40/38}Ar_{grav\ corr} = \delta^{40/38}Ar - \delta^{38/36}Ar \tag{5.17}$$

$$\delta Ar/N_{2\ grav\ corr} = \delta Ar/N_2 - 6 \cdot \delta^{38/36}Ar \tag{5.18}$$

However, preliminary age calculations tests show that the inclusion of the 1356.05 m, 1548.05 m and 1591 m samples does not provide satisfactory results since the final ages of all the samples appear too old. The presence of the sample in the data set influences the gas loss correction and the age calculation, so we removed those samples from the TALDICE data set. The Ar ratios values corrected for the gravitational effected versus the $\delta Ar/N_2$ gravitationally corrected values are showed in Figure 5.24.

Table 5.24: a. TALDICE samples $\delta^{40/36}Ar$ GravCorr (bluestars), $\delta^{40/38}Ar$ GravCorr (red dots) and $\delta^{38/36}Ar$ GravCorr (green triangles) plotted with $\delta Ar/N_{2GravCorr}$. b. TALDICE samples $\delta^{40/36}Ar$ GravCorr (bluestars), $\delta^{40/38}Ar$ GravCorr (red dots) and $\delta^{38/36}Ar$ GravCorr (green triangles) plotted versus depth (m).

5.2.4.4 Gas loss correction

In section 2.4.7.2 we observe that the $\delta^{18}O_{atm}$ isotopic values in TALDICE ice samples are affected by severe gas loss. Here we investigate the gas loss effect in TALDICE samples for the Ar isotopes. When air bubbles isolate from the atmosphere during the close-off process, the pressure inside the bubble increases and causes the expulsion of a small amount of gas characterized by molecules small enough (as Ar and N_2) to pass the ice. Due to their small size, Ar molecules tend to escape more easily than N_2, causing Ar loss and fractionation (Severinghaus & Battle, 2006). A similar process happens after the coring, especially when samples are conserved at temperatures of about -25°C for several years (Ikeda-Fukazawa et al., 2005; Kobashi et al., 2007; Severinghaus et al., 2003).
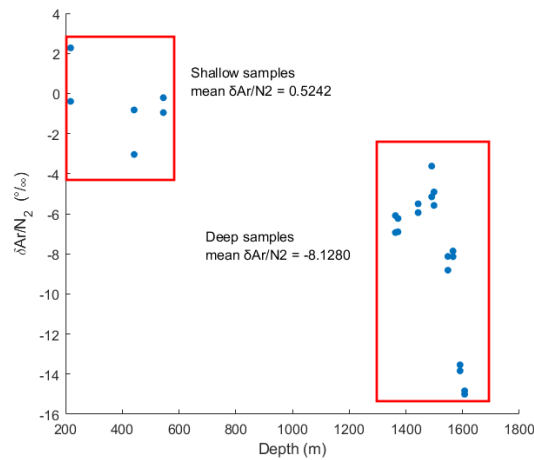
Figure 5.25: TALDICE samples $\delta Ar/N_2$ isotopic ratios evolution with respect to the core depth. The $\delta Ar/N_2$ are on average more negative in samples from deeper portion of the core in comparison to the shallower ones.

To check if TALDICE samples are affected by gas loss, we firstly observe $\delta Ar/N_2$ ratio, as it is considered a good proxy indicator for the amount of argon isotopic fractionation by gas loss (Kobashi et al., 2007; Severinghaus et al., 2003). The more negative is the $\delta Ar/N_2$ in a sample, the more it is affected by gas loss. We observe that TALDICE deeper samples are characterized by a more negative $\delta Ar/N_2$ values ($\delta Ar/N_2$ mean = -8.128‰) with respect to shallow samples ($\delta Ar/N_2$ mean= 0.5242‰) (Figure 5.25). Due to the large difference in the gas loss affecting shallow and deep samples, we decide to perform the gas loss correction separately.

The gas loss slope is calculated as the slope of the linear regression between $\delta^{40/36}Ar_{GravCorr}$ and $\delta Ar/N_{2\ GravCorr}$ and then is used to correct the Ar ratios (equation 5.19-5.21). We calculate two separate gas loss slopes for the shallow samples and for the deep samples as displayed in Table 5.6. We separated the two set of samples since the shallow samples are characterized by bubbly ice, while the deep samples are clathrate ice. Such a difference in the application of the gas loss correction indicates that bubbly ice (shallow samples) is less affected by the gas loss phenomenon with respect to clathrate ice, typical condition of deep ice (Ikeda-Fukazawa et al., 2005; Oyabu et al., 2021).

Samples	Gas loss slope ($\delta^{40/36}$Ar)	Intercept ($\delta^{40/36}$Ar)	R	p	std
Sallow samples	-0.0023	0.0057	-0.7375	0.2625	0.0015
Deep samples	-0.0249	0.0115	0.9305	4.931 10^{-7}	0.0027

Table 5.6: Gas loss slope and intercept calculated between $\delta^{40/36}Ar_{GravCorr}$ and $\delta Ar/N_{2GravCorr}$ for shallow and deep samples.

The calculated slopes are then applied to correct the Ar isotopic ratios for the gas loss effect as following:

$$\delta^{40/36}Ar_{GLCorr} = \delta^{40/36}Ar - GLSlope^{40/36}Ar \cdot \delta Ar/N_{2\ GravCorr} \tag{5.19}$$

$$\delta^{40/38}Ar_{GLCorr} = \delta^{40/38}Ar - GLSlope^{40/36}Ar/2 \cdot \delta Ar/N_{2\ GravCorr} \tag{5.20}$$

$$\delta^{38/36}Ar_{GLCorr} = \delta^{38/36}Ar\ - GLSlope^{40/36}Ar/2 \cdot \delta Ar/N_{2\ GravCorr} \tag{5.21}$$

The $\delta^{40/36}$Ar/4, $\delta^{40/38}$Ar/2 and $\delta^{38/36}$Ar/2 ratios not corrected and for the gas loss effect are plotted with δ^{15}N and displayed in Figures 5.26 and Figures 5.27 for both shallow and deep samples. The removal of the outliers from the data set, along with the gravitational and the gas loss correction, reduces the TALDICE samples PSTD for all the ratios. The gas loss corrected Ar ratios are ready for the age calculation (Figure 5.28).
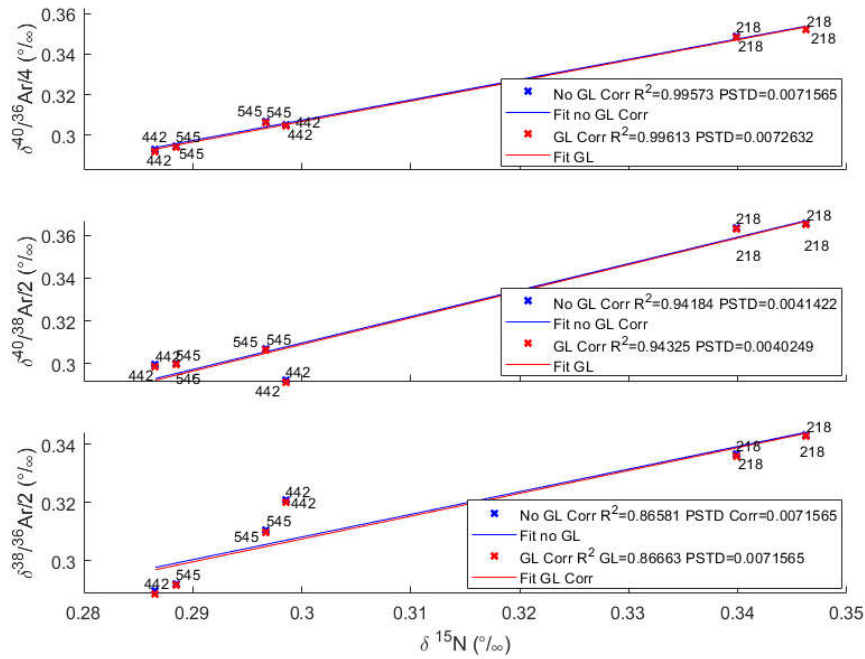
Figure 5.26: Comparison of $\delta^{40/36}$Ar/4, $\delta^{40/38}$Ar/2, $\delta^{38/36}$Ar/2 raw data (blue crosses) and gas loss corrected data (red crosses) plotted δ^{15}N versus for TALDICE shallow ice samples. Top. Shallow samples. Bottom. Deep samples. Analysis numbers corresponds to the progressive number of samples analysed over time.
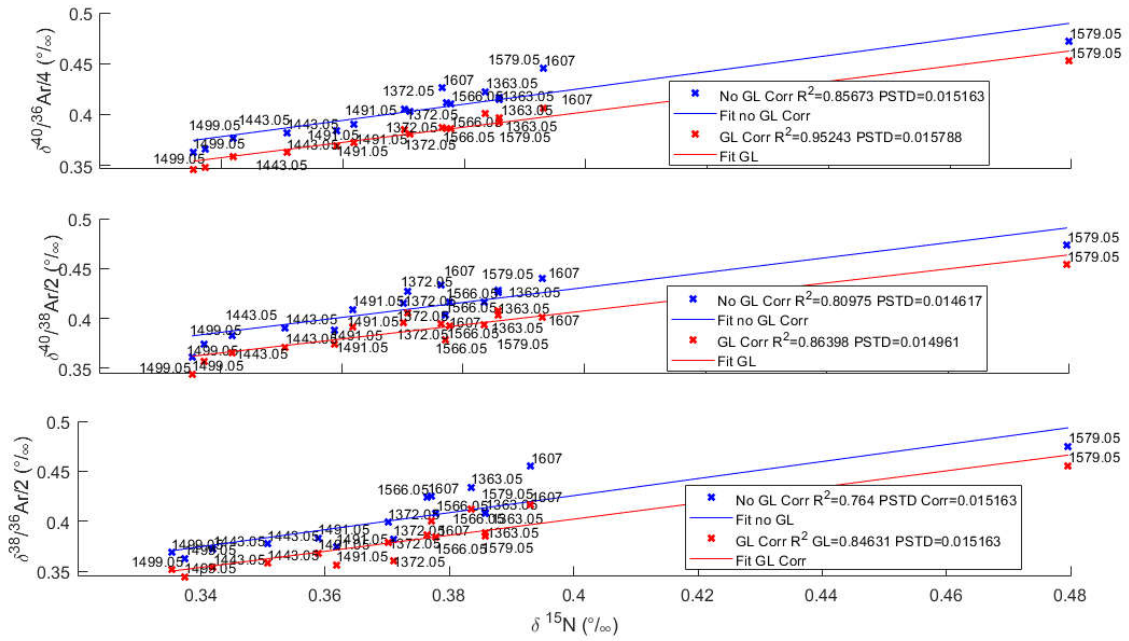
Figure 5.27: Comparison of $\delta^{40/36}$Ar/4, $\delta^{40/38}$Ar/2, $\delta^{38/36}$Ar/2 raw data (blue crosses) and gas loss corrected data (red crosses) plotted δ^{15}N versus for TALDICE deep ice samples. Top. Shallow samples. Bottom. Deep samples. Analysis numbers corresponds to the progressive number of samples analysed over time.
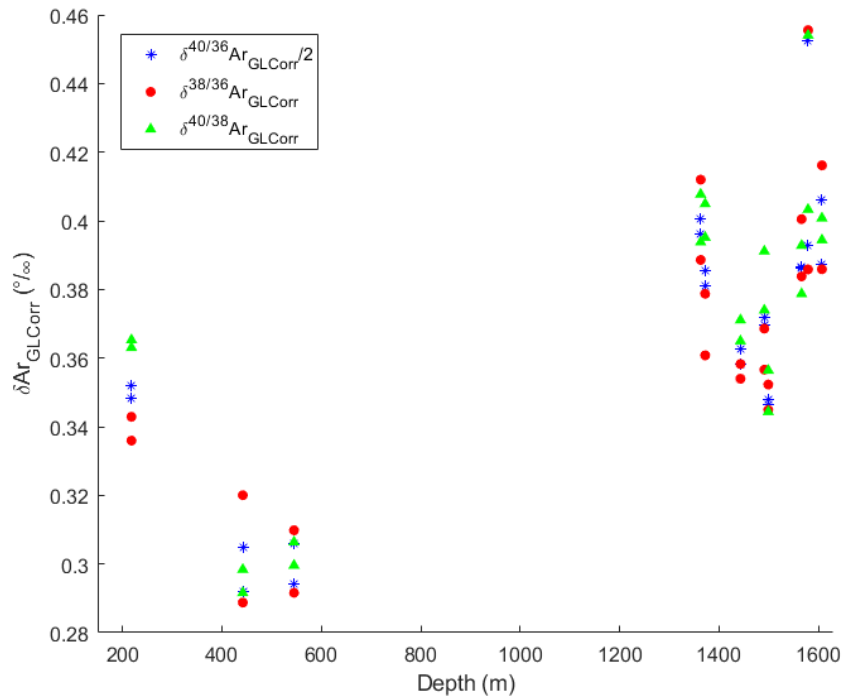
Figure 5.28: Comparison of $\delta^{40/36}$Ar per mass unit (blue stars), $\delta^{38/36}$Ar per mass unit (red dots) and $\delta^{40/38}$Ar per mass unit (green triangles) on depth corrected gas loss effect for TALDICE ice samples purified with the copper method.

5.2.5 TALDICE samples dating

To finally calculate the age of the TALDICE samples of the air trapped in the ice, we compute the paleoatmospheric ratios of $\delta^{40/36}$Ar and $\delta^{40/38}$Ar air contained in the ice from the gas loss corrected isotopic ratios. We use a slight different version of the equations used to calculate $Ar_{paleoatmsphere}$ (Bender et al., 2008; Yau et al., 2015), correcting gravitational fractionation with δ^{15}N instead of $\delta^{38/36}$Ar as following:

$$\delta^{40/36}Ar_{paleoatmosphere} = \delta^{40/36}Ar_{GL\,Corr} - 4 \cdot \delta^{15}N \tag{5.22}$$

$$\delta^{40/38}Ar_{paleoatmosphere} = (\delta^{40/38}Ar_{GL\,Corr} - 2 \cdot \delta^{15}N) + 2Bckg\,38\,excess \tag{5.23}$$

Where Bckg 38 excess is the excess for the mass is calculated in section 5.2.4.1.

Figure 5.24 shows that δAr ratios gravitationally corrected are characterized by an offset (since Ar values are positive) that need to be corrected using two different values for shallow (<600 m depth) and deep samples (> 600m depth). We attribute this offset to the effect of gas loss on argon isotopes which acts differently for shallow (bubbly ice) and deep samples (clathrate ice). We need to take this effect into account to get reliable $\delta^{40}Ar_{atm}$ value.

For bubbly ice (shallow samples, depth<600m), we calculate the offset for each sample as:

$$e_{shallow\,40/36Ar} = mean(\delta^{40/36}Ar_{GL\,Corr} - 4 \cdot \delta^{15}N) \tag{5.24}$$

$$e_{shallow\,40/38Ar} = mean(\delta^{40/38}Ar_{GL\,Corr} - 4 \cdot \delta^{15}N) \tag{5.25}$$

For clathrate ice (shallow samples, depth>600m), we calculate the offset by matching the isotopic composition of our shallowest sample to be 0.066 ‰ at 100 ka for the depth interval between 1300 and 1400 m. We use the $\delta^{40/36}$Ar, $\delta^{40/38}$Ar and δ^{15}N values of samples 1363.05 m depth and 1372.05 m depth for the offset calculation. The offset for the deeper samples is compute as following:

$$e_{deep40/36Ar} = 0.066 + mean(\delta^{40/36}Ar_{GL\,Corr} - 4 \cdot \delta^{15}N) \tag{5.26}$$

$$e_{deep40/38Ar} = 0.066 + mean(\delta^{40/38}Ar_{GL\,Corr} - 4 \cdot \delta^{15}N) \tag{5.27}$$

	$e_{shallow}$ (‰) (<600 m depth)	e_{deep} (‰) (>600 m depth)
e $_{40/36Ar}$	0.027	0.043
e $_{40/38Ar}$	0.033	0.051

Table 5.7: Calculated offset for deep and shallow samples for $\delta^{40/36}$Ar and $\delta^{40/3}$ Ar.

The Ar ages are then calculated applying the computed offsets (Table 5.7) differently for the shallow samples and deep samples applying the calculated offset coefficients:

$$^{40/36}Ar_{age} = (\delta^{40/36}Ar_{paleoatmosphere} - e_{40/36Ar})/0.066 \cdot 10^3 \tag{5.28}$$

$$^{40/38}Ar_{age} = (\delta^{40/38}Ar_{paleoatmosphere} - e_{40/38Ar})/0.066 \cdot 10^3 \tag{5.29}$$

The results of the Ar ages calculations are displayed in Table 5.8.

Top depth (m)	Bottom depth (m)	Mean depth (m)	$\delta^{40/36}Ar_{atm}$ (‰)	$\delta^{40/38}Ar_{atm}$ (‰)_	$^{40/36}Ar$ age (ka)	$^{40/38}Ar$ age (ka)
218	218.18	218.08	-0.005	-0.002	75.66	33.85
			0.006	0.005	-96.88	-75.54
442	442.18	442.08	-0.005	-0.005	78.88	82.74
			-0.002	-0.004	34.95	66.15
545	545.18	545.08	-0.004	-0.005	65.67	74.36
			0.010	0.012	-158.28	-181.55
1363.05	1363.25	1363.15	0.009	0.011	-131.68	-160.05
			-0.017	-0.018	260.34	266.97
1372.05	1372.25	1372.15	0.001	0.000	-22.45	-3.51
			-0.019	-0.020	293.79	296.58
1443.05	1443.25	1443.15	0.005	0.003	-81.51	-45.29
			-0.011	-0.011	168.98	171.50
1491.05	1491.25	1491.15	-0.018	-0.019	277.64	283.86
			-0.016	-0.018	249.43	265.16
1499.05	1499.25	1499.15	-0.015	-0.015	225.24	229.25
			-0.017	-0.014	258.51	213.13
1566.05	1566.25	1566.15	-0.025	-0.025	385.01	380.90
			-0.021	-0.017	321.36	259.85
1579.05	1579.25	1579.15	-0.168	-0.166	2547.73	2521.60
			-0.032	-0.032	484.18	486.79
1607.05	1607.25	1607.15	-0.015	-0.012	229.10	184.61
			-0.007	-0.006	104.37	85.02

Table 5.8: TALDICE samples paleoatmospheric values of $\delta^{40/38}Ar$ and $\delta^{40/36}Ar$ with the respective calculated Ar ages. The negative sign indicates that the calculated Ar ages are in the future.

We can observe in Table 5.8 that both $^{40/36}Ar$ and $^{40/38}Ar$ provide gas age values comparable to the gas age estimated by the chronologies AICC2012 TALDICE and TALDICEdeep1 (Bazin et al., 2013; Crotti et al., 2021). However, the difference between the $^{40/36}Ar$ ages and the published gas ages appear to be smaller with respect to the difference computed for the $^{40/38}Ar$ ages (Table 5.9). We choose to use the $^{40/36}Ar$ ages to finally date the samples. We estimate the $^{40/36}Ar$ dating uncertainty, calculating the pooled standard deviation of replicate measurements, equal to ±0.013‰ and corresponding to ±205 ka for all samples. One of the replicates of the sample at 1579 m depth shows a gas age which is too old (1516 ka), and is removed from the final data set and Figure 5.29. We observe a reliable increase in the age of

the samples up to 485 ka at 1579m depth, which is consistent with [81]Kr results. However, the last sample at 1607 m is biased high (150 ka). This observation matches results from other cores that showed anomalously high $d^{40}Ar_{atm}$ at the bottom of other ice cores (Yau et al., 2016). In conclusion, we suggest that the copper method for Ar dating on small samples (~65 g) provides reliable results, with an uncertainty of 0.013‰ or ±205 ka (1-σ).

Mean depth (m)	mean $^{40/36}$Ar age (ka)	mean $^{40/38}$Ar age (ka)	AICC2012, TALDICE-deep1 and [81]Kr		Difference $^{40/36}$Ar age – real gas age (ka)	Difference $^{40/38}$Ar age – real gas age (ka)
			gas age (ka)	std (ka)		
218.08	-11	-21	1.91	±0.10	-13	-22.755
442.08	57	74	5.73	±0.15	51	68.715
545.08	-46	-54	7.99	±0.16	-54	-61.585
1363.15	64	53	99.33	±1.54	-35	-45.87
1372.15	136	147	104.15	±1.56	32	42.385
1443.15	43	63	154.12	±3.77	-110	-91.015
1491.15	263	275	186.32	±2.40	77	88.19
1499.15	242	221	194.9	±2.19.	47	26.29
1566.15	353	320	397	±20	-44	-76.625
1579.15	484	487	-	-	-	-
1607.15	167	135	410	±20	-243	-275

Table 5.9: TALDICE samples mean and the respective $^{40/36}$Ar ages and $^{40/38}$Ar ages compared with samples ages from the AICC2012 and TALDICE deep1 age scales (Bazin et al., 2013; Crotti et al., 2021). The difference is calculated subtracting between the mean Ar age and the published gas age (Bazin et al., 2013) (Crotti et al., 2021).
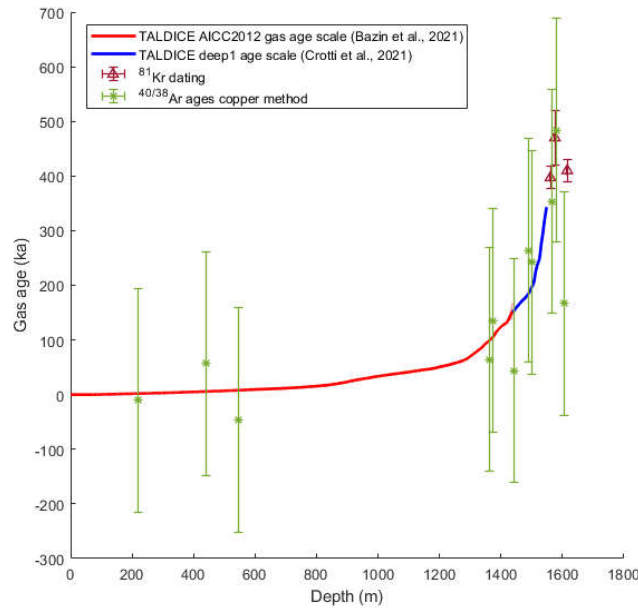
Figure 5.29: $^{40/36}$Ar ages values -copper method- (green stars) compared with the AICC2012 (red curve) (Bazin et al., 2013), TALDICE deep1 (blue curve) age scales and [81]Kr dated layers (purple triangles)(Crotti et al., 2021).

5.3   The getter method at LSCE

In this section the air extraction and purification methodology called *getter method*, used to extract and purify air from big ice samples (500-800 g) up to 1.5 kg, is presented. The methodology is time consuming with respect to the copper method because we can treat only one sample per day. The method is based on the initial work of Severinghaus et al. (2003) and the following developments by Bender et al. (2008) and Yau et al.(2016). Here the extraction protocols for both air and ice samples are described with the data treatment and the dating results.

5.3.1   Analytical methods

5.3.1.1 Air samples preparation

Air samples are purified with the getter method set up and analysed with the mass spectrometer, since outside air values are necessary to express the ice samples results with respect to the atmosphere. The modern air is stored in a stainless steel silco can attached to the extraction line. The silco can is refilled with the outside air using a pumping system (Figure 5.30) and a cold trap. The pumping system is placed in the laboratory and connected to the exterior of the lab, in order to pump inside the silco well mixed external air far from polluting sources. Once the silco is connected to the pumping system, a cold trap is prepared mixing liquid nitrogen and ethanol to reach a temperature between -80°C and -100°C. Valves 4 and 3 are opened, while valve 2 is closed to pump the line for 10 minutes. At first, the remaining air is removed from the silco opening valve 1 and turning on the pump number 1 until the pressure decreases at the value of -1 bar. Once the silco is evacuated, valve 1 is closed and the pump 3 is turned off. To fill the silco with external air, valve 2 is opened until the pressure reaches the value of 2 bar, then the silco valve is closed, valve 2 is opened and pump 2 is turned off.
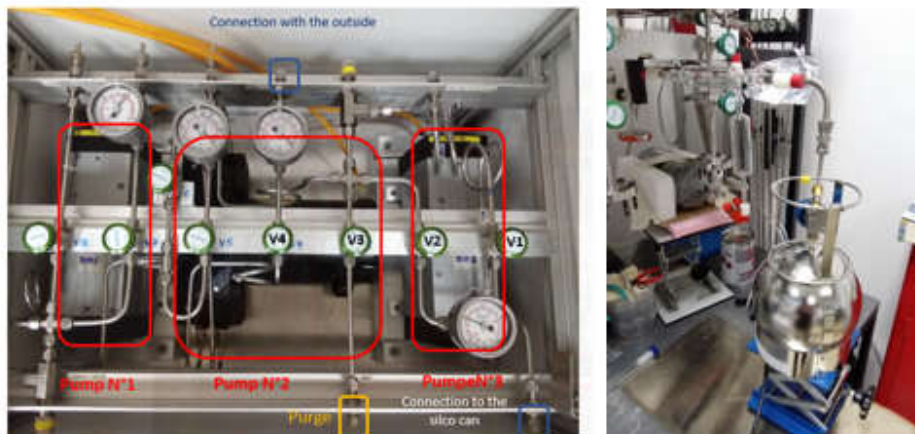
Figure 5.30: Left. Pumping system for the silco can at LSCE. Right. Silco can attached to the getter line.

5.3.1.2 Air samples purification and transfer protocol

The getter line at LSCE is based on the copper method line system, which has been modified in order to substitute the copper oven with a Pyrex tube wrapped in a heating resistence (Thermocoax SEI 15/200) and filled with a getter material (Saes Getters). The getter consists in metallic slotted strips

coated by a mixture of Zr 86% and Al 16%, specifically a mixture of two intermetallic compounds Zr_3Al_2 (the most abundant) and Zr_5Al_3. Those strips adsorb reactive gases as N_2, O_2, CO, CO_2, H_2O and H_2 when they are activated at the temperature of 900°C. In addition, the system is equipped with one water trap immersed in ethanol cooled at a temperature between -80°C and -100°C. The air flux is manually regulated by stainless steel bellows sealed valves (green Swagelok valves) and the pressure is continuously checked through one 10 Torr barotron gauge (Figures 5.31 and 5.32). Like for the copper method, it is necessary to purify and analyse modern air samples before starting the ice analysis campaign. The air analysis results are at first used to test the reproducibility of the method and once the desired precision is achieved, the air measurements are applied to perform air calibration on ice samples results.

The external air injected in the line is conserved in a stainless steel silco container attached to the line through 2 glass flasks used to expand the air volume. The air purification is performed using the getter. Once an aliquot from the bottle air is injected in the line, the air is left in the line to react with the getter activated at the temperature of 900°C for 40 min and then the air is transferred into a stainless steel dip tube (the same employed for the copper method) placed inside the He tank. No water trap is needed on the line since when filling the silco can, the water has been removed with a cold trap. Before starting the air purification and transfer, the line is evacuated overnight and the pressure inside the line has to be equal to 0 mbar.
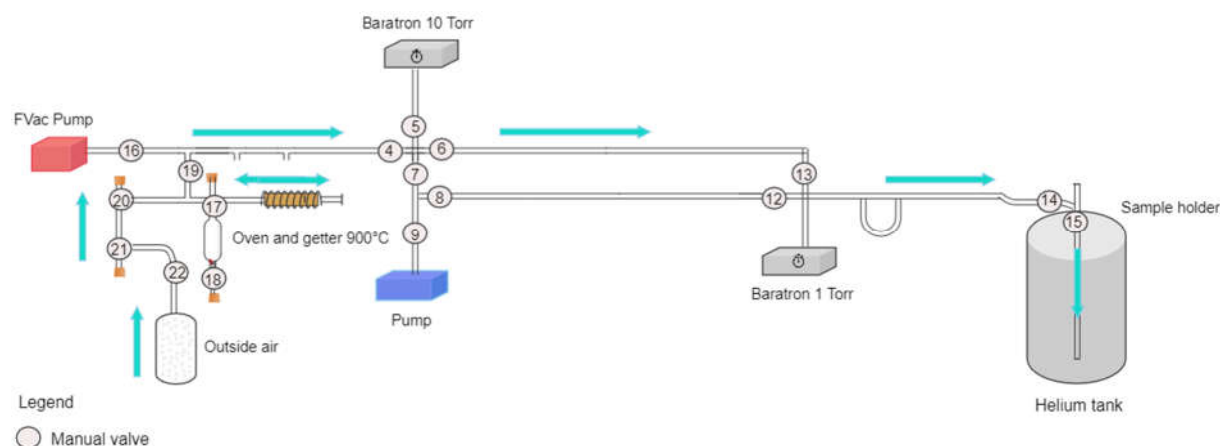
Figure 5.31: The getter method line setup for air samples at LSCE.

The extraction procedure follows a protocol applied to guarantee the quality and reproducibility of the measurements:

i.   The pressure in the line is checked to have reached the vacuum conditions and a leak test is performed in order to verify the presence of leakages in the line. The oven is turned on at 300°C for 10 min while all the valves of the line are open to pump the line and to let the oven to degas. When the 10 min are expired the oven temperature is set to 900°C for 10 min.

ii.   To inject the air sample from the silco can in the line the valve 22 is opened for 5 seconds and then closed. The air expands in the first glass flask where the valve 21 is open and the 20 is closed. The valve 21 is then closed and the air is let to equilibrate inside the flask.

iii.   The air is then expanded in the second flask and in the getter opening the valves 20 and 17, while valve 19 is kept closed. The air is left to react with the getter for 90 min and at the end the oven temperature is turned to 300°C for 5 min to re-adsorb the created H_2.

iv.   In the meantime, a clean dip tube is immersed in the liquid nitrogen tank to cool for 5 min and then is attached to the line. Valve 14 is opened and the line side from valve 19 to 14 is evacuated. Valves 8 and 12 are closed as this portion of the line is not used.

v.   When 90 min are expired, valve 9 is closed and valve 19 is opened to let the gas aliquot to expand in the line. Valve 15 on the dip tube is opened and the gas is let to transfer in the dip tube for 15 min. When the 15 min are elapsed the valve 15 is closed and the pressure inside the line is verified to be equal to 0 mbar.

vi.   Once the transfer is over, the valve 14 is closed and the dip tube is removed from the He tank.

vii.   All the valves are opened and the line is let to evacuate before starting the following air sample purification.

viii.   At the end of the laboratory day, the getter strips placed inside the oven need to be changed. Valve 19 is closed and the getter is removed from the oven with the help of tweezers because it should not be touched with bare hands. A new getter strip, made by 40 slots, is placed inside the oven and re-connected to the line. All the valves are then opened and the system is let to evacuate overnight.
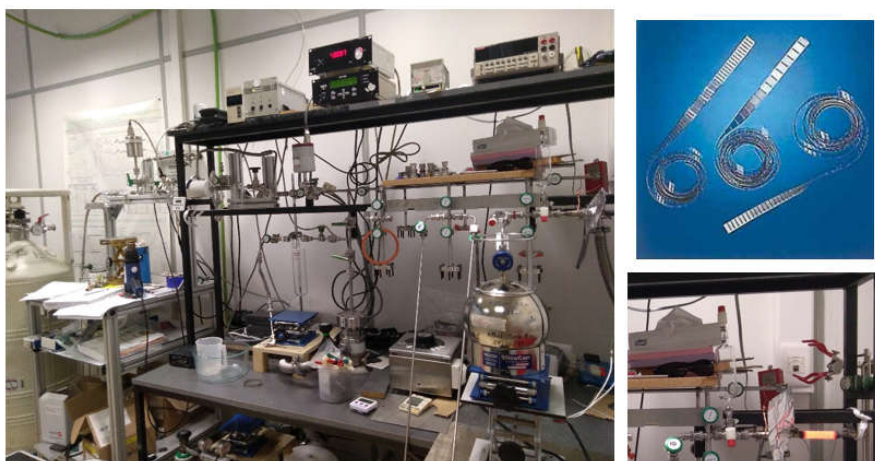
Figure 5.32: Left. Getter method line setup for air samples analysis at LSCE. Left. The extraction and purification line at LSCE. Top right. Getter strips. Bottom right. Getter activation.

5.3.1.3 Ice samples preparation in the cold room

Every day the ice samples need to be prepared in the cold room at -20°C for the analysis. The stainless steel vacuum chamber, which consist in a cylinder covered by a lid equipped with a copper

gasket, is carried in the cold room as it will serve as sample holder. TALDICE samples, which consist in ice sticks of about 15 cm length, are shaved with a ceramic knife in order to remove the 3-5mm layer that could be affected by contamination. Samples are also inspected to in order to eliminate cracks and melted layers. As the getter method requires about 500-800 g of ice, several samples belonging to neighbouring depths are selected and analysed together in order to reach the required weight (Table 5.10). A stir bar is also inserted in the chamber. Once all the ice pieces are placed in the chamber, the lid is placed on the top and close tightening the screws. The chamber is then taken outside the cold room and placed in a freezer close to the laboratory.

Figure 5.33: Stainless steel chamber with the lid placed on the getter line.

Sample number	Top depth (m)	Bottom depth (m)	Weight (g)
TD 460-463-466	459.71	465.94	784.7
TD 468-470-472	467.00	471.25	614.60
TD 532-534	531.06	533.94	536.6
TD1380-1390-1396-1404-1412-1420	1379.05	1419.25	685.70
TD 1428-1436-1441-1452-1459-1469-1472	1427.05	1471.25	929.80
TD 1476-1484-1508-1517-1524-1533-1541	1475.05	1540.25	891.80
TD 1552-1555-1559-1563-1570-1573	1551.05	1572.25	694.70
TD 1584-1588-1596-1602-1604-1614-1616-1618	1583.05	1617.25	792.30

Table 5.10: TALDICE ice samples extracted with the getter method. The weight refers to the weight of ice after shaving.

5.3.1.4 Ice samples purification and transfer protocol

The extraction line set up for air extraction from ice samples is very similar to the one employed for the air samples with an additional water trap. The ice chamber is connected to the main line through a flexible tube attached to a water trap (-100°C) (Figure 5.33), which was not present in the air samples configuration since the air samples are already dry (Figures 5.34 and 5.35). Before starting the air transfer and purification, the line is evacuated overnight and is leak checked in the morning.

The extraction and the purification procedures follow the protocol described here:

i.   The chamber containing the ice samples is connected to the line with valve 10 and placed inside a dewar full of ethanol at -25°C to keep the sample cool and avoid melting. The chamber at the top is covered with two frozen bricks.

ii.   Valves 19 and 6 are closed to keep clean the portion of the line that will be used later.

iii.   Valve 9 to the pump is closed and valves 10, 11, 8, 7, 4 and 16 are opened to evacuate the chamber with the fore vacuum pump until the pressure goes down to 1 mbar.

iv.   Valve 16 is closed and the valve 9 to the pump is opened again. The chamber is let to evacuate for 40 min. After 5 min, we measure the vapour pressure over ice on the 10 Torr baratron closing the valve 9 and the value is noted in the lab book. The pressure should be stable, if not is necessary to understand if there is a leakage from the lid of the ice chamber.

v.   In the meantime, the big thermos is turned on and filled with water at 40°C that will be used to melt the ice.

vi.   After 40 minutes the valve 9 is closed again to measure the pressure over ice and noted in the lab notebook. If no leaks are detected, the chamber has been properly evacuated and the ice sample is ready to melt.

vii.   A clean dip tube is cooled in liquid N_2 for some minutes, placed in the He tank and connected to the line through valve 14. Valve 6 is opened and this portion of the line is evacuated for 10 min at least.

viii.   At this stage the water trap is prepared. A dewar is filled with cold ethanol (-20°C) and cooled with liquid N_2 until it reaches the temperature of -100°C.

ix.   The valve 9 is closed and the valves 10 and 15 are opened to start the transfer.

x.   The cold bricks on the top of the chamber are taken away and the dewar filled with cold ethanol below the ice chamber is removed and substituted by the thermos with warm water at 40°C. The thermos is placed in a position so that the water only warms the bottom of the chamber.

xi.   The transfer takes about 60 min. During the transfer the water trap needs to be checked to avoid the temperature to increase above -80°C. The presence of ice in the chamber and the progressive melting is checked looking at the baratron and listening to the sound of cracking ice. When no sounds are produced from the ice and the pressure value is below 0.05 mbar we assume that the

ice is melted. At this stage the thermos is removed and the magnetic stirrer is turned on in order to promote the air transfer.

xii. When the pressure decreases below 0.010 mbar, the dip tube is lowered in the helium tank. After 10 minutes, when the pressure is close to zero, valves 10 and 15 are closed. The dip tube is removed from the helium tank and connected to the valve 20. Valves 19, 4, 17, 7 and 9 are opened to pump the line for 20 minutes. In the meantime, valve 8 is closed and the water trap and the ice chamber can be removed from the line to be cleaned. A dry water trap can be installed on the line and the chamber can be cleaned with milliQ water and let it dry for the following day.

xiii. When the 20 min are elapsed, the oven is turned on at 100°C for 10 min and then the temperature is increased at 900°C for other 10 min.

xiv. The part of the line involved in the getter procedure is isolated (valve 19 is closed) and the sample is injected in the line opening valve 21. The sample is left to react with the getter for 20 min and then the valve 21 is closed and the air sample in the line is left to react for another 40 min. When 60 min are elapsed, the oven temperature is decreased to 300°C for 5 minutes to re-adsorb the H_2 created during the reaction with the getter. Another clean dip tube is cooled in the liquid N_2 and placed in the He tank. Valves 14, 6, 7 and 9 are opened to evacuate the connection for 10 min.

xv. Valve 9 and 6 are closed while valve 19 is opened. The pressure of the gas after the first getter step is noted in the lab book. Valve 6 is opened again and also valve 15 of the dip tube. The gas sample is let to transfer for 15 min and after 5 min the dip tube is lowered in the He tank. When the pressure is equal to zero, the transfer is over and valve 15 is closed. The residual pressure (which should be stable) is noted in the lab book.

xvi. Since a little amount of air is probably left in the dip tube, a second getter step is necessary. Valve 19 is closed and the oven temperature is increased again at 900°C, the valve 21 is opened and the air leftover in the dip tube are left to react with the getter for 20 min. Then the temperature of the oven is decreased to 300°C for 5 minutes to re-adsorb the created H_2.

xvii. After the second getter step, the leftover gas needs to be transferred to the dip tube. Valve 9 to the pump is closed with valve 6. Valve 19 is opened to let the gas expand in the line. The pressure is noted in the lab book. Then valves 6 and 15 are opened to transfer the leftover gas in the dip tube for 15 min. After 2 min, the dip tube is lowered in the He tank. When 15 min are elapsed and the pressure in the line is close to zero, the valve 15 on the dip tube is closed and transfer is over. The residual pressure is noted in the lab notebook.

xviii. The valve 14 is closed and the dip tube is removed from the He tank. The sample needs to rest for about 2 hours before being analysed with the mass spectrometer.

xix. At the end of the transfer the line needs to be prepared for the following lab day. The air in the clean water trap needs to be evacuated and the getter has to be changed.

xx. To change the getter, the valves 17 and 19 are closed and the oven is dismounted. The getter strips are delicately removed with the help of tweezers and a new getter strip (40 pieces) are placed inside the oven, which is then re-mounted on the line.

xxi. The line is let to evacuate overnight to be ready for the following laboratory day.
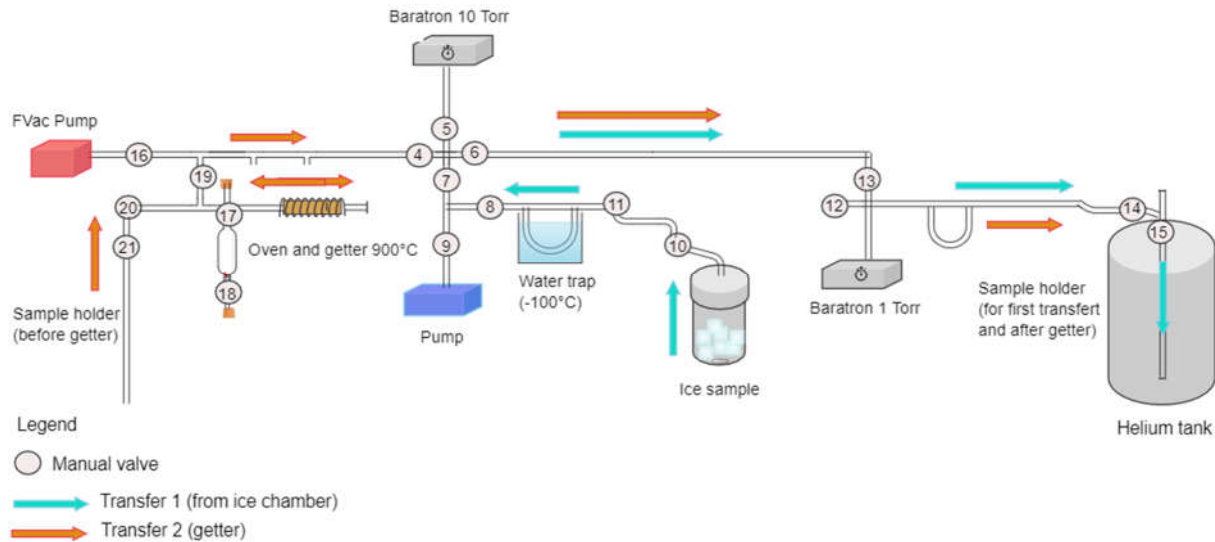
Figure 5.34: The getter method line setup for ice samples at LSCE. The gas path during the air transfer and during the getter steps are indicated with light blue and orange line respectively.

Figure 5.35: Getter method extraction line at LSCE. Left. Air transfer from the ice chamber to the dip tube. Right. Getter step.

5.3.2 Mass spectrometer analysis

The gas samples in the dip tubes are analysed, after the transfer and purification with the mass spectrometer.

5.3.2.1 The mass spectrometer

The analyses are performed on a dual inlet Thermo Fischer Scientific 253 Plus, the same instrument used to analyse the air samples extracted from TALDICE ice with the copper method. The resistors configuration, also in this case, has been changed (2021 configuration), in order to adapt the mass spectrometer to our samples and to the extraction method (Table 5.11). Considering the big size

of ice samples, the resistors configuration has been mainly changed for Ar and N_2 cups decreasing the amplification of the signal.

Amplifier housing channel	CUP	Gases/Masses	2018 config. (Ω)	2019 config. (Ω)	2020 config. (Ω)	2021 config. (Ω)
1	1	O_2 32 N_2 28	$3 \cdot 10^8$	$3 \cdot 10^8$	$3 \cdot 10^8$	$3 \cdot 10^8$
2a	2	Ar 36	$1 \cdot 10^{11}$	$1 \cdot 10^{11}$	$1 \cdot 10^{12}$	$3 \cdot 10^{11}$
2b		-	Not used	$1 \cdot 10^{12}$	$1 \cdot 10^{12}$	$1 \cdot 10^{12}$
3a	3	N_2 33	$3 \cdot 10^{11}$	$1 \cdot 10^{13}$	$3 \cdot 10^{11}$	$3 \cdot 10^{11}$
3b	-	-	Not used	$1 \cdot 10^{12}$	$1 \cdot 10^{12}$	$1 \cdot 10^{13}$
4a	4	Ar 38	$3 \cdot 10^{11}$	$1 \cdot 10^{12}$	$1 \cdot 10^{13}$	$1 \cdot 10^{12}$
4b		Kr 82 N_2 29	$3 \cdot 10^{10}$	$3 \cdot 10^{10}$	$3 \cdot 10^{10}$	$3 \cdot 10^{10}$
5	5	Kr 84 Xe 132	$1 \cdot 10^{13}$	$1 \cdot 10^{13}$	$1 \cdot 10^{13}$	$1 \cdot 10^{12}$
6a	6	Ar monitor	$1 \cdot 10^{13}$	$1\ 10^{13}$	$1 \cdot 10^{13}$	$1 \cdot 10^{13}$
6b		Xe 129 O_2 34	$1 \cdot 10^{11}$	$1 \cdot 10^{12}$	$1 \cdot 10^{11}$	$1 \cdot 10^{11}$
7a	7	Ar 40	$1 \cdot 10^{13}$	$1 \cdot 10^9$	$1 \cdot 10^{13}$	$1 \cdot 10^9$
7b		Kr 86	$3 \cdot 10^8$	$1 \cdot 10^{12}$	$3 \cdot 10^9$	$1 \cdot 10^{12}$
8a	8	Xe 136	$1 \cdot 10^{13}$	$1 \cdot 10^{13}$	$1 \cdot 10^{13}$	$1 \cdot 10^{13}$
8b		-	Not used	$1 \cdot 10^{13}$	$1 \cdot 10^{12}$	$3 \cdot 10^9$

Table 5.11: Resistors configuration changes performed on Thermo Fischer Scientific 253 Plus. The configuration 2021 is the one applied to analyse TALDICE air samples extracted and purified with the getter method. Changed resistors in 2021 configuration are underlined in black.

5.3.2.2 Analysis sequence

The TALDICE samples purified with the getter method are analysed with the dual inlet Thermo Fischer Scientific TM 253 Plus mass spectrometer. The sample introduction protocol follows the same procedure described in Section 5.2.2.2, while the analysis sequence has been modified to be adapted to the getter samples. For the getter method the pressure of the bellows is manually adjusted before the analysis to be ~30 mbar. The major difference, in comparison to the methodology applied for the samples treated with the wet line extraction, is that in this case we do not analyse the $\delta^{15}N$ since N_2 is removed by the getter.

The final sequence is composed by 4 blocks of Ar isotopes analysis, one block of Jump Ar Kr, 5 blocks for Kr isotopes and 3 peak jump blocks, 1 for Xe Ar and 2 for N_2 Ar. The standard-sample cycle injection and measurement is repeated 10 times per block and the raw delta value is computed by the mass spectrometer. The Pressure Imbalance Slope (PIS) blocks are treated in a separate sequence (Figure 5.36). The Kr PIS block is repeated 3 times, while the Ar PIS block is repeated 5 times. The Kr Ar jumps and Xe Ar jumps blocks are both repeated 3 times.

Figure 5.36: Complete analysis sequence applied to measure the TALDICE samples treated with the getter method to perform the Ar dating. Top. Full analysis sequence. Bottom. PIS sequence.

5.3.3   Data correction and calibration

The raw data obtained by the analysis of TALDICE ice samples need to be corrected for the same processes that influence the isotopic ratio during the mass spectrometer analysis of the samples purified with the copper method. In this section all the applied corrections are described in association with the improvements of the data set quality.

5.3.3.1 Background correction

As was described in Section 5.2.3.1, the low energy tail of ^{40}Ar is getting caught in the ^{38}Ar faraday cup. In the case of the copper method samples we corrected the measured ratios with a static background, using only one equation for each data set since the background was stable over time. For the samples treated with the getter method, on the other hand, we observed a dynamic behaviour of the background, which varies over time, that need to be corrected. The shape of the tail is monitored by running a high-voltage scan at the beginning and end of each block of 10 cycles. Each scan is processed to determine the real value of the background below the ^{38}Ar peak. This background is then related to the intensity measured on neighbouring cup 5 or cup 6 over several weeks. For the outside air samples measured with the getter method we observe that the background data could be separated in 3 groups

characterized by different slopes and intercepts to perform a more accurate correction (Figure 5.37 and Table 5.12). Such different equations are used to separately calculate the background for cup 5 and 6 for 3 different groups of outside air samples.
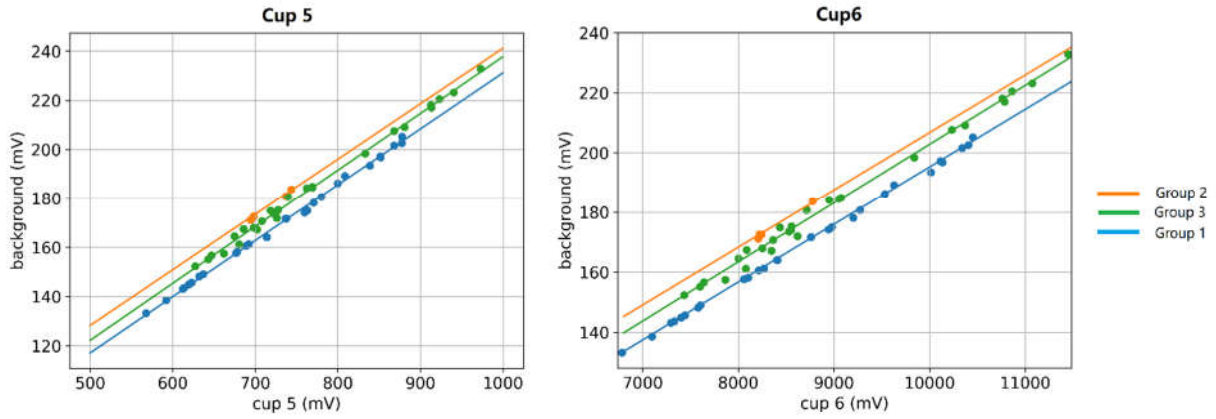
Figure 5.37: Correlation between the 6 signal and the background for cup 5 (left) and cup 6 (right). For each cup we defined 3 different background equations (group1, group 2 and group 3).
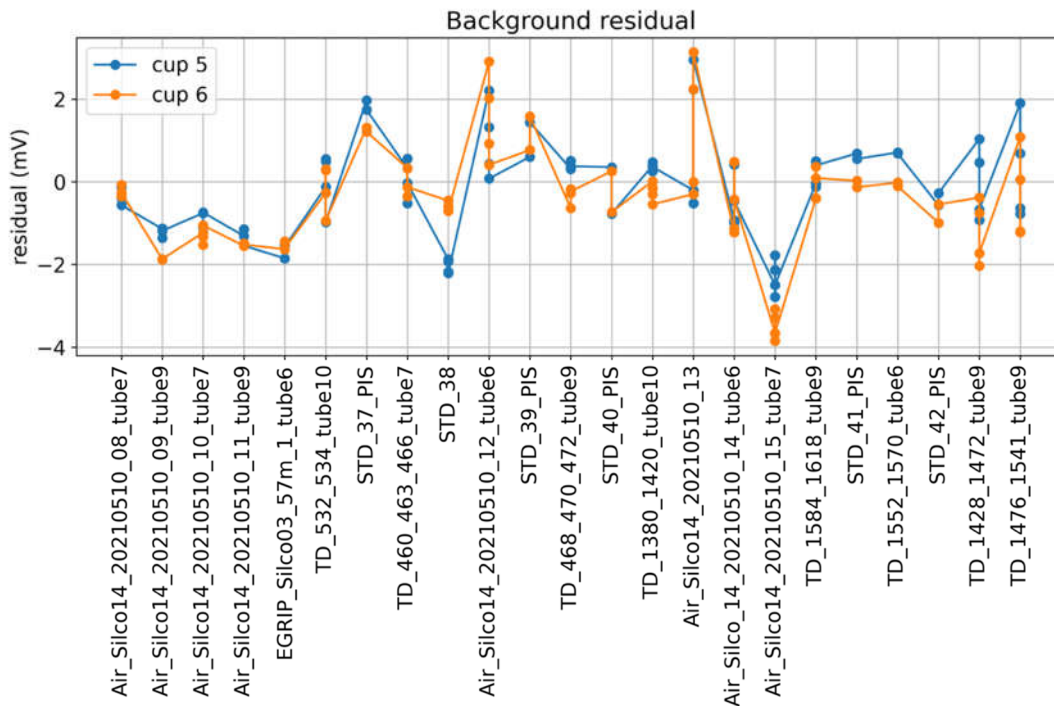
Figure 5.38: Background residuals calculated for both cup 5 (blue dots) and cup 6 (orange dots) for outside air and standard samples.

	Cup 5 slope	Cup 5 intercept	Cup 6 slope	Cup 6 intercept
Group 1 (blue)	0.228	3.120	0.0193	2.612
Group 2 (orange)	0.226	15.39	0.0192	14.500
Group 3 (green)	0.231	6.730	0.0197	5.853

Table 5.12: Cup 5 and cup 6 slopes and intercept values obtained from the linear regression of the background values. We define 3 different equations to correct the outside air measurements.

When the residuals become systematically different from zero, a new set is started, and a new regression made. Over several weeks of measurements, we noticed that the slope does not change much (0.0005 mV), but the intercept can change by up to 12 mV. The quality of the correction is assessed by looking at the residual of the determination of the background (Figure 5.38). The raw data are corrected using cup 6 since it minimizes the residuals.

5.3.3.2 Pressure imbalance sensitivity

The Ar and Kr ratios measured in both ice and air samples are corrected for the pressure imbalance sensitivity. For the getter method a separate PIS sequence is used (Figure 5.36) and is usually run during the day while the air extraction and purification from ice samples is performed. The sequence is made by 3 PIS blocks for Kr, A blocks for Ar, 3 for Kr/Ar Jump and 3 for Xe/Ar Jump. As the ice samples analysed with the getter method are not measured in replicates, the mean standard deviation of of block-averaged δ values within a sequence for all the samples on raw data and PIS corrected data is calculated. The PIS correction in well visible for the Ar ratios, while for the Kr ratios the correction does not change largely the data. For this reason in Figure 5.39 the Kr raw data and corrected data appear superimposed. The PIS correction clearly reduces the mean standard deviation in comparison to the raw data (Table 5.13).
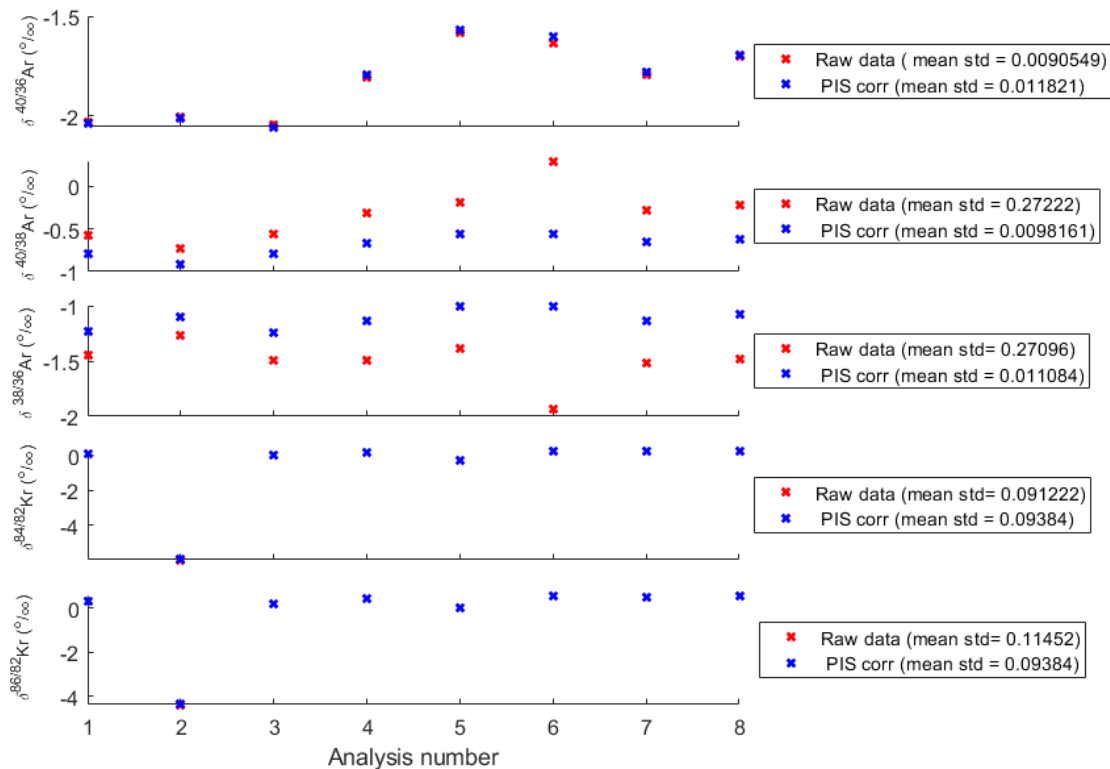
Figure 5.39: Comparison of $\delta^{40/36}$Ar, $\delta^{40/38}$Ar, $\delta^{38/36}$Ar, $\delta^{84/82}$Kr and $\delta^{86/82}$Kr before (red crosses) and after PIS correction (blue crosses) on TALDICE ice samples. Analysis numbers corresponds to the progressive number of samples analysed over time.

Permill (‰)	$\delta^{40/36}$Ar	$\delta^{40/38}$Ar	$\delta^{38/36}$Ar	$\delta^{84/82}$Kr	$\delta^{86/82}$Kr
Mean std raw	0.009	0.272	0.271	0.091	0.115
Mean std PIS corr	0.011	0.010	0.011	0.094	0.094

Table 5.13: Mean standard deviations calculated before and after PIS correction applied on Ar and Kr isotopes ratios.

5.3.3.3 Chemical Slope

For the getter method the chemical slope is based on the same principle already described for the copper method, but for the getter method the presence of Ar in the sample appears to interfere with measurement of Kr. In this case the chemical slope is defined through a set of measurements of standard samples in which the amount of pure Ar aliquot is progressively increased. The values of measured Kr ratios need to be corrected for this effect.
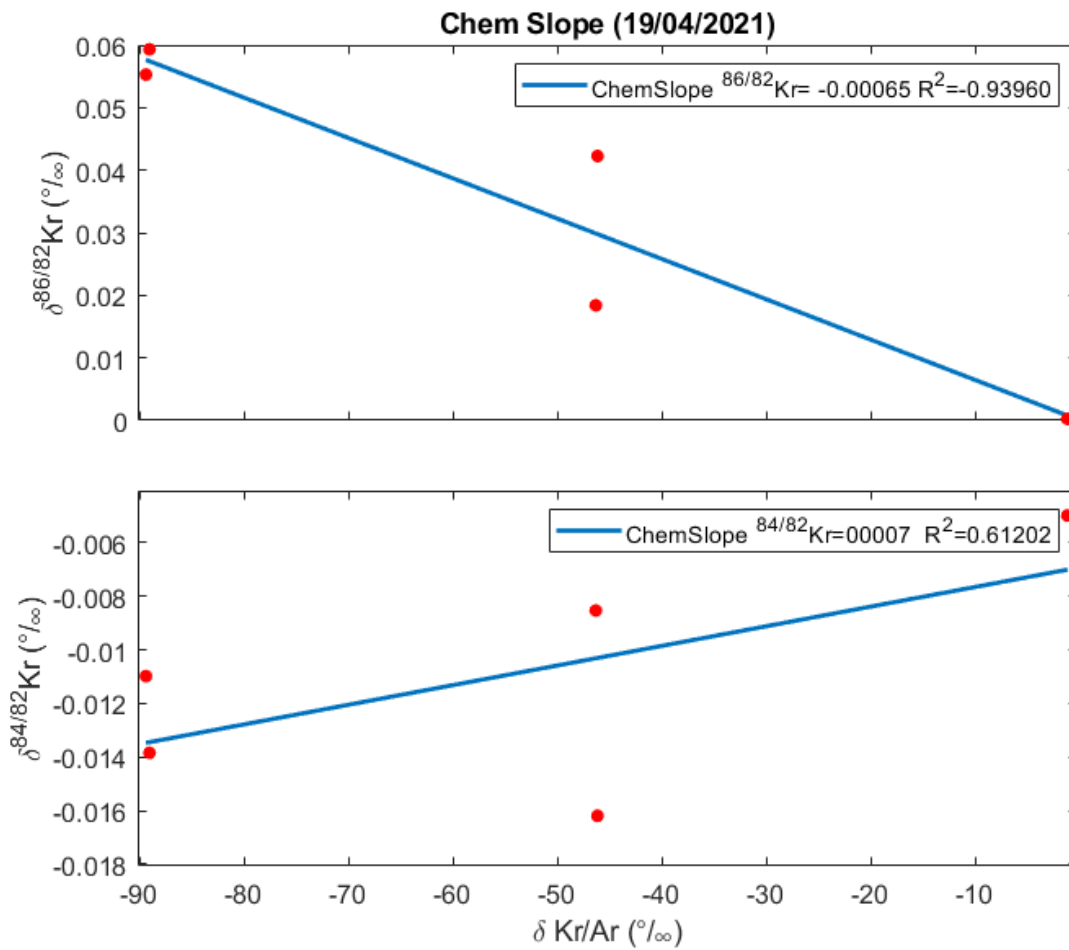
Figure 5.40: Chemical Slope applied for corrections on $\delta^{86/82}$Kr, $\delta^{84/82}$Kr isotopic ratios. We use the chemical those chemical slope to correct the TALDICE samples extracted and purified with the getter method.

The chemical slope (CS) for Kr is defined through the following equation:

$$CS = \frac{\Delta \delta Kr_{PIS\ corr}}{\Delta \delta Kr/Ar} \tag{5.30}$$

The chemical slope is applied on samples corrected for the pressure imbalance sensitivity as following:

$$\delta Kr_{CS\,corr} = \delta Kr_{PIS\,corr} - CS \cdot Kr/Ar_{measured} \tag{5.31}$$

For the TALDICE data set, we add aliquots of 0%, 5%, 10%, 15% and 20% of pure Ar to standard samples. In this case Ar values are not corrected for the chemical slope effect as they are not affected by it. The chemical slope correction is applied to the Kr ratios but is negligible (Figure 5.41).

This correction is also irrelevant for the final dating purpose as Kr measurements are not applied in the final gas age calculation. This is visible in Figure 5.41 where data corrected for both PIS and ChemSlope ae perfectly superimposed on only PIS corrected data.
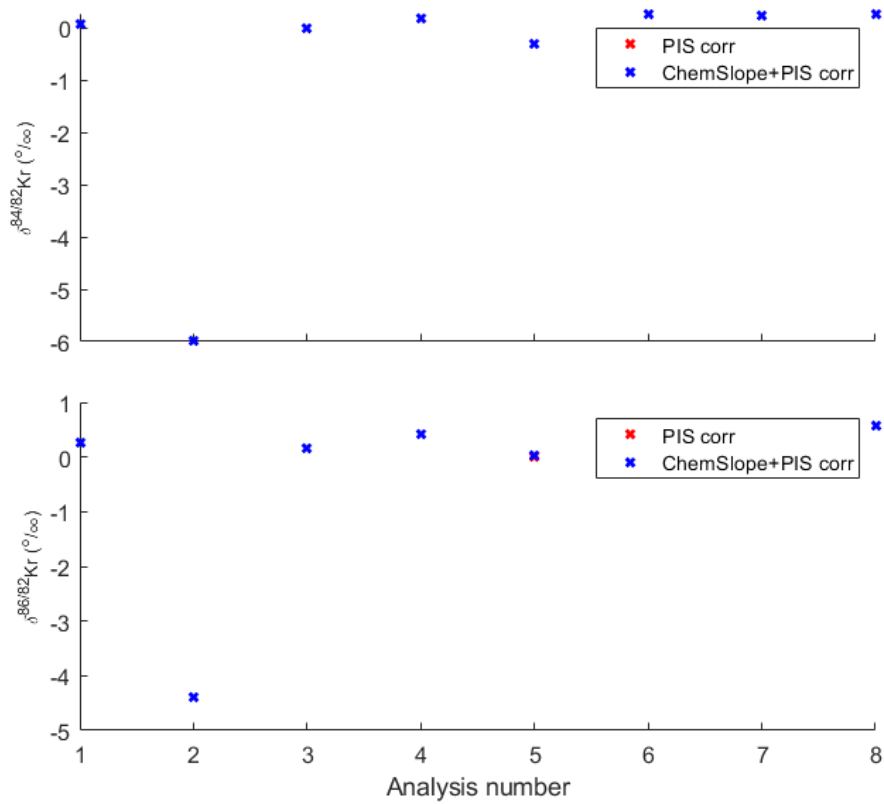
Figure 5.41: Comparison of $\delta^{84/82}$Kr and $\delta^{86/82}$Kr corrected for PIS (red crosses) and for PIS and Chemical Slope (blue crosses) on TALDICE ice samples. Analysis numbers corresponds to the progressive number of samples analysed over time. The Chemical Slope effect correction for the Kr ratios is negligible.

5.3.3.4 Calibration to the outside air

To perform the air calibration on TALDICE ice samples purified with the getter method, 22 outside air samples are measured. The air samples employed for the calibration come from the silco can filled with outside air, which is transferred and purified following the protocol described in Section 5.3.1.1. The air values are corrected for the background effect, the PIS and the chemical slope (except for the Ar ratios and δKr/Ar) as described in the previous sections. From the entire air data set we choose the last 10 samples (red box in Figure 5.42). We select the air samples data set that guarantee the best

reproducibility of the air data, with comparable isotopic values and the lowest standard deviations (Table 5.14). The delta values are averaged (δ_{air}) and used to correct the ice samples delta values (Figure 5.42):

$$\delta_{air\,corr} = \delta_{PIS,chem.slope} - \delta_{ext.air} \qquad (5.32)$$

(‰)	$\delta^{40/36}$Ar	$\delta^{40/38}$Ar	$\delta^{38/36}$Ar	$\delta^{86/82}$Kr	$\delta^{84/82}$Kr	δKr/Ar
Mean	-3.2681	-1.3572	-1.9454	-0.9426	-0.4842	-14.9169
Std	0.0206	0.0932	0.0632	0.0274	0.0282	0.3354

Table 5.14: Air samples from the silco can. Isotopic mean values for $\delta^{40/36}$Ar, $\delta^{40/38}$Ar, $\delta^{38/36}$Ar, $\delta^{84/82}$Kr, $\delta^{84/82}$Kr and δKr/Ar used for air calibration of TALDICE ice samples. We used the values of the mast 10 air measurements (red box in Figure 5.42).
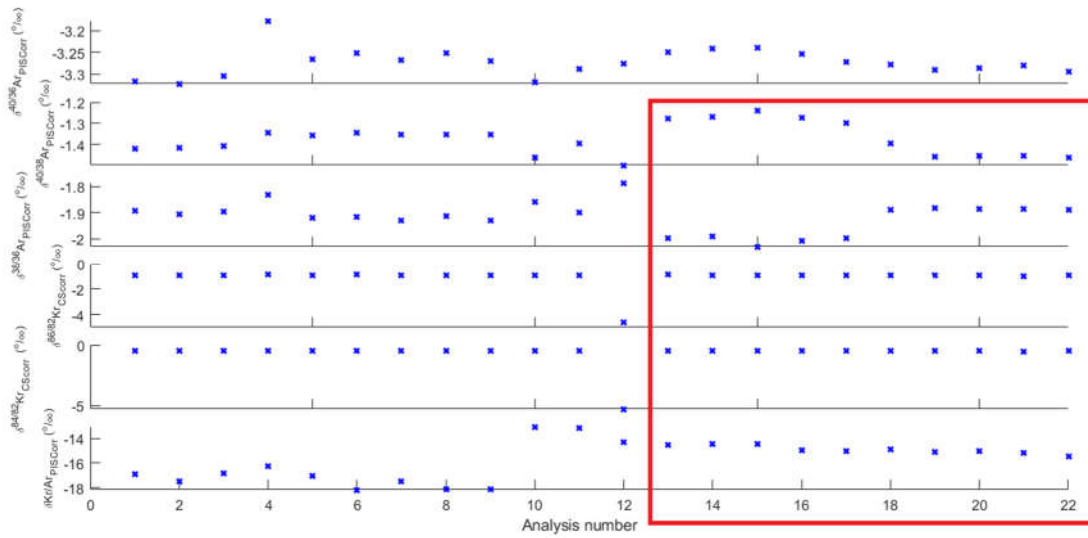
Figure 5.42: Air samples isotopic values data set for $\delta^{40/36}$Ar, $\delta^{40/38}$Ar, $\delta^{38/36}$Ar and δKr/Ar corrected for PIS and $\delta^{86/82}$Kr and $\delta^{84/82}$Kr corrected for chemical slope. The air data in the red box are used to calibrate the TALDICE ice samples and to calculate the Ar dating analytical uncertainty for the getter method.
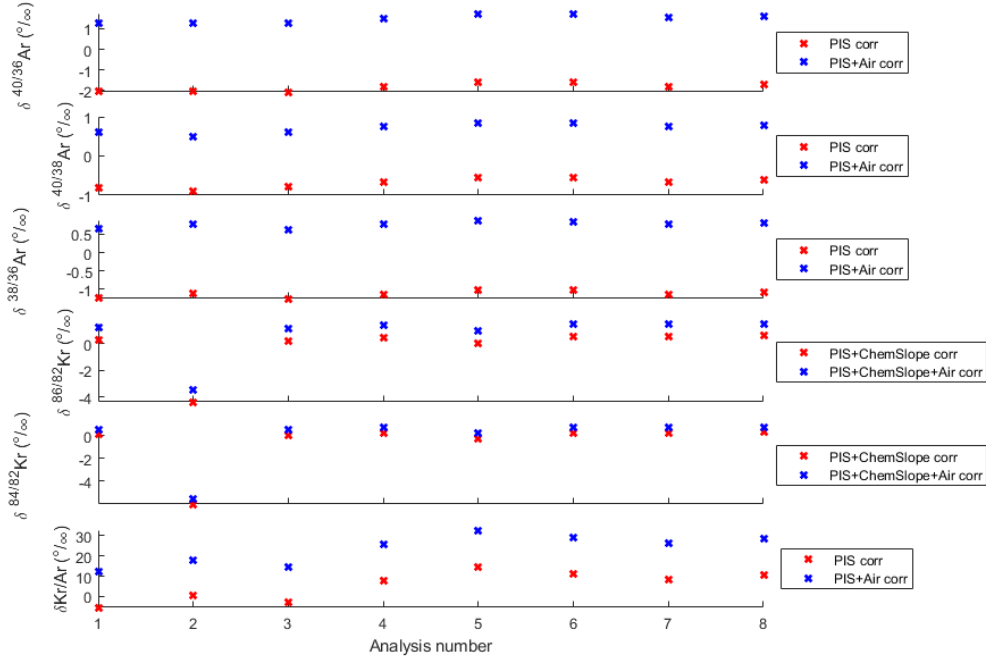
Figure 5.43: Comparison of $\delta^{40/36}$Ar, $\delta^{40/38}$Ar, $\delta^{38/36}$Ar and δKr/Ar corrected for PIS (red crosses) and for PIS and outside air (blue crosses) on TALDICE ice samples. Comparison of $\delta^{86/82}$Kr and $\delta^{84/82}$Kr corrected for PIS and chemical slope and corrected for PIS, chemical slope ad outside air analysis numbers corresponds to the progressive number of samples analysed over time.

5.3.4   Gravitation and gas loss corrections

In the case of the TALDICE gas samples extracted and purified with the getter method, no prior data cleaning is performed as ice samples are not measured in replicates. The evaluation of the data quality will be performed after the age calculation and the comparison with the TALDICE published chronologies.

5.3.4.1 Gravitational correction

We correct argon isotope from the Argon gas loss, as measured by the dKr/Ar ratio. As a first step, we need to correct the ratios from gravitational fractionation. Since δ^{15}N is not measured in TALDICE samples treated with the getter method, gravitational corrections of the measured isotopic ratios are performed substituting the δ^{15}N value with the $\delta^{84/82}$Kr ratio, which has a mass difference of 2 g/mol and with $\delta^{40/36}$Ar for Kr/Ar. The Ar isotopic ratios are corrected as following:

$$\delta^{40/36}Ar_{grav\,corr} = \delta^{40/36}Ar - 2 \cdot \delta^{84/82}Kr \tag{5.33}$$

$$\delta^{40/38}Ar_{grav\,corr} = \delta^{40/38}Ar - \cdot \delta^{84/82}Kr \tag{5.34}$$

$$\delta^{38/36}Ar_{grav\,corr} = \delta^{38/36}Ar - \cdot \delta^{84/82}Kr \tag{5.35}$$

$$\delta Kr/Ar_{grav\,corr} = \delta Kr/Ar - 12 \cdot \delta^{40/36}Ar \tag{5.36}$$

5.3.4.2 Gas loss correction

Here the Ar ratios are corrected for the gas loss effect using the δKr/Ar $_{GravCorr}$ ratios as in Severinghaus et al. (2003). The applied gas loss slope is calculated following the regression of $\delta^{40/36}$Ar$_{grav\ corr}$ and $\delta^{40/38}$Ar$_{grav\ corr}$ with respect to δKr/Ar$_{grav\ cor}$, discarding outliers that have values of $\delta^{40/36}$Ar$_{grav\ corr}$ >0.6 ‰. These outliers are caused by large errors in $\delta^{84/82}$Kr used for the gravitational correction. The regression values for all isotopes are presented in Table 5.15. Although we have few data points, and the R values are small, the gas loss slope of -0.0073‰/‰ for $\delta^{40/36}$Ar is coherent with values found in other cores and in the literature (Severinghaus et al., 2003).

	$\delta^{40/36}$Ar	$\delta^{40/38}$ Ar	$\delta^{38/36}$Ar
Gas loss slope	-0.0073	-0.0142	-0.0007
Intercept	0.1981	0.1446	0.0965
R	-0.4425	-0.4786	-0.1060
p	0.3796	0.0834	0.7304
std	0.0074	0.0075	0.0021

Table 5.15: Gas loss slopes, intercepts and statistical parameters for $\delta^{40/36}$Ar, $\delta^{40/38}$ Ar and $\delta^{38/36}$Ar.

In addition, the slope for all three isotope pairs, when scaled per mass unit is not significantly different, and we choose to scale the gas loss slope $\gamma(\delta^{40/36}$Ar$)$ to the other isotopes such that:

$$\gamma(\delta^{\frac{40}{38}}Ar) = \gamma(\delta^{\frac{38}{36}}Ar) = \gamma(\delta^{\frac{40}{36}}Ar)/2 \qquad (5.37)$$

This justifies that the gas loss correction cancels out in the calculation of δAr$_{atm}$.
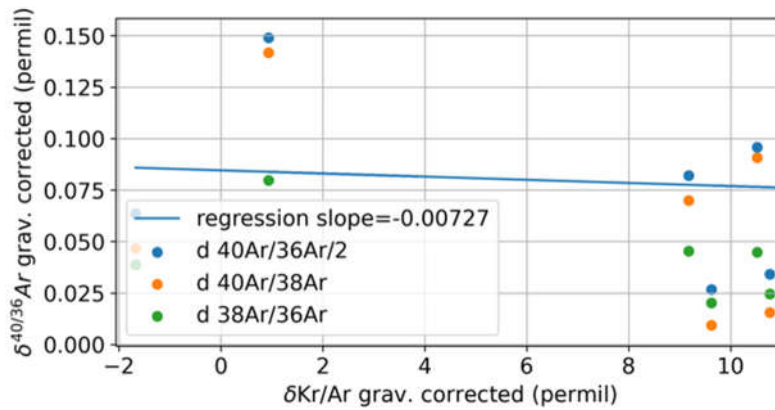
Table 5.44: Gas loss slope (blue line) computed for $\delta^{40/36}$Ar$_{GravCorr}$ (blue dots) and δKr/Ar$_{GravCorr.}$

5.3.5 TALDICE samples dating

After applying all the corrections, the $\delta^{40/38}$Ar $_{paleoatmospheric}$ ratio for TALDICE ice samples is computed applying the equation 5.1 published in Bender et al. (2008). To calculate the age of the air trapped in TALDICE ice samples treated with the getter method the following equation is applied:

$$^{40/38}Ar_{age} = -\ (\delta^{40/38}Ar_{paleoatmosphere} + e\ )/0.066 \cdot 10^3 \tag{5.38}$$

Where e is the value of the parameter applied for the age calculation used to correct the $\delta^{40/38}Ar_{paleoatmosphere}$ samples' values for the modern value of $\delta^{40/38}Ar_{atm}$. The value e is calculated as the average of the misfit of $\delta^{40/38}Ar_{paleoatmosphere}$ for TALDICE samples of know age between 0 and 200 ka.

$$e = mean(\delta^{40/38}Ar_{paleoatmosphere} - \frac{Age}{0.066} * 1000) = 0.0214 \tag{5.39}$$

The misfit is plotted for each sample in the Figure 5.45. We notice no obvious difference between bubbly and clathrate ice, as we saw in the copper method dataset, and this is likely due to the fact that gas loss fractionation is automatically corrected in the definition of $\delta^{40/38}Ar$ $_{paleoatmossphere}$.
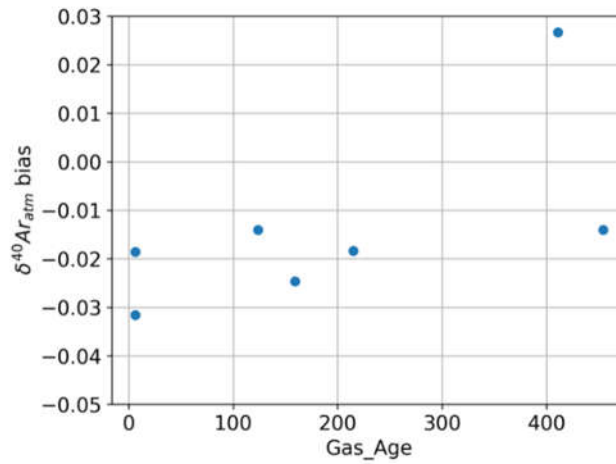
Figure 5.45: Misfits for $\delta^{40/38}Ar_{atm}$ plotted versus depth for the getter samples.

Since no replicate measurements are performed for the getter method, the minimum uncertainty on the gas age is calculated taking into the account the standard deviation of the air samples. The $\delta^{40/38}Ar_{paleoatmosphere}$ value (eq. 5.38) and the respective standard deviation are calculated on the dataset of 10 air samples (used also for air calibration), to evaluate the analytical uncertainty (red box in Figure 5.42). The $\delta^{40/38}Ar_{paleoatmosphere}$ standard deviation for air samples is equal to ±0.156‰ is then turned into gas age uncertainty applying the following equation:

$$^{40/38}Ar_{age} = (\delta^{40/38}Ar_{paleoatmosphere})/0.066 \cdot 10^3 \tag{5.40}$$

The uncertainty for the getter method dating calculated using the outside air samples is equal to ±2.36·10³ ka. However, this uncertainty appears overestimated and we propose two other approaches for its calculation. The uncertainty on the final Ar ages can also be estimated considering neighbouring samples in the TALDICE getter sample data set (Table 5.16) and calculating the standard deviation. For the shallow samples, samples 2 and 3 could be considered as neighbouring. The uncertainty calculated for Holocene samples is ±138 ka. For deeper samples, the standard deviation can be calculated between the neighbouring samples 5 and 6, and it is ±28 ka, which probably underestimates the true uncertainty.

Third, we can compute the standard deviation of the difference between the measured and expected age, when we know the age of the samples. We find ±0.0065‰ which corresponds to ±99 ka and is comparable to ±83 ka, the average uncertainty of shallow and deep samples.

Sample No.	Top depth (m)	Bottom depth (m)	Mean depth (m)	$\delta^{40/38}Ar_{paleoatm}$ (±0.0065) (‰)	$^{40/38}Ar$ age (±99) (ka)	AICC 2012 and TALDICE deep1 (ka)			
						gas age top	gas age bottom	avg gas age	std gas age
1	459.71	465.94	462.825	-0.287	4022.7	6.08	6.21	6.14	±0.15
2	467	471.25	469.125	-0.019	-37.5	6.24	6.29	6.26	±0.16
3	531.06	533.94	532.5	-0.032	160.0	7.65	7.71	7.68	±0.16
4	1379.05	1419.25	1399.15	-0.022	11.6	109.65	132.17	120.91	±2.15
5	1427.05	1471.25	1449.15	-0.033	168.1	140.13	172.84	156.48	±2.66
6	1475.05	1540.25	1507.65	-0.035	208.1	174.92	312.02	243.47	±1.91
7	1551.05	1572.25	1561.65	-0.0004	-318.2	-	-	397-[81]Kr	±20
8	1583.05	1617.25	1600.15	-0.044	341.8	-	-	410-[81]Kr	±20

Table 5.16: TALDICE samples values of $\delta^{40/38}Ar_{paleoatmospheric}$ and the respective calculated ages compared with samples ages from the AICC2012 and TALDICE deep1 age scales (Crotti et al., 2021; Veres et al., 2013). The minus sign (-) indicates that the calculate age is in the future. Shaded lines indicate outlier samples.

In Table 5.16 the Ar ages computed for TALDICE samples extracted and purified with the getter method are reported. Since the data cleaning procedure has not been performed at the initial stage of the data treatment, due to the lack of replicate measurements, the outliers are identified at this stage (shaded lines in Table 5.14). From our data set, samples 1 and 7 can be classified as outliers. In particular, the Ar age of samples 1 is far away too old (~4 Ma) in comparison to the real age, ~6 ka, which lies in the Holocene. Such old age estimation is connected to the low $\delta^{40/38}Ar_{paleoatmosphere}$ value (-0.287‰), which is probably due to the high $\delta^{38/36}Ar$ value (0.785‰), similar to the one obtained for older samples as number 4 and 5 (Table 5.17). Sample 2, on the other hand, even if it shows an Ar age in the future (-37.5 ka), is not removed from the data set as its Ar ratios are in accordance with the data from the other samples (Table 5.17). The second and last sample classified as outlier is sample number 7. It is characterized by an extremely small value of $\delta^{40/38}Ar_{paleoatmosphere}$ (-0.004‰) and an age evaluation in the future that does not lie in the uncertainty estimation (-318.2 ka). Sample number 7 is removed from the TALDICE data set, but the reason related to such a small paloeatmospheric is unknown since Ar ratios are in line with the other samples (Table 5.17).

Sample no.	Top depth (m)	Bottom depth (m)	$\delta^{40/36}Ar$ (‰)	$\delta^{40/38}Ar$ (‰)	$\delta^{38/36}Ar$ (‰)
1	459.71	465.94	1.288	0.500	0.785
2	467	471.25	1.244	0.615	0.632
3	531.06	533.94	1.263	0.615	0.645
4	1379.05	1419.25	1.504	0.740	0.761
5	1427.05	1471.25	1.516	0.741	0.772
6	1475.05	1540.25	1.607	0.785	0.818
7	1551.05	1572.25	1.697	0.843	0.842
8	1583.05	1617.25	1.729	0.842	0.884

Table 5.17: Values of $\delta^{40/36}Ar$, $\delta^{40/38}Ar$ and $\delta^{38/36}Ar$ for TALDICE samples extracted and purified with the getter method. Shaded lines indicate outlier samples.
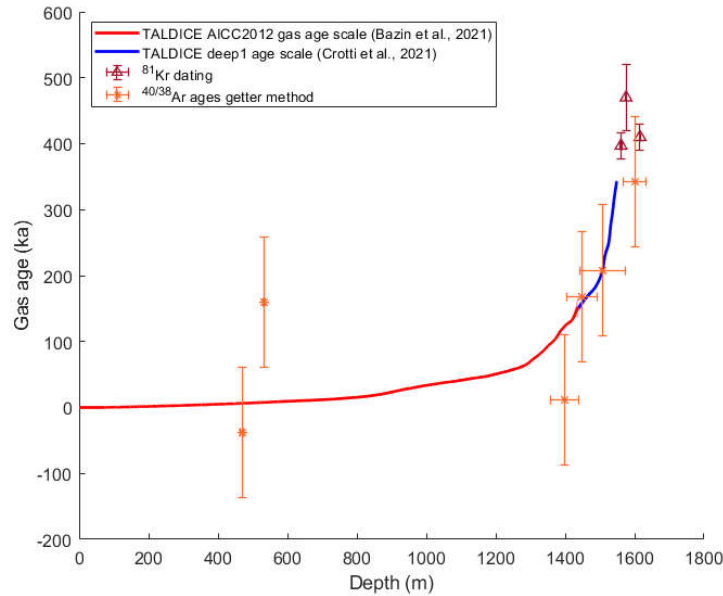
Figure 5.46: $^{40/38}$Ar ages values -getter method- (orange stars) compared with the AICC2012 (red curve) (Bazin et al., 2013), TALDICE deep1 (blue curve) age scales and ^{81}Kr dated layers (brown triangles) (Crotti et al., 2021).

The TALDICE samples that are not excluded from the data set display Ar ages, considering the uncertainty, that fall in the estimated gas age by the AICC2012 and TALIDCE deep1 chronologies. In addition, we can observe that the deeper samples Ar ages (from 5 to 8) nicely agree with the AICC2012 and TALIDCE deep1 gas ages. On the other hand, samples 3 is older (160 ka) with respect to real gas age (7.71 ka) and sample 4 has an Ar age of 11.6 ka, younger with respect to real gas age of 132.17 ka (Figure 5.46, Table 5.16). The Ar dating applied with the getter provide gas ages which are in good accordance with the established TALDICE chronology, however further improvements are needed in order to increase the precision of the dating and to reduce the uncertainty.

5.4 Conclusions and future perspectives

In this chapter two different Ar dating techniques, the copper method and the getter method, are presented and applied on two set of TALDICE samples. In the first part of the chapter new developments of the copper method, aiming at reducing the samples size down to ~65 g are illustrated. The extraction line and the protocols for both air and ice samples are presented. We also show the improvements on the mass spectrometer, consisting in the modification of the resistors configuration to amplify the signal for Ar and N_2 isotopes. In addition, all the corrections performed on the data and the outliers removal process is described. Our results suggest that for the TALDICE samples, the gas loss correction and the calculation of the $Ar_{paleoatmosphere}$ values should be performed separately on shallow (<600 m) and deep samples (>600 m depth). Moreover, such a difference in the application of the gas loss and $Ar_{paleoatmosphere}$ calculation indicates that the bubbly ice (shallow samples) is less affected by the gas loss phenomenon with respect to the deeper clathrate ice, typical condition of deep ice (Ikeda-Fukazawa et al., 2005; Oyabu et al., 2021). The TALDICE data suggest that the Ar dating applied on small ice samples purified

with the copper method can be performed using both the $\delta^{40/36}Ar$ and $\delta^{40/38}Ar$, but for the TALDICE data set the $^{40/36}Ar$ ages better agree with the gas ages estimated by the AICC2012 (Bazin et al., 2013) and TALDICE deep1 (Crotti et al., 2021) chronologies (Figure 5.47). Such preliminary test highlight that the copper method applied on small ice samples (~65 g) provide interesting Ar dating results, however further developments of on both analytical and correction sides are necessary to improve the precision of the technique and reduce the dating uncertainty.

The second part of this chapter is focused on the application of the classic Ar dating getter method (Bender et al., 2008; Severinghaus et al., 1998; Yau et al., 2016) on bigger TALDICE ice samples (500-800 g) neighbouring to the samples analysed with the copper method, in order to compare the two techniques. For the getter method the line set up, protocols and mass spectrometer setting are illustrated as well. The raw data treatment is performed differently in comparison to the one applied for the copper method. Due to great variability of the background slope, we applied different background equations to correct each sample differently. In addition, the chemical slope correction is not applied on the Ar ratios and the gas loss correction is not necessary since it cancels out with the mass scaling. The getter method traditionally uses $^{40/38}Ar_{paleoatmosphere}$ to compute the samples gas age and we adapted the correction to the TALDICE data set calculating the offset parameter. Moreover, we look for the outliers only when the Ar ages are computed for all the samples, since no replicates measurements are available due to large size of the samples. The computed TALDICE Ar ages show that, even if 2 samples are classified as outliers, Ar dating performed with the getter method provide gas ages which are in good accordance with the established TALDICE chronology (Figure 5.47).
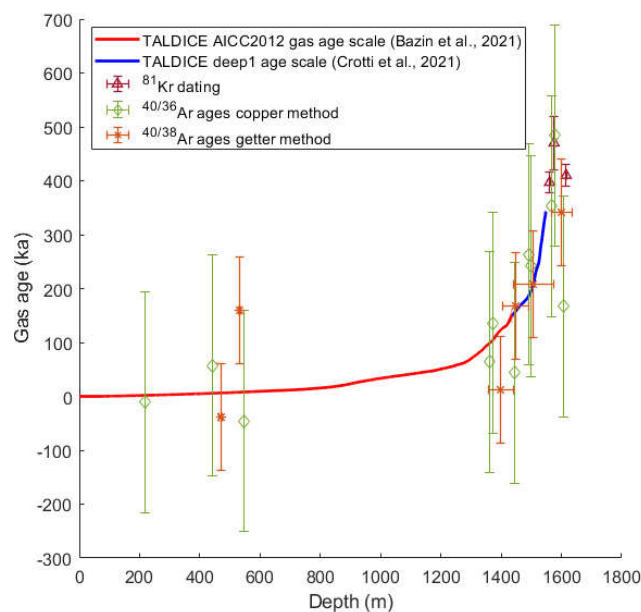
Figure 5.47: $^{40/36}Ar$ ages values -copper method- (green diamonds) and $^{40/38}Ar$ ages values -copper method- (orange stars) compared with the AICC2012 (red curve) (Bazin et al., 2013), TALDICE deep1 (blue curve) age scales and ^{81}Kr dated layers (purple triangles) (Crotti et al., 2021).

To conclude, we suggest that our preliminary results for the Ar dating performed on small size samples (~65 g) with the copper method produce promising results on TALDICE ice samples even if further improvements are needed. The dating technique is able to provide coherent gas ages with respect to established chronologies, however it is still affected by high uncertainties (±205 ka). Those experiments represent an encouraging starting point for further improvements and future applications under the light of the forthcoming European Project Beyond EPICA Oldest Ice, which aims at drilling a 1.5 Ma old ice core.

6. <u>Conclusions and future perspectives</u>

This Ph.D. thesis focuses on the investigation of the deeper portion of the TALDICE ice core through the combination of new techniques, as [81]Kr and Ar dating, and a multiproxy approach, with the combination of glaciological, marine core data and modelling experiments. This work led to a published paper, a submitted manuscript and a technical chapter detailing the Ar dating copper method developments and preliminary results.

In Chapter 3 the published paper Crotti et al. (2021) is presented. The article is centred on the definition of the TALDICE deep1 chronology, a new age scale that extends the AICC2012 age scale (Bazin et al., 2013) back to 343 ka (MIS 10.1) at 1548 m depth, including two older interglacial periods MIS 7.5 and MIS 9.3, which were not included in the previous chronology. The chronology stops at 1548 m depth since below this depth both δD and $δ^{18}O_{atm}$ profiles diverge from the EDC records and below 1570 m depth they assume a quasi-flat shape, indicating the lack of a preserved climatic signal. To better understand what mechanism caused the disruption of the climatic record in the ice below 1548 m depth, three layers have been dated with the absolute method of [81]Kr. The dating results indicate that below 1548 m depth the three dated layers show a similar age of ~450 ka due to the likely action of mixing and folding processes. Such disruption of the stratigraphic order may be connected to the presence of the adjacent subglacial hill that create disturbances in the ice located at the deepest portion of the valley. Further analyses are needed to better investigate the processes acting below 1548 m depth. Moreover, the construction of the new TALDICE deep1 chronology extends the climatic record back to 343 ka and allows the study the δD signal until MIS 10.1. Interestingly, the TALDICE isotopic record reveals some unique features during the interglacial periods MIS 7.5 and MIS 9.3 already observed for MIS 5.5 by Masson Delmotte et al. (2011) which need to be further investigated.

Chapter 4 addresses the scientific question formulated at the end of Chapter 3 regarding the interpretation of the unique shape of the TALDICE $δ^{18}O$ signal during past interglacial periods. In order to explain which phenomenon/a produced the so called "double-peak" shape, the manuscript presents a multiproxy approach associated with modelling sensitivity experiments. At first the TALDICE $δ^{18}O$ *d*-excess and ssNa[+] flux profiles data set is compared to EDC profile during interglacials, excluding the possibility that past sea ice extension variations and moisture sources changes might have generated the isotopic anomalies. The hypothesis that the temperature variations due to Talos Dome site elevation changes might have caused the isotopic anomalies is manly investigated in the manuscript, computing the elevation variations directly from the TALDICE isotopic record and comparing them with the site elevation variations obtained by 6 sensitivity experiments performed with the GRISLI ice sheet model (Quiquet et al., 2018). The results show that Talos Dome site has probably undergone elevation variations of 100-400 m during the past interglacials, with a major ice thickness variation during MIS 9.3, likely connected to Wilkes Subglacial Basin ice sheet great margin retreat.

To validate this elevation change hypothesis, the modelling results are matched with the ice rafted debris record (IBRD) and the Neodymium isotopes signal from the U1361A sediment core record (Wilson et al., 2018), which show that, during MIS 5.5 and especially during MIS 9.3, the Wilkes Subglacial Basin ice sheet has been subjected to ice discharge events. Such assumptions are also validated by new sediment core records from the Southern Ocean (Chadwick et al., 2020; Shukla et al., 2021), suggesting that a double phase ocean warming during interglacials might have contributed to the Wilkes Subglacial Basin ice sheet margin retreat and to the Talos Dome elevation variations. However, further investigations will be necessary to better understand the past response of the Wilkes Subglacial Basin ice sheet to atmospheric and oceanic warming, in order to predict its future dynamics in the context of global warming.

Chapter 5 is the last chapter and is a technical report of the preliminary tests performed with the application of the Ar copper method to date small TALDICE ice samples (~ 65 g). The extraction line and the protocols for both air and ice samples, the improvements on the mass spectrometer and the data treatment steps are presented. A tailored gas loss correction for the samples and specific coefficients applied to the age calculation are also introduced. Our results show that $^{40/36}$Ar ages agree well with the gas ages estimated by the AICC2012 (Bazin et al., 2013) and TALDICE deep1 (Crotti et al., 2021) chronologies, even if associated with ±205 ka uncertainty. In addition, to validate the quality of the measurements performed with the copper method, we performed Ar dating with the well-established getter method on big TALDICE ice samples (500-800 g) on neighbouring samples to the ones analysed with the copper method. In the chapter all corrections and data treatment procedures are presented. The final results show that with the getter method we obtain Ar ages that are comparable with both the Ar dating obtained with the copper method and the established TALDICE chronologies. Such outcome suggests that the Ar dating performed with the copper method produces promising results on small samples (65 g). Further improvements of this methodology would help in reducing the uncertainty and in making this technique available for future applications on the forthcoming 1.5 Ma ice core, in the framework of the European Project Beyond EPICA Oldest Ice.

This thesis work represents the first extensive study on the deep part (below 1438 m depth) of the TALDICE ice core. The definition of the TALDICE deep 1 chronology allows to extend the climatic record back to MIS 10.1 (Crotti et al., 2021). Moreover, the δD profile below 1438 m depth at 5 cm resolution is presented and interpreted in Chapter 4. The δD and δ^{18}O$_{atm}$ records point to a preserved climatic signal until 1548 m depth. However, below this depth limit it appears that the record is not preserved due to mixing/folding processes guessed from the ^{81}Kr dated layers, which show a similar age at different depths.

The lowermost layers of the TALDICE ice core are still poorly studied and additional researches could be carried on in future. Further studies might focus on different topics, from signal preservation to ice dynamics affecting the bottom part of the core. Here some future perspectives of this thesis work:

i.   *Completion of the TALDICE isotopic (δD and $\delta^{18}O$) record at 5cm resolution below 1300 m:* in this thesis the δD complete record at 5 cm resolution is presented for the core portion below 1438 m depth. The (δD and $\delta^{18}O$) upper part of the core, excluding the $\delta^{18}O$ record for the MIS 5.5 period published by Masson Delmotte et al. (2011), there is no complete record for the part below 1300 m. The completion of the record at 5 m resolution would allow to increase the resolution of the available data (mostly 1 m resolution) set and improve the climatic interpretation.

ii. *Increase the resolution of the $\delta^{18}O_{atm}$, $\delta^{15}N$ and $\delta O_2/N_2$ records:* thanks to the new measurements displayed in Chapter 3 the of oxygen and nitrogen isotopic records in the air bubbles have been extended until the bottom of the core and the resolution has been increased up to ~2.6 ka. Additional $\delta^{18}O_{atm}$ measurements would be helpful to increase the actual resolution in order to perform a more precise synchronization with other cores (e.g. EDC) and to better define the processes acting below 1548 m depth. In addition, further measurements of $\delta O_2/N_2$ on replicates samples in the deeper portion of the core would be helpful to better define the coefficient for the gas loss correction. Since the mass spectrometer measures also the $\delta^{15}N$ on the same samples, such data might be helpful to compute a more accurate LID and to improve the quality of the thinning function.

iii. *Definition of a new age scale for the whole TALDICE core:* at the moment the TALDICE AICC2012 (Bazin et al., 2013; Veres et al., 2013) and the TALDICE deep1 (Crotti et al., 2021) are the two newest chronologies for the core. The AICC2012 stops at 1438 m depth, while the TALDICE deep1 extends the AICC2012 until 1548 m depth. The improvement of the isotopic records (in both ice and gas matrixes) indicated above might represent a useful tool to define a revised and unique chronology for the entire core, reducing the uncertainties, especially in proximity of the layers of conjunction between the two age scales, and providing a coherent age scale from the top until 1548 m depth.

iv. *Investigation on the signal preservation:* it has been observed in Chapter 4 that the δD record in TALDICE is affected by an exponential decrease in resolution with depth. During the interglacial periods the temporal resolution drops from 0.63 ka/m for MIS 5.5 to 3.8 ka/m for MIS 9.3, almost 10 times less resolved in comparison to EDC for the same time periods. In addition, a great smoothing acting on the TALDICE isotopic signal (δD and $\delta^{18}O$) and erasing the high-frequencies can be observed for MIS 9.3. Such phenomenon could be caused either by the high compression of the ice and by diffusion processes acting in the lowermost portion of the core. Understanding how and on which extent the signal is preserved in the deepest layers of the core (Jones et al., 2017; Pol et al., 2010) is essential to provide an accurate interpretation of the

climatic record. Moreover, even if the climate signal is disrupted below 1548 m depth, additional studies might be performed on the bottom part of the core to understand which processes affected the ice.

In Chapter 5 are presented results on preliminary tests performed with the copper method-Ar dating technique on small TALDICE ice samples (~65 g), compared with the results obtained with the well-established copper method on large samples (500-800 g) and the AICC2012 and TALDICE deep1 chronologies. Those preliminary results indicate that the copper method applied for Ar dating provides encouraging results even if the associated uncertainties are still large (±205 ka). Further developments are necessary to increase the replicates accuracy and precision.

In particular, would be helpful to perform additional tests as following:

i. *Analyse additional TALDICE samples:* the measurements of other TALDICE samples, especially in the portion below 1300 m depth, might be helpful to define a more precise value for the background effect and for the offset applied to calculate the Ar dating (eq. 5.28 and 5.29). Depending on the samples depth, different offsets could be computed at different depths to perform a more accurate dating calculation.

ii. *Test the methodology on different ice cores:* Ar dating performed with the copper method might be tested on different ice cores of known age to determine if different cores with diverse ice characteristics (e.g. affected by minor gas loss), provide comparable results. Analysis are now in progress on samples of the EDC core. Such results will be essential to validate the feasibility of this dating technique.

References

Abbott, P. M., Davies, S. M., Steffensen, J. P., Pearce, N. J. G., Bigler, M., Johnsen, S. J., Seierstad, I. K., Svensson, A., & Wastegård, S. (2012). A detailed framework of Marine Isotope Stages 4 and 5 volcanic events recorded in two Greenland ice-cores. *Quaternary Science Reviews*, *36*, 59–77. https://doi.org/10.1016/j.quascirev.2011.05.001

Abram, N. J., Wolff, E. W., & Curran, M. A. J. (2013). A review of sea ice proxy information from polar ice cores. *Quaternary Science Reviews*, *79*, 168–183. https://doi.org/10.1016/j.quascirev.2013.01.011

Abreu, J. A., Beer, J., Steinhilber, F., Christl, M., & Kubik, P. W. (2013). in Ice Cores and 14 C in Tree Rings : Separation of Production and Climate Effects. *Space Science Reviews*, *176*, 343–349. https://doi.org/10.1007/s11214-011-9864-y

Adusumilli, S., Fricker, H. A., Medley, B., Padman, L., & Siegfried, M. R. (2020). Interannual variations in meltwater input to the Southern Ocean from Antarctic ice shelves. *Nature Geoscience*, *13*(September). https://doi.org/10.1038/s41561-020-0616-z

Aeschbach-Hertig, W. (2014). Radiokrypton dating finally takes off. *Proceedings of the National Academy of Sciences of the United States of America*, *111*(19), 6856–6857. https://doi.org/10.1073/pnas.1405830111

Albani, S., Delmonte, B., Maggi, V., Baroni, C., Petit, J. R., Stenni, B., Mazzola, C., & Frezzotti, M. (2012). Interpreting last glacial to Holocene dust changes at Talos Dome (East Antarctica): Implications for atmospheric variations from regional to hemispheric scales. *Climate of the Past*, *8*(2), 741–750. https://doi.org/10.5194/cp-8-741-2012

Allègre, C. J., Hofmann, A., & O'Nions, K. (1996). The Argon constraints on mantle structure. *Geophysical Research Letters*, *23*(24), 3555–3557. https://doi.org/10.1029/96GL03373

Andersen, K. K., Azuma, N., Barnola, J. M., Bigler, M., Biscaye, P., Caillon, N., Chappellaz, J., Clausen, H. B., Dahl-Jensen, D., Fischer, H., Flückiger, J., Fritzsche, D., Fujii, Y., Goto-Azuma, K., Grønvold, K., Gundestrup, N. S., Hansson, M., Huber, C., Hvidberg, C. S., … White, J. W. C. (2004). High-resolution record of Northern Hemisphere climate extending into the last interglacial period. *Nature*, *431*(7005), 147–151. https://doi.org/10.1038/nature02805

Aoki, N., & Makide, Y. (2005). *The Concentration of Krypton in the Atmosphere — Its Revision after Half a Century —*. *34*(10), 10–11. https://doi.org/10.1246/cl.2005.1396

Arienzo, M. M., McConnell, J. R., Chellman, N., Criscitiello, A. S., Curran, M., Fritzsche, D., Kipfstuhl, S., Mulvaney, R., Nolan, M., Opel, T., Sigl, M., & Steffensen, J. P. (2016). A Method for Continuous 239Pu Determinations in Arctic and Antarctic Ice Cores. *Environmental Science and Technology*, *50*(13), 7066–7073. https://doi.org/10.1021/acs.est.6b01108

Aschwanden, A., Fahnestock, M. A., Truffer, M., Brinkerhoff, D. J., Hock, R., Khroulev, C., Mottram, R., & Khan, S. A. (2019). *Contribution of the Greenland Ice Sheet to sea level over the next millennium*.

Baccolo, G., Delmonte, B., Niles, P. B., Cibin, G., Di Stefano, E., Hampai, D., Keller, L., Maggi, V., Marcelli, A., Michalski, J., Snead, C., & Frezzotti, M. (2021). Jarosite formation in deep Antarctic ice provides a window into acidic, water-limited weathering on Mars. *Nature Communications*, *12*(1), 1–8. https://doi.org/10.1038/s41467-020-20705-z

Bazin, L., Landais, A., Lemieux-Dudon, B., Toyé Mahamadou Kele, H., Veres, D., Parrenin, F., Martinerie, P., Ritz, C., Capron, E., Lipenkov, V., Loutre, M. F., Raynaud, D., Vinther, B., Svensson, A., Rasmussen, S. O., Severi, M., Blunier, T., Leuenberger, M., Fischer, H., … Wolff, E. (2013). An optimized multi-proxy, multi-site Antarctic ice and gas orbital chronology (AICC2012): 120-800 ka. *Climate of the Past*, *9*(4), 1715–1731. https://doi.org/10.5194/cp-9-

1715-2013

Bazin, Lucie, Landais, A., Capron, E., Masson-Delmotte, V., Ritz, C., Picard, G., Jouzel, J., Dumont, M., & Leuenberger, M. (2016). Phase relationships between orbital forcing and the composition of air trapped in Antarctic ice cores. *Climate of the Past*, *12*(3), 729–748. https://doi.org/10.5194/cp-12-729-2016

Becagli, S., Proposito, M., Benassai, S., Flora, O., Genoni, L., Gragnani, R., Largiuni, O., Pili, S. L., Severi, M., Stenni, B., Traversi, R., Udisti, R., & Frezzotti, M. (2004). Chemical and isotopic snow variability in East Antarctica along the 2001/02 ITASE traverse. *Annals of Glaciology*, *39*, 473–482. https://doi.org/10.3189/172756404781814636

Bender, M., Barnett, B., Dreyfus, G., Jouzel, J., & Porcelli, D. (2008). The contemporary degassing rate of 40Ar from the solid Earth. *Proceedings of the National Academy of Sciences of the United States of America*, *105*(24), 8232–8237. https://doi.org/10.1073/pnas.0711679105

Bender, M. L. (2002). Orbital tuning chronology for the Vostok climate record supported by trapped gas composition. *Earth and Planetary Science Letters*, *204*(1–2), 275–289. https://doi.org/10.1016/S0012-821X(02)00980-9

Bender, M., Sowers, T., Dickson, M., Orchardo, J., Grootes, P., Mayewski, P., & Meese, D. (1994). Climate correlations between Greenland and Antarctica during the past 100,000. *Letters to Nature*, *372*, 663–666.

Bender, M., Tans, P., Ellis, J. T., Orchado, J., & Habfast, K. (1994). A high precision isotope ratio mass spectrometry method for measuring the O2/N2 ratio of air. *Geochimica et Cosmochimica Acta*, *58*(21), 4751–4758.

Bender, Michael, Sowers, T., & Labeyrie, L. (1994). The Dole Effect and its variations during the last 130,000 years as measured in the Vostok Ice Core. *Global Biogeochemical Cycles*, *8*(3), 363–376. https://doi.org/10.1029/94GB00724

Berden, G., Peeters, R., & Meijer, G. (2000). Cavity ring-down spectroscopy: Experimental schemes and applications. *International Reviews in Physical Chemistry*, *19*(4), 565–607. https://doi.org/10.1080/014423500750040627

Bergeron, T. (1935). On the physics of cloud and precipitation. *Proc. 5th Assembly U.G.G.I. Lisbon*, Vol. 2, . p. 156.

Berggren, A., Beer, J., Possnert, G., Aldahan, A., Kubik, P., Christl, M., Johnsen, S. J., Abreu, J., & Vinther, B. M. (2009). A 600-year annual Be record from the NGRIP ice core , Greenland. *Geophysical Research Letters*, *36*, 1–5. https://doi.org/10.1029/2009GL038004

Bernasconi, S. M., Hu, B., Wacker, U., Fiebig, J., Breitenbach, S. F. M., & Rutz, T. (2013). Background effects on Faraday collectors in gas-source mass spectrometry and implications for clumped isotope measurements. *Rapid Communications in Mass Spectrometry*, *27*(5), 603–612. https://doi.org/10.1002/rcm.6490

Bintanja, R., Van De Wal, R. S. W., & Oerlemans, J. (2005). Modelled atmospheric temperatures and global sea levels over the past million years. *Nature*, *437*, 125–128. https://doi.org/10.1038/nature03975

Blackburn, T., Edwards, G. H., Tulaczyk, S., Scudder, M., Piccione, G., Hallet, B., McLean, N., Zachos, J. C., Cheney, B., & Babbe, J. T. (2020). Ice retreat in Wilkes Basin of East Antarctica during a warm interglacial. *Nature*, *583*(7817), 554–559. https://doi.org/10.1038/s41586-020-2484-5

Blunier, T., & Brook, E. J. (2001). Timing of millennial-scale climate change in antarctica and greenland during the last glacial period. *Science*, *291*(5501), 109–112. https://doi.org/10.1126/science.291.5501.109

Blunier, T., & Schwander, J. (2000). Gas enclosure in ice : age difference and fractionation. *Physics of Ice Core Records*, 307–326. http://hdl.handle.net/2115/32473

Blunier, T., Spahni, R., Barnola, J. ., Chappellaz, J., Loulergue, L., & Schwander, J. (2007). Synchronization of ice core records via atmospheric gases. *Climate of the Past*, *3*(2), 325–330. https://doi.org/10.5194/cp-3-325-2007

Bo, S., Siegert, M. J., Mudd, S. M., Sugden, D., Fujita, S., Xiangbin, C., Yunyun, J., Xueyuan, T., & Yuansheng, L. (2009). The Gamburtsev mountains and the origin and early evolution of the Antarctic Ice Sheet. *Nature*, *459*(7247), 690–693. https://doi.org/10.1038/nature08024

Bradley, R. (2015). *Paleoclimatology: Reconstructing Climates of the Quaternary* (Third Edit). Elsevier. https://doi.org/10.2307/1552264

Bradley, S., Siddall, M., Milne, G. A., Masson-Delmotte, V., & Wolff, E. (2012). Where might we find evidence of a Last Interglacial West Antarctic Ice Sheet collapse in Antarctic ice core records? *Global and Planetary Change*, *88–89*, 64–75. https://doi.org/10.1016/j.gloplacha.2012.03.004

Bradley, S., Siddall, M., Milne, G. A., Masson-Delmotte, V., & Wolff, E. (2013). Combining ice core records and ice sheet models to explore the evolution of the East Antarctic Ice sheet during the Last Interglacial period. *Global and Planetary Change*, *100*, 278–290. https://doi.org/10.1016/j.gloplacha.2012.11.002

Buiron, D., Chappellaz, J., Stenni, B., Frezzotti, M., Baumgartner, M., Capron, E., Landais, A., Lemieux-Dudon, B., Masson-Delmotte, V., Montagnat, M., Parrenin, F., & Schilt, A. (2011). TALDICE-1 age scale of the Talos Dome deep ice core, East Antarctica. *Climate of the Past*, *7*(1), 1–16. https://doi.org/10.5194/cp-7-1-2011

Buiron, D., Stenni, B., Chappellaz, J., Landais, A., Baumgartner, M., Bonazza, M., Capron, E., Frezzotti, M., Kageyama, M., Lemieux, B., Masson-Delmotte, V., Parrenin, F., Schilt, A., Selmo, E., Severi, M., Swingedouw, D., & Udisti, R. (2012). Regional imprints of millennial variability during the MIS 3 period around. *Quaternary Science Reviews*, *48*, 99–112.

Buizert, C., Baggenstos, D., Jiang, W., Purtschert, R., Petrenko, V., Lu, Z. T., Müller, P., Kuhl, T., Lee, J., Severinghaus, J. P., & Brook, E. J. (2014). Radiometric 81Kr dating identifies 120,000-year-old ice at Taylor Glacier, Antarctica. *Proceedings of the National Academy of Sciences of the United States of America*, *111*(19), 6876–6881. https://doi.org/10.1073/pnas.1320329111

Buizert, C, Cuffey, K. M., Severinghaus, J. P., Baggenstos, D., Fudge, T. J., Steig, E. J., Markle, B. R., Winstrup, M., Rhodes, R. H., Brook, E. J., Sowers, T. A., Clow, G. D., Cheng, H., Edwards, R. L., Sigl, M., Mcconnell, J. R., & Taylor, K. C. (2015). *The WAIS Divide deep ice core WD2014 chronology – Part 1 : Methane synchronization (68 – 31 ka BP) and the gas age – ice age*. 153–173. https://doi.org/10.5194/cp-11-153-2015

Buizert, Christo, Fudge, T. J., Roberts, W. H. G., Steig, E. J., Sherriff-tadano, S., Ritz, C., Lefebvre, E., Edwards, J., Kawamura, K., Oyabu, I., Motoyama, H., Kahle, E. C., Jones, T. R., Abe-ouchi, A., Obase, T., Martin, C., Corr, H., Severinghaus, J. P., Beaudette, R., … Schwander, J. (2021). Antarctic surface temperature and elevation during the Last Glacial Maximum. *Science*, *372*(6546), 1097–1101. https://doi.org/10.1126/science.abd2897

Buizert, Christo, Sowers, T., & Blunier, T. (2013). Assessment of diffusive isotopic fractionation in polar firn, and application to ice core trace gas records. *Earth and Planetary Science Letters*, *361*, 110–119. https://doi.org/10.1016/j.epsl.2012.11.039

Capron, E., Landais, A., Lemieux-Dudon, B., Schilt, A., Masson-Delmotte, V., Buiron, D., Chappellaz, J., Dahl-Jensen, D., Johnsen, S., Leuenberger, M., Loulergue, L., & Oerter, H. (2010). Synchronising EDML and NorthGRIP ice cores using δ18O of atmospheric oxygen (δ18Oatm) and CH4 measurements over MIS5 (80-123 kyr). *Quaternary Science Reviews*, *29*(1–2), 222–234. https://doi.org/10.1016/j.quascirev.2009.07.014

Casado, M., Landais, A., Picard, G., Münch, T., Laepple, T., Stenni, B., Dreossi, G., Ekaykin, A., Arnaud, L., Genthon, C., Touzeau, A., Masson-Delmotte, V., & Jouzel, J. (2018). Archival processes of the water stable isotope signal in East Antarctic ice cores. *Cryosphere*, *12*(5), 1745–1766. https://doi.org/10.5194/tc-12-1745-2018

Casado, M., Münch, T., & Laepple, T. (2019). Climatic information archived in ice cores: impact of intermittency and diffusion on the recorded isotopic signal in Antarctica. *Climate of The Past Discussions*, *November*, 1–27. https://doi.org/10.5194/cp-2019-134

Chadwick, M., Allen, C. S., Sime, L. C., & Hillenbrand, C. D. (2020). Analysing the timing of peak warming and minimum winter sea-ice extent in the Southern Ocean during MIS 5e. *Quaternary Science Reviews*, *229*, 106134. https://doi.org/10.1016/j.quascirev.2019.106134

Chappellaz, J., Brook, E., Blunier, T., & Malaizé, B. (1997). CH4 and δ18O of O2 records from Antarctic and Greenland ice: A clue for stratigraphic disturbance in the bottom part of the Greenland Ice Core Project and the Greenland Ice Sheet Project 2 ice cores. *Journal of Geophysical Research*, *102*, 547–557.

Chen, C. Y., Li, Y. M., Bailey, K., O'Connor, T. P., Young, L., & Lu, Z. T. (1999). Ultrasensitive isotope trace analyses with a magneto-optical trap. *Science*, *286*(5442), 1139–1141. https://doi.org/10.1126/science.286.5442.1139

Cheng, C. F., Yang, G. M., Jiang, W., Sun, Y. R., Tu, L. Y., & Hu, S. M. (2013). Normalization of the single atom counting rate in an atom trap. *Optics Letters*, *38*(1), 31. https://doi.org/10.1364/ol.38.000031

Cheng, C., Jiang, W., Yang, G., Sun, Y., Pan, H., Gao, Y., Liu, A.-W., & Hu, S. (2010). An efficient magneto-optical trap of metastable krypton atoms. *Review of Scientific Instruments*, *81*(123106), 1–3. https://doi.org/10.1063/1.3520133

Ciais, P., & Jouzel, J. (1994). Deuterium and oxygen 18 in precipitation : Isotopic model , including mixed cloud processes. *Journal of Geophysical Research*, *99*(D8), 16,793-16,803.

Collon, P., Kutschera, W., Loosli, H. H., Lehmann, B. E., Purtschert, R., Love, A., Sampson, L., Anthony, D., Cole, D., Davids, B., Morrissey, D. J., Sherrill, B. M., Steiner, M., Pardo, R. C., & Paul, M. (2000). 81Kr in the Great Artesian Basin, Australia: A new method for dating very old groundwater. *Earth and Planetary Science Letters*, *182*(1), 103–113. https://doi.org/10.1016/S0012-821X(00)00234-X

Cook, C. P., Van De Flierdt, T., Williams, T., Hemming, S., Iwai, M., Kobayashi, M., Jimenez-Espejo, F. J., Escutia, C., González, J. J., Khim, B. K., McKay, R. M., Passchier, S., Bohaty, S. M., Riesselman, C. R., Tauxe, L., Sugisaki, S., Galindo, A. L., Patterson, M. O., Sangiorgi, F., … Yamane, M. (2013). Dynamic behaviour of the East Antarctic ice sheet during Pliocene warmth. *Nature Geoscience*, *6*(9), 765–769. https://doi.org/10.1038/ngeo1889

Craig, H. (1961). Isotopic Variations in Meteoric Waters. *Science*, *133*(3465), 1702–1703.

Craig, H., & Gordon, L. (1965). Deuterium and oxygen 18 variations in the ocean and the marine atmosphere. *Stable Isotopes in Oceanographic Studies and Paleotemperatures*. http://yncenter.sites.yale.edu/sites/default/files/shen_jing_jan_2013.pdf

Craig, H., Horibe, Y., & Sowers, T. (1988). Gravitational separation of gases and isotopes in polar ice caps. *Science*, *242*(4886), 1675–1678. https://doi.org/10.1126/science.242.4886.1675

Cressey, D. (2012). 'Too soon' to confirm success of Antarctic lake drilling. *Nature*. https://doi.org/10.1038/nature.2012.9986

Criss, R. E. (1999). *Principles of stable isotopes distribution*. Oxford University Press.

Crotti, I., Landais, A., Stenni, B., Bazin, L., Frezzotti, M., Ritterbusch, F., Lu, Z., Jiang, W., Yang, G.,

Orsi, A., Jacob, R., Fourr, E., Dreossi, G., & Barbante, C. (2021). An extension of the TALDICE ice core age scale reaching back to MIS 10.1. *Quaternary Science Reviews*, *266*(107078). https://doi.org/10.1016/j.quascirev.2021.107078

Dansgaard, W. (1964). Stable isotopes in precipitation. *Tellus*, *16*(4), 436–468. https://doi.org/10.3402/tellusa.v16i4.8993

DeConto, R. M., & Pollard, D. (2016). Contribution of Antarctica to past and future sea-level rise. *Nature*, *531*(7596), 591–597. https://doi.org/10.1038/nature17145

Delmas, R. J., Beer, J., Synal, H.-A., Muscheler, R., Petit, J.-R., & Pourchet, M. (2004). Bomb-test 36 Cl measurements in Vostok snow (Antarctica) and the use of 36 Cl as a dating tool for deep ice cores . *Tellus B: Chemical and Physical Meteorology*, *56*(5), 492–498. https://doi.org/10.3402/tellusb.v56i5.16454

Denton, G. H., Anderson, R. F., Toggweiler, J. R., Oceanic, N., Schaefer, J. M., & Putnam, A. E. (2010). The Last Glacial Termination. *Science*, *328*, 1652–1656. https://doi.org/10.1126/science.1184119

Dong, X. Z., Ritterbusch, F., Chu, Y. Q., Gu, J. Q., Hu, S. M., Jiang, W., Lu, Z. T., Yang, G. M., & Zhao, L. (2019). Dual Separation of Krypton and Argon from Environmental Samples for Radioisotope Dating. *Analytical Chemistry*, *91*(21), 13576–13581. https://doi.org/10.1021/acs.analchem.9b02716

Dreyfus, G. B., Parrenin, F., Lemieux-Dudon, B., Durand, G., Masson-Delmotte, V., Jouzel, J., Barnola, J. M., Panno, L., Spahni, R., Tisserand, A., Siegenthaler, U., & Leuenberger, M. (2007). Anomalous flow below 2700 m in the EPICA Dome C ice core detected using $\delta18O$ of atmospheric oxygen measurements. *Climate of the Past*, *3*(2), 341–353. https://doi.org/10.5194/cp-3-341-2007

Dutton, A., Carlson, A. E., Long, A. J., Milne, G. A., Clark, P. U., DeConto, R., Horton, B. P., Rahmstorf, S., & Raymo, M. E. (2015). Sea-level rise due to polar ice-sheet mass loss during past warm periods. *Science*, *349*(6244). https://doi.org/10.1126/science.aaa4019

Edwards, T. L., Nowicki, S., Marzeion, B., Hock, R., Goelzer, H., Seroussi, H., Jourdain, N. C., Slater, D. A., Turner, F. E., Smith, C. J., McKenna, C. M., Simon, E., Abe-Ouchi, A., Gregory, J. M., Larour, E., Lipscomb, W. H., Payne, A. J., Shepherd, A., Agosta, C., … Zwinger, T. (2021). Projected land ice contributions to twenty-first-century sea level rise. *Nature*, *593*(7857), 74–82. https://doi.org/10.1038/s41586-021-03302-y

EPICA community members. (2004). Eight glacial cycles from an Antarctic ice core. *Nature*, *429*(1), 623–628. https://doi.org/10.1016/S0921-8181(99)00023-5

Epstein, S., & Mayeda, T. (1953). Variation of O18 content of waters from natural sources. *Geochimica et Cosmochimica Acta*, *4*(5), 213–224. https://doi.org/10.1016/0016-7037(53)90051-9

Escutia, C., Brinkhuis, H., & Klaus, A. (2011). IODP expedition 318: From greenhouse to icehouse at the Wilkes Land Antarctic margin. *Scientific Drilling*, *12*, 15–23. https://doi.org/10.2204/iodp.sd.12.02.2011

Extier, T., Landais, A., Bréant, C., Prié, F., Bazin, L., Dreyfus, G., Roche, D. M., & Leuenberger, M. (2018). On the use of $\delta18Oatm$ for ice core dating. *Quaternary Science Reviews*, *185*, 244–257. https://doi.org/10.1016/j.quascirev.2018.02.008

Faber, A., Vinther, B. M., Sjolte, J., & Pedersen, R. A. (2017). *How does sea ice influence $\delta 18 O$ of Arctic precipitation ?* 5865–5876. https://doi.org/10.5194/acp-17-5865-2017

Fang, L., Jenk, T. M., Singer, T., Hou, S., & Schwikowski, M. (2021). Radiocarbon dating of alpine ice cores with the dissolved organic carbon (DOC) fraction. *Cryosphere*, *15*(3), 1537–1550. https://doi.org/10.5194/tc-15-1537-2021

Fischer, H., Siggaard-Andersen, M. L., Ruth, U., Röthlisberger, R., & Wolff, E. (2007).

Glacial/interglacial changes in mineral dust and sea-salt records in polar ice cores: Sources, transport, and deposition. *Reviews of Geophysics*, *45*(1), 1–26. https://doi.org/10.1029/2005RG000192

Fogwill, C. J., Turney, C. S. M., Meissner, K. J., Golledge, N. R., Spence, P., Roberts, J. L., England, M. H., Jones, R. T., & Carter, L. (2014). Testing the sensitivity of the East Antarctic Ice Sheet to Southern Ocean dynamics: Past changes and future implications. *Journal of Quaternary Science*, *29*(1), 91–98. https://doi.org/10.1002/jqs.2683

Fox-Kemper, B., Hewitt, H., Xiao, C., Aðalgeirsdóttir, G., Drijfhout, S., Edwards, T., Golledge, N., Hemer, M., Kopp, R., Krinner, G., Mix, A., Notz, D., Nowiciki, S., Nurhati, I., Ruiz, J., Sallée, J., Slangen, A., & Yu, Y. (2021). Ocean, Cryosphere and Sea Level Change. *Climate Change 2021: The Physical Science Basis. Contribution of Working Group I to the Sixth Assessment Report of the Intergovernmental Panel on Climate ChangeScience Basis. Contribution of Working Group I to the Sixth Assessment Report of the Intergover*, *2018*(August), 1–257.

Fretwell, P., Pritchard, H. D., Vaughan, D. G., Bamber, J. L., Barrand, N. E., Bell, R., Bianchi, C., Bingham, R. G., Blankenship, D. D., Casassa, G., Catania, G., Callens, D., Conway, H., Cook, A. J., Corr, H. F. J., Damaske, D., Damm, V., Ferraccioli, F., Forsberg, R., … Zirizzotti, A. (2013). Bedmap2: Improved ice bed, surface and thickness datasets for Antarctica. *Cryosphere*, *7*(1), 375–393. https://doi.org/10.5194/tc-7-375-2013

Frezzotti, M., Bitelli, G., De Michelis, P., Deponti, A., Forieri, A., Gandolfi, S., Maggi, V., Mancini, F., Remy, F., Tabacco, I. E., Urbini, S., Vittuari, L., & Zirizzottl, A. (2004). Geophysical survey at Talos Dome, East Antarctica: The search for a new deep-drilling site. *Annals of Glaciology*, *39*(2002), 423–432. https://doi.org/10.3189/172756404781814591

Frezzotti, M., Cimbelli, A., & Ferrigno, J. G. (1998). Ice-front change and iceberg behaviour along Oates and George V Coasts, Antarctica, 1912-96. *Annals of Glaciology*, *27*(January 1998), 643–650. https://doi.org/10.3189/1998aog27-1-643-650

Fujita, S., Okuyama, J., Hori, A., & Hondoh, T. (2009). Metamorphism of stratified firn at Dome Fuji, Antarctica: A mechanism for local insolation modulation of gas transport conditions during bubble close off. *Journal of Geophysical Research: Earth Surface*, *114*(3), 1–21. https://doi.org/10.1029/2008JF001143

Galewsky, J., Steen-larsen, H. C., Field, R. D., Worden, J., Risi, C., & Schneider, M. (2016). *Reviews of Geophysics Stable isotopes in atmospheric water vapor and applications to the hydrologic cycle*. 809–865. https://doi.org/10.1002/2015RG000512

Gehre, M., Hoefling, R., Kowski, P., & Strauch, G. (1996). Sample preparation device for quantitative hydrogen isotope analysis using chromium metal. *Analytical Chemistry*, *68*(24), 4414–4417. https://doi.org/10.1021/ac9606766

Gkinis, V., Popp, T. J., Johnsen, S. J., & Blunier, T. (2010). A continuous stream flash evaporator for the calibration of an IR cavity ring-down spectrometer for the isotopic analysis of water. *Isotopes in Environmental and Health Studies*, *46*(4), 463–475. https://doi.org/10.1080/10256016.2010.538052

Golledge, N. R., Clark, P. U., He, F., Dutton, A., Turney, C. S. M., Fogwill, C. J., Naish, T. R., Levy, R. H., McKay, R. M., Lowry, D. P., Bertler, N. A. N., Dunbar, G. B., & Carlson, A. E. (2021). Retreat of the Antarctic Ice Sheet During the Last Interglaciation and Implications for Future Change. *Geophysical Research Letters*, *48*(17), 1–11. https://doi.org/10.1029/2021GL094513

Golledge, N. R., Kowalewski, D. E., Naish, T. R., Levy, R. H., Fogwill, C. J., & Gasson, E. G. W. (2015). The multi-millennial Antarctic commitment to future sea-level rise. *Nature*, *526*(7573), 421–425. https://doi.org/10.1038/nature15706

Golledge, N. R., Levy, R. H., McKay, R. M., & Naish, T. R. (2017). East Antarctic ice sheet most

vulnerable to Weddell Sea warming. *Geophysical Research Letters*, *44*(5), 2343–2351. https://doi.org/10.1002/2016GL072422

Golledge, N. R., Menviel, L., Carter, L., Fogwill, C. J., England, M. H., Cortese, G., & Levy, R. H. (2014). Antarctic contribution to meltwater pulse 1A from reduced Southern Ocean overturning. *Nature Communications*, *5*, 1–10. https://doi.org/10.1038/ncomms6107

Goursaud, S., Holloway, M., Sime, L., Wolff, E., Valdes, P., Steig, E. J., & Pauling, A. (2020). Antarctic Ice Sheet elevation impacts on water isotope records during the Last Interglacial. *Geophysical Research Letters*. https://doi.org/10.1029/2020gl091412

Grachev, A. M., & Severinghaus, J. P. (2003a). Determining the thermal diffusion factor for 40Ar/36Ar in air to aid paleoreconstruction of abrupt climate change. *Journal of Physical Chemistry A*, *107*(23), 4636–4642. https://doi.org/10.1021/jp027817u

Grachev, A. M., & Severinghaus, J. P. (2003b). Laboratory determination of thermal diffusion constants for 29N2/28N2 in air at temperatures from -60 to 0°C for reconstruction of magnitudes of abrupt climate changes using the ice core fossil-air plaeothermometer. *Geochimica et Cosmochimica Acta*, *67*(3), 345–360. https://doi.org/10.1016/S0016-7037(02)01115-8

Grootes, P. M., Steig, E. J., Stuiver, M., Waddington, E. D., Morse, D. L., & Nadeau, M. J. (2001). The Taylor Dome Antarctic 18O record and globally synchronous changes in climate. *Quaternary Research*, *56*(3), 289–298. https://doi.org/10.1006/qres.2001.2276

Hammer, C., Clausen, H. B., Dansgaard, W., Gundestrup, N., & Johnsen, S., and Reeh, N. (1978). DATING OF GREENLA N D ICE CORES BY FLOW MODELS , ISOTOPES , VOLCANIC DEBRIS , AND CONTINENTAL DUST (G eophysical I sotop e Laboratory , U niversity of Copenhagen , Haraldsgade 6 , DK-2200. *Journal of Glaciology*, *20*(82), 3–26.

Hammer, C. U. (1980). Acidity of Polar Ice Cores in Relation to Absolute Dating, Past Volcanism, and Radio–Echoes. *Journal of Glaciology*, *25*(93), 359–372. https://doi.org/10.3189/s0022143000015227

Hanna, E., Pattyn, F., Navarro, F., Favier, V., Goelzer, H., Broeke, M. R. Van Den, Vizcaino, M., Whitehouse, P. L., Ritz, C., Bulthuis, K., & Smith, B. (2020). Earth-Science Reviews Mass balance of the ice sheets and glaciers – Progress since AR5 and challenges. *Earth-Science Reviews*, *201*(September 2019), 102976. https://doi.org/10.1016/j.earscirev.2019.102976

Herron, M., & Langway, C. (1980). Firn densification: an empirical model. *Journal of Glaciology*, *25*(93), 373–385.

Hoefs, J. (2015). Stable isotope geochemistry. In *Stable Isotope Geochemistry (7th edition)*. https://doi.org/10.1017/cbo9780511809323.008

Hoffmann, G., Jouzel, J., & Masson-Delmotte, V. (2000). Stable water isotopes in atmospheric general circulation models. *Hydrological Processes*, *14*(1385–1406).

Hoffmann, H., Preunkert, S., Legrand, M., Leinfelder, D., Bohleber, P., Friedrich, R., & Wagenbach, D. (2018). A new sample preparation system for micro-14C dating of glacier ice with a first application to a high alpine ice core from colle gnifetti (Switzerland). *Radiocarbon*, *60*(2), 517–533. https://doi.org/10.1017/RDC.2017.99

Holden, N. E., Coplen, T. B., Böhlke, J. K., Tarbox, L. V, Benefield, J., de Laeter, J. R., Mahaffy, P. G., O'Connor, G., Roth, E., Tepper, D. H., Walczyk, T., Wieser, M. E., & Yoneda, S. (2018). IUPAC Periodic Table of the Elements and Isotopes (IPTEI) for the Education Community (IUPAC Technical Report). *Pure and Applied Chemistry*, *90*(12), 1833–2092. https://doi.org/doi:10.1515/pac-2015-0703

Holloway, M. D., Sime, L. C., Singarayer, J. S., Tindall, J. C., Bunch, P., & Valdes, P. J. (2016). Antarctic last interglacial isotope peak in response to sea ice retreat not ice-sheet collapse. *Nature*

Communications, 7, 1–9. https://doi.org/10.1038/ncomms12293

Horita, J., Rozanski, K., & Cohen, S. (2008). Isotope effects in the evaporation of water: A status report of the Craig-Gordon model. *Isotopes in Environmental and Health Studies*, *44*(1), 23–49. https://doi.org/10.1080/10256010801887174

Horita, J., Ueda, A., Mizukami, K., & Takatori, I. (1989). Automatic δD and δ18O analyses of multi-water samples using H2- and CO2-water equilibration methods with a common equilibration set-up. *International Journal of Radiation Applications and Instrumentation. Part A. Applied Radiation and Isotopes*, *40*(9), 801–805. https://doi.org/10.1016/0883-2889(89)90100-7

Horiuchi, K., Uchida, T., Sakamoto, Y., Ohta, A., Matsuzaki, H., Shibata, Y., & Motoyama, H. (2008). Ice core record of 10Be over the past millennium from Dome Fuji, Antarctica: A new proxy record of past solar activity and a powerful tool for stratigraphic dating. *Quaternary Geochronology*, *3*(3), 253–261. https://doi.org/10.1016/j.quageo.2008.01.003

Ikeda-Fukazawa, T., Fukumizu, K., Kawamura, K., Aoki, S., Nakazawa, T., & Hondoh, T. (2005). Effects of molecular diffusion on trapped gas composition in polar ice cores. *Earth and Planetary Science Letters*, *229*(3–4), 183–192. https://doi.org/10.1016/j.epsl.2004.11.011

IPCC. (1992). CLIMAT E CHANGE : The 1990 and 1992 IPCC Assessments. In *IPCC First Assesment Report Overview and Policymaker Summaries and 1992 IPCC Supplement*. https://doi.org/10.1007/978-94-011-2280-1_3

Jiang, W., Bailey, K., Lu, Z. T., Mueller, P., O'Connor, T. P., Cheng, C. F., Hu, S. M., Purtschert, R., Sturchio, N. C., Sun, Y. R., Williams, W. D., & Yang, G. M. (2012). An atom counter for measuring 81Kr and 85Kr in environmental samples. *Geochimica et Cosmochimica Acta*, *91*, 1–6. https://doi.org/10.1016/j.gca.2012.05.019

Jiang, Wei, Hu, S. M., Lu, Z. T., Ritterbusch, F., & Yang, G. min. (2020). Latest development of radiokrypton dating – A tool to find and study paleogroundwater. *Quaternary International*, *547*(April 2019), 166–171. https://doi.org/10.1016/j.quaint.2019.04.025

Jones, T. R., Cuffey, K. M., White, J. W. C., Steig, E. J., Buizert, C., Markle, B. R., McConnell, J. R., & Sigl, M. (2017). Water isotope diffusion in the WAIS Divide ice core during the Holocene and last glacial. *Journal of Geophysical Research: Earth Surface*, *122*(1), 290–309. https://doi.org/10.1002/2016JF003938

Jordan, T. Ferraccioli, F. Corr, H. Robinson, C. Caneva, G. Armadillo, E. Bozzo, E. Frearson, N. (2008). Linking the Wilkes Subglacial Basin the Transantarctic Mountains and the Ross Sea with a new airborne gravity survey. *Terra Antarctica Reports*, *13*, 37–54.

Jouzel, J. (2013). A brief history of ice core science over the last 50 yr. *Climate of the Past*, *9*(6), 2525–2547. https://doi.org/10.5194/cp-9-2525-2013

Jouzel, J., Masson-Delmotte, V., Cattani, O., Dreyfus, G., Falourd, S., Hoffmann, G., Minster, B., Nouet, J., Barnola, J. M., Chappellaz, J., Fischer, H., Gallet, J. C., Johnsen, S., Leuenberger, M., Loulergue, L., Luethi, D., Oerter, H., Parrenin, F., Raisbeck, G., … Wolff, E. W. (2007). Orbital and millennial antarctic climate variability over the past 800,000 years. *Science*, *317*(5839), 793–796. https://doi.org/10.1126/science.1141038

Jouzel, J., & Merlivat, L. (1984). Deuterium and oxygen 18 in precipitation: modeling of the isotopic effects during snow formation. *Journal of Geophysical Research*, *89*(D7), 749–757. https://doi.org/10.1029/jd089id07p11749

Jouzel, J., Vimeux, F., Caillon, N., Delaygue, G., Hoffmann, G., Masson-Delmotte, V., & Parrenin, F. (2003). Magnitude of isotope/temperature scaling for interpretation of central Antarctic ice cores. *Journal of Geophysical Research Atmospheres*, *108*(12). https://doi.org/10.1029/2002jd002677

Jouzel, J, Waelbroeck, C., Malaize, B., Bender, M., Petit, J. R., Stievenard, M., Barkov, N. I., Barnola,

J. M., King, T., Kotlyakov, V. M., Lipenkov, V., Lorius, C., Raynaud, D., Ritz, C., & Sowers, T. (1996). Climatic interpretation of the recently extended Vostok ice records. *Climate Dynamics*, *12*, 513–521.

Jouzel, Jean, Delaygue, G., Landais, A., Masson-Delmotte, V., Risi, C., & Vimeux, F. (2013). Water isotopes as tools to document oceanic sources of precipitation. *Water Resources Research*, *49*(11), 7469–7486. https://doi.org/10.1002/2013WR013508

Kawamura, K., Parrenin, F., Lisiecki, L., Uemura, R., Vimeux, F., Severinghaus, J. P., Hutterli, M. A., Nakazawa, T., Aoki, S., Jouzel, J., Raymo, M. E., Matsumoto, K., Nakata, H., Motoyama, H., Fujita, S., Goto-Azuma, K., Fujii, Y., & Watanabe, O. (2007). Northern Hemisphere forcing of climatic cycles in Antarctica over the past 360,000 years. *Nature*, *448*(7156), 912–916. https://doi.org/10.1038/nature06015

Killick, R., Fearnhead, P., & Eckley, I. A. (2012). Optimal detection of changepoints with a linear computational cost. *Journal of the American Statistical Association*, *107*(500), 1590–1598. https://doi.org/10.1080/01621459.2012.737745

Kindler, P., Guillevic, M., Baumgartner, M., Schwander, J., Landais, A., & Leuenberger, M. (2014). Temperature reconstruction from 10 to 120 kyr b2k from the NGRIP ice core. *Climate of the Past*, *10*(2), 887–902. https://doi.org/10.5194/cp-10-887-2014

Kobashi, T., Severinghaus, J. P., Brook, E. J., Barnola, J. M., & Grachev, A. M. (2007). Precise timing and characterization of abrupt climate change 8200 years ago from air trapped in polar ice. *Quaternary Science Reviews*, *26*(9–10), 1212–1222. https://doi.org/10.1016/j.quascirev.2007.01.009

Kobashi, T., Severinghaus, J. P., & Kawamura, K. (2008). Argon and nitrogen isotopes of trapped air in the GISP2 ice core during the Holocene epoch (0-11,500 B.P.): Methodology and implications for gas loss processes. *Geochimica et Cosmochimica Acta*, *72*(19), 4675–4686. https://doi.org/10.1016/j.gca.2008.07.006

Koornneef, J. M., Bouman, C., Schwieters, J. B., & Davies, G. R. (2014). Measurement of small ion beams by thermal ionisation mass spectrometry using new 1013Ohm resistors. *Analytica Chimica Acta*, *819*, 49–55. https://doi.org/10.1016/j.aca.2014.02.007

Landais, A., Barnola, J. M., Kawamura, K., Caillon, N., Delmotte, M., Van Ommen, T., Dreyfus, G., Jouzel, J., Masson-Delmotte, V., Minster, B., Freitag, J., Leuenberger, M., Schwander, J., Huber, C., Etheridge, D., & Morgan, V. (2006). Firn-air δ15N in modern polar sites and glacial-interglacial ice: A model-data mismatch during glacial periods in Antarctica? *Quaternary Science Reviews*, *25*(1–2), 49–62. https://doi.org/10.1016/j.quascirev.2005.06.007

Landais, A., Caillon, N., Severinghaus, J. P., Jouzel, J., & Masson-Delmotte, V. (2003). Analyses isotopiques à haute précision de l'air piégé dans les glaces polaires pour la quantification des variations de température: methode et limites. *Notes Des Activités Instrumentales de l'IPSL*, *39*.

Landais, A., Chappellaz, J., Delmotte, M., Jouzel, J., Blunier, T., Bourg, C., Caillon, N., Cherrier, S., Malaizé, B., Masson-Delmotte, V., Raynaud, D., Schwander, J., & Steffensen, J. P. (2003). A tentative reconstruction of the last interglacial and glacial inception in Greenland based on new gas measurements in the Greenland Ice Core Project (GRIP) ice core. *Journal of Geophysical Research: Atmospheres*, *108*(18). https://doi.org/10.1029/2002jd003147

Landais, A., Dreyfus, G., Capron, E., Masson-Delmotte, V., Sanchez-Goñi, M. F., Desprat, S., Hoffmann, G., Jouzel, J., Leuenberger, M., & Johnsen, S. (2010a). What drives the millennial and orbital variations of δ18Oatm? *Quaternary Science Reviews*, *29*(1–2), 235–246. https://doi.org/10.1016/j.quascirev.2009.07.005

Landais, A., Dreyfus, G., Capron, E., Masson-Delmotte, V., Sanchez-Goñi, M. F., Desprat, S., Hoffmann, G., Jouzel, J., Leuenberger, M., & Johnsen, S. (2010b). What drives the millennial and

orbital variations of δ18Oatm? *Quaternary Science Reviews*, *29*(1–2), 235–246. https://doi.org/10.1016/j.quascirev.2009.07.005

Landais, A., Dreyfus, G., Capron, E., Pol, K., Loutre, M. F., Raynaud, D., Lipenkov, V. Y., Arnaud, L., Masson-Delmotte, V., Paillard, D., Jouzel, J., & Leuenberger, M. (2012). Towards orbital dating of the EPICA Dome C ice core using δO 2/N 2. *Climate of the Past*, *8*(1), 191–203. https://doi.org/10.5194/cp-8-191-2012

Landais, A., Stenni, B., Masson-Delmotte, V., Jouzel, J., Cauquoin, A., Fourre, E., Minster, B., Selmo, E., Extier, T., Werner, M., Vimeux, F., Uemura, R., Crotti, I., & Grisart, A. (2021). Interglacial Antarctic-Southern Ocean climate decoupling due to moisture source area shifts. *Nature Geoscience*, *14*, 918–923. https://doi.org/10.1038/s41561-021-00856-4

Langway, C. C. (2008). The history of early polar ice cores. *Cold Regions Science and Technology*, *52*(2), 101–117. https://doi.org/10.1016/j.coldregions.2008.01.001

Lemieux-Dudon, B., Blayo, E., Petit, J. R., Waelbroeck, C., Svensson, A., Ritz, C., Barnola, J. M., Narcisi, B. M., & Parrenin, F. (2010). Consistent dating for Antarctic and Greenland ice cores. *Quaternary Science Reviews*, *29*(1–2), 8–20. https://doi.org/10.1016/j.quascirev.2009.11.010

Lilien, D. A., Steinhage, D., Taylor, D., Parrenin, F., Ritz, C., Mulvaney, R., Martín, C., Yan, J. B., O'Neill, C., Frezzotti, M., Miller, H., Gogineni, P., Dahl-Jensen, D., & Eisen, O. (2021). Brief communication: New radar constraints support presence of ice older than 1.5 Myr at Little Dome C. *Cryosphere*, *15*(4), 1881–1888. https://doi.org/10.5194/tc-15-1881-2021

Lisiecki, L. E., & Raymo, M. E. (2005). A Pliocene-Pleistocene stack of 57 globally distributed benthic δ 18O records. *Paleoceanography*, *20*(1), 1–17. https://doi.org/10.1029/2004PA001071

Loosli, H., & Oeschger, H. (1969). 37Ar and 81Kr in the atmosphere. *Earth and Planetary Science Letters*, *7*, 67–71.

Lorius, C., & Merlivat, L. (1975). Distribution of mean surface stable isotopes values in East Antarctica: observed changes in coastal area. *General Assembly of the International Union of Geodesy and Geophysics. Grenoble, France. CEA -CONF --3397.*

Lorius, C., Merlivat, L., & Hagemann, R. (1969). Variation in the Mean Deuterium Content of Precipitations in Antarctica. *Journal of Geophysical Research*, *74*(28), 7027–7031. https://doi.org/10.1029/JC074i028p07027

Loulergue, L., Schilt, A., Spahni, R., Masson-Delmotte, V., Blunier, T., Lemieux, B., Barnola, J. M., Raynaud, D., Stocker, T. F., & Chappellaz, J. (2008). Orbital and millennial-scale features of atmospheric CH4 over the past 800,000 years. *Nature*, *453*(7193), 383–386. https://doi.org/10.1038/nature06950

Lu, Z. T., Schlosser, P., Smethie, W. M., Sturchio, N. C., Fischer, T. P., Kennedy, B. M., Purtschert, R., Severinghaus, J. P., Solomon, D. K., Tanhua, T., & Yokochi, R. (2014). Tracer applications of noble gas radionuclides in the geosciences. *Earth-Science Reviews*, *138*, 196–214. https://doi.org/10.1016/j.earscirev.2013.09.002

Lu, Zheng Tian. (2013). What trapped atoms reveal about global groundwater. *Physics Today*, *66*(3), 74–75. https://doi.org/10.1063/PT.3.1926

Lunt, D. J., Foster, G. L., Haywood, A. M., & Stone, E. J. (2008). Late Pliocene Greenland glaciation controlled by a decline in atmospheric CO2 levels. *Nature*, *454*(7208), 1102–1105. https://doi.org/10.1038/nature07223

Lüthi, D., Le Floch, M., Bereiter, B., Blunier, T., Barnola, J. M., Siegenthaler, U., Raynaud, D., Jouzel, J., Fischer, H., Kawamura, K., & Stocker, T. F. (2008). High-resolution carbon dioxide concentration record 650,000-800,000 years before present. *Nature*, *453*(7193), 379–382. https://doi.org/10.1038/nature06949

M. Montagnat , D. Buiron , L. Arnaud , A. Broquet a, P. Schlitz, R. Jacob, S. K. (2012). Measurements and numerical simulation of fabric evolution along the Talos Dome ice core, Antarctica. *Earth and Planetary Science Letters*, *357–358*, 168–178.

Magand, O., Frezzotti, M., Pourchet, M., Stenni, B., Genoni, L., & Fily, M. (2004). Climate variability along latitudinal and longitudinal transects in East Antarctica. *Annals of Glaciology*, *39*, 351–358. https://doi.org/10.3189/172756404781813961

Masson-Delmotte, V., Stenni, B., & Jouzel, J. (2004). Common millennial-scale variability of Antarctic and Southern Ocean temperatures during the past 5000 years reconstructed from the EPICA Dome C ice core. *Holocene*, *14*(2), 145–151. https://doi.org/10.1191/0959683604hl697ft

Masson Delmotte, V., Buiron, D., Ekaykin, A., Frezzotti, M., Gallée, H., Jouzel, J., Krinner, G., Landais, A., Motoyama, H., Oerter, H., Pol, K., Pollard, D., Ritz, C., Schlosser, E., Sime, L. C., Sodemann, H., Stenni, B., Uemura, R., & Vimeux, F. (2011). A comparison of the present and last interglacial periods in six Antarctic ice cores. *Climate of the Past*, *7*(2), 397–423. https://doi.org/10.5194/cp-7-397-2011

Masson Delmotte, V, Jouzel, J., Landais, A., Stievenard, M., Johnsen, S. J., White, J. W. C., Werner, M., Sveinbjornsdottir, A., & Fuhrer, K. (2005). Atmospheric science: GRIP deuterium excess reveals rapid and orbital-scale changes in greenland moisture origin. *Science*, *309*(5731), 118–121. https://doi.org/10.1126/science.1108575

Masson Delmotte, Valérie, Hou, S., Ekaykin, A., Jouzel, J., Aristarain, A., Bernardo, R. T., Bromwich, D., Cattani, O., Delmotte, M. M., Falourd, S., Frezzotti, M., Gallée, H., Genoni, L., Isaksson, E., Landais, A., Helsen, M. M., Hoffmann, G., Lopez, J., Morgan, V., … White, J. W. C. (2008). A review of antarctic surface snow isotopic composition: Observations, atmospheric circulation, and isotopic modeling. *Journal of Climate*, *21*(13), 3359–3387. https://doi.org/10.1175/2007JCLI2139.1

McKinney, C. R., McCrea, J. M., Epstein, S., Allen, H. A., & Urey, H. C. (1950). Improvements in mass spectrometers for the measurement of small differences in isotope abundance ratios. *Review of Scientific Instruments*, *21*(8), 724–730. https://doi.org/10.1063/1.1745698

Meese, D. A., Gow, A. J., Alley, R. B., Zielinski, G. A., Grootes, P. M., Ram, M., Taylor, K. C., Mayewski, P. A., & Bolzan, J. F. (1997). The Greenland Ice Sheet Project 2 depth-age scale: Methods and results. *Journal of Geophysical Research: Oceans*, *102*(C12), 26411–26423. https://doi.org/10.1029/97JC00269

Mengel, M., & Levermann, A. (2014). Ice plug prevents irreversible discharge from east Antarctica. *Nature Climate Change*, *4*(6), 451–455. https://doi.org/10.1038/nclimate2226

Mezgec, K., Stenni, B., Crosta, X., Masson-Delmotte, V., Baroni, C., Braida, M., Ciardini, V., Colizza, E., Melis, R., Salvatore, M. C., Severi, M., Scarchilli, C., Traversi, R., Udisti, R., & Frezzotti, M. (2017). Holocene sea ice variability driven by wind and polynya efficiency in the Ross Sea. *Nature Communications*, *8*(1). https://doi.org/10.1038/s41467-017-01455-x

Miles, B., Stokes, C. R., & Jamieson, S. S. R. (2018). Velocity increases at Cook Glacier, East Antarctica, linked to ice shelf loss and a subglacial flood event. *Cryosphere*, *12*(10), 3123–3136. https://doi.org/10.5194/tc-12-3123-2018

Morgan, V., Delmotte, M., Van Ommen, T., Jouzel, J., Chappellaz, J., Woon, S., Masson-Delmotte, V., & Raynaud, D. (2002). Relative timing of deglacial climate events in Antarctica and Greenland. *Science*, *297*(5588), 1862–1864. https://doi.org/10.1126/science.1074257

Morlighem, M., Rignot, E., Binder, T., Blankenship, D., Drews, R., Eagles, G., Eisen, O., Ferraccioli, F., Forsberg, R., Fretwell, P., Goel, V., Greenbaum, J. S., Gudmundsson, H., Guo, J., Helm, V., Hofstede, C., Howat, I., Humbert, A., Jokat, W., … Smith, E. C. (2020). Deep glacial troughs and stabilizing ridges ice sheet. *Nature Geoscience*, *13*(FebruarY). https://doi.org/10.1038/s41561-

019-0510-8

Münch, T., Kipfstuhl, S., Freitag, J., Meyer, H., & Laepple, T. (2017). Constraints on post-depositional isotope modifications in East Antarctic firn from analysing temporal changes of isotope profiles. *Cryosphere*, *11*(5), 2175–2188. https://doi.org/10.5194/tc-11-2175-2017

Münch, T., & Laepple, T. (2018). What climate signal is contained in decadal - To centennial-scale isotope variations from Antarctic ice cores? *Climate of the Past*, *14*(12), 2053–2070. https://doi.org/10.5194/cp-14-2053-2018

Muscheler, R., Kubik, P. W., & Synal, H. (2005). Geomagnetic field intensity during the last 60 , 000 years based on 10 Be and 36 Cl from the Summit ice cores and 14 C. *Quaternary Science Reviews*, *24*, 1849–1860. https://doi.org/10.1016/j.quascirev.2005.01.012

Nakayama, Y., Manucharyan, G., Zhang, H., Dutrieux, P., Torres, H. S., Klein, P., Seroussi, H., Schodlok, M., Rignot, E., & Menemenlis, D. (2019). Pathways of ocean heat towards Pine Island and Thwaites grounding lines. *Scientific Reports*, *9*(1), 1–9. https://doi.org/10.1038/s41598-019-53190-6

NEEM community members. (2013). Eemian interglacial reconstructed from a Greenland folded ice core. *Nature*, *493*, 489–494. https://doi.org/10.1038/nature11789

Noone, D. (2004). Sea ice control of water isotope transport to Antarctica and implications for ice core interpretation. *Journal of Geophysical Reserach*, *109*, 1–13. https://doi.org/10.1029/2003JD004228

North Greenland Ice Core Project members. (2004). High-resolution record of Northern Hemisphere climate extending into the last interglacial period. *Nature*, *431*(September), 147–151.

Nowicki, S. M. J., Payne, A., Larour, E., Seroussi, H., Goelzer, H., Lipscomb, W., Gregory, J., Abe-Ouchi, A., & Shepherd, A. (2016). Ice Sheet Model Intercomparison Project (ISMIP6) contribution to CMIP6. *Geoscientific Model Development*, *9*(12), 4521–4545. https://doi.org/10.5194/gmd-9-4521-2016

O'Leary, M. J., Hearty, P. J., Thompson, W. G., Raymo, M. E., Mitrovica, J. X., & Webster, J. M. (2013). Ice sheet collapse following a prolonged period of stable sea level during the last interglacial. *Nature Geoscience*, *6*(9), 796–800. https://doi.org/10.1038/ngeo1890

Ohno, H., Lipenkov, V. Y., & Hondoh, T. (2004). Air bubble to clathrate hydrate transformation in polar ice sheets: A reconsideration based on the new data from Dome Fuji ice core. *Geophysical Research Letters*, *31*(21), 2–5. https://doi.org/10.1029/2004GL021151

Orombelli, G., Maggi, V., & Delmonte, B. (2010). Quaternary stratigraphy and ice cores. *Quaternary International*, *219*(1–2), 55–65. https://doi.org/10.1016/j.quaint.2009.09.029

Oyabu, I., Kawamura, K., Uchida, T., Fujita, S., Kitamura, K., Hirabayashi, M., Aoki, S., Morimoto, S., Nakazawa, T., Severinghaus, J. P., & Morgan, J. (2021). Fractionation of O2/N2 and Ar/N2 in the Antarctic ice sheet during bubble formation and bubble-clathrate hydrate transition from precise gas measurements of the Dome Fuji ice core. *The Cryosphere Discussions*, *2021*, 1–45. https://doi.org/10.5194/tc-2021-147

Parrenin, F., Barker, S., Blunier, T., Chappellaz, J., Jouzel, J., Landais, A., Masson-Delmotte, V., Schwander, J., & Veres, D. (2012). On the gas-ice depth difference (Δdepth) along the EPICA Dome C ice core. *Climate of the Past*, *8*(4), 1239–1255. https://doi.org/10.5194/cp-8-1239-2012

Parrenin, F., Barnola, J. M., Beer, J., Blunier, T., Castellano, E., Chappellaz, J., Dreyfus, G., Fischer, H., Fujita, S., Jouzel, J., Kawamura, K., Lemieux-Dudon, B., Loulergue, L., Masson-Delmotte, V., Narcisi, B., Petit, J. R., Raisbeck, G., Raynaud, D., Ruth, U., … Wolff, E. (2007). The EDC3 chronology for the EPICA Dome C ice core. *Climate of the Past*, *3*(3), 485–497. https://doi.org/10.5194/cp-3-485-2007

Parrenin, F., Bazin, L., Capron, E., Landais, A., Lemieux-Dudon, B., & Masson-Delmotte, V. (2015). IceChrono1: A probabilistic model to compute a common and optimal chronology for several ice cores. *Geoscientific Model Development*, *8*(5), 1473–1492. https://doi.org/10.5194/gmd-8-1473-2015

Parrenin, F., Cavitte, M. G. P., Blankenship, D. D., Chappellaz, J., Fischer, H., Gagliardini, O., Masson-Delmotte, V., Passalacqua, O., Ritz, C., Roberts, J., Siegert, M. J., & Young, D. A. (2017). Is there 1.5-million-year-old ice near Dome C, Antarctica? *Cryosphere*, *11*(6), 2427–2437. https://doi.org/10.5194/tc-11-2427-2017

Parrenin, F., Dreyfus, G., Durand, G., Fujita, S., Gagliardini, O., Gillet, F., Jouze, J., Kawamura, K., Lhomme, N., Masson-Delmotte, V., Ritz, C., Schwander, J., Shoji, H., Uemura, R., Watanabe, O., & Yoshida, N. (2007). 1-D-ice flow modelling at EPICA Dome C and Dome Fuji, East Antarctica. *Climate of the Past*, *3*(2), 243–259. https://doi.org/10.5194/cp-3-243-2007

Parrenin, F., Rémy, F., Ritz, C., Siegert, M. J., & Jouzel, J. (2004). New modeling of the Vostok ice flow line and implication for the glaciological chronology of the Vostok ice core. *Journal of Geophysical Research D: Atmospheres*, *109*(20). https://doi.org/10.1029/2004JD004561

Patterson, M. O., McKay, R., Naish, T., Escutia, C., Jimenez-Espejo, F. J., Raymo, M. E., Meyers, S. R., Tauxe, L., Brinkhuis, H., Klaus, A., Fehr, A., Bendle, J. A. P., Bijl, P. K., Bohaty, S. M., Carr, S. A., Dunbar, R. B., Flores, J. A., Gonzalez, J. J., Hayden, T. G., … Yamane, M. (2014). Orbital forcing of the East Antarctic ice sheet during the Pliocene and Early Pleistocene. *Nature Geoscience*, *7*(11), 841–847. https://doi.org/10.1038/ngeo2273

Pausata, F. S. R., & Löfverström, M. (2015). *On the enigmatic similarity in Greenland 18O between the Oldest and Younger Dryas*. 470–477. https://doi.org/10.1002/2015GL066042.Received

Payne, A. J., Vieli, A., Shepherd, A. P., Wingham, D. J., & Rignot, E. (2004). Recent dramatic thinning of largest West Antarctic ice stream triggered by oceans. *Geophysical Research Letters*, *31*(23), 1–4. https://doi.org/10.1029/2004GL021284

Petit, J., Jouzel, J., Raynaud, D., Barkov, N. I., Barnola, J. M., Basile, I., Bender, M., Chappellaz, J., Davis, M., Delaygue, G., Delmotte, M., Kotiyakov, V. M., Legrand, M., Lipenkov, V. Y., Lorius, C., Pépin, L., Ritz, C., Saltzman, E., & Stievenard, M. (1999). Climate and atmospheric history of the past 420,000 years from the Vostok ice core, Antarctica. *Nature*, *399*(6735), 429–436. https://doi.org/10.1038/20859

Pol, K., Masson-Delmotte, V., Johnsen, S., Bigler, M., Cattani, O., Durand, G., Falourd, S., Jouzel, J., Minster, B., Parrenin, F., Ritz, C., Steen-Larsen, H. C., & Stenni, B. (2010). New MIS 19 EPICA Dome C high resolution deuterium data: Hints for a problematic preservation of climate variability at sub-millennial scale in the "oldest ice." *Earth and Planetary Science Letters*, *298*(1–2), 95–103. https://doi.org/10.1016/j.epsl.2010.07.030

Pollard, D., & DeConto, R. M. (2009). Modelling West Antarctic ice sheet growth and collapse through the past five million years. *Nature*, *458*(7236), 329–332. https://doi.org/10.1038/nature07809

Putman, A. L., Fiorella, R. P., Bowen, G. J., & Cai, Z. (2019). global perspective on local meteoric water lines: Meta-analytic insight into fundamental controls and practical constraints. *Water Resources Research*, *55*, 6896–6910. https://doi.org/10.1029/2019WR025181

Quiquet, A., Dumas, C., Ritz, C., Peyaud, V., & Roche, D. M. (2018). The GRISLI ice sheet model (version 2 . 0): calibration and validation for multi-millennial changes of the Antarctic ice sheet. *Geoscientific Model Development*, *11*, 5003–5025. https://doi.org/http//doi.org/10.5194/gmd-11-5003-2018

Raisbeck, G. M., Cauquoin, A., Jouzel, J., Landais, A., Petit, J. R., Lipenkov, V. Y., Beer, J., Synal, H. A., Oerter, H., Johnsen, S. J., Steffensen, J. P., Svensson, A., & Yiou, F. (2017). An improved north-south synchronization of ice core records around the 41ĝ€kyr 10Be peak. *Climate of the*

Past, *13*(3), 217–229. https://doi.org/10.5194/cp-13-217-2017

Raynaud, D., Jouzel, J., & Delmas, R. (1993). The Ice Record of Greenhouse Gases. *Science*, *259*(5097), 926–934. https://doi.org/10.1126/science.259.5097.926

Raynaud, D., Lipenkov, V., Lemieux-Dudon, B., Duval, P., Loutre, M. F., & Lhomme, N. (2007). The local insolation signature of air content in Antarctic ice. A new step toward an absolute dating of ice records. *Earth and Planetary Science Letters*, *261*(3–4), 337–349. https://doi.org/10.1016/j.epsl.2007.06.025

Ricci, R. W., & Ditzler, M. A. (1994). *Discovering the Beer-Lambert Law*. *71*(11), 983–985.

Rignot, E., Jacobs, S., Mouginot, J., & Scheuchl, B. (2013). Ice-shelf melting around antarctica. *Science*, *341*(6143), 266–270. https://doi.org/10.1126/science.1235798

Rignot, E., Mouginot, J., Scheuchl, B., Van Den Broeke, M., Van Wessem, M. J., & Morlighem, M. (2019). Four decades of Antarctic ice sheet mass balance from 1979–2017. *Proceedings of the National Academy of Sciences of the United States of America*, *116*(4), 1095–1103. https://doi.org/10.1073/pnas.1812883116

Ritter, F., Christian Steen-Larsen, H., Werner, M., Masson-Delmotte, V., Orsi, A., Behrens, M., Birnbaum, G., Freitag, J., Risi, C., & Kipfstuhl, S. (2016). Isotopic exchange on the diurnal scale between near-surface snow and lower atmospheric water vapor at Kohnen station, East Antarctica. *Cryosphere*, *10*(4), 1647–1663. https://doi.org/10.5194/tc-10-1647-2016

Ritterbusch, F., Chu, Y.-Q., Crotti, I., Dong, X.-Z., Gu, J.-Q., Hu, S.-M., Jiang, W., Landais, A., Lipenkov, V., Lu, Z.-T., Shao, L., Stenni, B., Team, T., Tian, L., Tong, A.-M., Wang, W.-H., & Zhao, L. (2020). Constraining ice core chronologies with 39Ar and 81Kr. *EGU General Assembly 2020*. https://doi.org/10.5194/egusphere-egu2020-21651

Ritz, C., Rommelaere, V., & Dumas, C. (2001). Modeling the evolution of Antarctic ice sheet over the last 420 , 000 years ' Implications for altitude changes in the Vostok region. *Journal of Geophysical Research*, *106*(D.23), 31,943-31,964.

Roberts, J., Galton-fenzi, B. K., Paolo, F. S., Donnelly, C., Gwyther, D. E., Padman, L., Young, D., Warner, R., Greenbaum, J., Fricker, H. A., Payne, J., Cornford, S., Brocq, A. L. E., Ommen, T. A. S. V. A. N., Blankenship, D. O. N., & Siegert, M. J. (2018). *Ocean forced variability of Totten Glacier mass loss*. 175–186.

Rohling, E. (2013). *Encyclopedia of Quaternary Science* (C. J. Elias, Scott A. Mock (ed.); Vol. 2). Elsevier.

Rohling, E., Hibbert, F., Grant, K., Galaasen, E., Irvalı, N., Kleiven, H., Marino, G., Ninnemann, U., Roberts, A., Rosenthal, Y., Schulz, H., Williams, F., & Yu, J. (2019). Asynchronous Antarctic and Greenland ice-volume contributions to the last interglacial sea-level highstand. *Nature Communications*, *10*(1). https://doi.org/10.1038/s41467-019-12874-3

Roland.C. Warner and W.F. Budd. (1998). Modelling the long-term response of the Antarctic ice sheet to global warnling. *Annals of Glaciology*, *27*, 161–168.

Rozanski, K., Araguas-Araguas, L., & Gonfiantini, R. (1992). Isotopic patterns in modern global precipitation. In *Climate change in continental isotopic records; In P. K. Swart, K. C. Lohmann, J. Mckenzie, & S. Savin (Eds.)* (Vol. 78, Issue Geophysical Monograph Series,). American Geophysical Union. https://doi.org/10.1029/GM078p0001

Scarchilli, C., Frezzotti, M., & Ruti, P. M. (2011). Snow precipitation at four ice core sites in East Antarctica: Provenance, seasonality and blocking factors. *Climate Dynamics*, *37*(9–10), 2107–2125. https://doi.org/10.1007/s00382-010-0946-4

Schilt, A., Baumgartner, M., Blunier, T., Schwander, J., Spahni, R., Fischer, H., & Stocker, T. F. (2010).

Glacial – interglacial and millennial-scale variations in the atmospheric nitrous oxide concentration during the last 800 , 000 years. *Quaternary Science Reviews*, *29*(1–2), 182–192. https://doi.org/10.1016/j.quascirev.2009.03.011

Schoof, C. (2007). Ice sheet grounding line dynamics: Steady states, stability, and hysteresis. *Journal of Geophysical Research: Earth Surface*, *112*(3), 1–19. https://doi.org/10.1029/2006JF000664

Schröder, L., Horwath, M., Dietrich, R., Helm, V., van den Broeked, M., & Ligtenberg, S. R. M. (2019). Four decades of surface elevation change of the Antarctic Ice Sheet from multi-mission satellite altimetry. *The Cryosphere*, *13*, 427–449. https://doi.org/10.5194/tc-2018-49

Schüpbach, S., Federer, U., Bigler, M., Fischer, H., & Stocker, T. F. (2011). A refined TALDICE-1a age scale from 55 to 112 ka before present for the Talos Dome ice core based on high-resolution methane measurements. *Climate of the Past*, *7*(3), 1001–1009. https://doi.org/10.5194/cp-7-1001-2011

Schüpbach, S., Federer, U., Kaufmann, P. R., Albani, S., Barbante, C., Stocker, T. F., & Fischer, H. (2013). High-resolution mineral dust and sea ice proxy records from the Talos Dome ice core. *Climate of the Past*, *9*(6), 2789–2807. https://doi.org/10.5194/cp-9-2789-2013

Severi, M., Udisti, R., Becagli, S., Stenni, B., & Traversi, R. (2012). Volcanic synchronisation of the EPICA-DC and TALDICE ice cores for the last 42 kyr BP. *Climate of the Past*, *8*(2), 509–517. https://doi.org/10.5194/cp-8-509-2012

Severinghaus, J., Grachev, A., Luz, B., & Caillon, N. (2003). A method for precise measurement of argon 40/36 and krypton/argon ratios in trapped air in polar ice with applications to past firn thickness and abrupt climate change in Greenland and at Siple Dome, Antarctica. *Geochimica et Cosmochimica Acta*, *67*(3), 325–343. https://doi.org/10.1016/S0016-7037(02)00965-1

Severinghaus, J. P., & Brook, E. J. (1999). Abrupt climate change at the end of the last glacial period inferred from trapped air in polar ice. *Science*, *286*(5441), 930–934. https://doi.org/10.1126/science.286.5441.930

Severinghaus, J., Sowers, T., Brook, E. J., Alley, R. B., & Bender, M. L. (1998). Timing of abrupt climate change at the end of the younger dryas interval from thermally fractionated gases in polar ice. *Nature*, *391*(6663), 141–146. https://doi.org/10.1038/34346

Severinghaus, Jeffrey P., Beaudette, R., Headly, M. A., Taylor, K., & Brook, E. J. (2009). Oxygen-18 of O2 records the impact of abrupt climate change on the terrestrial biosphere. *Science*, *324*(5933), 1431–1434. https://doi.org/10.1126/science.1169473

Sharp, Z. (2017). *Principles of Stable Isotope Geochemistry, 2nd Edition.* https://doi.org/https://doi.org/10.25844/h9q1-0p82

Shen, Q., Wang, H., Shum, C. K., Jiang, L., Hsu, H. T., & Dong, J. (2018). Recent high-resolution Antarctic ice velocity maps reveal increased mass loss in Wilkes Land, East Antarctica. *Scientific Reports*, *8*(1), 1–8. https://doi.org/10.1038/s41598-018-22765-0

Shukla, S. K., Crosta, X., & Ikehara, M. (2021). Sea Surface Temperatures in the Indian Sub-Antarctic Southern Ocean for the Last Four Interglacial Periods. *Geophysical Research Letters*, *48*(8), 1–11. https://doi.org/10.1029/2020GL090994

Sigl, M., Jenk, T. M., Kellerhals, T., Szidat, S., Ga, H. W., Wacker, L., Synal, H., Boutron, C., Barbante, C., & Gabrieli, J. (2009). *Instruments and Methods Towards radiocarbon dating of ice cores.* *55*(194), 985–996.

Sime, L. C., Tindall, J. C., Wolff, E. W., Connolley, W. M., & Valdes, P. J. (2008). Antarctic isotopic thermometer during a CO2 forced warming event. *Journal of Geophysical Research*, *113*(D24119), 1–16. https://doi.org/10.1029/2008JD010395

Sime, L. C., Wolff, E. W., Oliver, K. I. C., & Tindall, J. C. (2009). Evidence for warmer interglacials in East Antarctic ice cores. *Nature*, *462*. https://doi.org/10.1038/nature08564

Sodemann, H., Schwierz, C., & Wernli, H. (2008). *Interannual variability of Greenland winter precipitation sources : Lagrangian moisture diagnostic and North Atlantic Oscillation influence*. *113*, 1–17. https://doi.org/10.1029/2007JD008503

Sodemann, H., & Stohl, A. (2009). Asymmetries in the moisture origin of Antarctic precipitation. *Geophysical Research Letters*, *36*(22), 1–5. https://doi.org/10.1029/2009GL040242

Sowers, T., Bender, M., & Raynaud, D. (1989). Elemental and isotopic composition of occluded O2 and N2 in polar ice. *Journal of Geophysical Research*, *94*(D4), 5137–5150. https://doi.org/10.1029/JD094iD04p05137

Sowers, T., Bender, M., Raynaud, D., & Korotkevich, Y. S. (1992). δ15N of N2 in air trapped in polar ice: a tracer of gas transport in the firn and a possible constraint on ice age-gas age differences. *Journal of Geophysical Research*, *97*(D14). https://doi.org/10.1029/92jd01297

Sowers, Todd, & Bender, M. (1995). Climate records covering the last deglaciation. *Science*, *269*(5221), 210–214. https://doi.org/10.1126/science.269.5221.210

Sowers, Todd, Bender, M., Labeyrie, L., Martinson, D., Jouzel, J., Raynaud, D., Pichon, J. J., & Korotkevich, Y. S. (1993). A 135,000-year Vostok-SPECMAP common temporal framework. *Paleoceanography*, *8*(6), 737–766.

Spratt, R. M., & Lisiecki, L. E. (2016). A Late Pleistocene sea level stack. *Climate of the Past*, *12*(4), 1079–1092. https://doi.org/10.5194/cp-12-1079-2016

Steen-Larsen, H. C., Masson-Delmotte, V., Hirabayashi, M., Winkler, R., Satow, K., Prié, F., Bayou, N., Brun, E., Cuffey, K. M., Dahl-Jensen, D., Dumont, M., Guillevic, M., Kipfstuhl, S., Landais, A., Popp, T., Risi, C., Steffen, K., Stenni, B., & Sveinbjörnsdottír, A. E. (2014). What controls the isotopic composition of Greenland surface snow? *Climate of the Past*, *10*(1), 377–392. https://doi.org/10.5194/cp-10-377-2014

Steig, E. J., Morse, D. L., Waddington, E. D., Grootes, P. M., Mayewski, P. A., Twickler, M. S., & Whitlow, S. I. (2000). Wisconsinan and Holocene Climate History From an Ice Core At Taylor Dome ,. *Geografiska Annaler, Series A: Physical Geography*, *82*, 213–235.

Stenni, B., Buiron, D., Frezzotti, M., Albani, S., Barbante, C., Bard, E., Barnola, J. M., Baroni, M., Baumgartner, M., Bonazza, M., Capron, E., Castellano, E., Chappellaz, J., Delmonte, B., Falourd, S., Genoni, L., Iacumin, P., Jouzel, J., Kipfstuhl, S., … Udisti, R. (2011). Expression of the bipolar see-saw in Antarctic climate records during the last deglaciation. *Nature Geoscience*, *4*(1), 46–49. https://doi.org/10.1038/ngeo1026

Stenni, B., Masson-Delmotte, V., Johnsen, S., Jouzel, J., Longinelli, A., Monnin, E., Röthlisberger, R., & Selmo, E. (2001). An oceanic cord reversal during the last deglaciation. *Science*, *293*(5537), 2074–2077. https://doi.org/10.1126/science.1059702

Stenni, B., Masson-Delmotte, V., Selmo, E., Oerter, H., Meyer, H., Röthlisberger, R., Jouzel, J., Cattani, O., Falourd, S., Fischer, H., Hoffmann, G., Iacumin, P., Johnsen, S. J., Minster, B., & Udisti, R. (2010). The deuterium excess records of EPICA Dome C and Dronning Maud Land ice cores (East Antarctica). *Quaternary Science Reviews*, *29*(1–2), 146–159. https://doi.org/10.1016/j.quascirev.2009.10.009

Stenni, B., Proposito, M., Gragnani, R., Flora, O., Jouzel, J., Falourd, S., & Frezzotti, M. (2002). Eight centuries of volcanic signal and climate change at Talos Dome (East Antarctica). *Journal of Geophysical Research: Atmospheres*, *107*(9–10). https://doi.org/10.1029/2000jd000317

Sutter, J., Eisen, O., Werner, M., Grosfeld, K., Kleiner, T., & Fischer, H. (2020). Limited Retreat of the Wilkes Basin Ice Sheet During the Last Interglacial. *Geophysical Research Letters*, *47*(13).

https://doi.org/10.1029/2020GL088131

Suwa, M., & Bender, M. L. (2008). Chronology of the Vostok ice core constrained by O2/N2 ratios of occluded air, and its implication for the Vostok climate records. *Quaternary Science Reviews*, *27*(11–12), 1093–1106. https://doi.org/10.1016/j.quascirev.2008.02.017

Svensson, A., Andersen, K. K., Bigler, M., Clausen, H. B., Dahl-Jensen, D., Davies, S. M., Johnsen, S. J., Muscheler, R., Parrenin, F., Rasmussen, S. O., Röthlisberger, R., Seierstad, I., Steffensen, J. P., & Vinther, B. M. (2008). A 60 000 year Greenland stratigraphic ice core chronology. *Climate of the Past*, *4*(1), 47–57. https://doi.org/10.5194/cp-4-47-2008

T. Blunier, J. Chappellaz, J. Schwander, A. Da llenbach, B. Stauffer, T. F. Stocker, D. Raynaud, J. Jouzel, & H. B. Clausen, C. U. H. & S. J. J. (1998). Asynchrony of Antarctic and Greenland climate change during the last glacial period. *Nature*, *394*, 739–743.

Tauxe, L., Stickley, C. E., Sugisaki, S., Bijl, P. K., Bohaty, S. M., Brinkhuis, H., Escutia, C., Flores, J. A., Houben, A. J. P., Iwai, M., Jiménez-Espejo, F., McKay, R., Passchier, S., Pross, J., Riesselman, C. R., Rhl, U., Sangiorgi, F., Welsh, K., Klaus, A., … Yamane, M. (2012). Chronostratigraphic framework for the IODP Expedition 318 cores from the Wilkes Land Margin: Constraints for paleoceanographic reconstruction. *Paleoceanography*, *27*(2), 1–19. https://doi.org/10.1029/2012PA002308

Taylor, K. C., Alley, R. B., Meese, D. A., Spencer, M. K., Brook, E. J., Dunbar, N. W., Finkel, R. C., Gow, A. J., Kurbatov, A. V., Lamorey, G. W., Mayewski, P. A., Meyerson, E. A., Nishiizumi, K., & Zielisnki, G. A. (2004). Dating the Siple Dome (Antarctica) ice core by manual and computer interpretation of annual layering. *Journal of Glaciology*, *50*(170), 453–461. https://doi.org/10.3189/172756504781829864

The IMBIE Team. (2018). Mass balance of the Antarctic ice sheet from 1992 to 2017. *Nature*, *558*, 219–222. https://doi.org/10.1098/rsta.2006.1792

Tian, L., Ritterbusch, F., Gu, J. Q., Hu, S. M., Jiang, W., Lu, Z. T., Wang, D., & Yang, G. M. (2019). 81Kr Dating at the Guliya Ice Cap, Tibetan Plateau. *Geophysical Research Letters*, *46*(12), 6636–6643. https://doi.org/10.1029/2019GL082464

Tindall, J. C., Valdes, P. J., & Sime, L. C. (2009). Stable water isotopes in HadCM3 : Isotopic signature of El Nino – Southern Oscillation and the tropical amount effect. *Journal of Geophysical Research*, *114*, 1–12. https://doi.org/10.1029/2008JD010825

Tison, J.-L., Barnola, J.-M., & Petit, J.-R. (2015). Retrieving the paleoclimatic signal from the deeper part of the EPICA Dome C ice core. *The Cryosphere*, *9*(4), 1633–1648. https://doi.org/10.5194/tc-9-1633-2015-supplement

Traversi, R., Becagli, S., Castellano, E., Marino, F., Rugi, F., Severi, M., De Angelis, M., Fischer, H., Hansson, M., Stauffer, B., Steffensen, J. P., Bigler, M., & Udisti, R. (2009). Sulfate spikes in the deep layers of EPICA-dome C ice core: Evidence of glaciological artifacts. *Environmental Science and Technology*, *43*(23), 8737–8743. https://doi.org/10.1021/es901426y

Tsai, V. C., Stewart, A. L., & Thompson, A. F. (2015). Marine ice-sheet profiles and stability under Coulomb basal conditions. *Journal of Glaciology*, *61*(226), 205–215. https://doi.org/10.3189/2015JoG14J221

Tu, L. Y., Yang, G. M., Cheng, C. F., Liu, G. L., Zhang, X. Y., & Hu, S. M. (2014). Analysis of krypton-85 and krypton-81 in a few liters of air. *Analytical Chemistry*, *86*(8), 4002–4007. https://doi.org/10.1021/ac500415a

Turney, C. S. M., Fogwill, C. J., Golledge, N. R., McKay, N. P., van Sebille, E., Jones, R. T., Etheridge, D., Rubino, M., Thornton, D. P., Davies, S. M., Ramsey, C. B., Thomas, Z. A., Bird, M. I., Munksgaard, N. C., Kohno, M., Woodward, J., Winter, K., Weyrich, L. S., Rootes, C. M., … Cooper, A. (2020). Early Last Interglacial ocean warming drove substantial ice mass loss from

Antarctica. *Proceedings of the National Academy of Sciences of the United States of America*, *117*(8), 3996–4006. https://doi.org/10.1073/pnas.1902469117

Uemura, R., Masson-Delmotte, V., Jouzel, J., Landais, A., Motoyama, H., & Stenni, B. (2012). Ranges of moisture-source temperature estimated from Antarctic ice cores stable isotope records over glacial-interglacial cycles. *Climate of the Past*, *8*(3), 1109–1125. https://doi.org/10.5194/cp-8-1109-2012

Uemura, R., Motoyama, H., Masson-Delmotte, V., Jouzel, J., Kawamura, K., Goto-Azuma, K., Fujita, S., Kuramoto, T., Hirabayashi, M., Miyake, T., Ohno, H., Fujita, K., Abe-Ouchi, A., Iizuka, Y., Horikawa, S., Igarashi, M., Suzuki, K., Suzuki, T., & Fujii, Y. (2018). Asynchrony between Antarctic temperature and CO 2 associated with obliquity over the past 720,000 years. *Nature Communications*, *9*(1), 1–11. https://doi.org/10.1038/s41467-018-03328-3

Urbini, S., Cafarella, L., Zirizzotti, A., Bianchi, C., Tabacco, I., & Frezzotti, M. (2006). Location of a new ice core site at Talos Dome (East Antarctica). *Annals of Geophysics*, *49*(4–5), 1133–1138. https://doi.org/10.4401/ag-3104

Urbini, S., Frezzotti, M., Gandolfi, S., Vincent, C., Scarchilli, C., Vittuari, L., & Fily, M. (2008). Historical behaviour of Dome C and Talos Dome (East Antarctica) as investigated by snow accumulation and ice velocity measurements. *Global and Planetary Change*, *60*(3–4), 576–588. https://doi.org/10.1016/j.gloplacha.2007.08.002

Vaughn, B. H., White, J. W. C., Delmotte, M., Trolier, M., Cattani, O., & Stievenard, M. (1998). An automated system for hydrogen isotope analysis of water. *Chemical Geology*, *152*(3–4), 309–319. https://doi.org/10.1016/S0009-2541(98)00117-X

Veres, D., Bazin, L., Landais, A., Toyé Mahamadou Kele, H., Lemieux-Dudon, B., Parrenin, F., Martinerie, P., Blayo, E., Blunier, T., Capron, E., Chappellaz, J., Rasmussen, S. O., Severi, M., Svensson, A., Vinther, B., & Wolff, E. W. (2013). The Antarctic ice core chronology (AICC2012): An optimized multi-parameter and multi-site dating approach for the last 120 thousand years. *Climate of the Past*, *9*(4), 1733–1748. https://doi.org/10.5194/cp-9-1733-2013

Vimeux, F., Cuffey, K. M., & Jouzel, J. (2002). New insights into southern Hemisphere temperature changes from Vostok ice cores using deuterium excess correction. *Earth and Planetary Science Letters*, *203*(3–4), 829–843. https://doi.org/10.1016/S0012-821X(02)00950-0

Waelbroeck, C., Labeyrie, L., Michel, E., Duplessy, J. C., & Mcmanus, J. F. (2002). Sea-level and deep water temperature changes derived from benthic foraminifera isotopic records. *Quaternary Science Reviews*, *21*, 295–305.

Werner, M., Jouzel, J., Masson-Delmotte, V., & Lohmann, G. (2018). Reconciling glacial Antarctic water stable isotopes with ice sheet topography and the isotopic paleothermometer. *Nature Communications*, *9*(1), 1–10. https://doi.org/10.1038/s41467-018-05430-y

Wieser, M. E., & Schwieters, J. B. (2005). The development of multiple collector mass spectrometry for isotope ratio measurements. *International Journal of Mass Spectrometry*, *242*(2–3), 97–115. https://doi.org/10.1016/j.ijms.2004.11.029

Willi Dansgaard. (n.d.). *Frozen Annals* (O. At & D. The University of Copenhagen (eds.); 2004th ed.). Narayana Press, Odder, Denmark.

Wilson, D. J., Bertram, R. A., Needham, E. F., van de Flierdt, T., Welsh, K. J., McKay, R. M., Mazumder, A., Riesselman, C. R., Jimenez-Espejo, F. J., & Escutia, C. (2018). Ice loss from the East Antarctic Ice Sheet during late Pleistocene interglacials. *Nature*, *561*(7723), 383–386. https://doi.org/10.1038/s41586-018-0501-8

Winstrup, M., Svensson, A. M., Rasmussen, S. O., Winther, O., Steig, E. J., & Axelrod, A. E. (2012). An automated approach for annual layer counting in ice cores. *Climate of the Past*, *8*(6), 1881–1895. https://doi.org/10.5194/cp-8-1881-2012

Winstrup, Mai, Vallelonga, P., Kjær, H. A., Fudge, T. J., Lee, J. E., Riis, M. H., Edwards, R., Bertler, N. A. N., Blunier, T., Brook, E. J., Buizert, C., Ciobanu, G., Conway, H., Dahl-Jensen, D., Ellis, A., Emanuelsson, B. D., Hindmarsh, R. C. A., Keller, E. D., Kurbatov, A. V., … Wheatley, S. (2019). A 2700-year annual timescale and accumulation history for an ice core from Roosevelt Island, West Antarctica. *Climate of the Past*, *15*(2), 751–779. https://doi.org/10.5194/cp-15-751-2019

Wolff, E. W., Fischer, H., Fundel, F., Ruth, U., Twarloh, B., Littot, G. C., Mulvaney, R., Röthlisberger, R., De Angelis, M., Boutron, C. F., Hansson, M., Jonsell, U., Hutterli, M. A., Lambert, F., Kaufmann, P., Stauffer, B., Stocker, T. F., Steffensen, J. P., Bigler, M., … Gaspari, V. (2006). Southern Ocean sea-ice extent, productivity and iron flux over the past eight glacial cycles. *Nature*, *440*(7083), 491–496. https://doi.org/10.1038/nature04614

Yang, G.-M., Cheng, C. F., Jiang, W., Lu, Z.-T., Purtschert, R., Sun, Y.-R., Tu, L.-Y., & Hu, S.-M. (2013). Analysis of 85 Kr: a comparison at the 10 -14 level using micro-liter samples. *Scientific Reports*, *3*(1596), 1–5. https://doi.org/10.1038/srep01596

Yau, A., Bender, M., Blunier, T., & Jouzel, J. (2016). Setting a chronology for the basal ice at Dye-3 and GRIP: Implications for the long-term stability of the Greenland Ice Sheet. *Earth and Planetary Science Letters*, *451*, 1–9. https://doi.org/10.1016/j.epsl.2016.06.053

Yau, A., Bender, M., Marchant, D., & Mackay, S. (2015). Quaternary Geochronology Geochemical analyses of air from an ancient debris-covered glacier , Antarctica. *Quaternary Geochronology*, *28*, 29–39. https://doi.org/10.1016/j.quageo.2015.03.008

Yokochi, R. (2016). Recent developments on field gas extraction and sample preparation methods for radiokrypton dating of groundwater. *Journal of Hydrology*, *540*, 368–378. https://doi.org/10.1016/j.jhydrol.2016.06.020

Yokochi, R., Heraty, L. J., & Sturchio, N. C. (2008). Method for purification of Kr from environmental samples for analysis of radiokrypton isotopes. *AGU Fall Meeting Abstracts*, *2008*, H51C-0826.

Zappala, J. C., Baggenstos, D., Gerber, C., Jiang, W., Kennedy, B. M., Lu, Z. T., Masarik, J., Mueller, P., Purtschert, R., & Visser, A. (2020). Atmospheric 81Kr as an Integrator of Cosmic-Ray Flux on the Hundred-Thousand-Year Time Scale. *Geophysical Research Letters*, *47*(3), 1–7. https://doi.org/10.1029/2019GL086381

Università Ca'Foscari Venezia

DEPOSITO ELETTRONICO DELLA TESI DI DOTTORATO

DICHIARAZIONE SOSTITUTIVA DELL'ATTO DI NOTORIETA'

(Art. 47 D.P.R. 445 del 28/12/2000 e relative modifiche)

Io sottoscritto …Ilaria Crotti……………………………………………………………………………

nata …   a ……Seriate   (prov. BG) il 03/11/1190………………

residente a …Torre Boldone… in …Via Lomabrdia… n. 19……

Matricola (se posseduta) …956336………

Autore della tesi di dottorato dal titolo:

Dating and investigating climate variability at high resolution in the deep portion of the TALDICE ice core

Dottorato di ricerca in Scienza e gestione dei cambiamenti climatici

(in cotutela con l'Università di Paris-Saclay) Ciclo 33……………………

Anno di conseguimento del titolo 2022…………………

DICHIARO

di essere a conoscenza:

1) del fatto che in caso di dichiarazioni mendaci, oltre alle sanzioni previste dal codice penale e dalle Leggi speciali per l'ipotesi di falsità in atti ed uso di atti falsi, decado fin dall'inizio e senza necessità di nessuna formalità dai benefici conseguenti al provvedimento emanato sulla base di tali dichiarazioni;

2) dell'obbligo per l'Università di provvedere, per via telematica, al deposito di legge delle tesi di dottorato presso le Biblioteche Nazionali Centrali di Roma e di Firenze al fine di assicurarne la conservazione e la consultabilità da parte di terzi;

3) che l'Università si riserva i diritti di riproduzione per scopi didattici, con citazione della fonte;

4) del fatto che il testo integrale della tesi di dottorato di cui alla presente dichiarazione viene archiviato e reso consultabile via Internet attraverso l'Archivio Istituzionale ad Accesso Aperto dell'Università Ca'Foscari, oltre che attraverso i cataloghi delle Biblioteche Nazionali Centrali di Roma e Firenze;

5) del fatto che, ai sensi e per gli effetti di cui al D.Lgs. n. 196/2003, i dati personali raccolti saranno trattati,anche con strumenti informatici, esclusivamente nell'ambito del procedimento per il quale la presentazioneviene resa;

6) del fatto che la copia della tesi in formato elettronico depositato nell'Archivio Istituzionale ad Accesso Aperto è del tutto corrispondente alla tesi in formato cartaceo, controfirmata dal tutor, consegnata presso lasegreteria didattica del dipartimento di riferimento del corso di dottorato ai fini del deposito presso l'Archiviodi Ateneo, e che di conseguenza va esclusa qualsiasi responsabilità dell'Ateneo stesso per quantoriguarda eventuali errori, imprecisioni o omissioni nei contenuti della tesi;

7) del fatto che la copia consegnata in formato cartaceo, controfirmata dal tutor, depositata nell'Archivio di Ateneo, è l'unica alla quale farà riferimento l'Università per rilasciare, a richiesta, la dichiarazione di conformità di eventuali copie;

Data 09/12/2021   **Firma**   _Ilaria Crotti_

NON AUTORIZZO

l'Università a riprodurre ai fini dell'immissione in rete e a comunicare al pubblico tramite servizio on line entro l'Archivio Istituzionale ad Accesso Aperto la tesi depositata per un periodo di 12 (dodici) mesi apartire dalla data di conseguimento del titolo di dottore di ricerca.

DICHIARO

1) che la tesi, in quanto caratterizzata da vincoli di segretezza, non dovrà essere consultabile on line da terzi per un periodo di 12 (dodici) mesi a partire dalla data di conseguimento del titolo di dottore di ricerca;

2) di essere a conoscenza del fatto che la versione elettronica della tesi dovrà altresì essere depositata a cura dell'Ateneo presso le Biblioteche Nazionali Centrali di Roma e Firenze dove sarà comunque consultabile su PC privi di periferiche; la tesi sarà inoltre consultabile in formato cartaceo presso l'Archivio Tesi di Ateneo;

3) di essere a conoscenza che allo scadere del dodicesimo mese a partire dalla data di conseguimento deltitolo di dottore di ricerca la tesi sarà immessa in rete e comunicata al pubblico tramite servizio on line entrol'Archivio Istituzionale ad Accesso Aperto.

Specificare la motivazione:

☐ motivi di segretezza e/o di proprietà dei risultati e/o informazioni sensibili dell'Università Ca' Foscari diVenezia.

X motivi di segretezza e/o di proprietà dei risultati e informazioni di enti esterni o aziende private chehanno partecipato alla realizzazione del lavoro di ricerca relativo alla tesi di dottorato.

☐ dichiaro che la tesi di dottorato presenta elementi di innovazione per i quali è già stata attivata / siintende attivare la seguente procedura di tutela:

Embargo;

☐ Altro (specificare): all'inetrno del manoscritto sono presenti dati e figure che non sono ancora stati pubblicati.

A tal fine:

- dichiaro di aver consegnato la copia integrale della tesi in formato elettronico tramite auto-archiviazione (upload) nel sito dell'Università; la tesi in formato elettronico sarà caricata automaticamente nell'Archivio Istituzionale ad Accesso Aperto dell'Università Ca' Foscari, dove rimarrà non accessibile fino allo scadere dell'embargo, e verrà consegnata mediante procedura telematica per il deposito legale presso la BibliotecaNazionale Centrale di Firenze;

- consegno la copia integrale della tesi in formato cartaceo presso la segreteria didattica del dipartimento diriferimento del corso di dottorato ai fini del deposito presso l'Archivio di Ateneo.

Data 0 9 / 1 2 / 2 0 2 0 …………………… Firma *Ilaria Crotti*
……………………………………………………………

La presente dichiarazione è sottoscritta dall'interessato in presenza del dipendente addetto, ovvero sottoscritta einviata, unitamente a copia fotostatica non autenticata di un documento di identità del dichiarante, all'ufficio competente via fax, ovvero tramite un incaricato, oppure a mezzo posta.

Firma del dipendente addetto ……………………………………………………………

Ai sensi dell'art. 13 del D.Lgs. n. 196/03 si informa che il titolare del trattamento dei dati forniti è l'Università Ca'Foscari - Venezia.

I dati sono acquisiti e trattati esclusivamente per l'espletamento delle finalità istituzionali d'Ateneo; l'eventuale rifiuto difornire i propri dati personali potrebbe comportare il mancato espletamento degli adempimenti necessari e delle procedure amministrative di gestione delle carriere studenti. Sono comunque riconosciuti i diritti di cui all'art. 7 D. Lgs.n. 196/03.

Estratto per riassunto della tesi di dottorato

Studente: Ilaria Crotti

Matricola: 956336

Dottorato: Scienza e Gestione dei Cambiamenti Climatici

Ciclo: 33

Titolo della tesi: Dating and investigating climate variability at high resolution in the deep portion of the TALDICE ice core

Abstract:

Le carote di ghiaccio sono lunghi cilindri estratti dalle calotte polari e contengono informazioni riguardanti le passate condizioni climatiche ed ambientali. La carota di ghiaccio TALDICE, profonda 1620 m, é stata estratta a Talos Dome, in Antartide orientale. Studi precedenti si sono focalizzati sulla datazione di questo archivio e sulla costruzione della sua cronologia, che è stata definita fino alla profondità di 1438 m, corrispondente ad un'età di 150,000 anni fa. Questa tesi si concentra sull'esplorazione della porzione di TALDICE al di sotto di 1438 m di profondità.

Nella prima parte delle tesi, le nuove misure isotopiche effettuate sia nella matrice ghiaccio che in quella gas vengono utilizzate per costruire la scala d'età TALDICE deep1, con l'applicazione del modello IceChrono1. La cronologia della parte più profonda della carota è definita fino alla profondità di 1548 m ed estende il record climatico fino all'età di 343,000 anni. La seconda sezione della tesi è dedicata all'interpretazione del segnale isotopico di TALDICE durante i passati tre periodi interglaciali. L'ipotesi qui proposta è che le anomalie osservate nel segnale isotopico sono state prodotte dalla diminuzione dell'altitudine del sito di Talos Dome, dovuta alla perdita di volume di ghiaccio conseguente all'arretramento della linea di ancoraggio della calotta del bacino subglaciale Wilkes. La terza sezione della tesi è invece dedicata allo sviluppo della metodologia di datazione con l'argon, riducendo la quantità di ghiaccio necessaria. Questo nuovo metodo è applicato per datare 9 campioni di ghiaccio di TALDICE, e qui vengono presentati i risultati preliminari.

Ice cores are long cylinders extracted from ice sheets containing information about past environmental and climatic conditions. The TALDICE ice core is a 1620 m depth core drilled at Talos Dome, in East Antarctica. Several previous studies focused on dating this core and an age scale has been defined only until 1438 m depth at an age of about 150,000 years ago, limiting the past climate reconstructions to the last climatic cycle. This thesis focuses on the poorly explored deep portion of the core below 1438 m depth.

In the first part of the thesis, new TALDICE isotopic measurements in both ice and gas matrixes below 1438 m are used to build the final TALDICE deep1 ice/gas age-depth relationship with the IceChrono1 model. The chronology for the deeper part of the core is here defined until 1548 m depth and extends the climatic record back to 343,000 years ago. The second part of this thesis is centred on the interpretation of the unique TALDICE isotopic signal during past interglacials. The proposed interpretation indicates that the interglacial anomalies in the isotopic record have been produced by lowering of the site elevation at Talos Dome due to ice loss and inland retreat of the Wilkes Subglacial Basin grounding line. The third and last part of this work focuses on the development of the argon dating technique, with the aim of reducing the amount of ice employed. The novel methodology has been tested on 9 TALDICE samples, and preliminary results are here shown.

Firma dello studente

Ilaria Crotti